

Search for Higgs Bosons Decaying into Long-Lived Exotic Particles in the LHCb Experiment

THÈSE N° 5025 (2011)

PRÉSENTÉE LE 13 MAI 2011
À LA FACULTÉ SCIENCES DE BASE
LABORATOIRE DE PHYSIQUE DES HAUTES ÉNERGIES 1
PROGRAMME DOCTORAL EN PHYSIQUE

ÉCOLE POLYTECHNIQUE FÉDÉRALE DE LAUSANNE

POUR L'OBTENTION DU GRADE DE DOCTEUR ÈS SCIENCES

PAR

Neal GAUVIN

acceptée sur proposition du jury:

Prof. M. Q. Tran, président du jury
Prof. A. Bay, directeur de thèse
Dr W. Hulsbergen, rapporteur
Dr P. Jablonka, rapporteur
Prof. C. Matteuzzi, rapporteur



ÉCOLE POLYTECHNIQUE
FÉDÉRALE DE LAUSANNE

Suisse
2011

Résumé

LES QUATRE EXPÉRIENCES du Grand Collisionneur de Hadrons (LHC) au CERN ont commencé à prendre leur premières données à $\sqrt{s} = 7$ TeV, ouvrant une nouvelle ère trépidante pour la physique des particules. Le détecteur LHCb est un spectromètre à un seul bras dédié à la mesure précise de la violation \mathcal{CP} , et à l'étude de désintégrations rares des hadrons b .

Dans ce travail, nous avons exploité l'excellente capacité du détecteur à reconstruire les vertex de désintégration dans la région proche du point d'interaction avec une résolution de quelques dizaines de microns.

Pour obtenir une telle résolution, une mesure précise des trajectoires des particules chargées est essentielle. Le trajectographe interne (IT) reconstruit les trajectoires des particules volant dans la partie interne de l'expérience LHCb. Pendant mon travail de thèse, j'ai participé à la construction de l'IT à travers l'établissement d'une procédure détaillée pour son assemblage. Cela inclut la préparation et le test minutieux de nombreuses pièces, parmi lesquelles 386 senseurs. Les douze boîtes composant l'IT ont été intégrées à l'expérience durant l'été 2008. Après alignement, la précision globale sur la position des modules de l'IT est en moyenne de $19\text{ }\mu\text{m}$. La rigueur et les tests systématiques entourant l'assemblage de l'IT ont permis de garder la fraction des pistes inutilisables au-dessous de 1%.

Plusieurs modèles théoriques au-delà du Modèle Standard prédisent l'existence de particules exotiques à long temps de vie qui sont potentiellement détectables dans des expériences comme LHCb. Nous avons adapté les programmes de simulation de manière à simuler certains de ces modèles, produisant un ensemble pertinent de topologies.

Des algorithmes et méthodes ont été développés pour sélectionner les vertex qui sont compatibles avec la désintégration de particules exotiques à long temps de vie. Les caractéristiques des candidats des différents modèles sont exhibées, menant à la confection de sélections au niveau du trigger et de l'analyse.

Finalement, les données prises en 2010 ont été analysées pour identifier des vertex secondaires pouvant être associés avec la désintégration de telles particules. Les paires de candidats ont été combinées pour reconstruire un candidat Higgs. L'analyse a sélectionné zéro candidat, avec une efficacité sur le signal de l'ordre de 0.2-0.3% pour certains points de l'espace des paramètres d'un modèle choisi. Cela nous a permis de mettre une limite à leur section efficace de production. L'analyse du bruit MC est cohérente avec zéro événement attendu pour la luminosité intégrée.

Mots clés : CERN, LHC, LHCb, Inner Tracker, Physique au-delà du Modèle Standard, particules exotiques à long temps de vie.

Abstract

THE FOUR EXPERIMENTS of the Large Hadron Collider (LHC) at CERN have collected their first data at $\sqrt{s} = 7$ TeV, hailing an exciting era in particle physics. The LHCb detector is a single-arm forward spectrometer, dedicated to precision measurements of \mathcal{CP} violation, as well as to the study of rare b -hadron decays. In this work the excellent capability of the detector to reconstruct decay vertices in the region close to the interaction point with a resolution of few tenths of microns has been exploited.

To achieve such a resolution, a precise measurement of the charged particle trajectories is essential. The Inner Tracker is the detector that provides tracking information for the particles flying in the innermost part of LHCb. While preparing this thesis, I contributed to the construction of the Inner Tracker by setting up of an assembly procedure for the twelve detector boxes. This included the preparation and thorough testing of numerous pieces, among them 386 sensor modules. Inner Tracker detector boxes have been installed in the LHCb cavern in Summer 2008. After software alignment, the overall precision of the Inner Tracker modules position is on average $19\text{ }\mu\text{m}$ along the relevant direction. The careful box assembly and the quality tests along the procedure allowed to keep the fraction of dead strips below 1%.

Several theoretical models beyond the Standard Model predict the existence of exotic long-lived particles that are potentially detectable in accelerator experiments like LHCb. The simulation software have been adapted in order to simulate some of the models producing a relevant set of topologies. The main features of these selected models are shown at generator level.

Algorithms and methods have been developed to select events with vertices that are consistent with the decay of exotic long-lived particles. Key features of the candidates for the selected models are shown, leading to the design of on-line (trigger) and offline selections.

Finally, we have analysed the LHCb data collected in 2010 to identify secondary vertices which can be associated with the decay of such particles. Pairs of candidates have been combined to reconstruct Higgs boson candidates. The analysis has selected zero candidate, with an efficiency to the signal at the level of 0.2-0.3% for some chosen points in the parameter space of a chosen theoretical model. This allowed to set limits on their production cross-section. The analysis of background MC events is consistent with an expectation of zero event for our integrated luminosity.

Keywords : CERN, LHC, LHCb, Inner Tracker, Physics beyond the Standard Model, long-lived exotic particles.

Contents

Introduction	1
1 Theoretical Models	3
1.1 Standard Model	3
1.2 Limits of the Standard Model	6
1.3 Beyond the Standard Model : Supersymmetry	13
1.3.1 mSUGRA with Baryon Number Violation	23
1.3.2 Bilinear R-parity violating supersymmetric models	27
1.3.3 Gauge-Mediated Supersymmetry Breaking Models	29
1.3.4 Split Supersymmetry	30
1.4 Beyond the Standard Model :	
Hidden Valley models	33
1.5 Beyond the Standard Model : And Many More...	36
2 The LHC and LHCb experiment	39
2.1 The LHC challenge	39
2.2 The LHC Experiments	41
2.3 The LHCb Experiment	43
2.3.1 The Particle Identification System	45
2.3.2 The Tracking System	47
2.3.2.a The Vertex Locator	49
2.3.2.b The Track Reconstruction	53
2.3.2.c Interactions with the Detector	55
2.3.2.d Performance	56
2.3.3 The Trigger System	56
2.3.3.a The Level-0 Trigger	58
2.3.3.b The High-Level Trigger : HLT1	59
2.3.3.c The High-Level Trigger : Hlt2	60
2.3.3.d Global Event Cut	61
2.3.4 The Stripping Framework	61
2.3.5 The LHCb Software	62

3	Assembly of the Inner Tracker	65
3.1	Preparation of the different Components	68
3.1.1	The Detector Modules	68
3.1.1.a	Burn-in Tests	68
3.1.1.b	Metrological Survey	70
3.1.1.c	Preparation	73
3.1.2	The Cover	73
3.1.2.a	The Cover Preparation	74
3.1.3	The Box Container	76
3.1.4	The Cooling Rods	78
3.1.5	The Assembly Set-ups	81
3.2	Assembly Procedure of an Inner Tracker Detector Box	82
3.2.1	Mounting of the Cover on the Sliding set-up	83
3.2.2	Adjustment of the Detector Box Position	83
3.2.3	Mounting the first Cooling Rod (type B or V-X2)	83
3.2.4	Fixation of the first Cooling Rod under the Cover	85
3.2.5	Mounting of the second Cooling Rod	85
3.2.6	High Voltage Test of the Modules	86
3.2.7	Closing of the cooling Circuit by connecting the two cooling Rods	86
3.2.8	Cooling Circuit Leak Test	87
3.2.9	Survey of the visible Layers X1 and X2	88
3.2.10	Full electrical Tests	88
3.2.11	Test of the Height of the Modules	88
3.2.12	Final Insertion of the Detector into the Container	90
3.3	Performance of the Inner Tracker	92
4	Generation and Simulation of the Data Samples	95
4.1	The Interface to Pythia : PythiaProduction	95
4.2	A new Selection Tool : PythiaLSP	97
4.3	A new Interface to Geant4 : GenerationToSimulation	98
4.4	Simulation in Geant4	98
4.5	New Event Type Numbers for Supersymmetry	99
4.6	New Option Files	99
4.7	Choice of the generator cuts	100
5	Characteristics of the Selected Models	103
5.1	LLP and the LHCb Acceptance	103
5.2	Distance of flight and radial distance	104
5.3	Track multiplicity	107

5.4	Reconstructed mass from charged particles	108
5.5	Transverse momentum of the daughters	111
5.6	The Mother	112
5.7	Expected Number of Events	112
6	Inclusive Selection of Events with Displaced Vertices	115
6.1	Presentation of the Algorithms	116
6.1.1	Reconstruction of the Vertices	116
6.1.2	A Beam Line Position Algorithm	118
6.1.3	Preselection of the LLPs	119
6.1.3.a	Estimation of the Track Momentum	119
6.1.3.b	Track Quality Check	120
6.1.4	The Selection of the Displaced Vertices	121
6.2	Optimisation of the Algorithms	122
6.2.1	The Reconstruction Procedure	122
6.2.2	Selection of the Primary Vertices	125
6.2.3	Preselection and Selection of the LLPs	127
6.2.3.a	Primary Vertices	127
6.2.3.b	Problem with LHCb MC Simulation	130
6.2.3.c	Particle-gas Interactions	130
6.2.3.d	Interactions with Detector Matter	132
6.2.3.e	SM LLPs and other Cuts	135
6.2.4	Back to the Optimisation of the Reconstruction	138
6.2.5	Vertex Reconstruction Efficiency	139
6.2.6	Perspective	140
6.3	Properties of the Selected LLPs	145
6.4	Trigger and Stripping	151
7	Search for Higgs Bosons decaying into LLPs	153
7.1	Samples of Data and MC Events	153
7.2	Selection of Pairs of LLP Candidates	155
7.3	Selection of the Mother Candidates	161
7.4	Final Selection	166
7.5	The Event	169
7.6	Systematic Effects	171
7.6.1	Cross Check with Vertices from Matter Interactions	171
7.6.2	Contributions to the Efficiency and Systematics Estimate	174
7.7	Discussion and Outlook	177
7.7.1	Background	177
7.7.2	How to present these Results ?	179
7.7.3	Results from more Points in the BV Parameter Space	180

Conclusion	185
A Properties of the Selected PVs	189
B Optimisation of the Vertex Reconstruction	197
C Re-Optimisation of the Vertex Reconstruction	201
D The Three Trigger Selections	207
E The Four Stripping Selections	211
F More Figures	215
Acronyms	221
Bibliography	242

Introduction

There is a fifth dimension beyond that which is known to man. It is a dimension as vast as space and as timeless as infinity. It is the middle ground between light and shadow, between science and superstition; and it lies between the pit of man's fears and the summit of his knowledge. This is the dimension of imagination. It is an area which we call "the Twilight Zone."

Rod Sterling

THE OPERATION of the Large Hadron Collider at CERN promises an eventful decade of both confirmation and, hopefully, surprise. Its primary goal of observing the Higgs boson would provide the final piece in the Standard Model jigsaw. However, there is a very strong possibility of finding evidence of supersymmetric particles or other new physics beyond the Standard Model. Either of these will herald the dawn of a new era in particle physics. The current century may be as profoundly exciting as that last.

This thesis is organised as follows :

Chapter 1 presents the Standard Model of Particle Physics and raises its limitations. I discuss some theoretical models to go beyond it in a coherent and more general framework, focusing on the ones predicting long-lived particles that would be potentially detectable in accelerator experiments, like LHCb.

Chapter 2 introduces the LHC experiments and in particular the LHCb detector. Its particle identification and tracking systems, as well as the trigger system, are examined. This chapter closes with the presentation of the common software for simulation and analysis of the data.

I had the opportunity to accompany the LHCb Inner Tracker from the testing of the detector modules to the integration of the detector boxes in the experiment. Chapter 3 addresses my contribution to the testing of the modules and the assembly of the detector boxes. The assembly procedure is given in details and the current state of the Inner Tracker is given.

Chapter 4 reviews the adaptations to the LHCb software chain that were necessary to properly simulate the data samples presented in Chap. 1.

Chapter 5 explores the interesting features at generator level of the selected models that would allow to bring to light the existence of long-lived “exotic” particles, as well as their expected number of events. The attention will also be given to the case of the decay of a Higgs-like boson into two such long-lived particles.

In Chapter 6, I present the algorithms and their optimisation used to select events with vertices that are consistent with the decay of exotic long-lived particles. Key features of the candidates for the selected models are exhibited, leading to the design of trigger and offline selections.

Finally, I have analysed in Chap. 7 the data collected in 2010 to identify secondary vertices which can be associated long-lived exotic particles. In the final analysis, the candidates have been combined to reconstruct a parent Higgs boson.

Chapter 1

Theoretical Models



The Standard Model of Particle Physics provides a successful description of phenomena up to the 100 GeV energy scale. It nevertheless shows strong limitations that are raised here. We discuss here some theoretical models to go beyond it in a coherent and more general framework, focusing on the ones predicting long-lived particles that would be potentially detectable in a collider experiment.

1.1 Standard Model

AT THE TURN OF the 20th century, physicists began to glimpse the remarkable nature of ordinary matter. The atomic theory was dominating. One of the philosophical motivations behind the atomic theory was the desire to explain the diversity of matter by assuming the existence of just a few fundamental and indivisible atoms. But by that time over 90 varieties of atoms were already known. This is obviously an uncomfortably large number for a description of nature assumed to be fundamental. Relative weights of the atoms are approximately multiples of the weights of the hydrogen atom (Prout). The mass of each atoms is associated with a specific quantity of electrical charge (Faraday and Webber). These are very troubling facts.

What is more, classical physics of mechanics, thermodynamics and electromagnetism were found to be inadequate to account for apparent mysteries in the behaviour of matter and light.

Then, early atomic experiments quickly revealed an unexpected richness in the structure of matter. The discovery of electrons (which may originate from within indivisible atoms) by Thomson, X-rays by Röntgen, and the evidence for disintegration of atoms with the discovery of radioactivity (α , β and γ rays), all these among other significant facts forced upon physicists more sophisticated descriptions of the natural world. Modern physics was upon to begin. From the constancy of the speed of light came out special relativity and from the interaction of light with matter quantum mechanics. A later combination of both gave birth to the relativistic quantum theory. Its consistency led to the discovery of the first anti-particle, the positron e^+ , which led in turn to the concept of quantum fields. The theory of interacting quantum fields provides us with the most satisfactory description of the behaviour of matter. The quantum electrodynamics (QED) successfully describes the interactions of electrically charged particles via photons. All calculations in quantum field theory follow from the specification of the correct Lagrangian, which is determined by the conservation obeyed by the force under study.

Similar treatment was applied to the weak force, discovered in the β decay of nuclei, already in the 30s. This gives rise to the Fermi theory and the current-current theory of weak interactions. The desire to understand the weak force, in particular, led eventually to recognition of the role of gauge symmetry as a vital ingredient in theories of the micro-world. The basic method of gauge theory is to ensure that the Lagrangian describing the interaction of particle wave-functions remains invariant under certain symmetry transformations which reflect conservation laws observed in nature.

However, gauge invariance requires the gauge particles to be mass-less. The non-observation so far of any weak gauge bosons was pushing forward the idea of a high mass.

In the late 60s, Weinberg and Salam independently formulated a unified theory for the weak and electromagnetic interactions, based in part on the work of Glashow. It included the successful theory of QED and provided a description of the weak force in terms of the exchange of massive vector bosons. It ensures the masslessness of the photon, whilst giving mass to the weak interaction gauge bosons W^\pm and Z^0 . This is achieved by the Higgs mechanism and a suitable choice of Higgs fields. This theory is called the Glashow-Weinberg-Salam electro-weak theory.

In 1983, the discovery of the W^\pm and Z^0 bosons at CERN with the predicted masses was a great triumph for the electro-weak theory and indeed for the concept of non-Abelian gauge theories.

At about the same time as the electro-weak model was being developed, physicists started to use “deep inelastic scattering” experiments to probe the

interior of the proton. They gave the first indications that the proton was not truly elementary, but composed of point-like objects, called quarks. As the physical reality of quarks gained wider acceptance, a new gauge theory was formulated in an attempt to explain the strong force between them : quantum chromodynamics (QCD), which attributes the strong force to the exchange of certain gauge bosons called gluons. The strong interaction is named after the fact that it couples particles with a strength 10^2 times larger than the electromagnetic force and 10^{13} times larger than the weak interaction. It is also called the nuclear or colour force, and is responsible for the cohesion of quarks in the hadrons and of hadrons together, like the neutrons and the protons in an atomic nucleus.

Together, QCD and the Glashow-Weinberg-Salam electro-weak theory constitute the so-called “Standard Model of elementary particle physics” (SM), formulated in the early seventies. Mathematically, the particles and their interactions obey the structure given by the non-abelian local gauge symmetry theory underlying the model, namely

$$SU(3)_c \otimes SU(2)_L \otimes U(1)_Y \quad (1.1)$$

The $SU(3)_c$ group describes the strong interaction by the QCD. The strong force is governed by 8 mass-less gluons (the generators of the group) as mediator particles and acts on the “colour” charged particles, namely the quarks. The three colours are red, blue and green. Gluons carry two colours.

The $SU(2)_L \otimes U(1)_Y$ denotes the electro-weak interactions. In particular, $SU(2)_L$ refers to weak isospin, involving only left-handed particles, while $U(1)_Y$ refers to weak hyper-charge including particles of both chiralities. The weak interactions exist through charged current interactions mediated by the W^\pm bosons, acting on exclusively left-handed particles and right-handed antiparticles, while neutral current interactions take place through the Z^0 boson and affect both chiralities. The weak interaction acts on the flavor of the quarks and leptons. The vector boson of the electromagnetic force is the photon γ .

The Standard Model (SM) includes two families of particles, 6 leptons ($e, \mu, \tau, \nu_e, \nu_\mu, \nu_\tau$) and 6 quarks (u, d, c, s, t, b) plus their anti-matter conjugates. Quarks and leptons are the two fundamental building blocks of the “material” world. Yet only the up and down quarks and the electron are stable enough to form the “ordinary” matter, namely atoms, out of which we ourselves are made.

Equality in the number of quarks and leptons generations (families) is needed to obtain the triangular anomaly cancellation [1], and thus the consistency of the SM. If a fourth generation of quarks were to be detected, one

would expect to encounter a fourth generation of leptons as well. Experimental studies of the Z decay width at large electron–positron collider (LEP) have yield to the remarkable number of 2.9841 ± 0.0083 for the number of generations [3]. Although not an absolute proof, this a strong hint in favour of just three generations of quarks and leptons and of the completeness of the observed particle spectrum.

At this point, the SM implies mass-less fields, contrary to the experimentally observed mass spectrum. As a remedy, the SM introduces the Higgs Mechanism (1964), so called from its author Peter Higgs.

In its simplest form, the Higgs mechanism calls for the existence of an electrically neutral scalar boson to generate masses for the gauge bosons and exploits the spontaneous breaking of the gauge symmetry (SSB) of $SU(2)_L \otimes U(1)_Y$ (the electro-weak part) down to $U(1)_{EM}$ (electromagnetic) symmetry. The fermion masses arise then through couplings (Yukawa) to this new boson. Nonetheless such a mechanism does not provide an explanation for the observed hierarchy of masses. They are essentially free parameters in the theory and have to be measured. Whether or not the Higgs mechanism is the correct symmetry-breaking mechanism remains to be determined.

At the time of writing this thesis, the Higgs boson remains unobserved. Its mass is strongly constrained, both theoretically and experimentally (electro-weak precision measurements). In particular, all SM processes receive quantum correction corresponding to loops involving virtual Higgs bosons. Precision measurements of these processes suggest that the most likely value for the Higgs is around 117 GeV. The LEP[2] experiments put a lower bound at 114.4 GeV. The Higgs may be just around the corner ! Masses around 160 GeV are excluded from Tevatron experiments. The large hadron collider (LHC)¹, when reaching its design energy of 14 TeV, will be able to cover a mass range up to 1 TeV. Until the discovery of the Higgs (or equivalent) the SM will not be proved. Most extensions of the SM retain this mechanism as the primary method, but with more complicated Higgs sectors and more Higgs bosons, as in case of supersymmetry, for example.

For a broader review of the SM, please consult [5][6][7][14].




1.2 Limits of the Standard Model

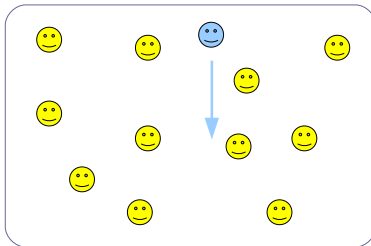
The SM provides us with a convincing picture of the fundamental structure of observable matter in terms of certain point-like elementary particles, interacting together via bosons. All other physics (nuclear, atomic, nano, chemistry, ...) is believed to derive from the SM. In the 90s, a decade of

¹See Sec. 2.1.

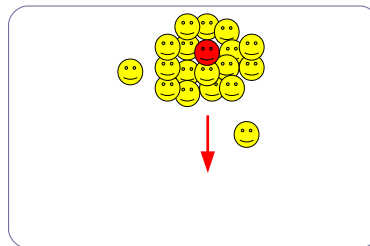
Representation of the Higgs Mechanism

Let's introduce a person in a room full of journalists, symbolizing the Higgs field.

 = unknown people  = journalist  = a "people"



Easy moving



Difficult moving, more inertia

The most popularity ~ the greater the degree of interaction with the Higgs field ~ the heavier the mass of the particle

The Higgs boson would be like an agglutination of journalists propagating a rumour...

experiments has confirmed the SM and its generation structure of quarks, leptons and gauge bosons with an impressive accuracy, and has established it beyond reasonable doubt. Not one of the numerous measurements performed has shown a significant deviation from the SM predictions.

For example, the electron has a magnetic moment of modulus $g|e|\hbar/(4m_e c)$, where g is called the gyromagnetic ratio. While classical electrodynamics erroneously suggest $g = 1$, the Dirac equation gives $g = 2$ and QED predicts a small deviation from this value. The theoretical prediction, computed perturbatively up to order α^4 is

$$\left(\frac{g-2}{2}\right)\Big|_{\text{th}} = 0.001159652140(5)(4)(27)$$

while the experimentally measured value - one of the most accurate ever performed in the history of science - is

$$\left(\frac{g-2}{2}\right)\Big|_{\text{exp}} = 0.001159652187(4)$$

The agreement between theory and experiment at the level of 10 decimals is spectacular.

If the SM is undoubtedly one of the crowning achievements of the 20th century, it still has its *limitations*...

The most striking one is the absence of gravity. There is nowadays no quantum field theory to account for the general relativity and the gravitational force, which could be incorporated in the SM. The SM therefore does not provide a full description of the observed natural phenomena. It is neither a good theory to describe the very early Universe.

Furthermore, observations of supernovae in the late nineties, strongly corroborated by the analysis of the cosmic microwave background (CMB) [33], led astronomers to conclude that the Universe is presently undergoing an accelerated expansion [32]. Naively, the gravitational interaction between the constituents of the Universe was expected to slow down its expansion. The most plausible explanation is to resort to the existence of an unknown form of energy that drives the acceleration: the “dark energy”.

Another limits was found in the precise observation of the rotational speeds of galaxies which pointed out the lack of luminous matter (e.g. stars, dust, gas)[31]. If General Relativity is correct, unexplained matter must be distributed throughout the galaxies in order to explain the data. The SM does not furnish any such candidate for filling the Universe. More evidence for “dark” (invisible) matter has been provided recently by the observation of gravitational lensing effects by the Hubble Space Telescope.

“Dark” matter and “dark” energy are believed to make up 21.4% and 74.2%, respectively, of the total energy density of the Universe today. This is a great setback for the SM. The baryonic matter, described by the SM, account only for 4.4% of the content of the Universe.

If the Big Bang would have produced an equal amount of matter and anti-matter, they would have annihilated during the cool-down, resulting in photons exclusively. The obvious presence of matter in the Universe, a left-over of the annihilation, tells us that matter was produced in excess with respect to antimatter. This is called the Baryon asymmetry. Even though the \mathcal{CP} violation explains a matter-antimatter asymmetry, precise measurements of the \mathcal{CP} violating processes within the SM indicate that these processes are not sufficiently large to account for this predominance.

Another cloud in the blue sky of the SM comes with the requirement of at least 19 independent and arbitrary input parameters :

- 6 quarks masses, 3 lepton masses,
- 3 gauge couplings (e , θ_W and α_s),
- 3 Cabibbo mixing angles and the \mathcal{CP} -violating Kobayashi-Maskawa complex phase,
- the QCD vacuum angle,
- the Higgs mass and the vacuum expectation value v .

That’s quite a lot for a model that aspires to be a fundamental theory. And already a strong reason to believe that there must be a simpler theory underlying the SM. Think about the early days of chemistry, when the properties of hundreds of elements were catalogued in the periodic table. As well as when the myriad of hadrons were explained to be composed of only six quarks.

Besides, discoveries made at, for example, Super-Kamiokande [8] or SNO [9], showed a mixing between neutrino flavours, similar to the one between quarks, and hence opened the way for neutrino masses. At least nine more parameters could be introduced to accommodate neutrinos oscillations

- 3 neutrino masses,
- 3 real mixing angles,
- 3 \mathcal{CP} -violating phases.

This has grave consequence for the SM in its present form. In the SM, quarks (fermions) get their mass from gauge-invariant terms in the Lagrangian coupling a left-handed quark, a right-handed quark and a Higgs boson (three-particle Yukawa interaction). No right-handed neutrinos exist in the SM, therefore no such terms can arise, and neutrinos cannot acquire a mass.

A minimal extension of the SM can be the addition of a “sterile” right-handed neutrino, that is to say, which carries no charge with respect to any other multiplet of the SM gauge group, and therefore does not interact. This trick paves the way for a Yukawa term, allowing the neutrinos to gain mass in the same way as all other fermions in the SM. There is however something rather disturbing. The cosmological observations set an upper bound for the sum of absolute neutrino masses of about 0.7 eV. Bear in mind that the electron mass is 511 keV, 6 order of magnitude larger. If the neutrinos acquire their mass the same manner as all other fermions, why should they be so tiny ?

Neutrino oscillations represent the first concrete evidence that the SM is incomplete and that there *is* physics that goes “beyond the Standard Model” (BSM), but which reproduces the results of the SM in the regimes where the SM has been shown to be experimentally correct.

If we step aside and take a more distanced look, the core of the SM, based on the paradigms of quantum mechanics, Lorentz and Gauge invariance, is an untidy mixture of unexplained structures, forced upon us by consistency requirements.

Why are there three families of fermions ? Why is there such an unbalance in the fermion mass distribution, with a 511 keV electron facing a 175 GeV top quark, not mentioning a possible neutrino at the eV scale ? Why do the quarks mix, a little bit. Why are neutrinos observed to mix so strongly ? Why are there three gauge groups with so different couplings at the actual experimental energy scale ?

Apart from the results of the neutrino oscillation experiments, there is presently no data which contradicts the SM and which would point towards new theories.

A pragmatic way out is to ask how some of the unexplained structure of the SM could be explained resorting to new beyond the Standard Model (BSM) theories at higher energy scales. Remembering the electro-weak theory, we know that the apparent gauge symmetry of a theory is not necessarily the actual gauge symmetry of the theory. The gauge symmetry can be spontaneously broken in the vacuum.

Could it be that the full $SU(3)_c \otimes SU(2)_L \otimes U(1)_Y$ gauge symmetry of the SM is itself just the remnant of some larger, broken, gauge symmetry ?

Just a single group, with a single coupling constant ? Here we come to the grand unified theories (GUTs), first proposed by Georgi and Glashow in the 70's. The larger gauge symmetry is necessarily broken at an energy scale which is larger than that which we currently observe. Let us call this energy, or mass, M_{GUT} . At this scale, GUTs postulate that $SU(3)$, $SU(2)$ and $U(1)$ SM couplings g_1 , g_2 and g_3 are equal at M_{GUT} .

In the simplest GUT, the SM is embedded in the larger group $SU(5)$, just large enough to fit all of the SM gauge groups into it. The five multiplets of each fermion family in the SM can be amalgamated into just two multiplets of the group $SU(5)$. The multiplets have to be grouped in such a way that $SU(3)$, $SU(2)$ and $U(1)$ SM charges are assigned correctly. In particular, it is remarkable that the seemingly arbitrary hyper-charge assignments of the SM ($1/3$ for the left-handed quark multiplet, -1 for the left-handed lepton multiplet, and so on) are just what is required for $SU(5)$ unification.

The next simplest GUT is based on a slightly larger group called $SO(10)$. All the SM fermions can be put into a single multiplet, containing 16 states. The sixteenth state, which is missing in the SM, has just the right quantum numbers to be a right-handed neutrino, with expected mass of $M_{\text{GUT}} \sim 10^{15}$ GeV. A perfect candidate for the seesaw mechanism [10], a GUT which provides a simple explanation on the smallness of neutrino masses.

As leptons and quarks are grouped in the same multiplets, there are unavoidable processes which allow to convert them into one another. These processes thus violate the baryon and lepton numbers conservation, and have as a consequence the instability of the proton. Even though the proton decay width as predicted in GUTs is very small, going as the inverse-fourth power of M_{GUT} , the current lower bound of around 10^{33} years on the proton life-time is enough to exclude the simplest $SU(5)$ GUT. On the positive side, this possibility could explain the observed huge predominance of matter over antimatter, arisen in the early Universe.

Weak, strong and electromagnetic coupling constants are called “running coupling constants”² because of the fact that these are not completely constant and known to “run” slowly with energy. This is theoretically caused by the screening and anti-screening effects of virtual particles. If we plot the measured running coupling constants as a function of energy and extrapolate to high energies using the renormalisation-group equations, we find that they converge at high energy, but not at an unique point. The couplings almost unify, but not quite, at a extraordinarily high scale of $M_{\text{GUT}} \sim 10^{15}$ GeV, as shown in Fig. 1.1.

Inclusion of new massive particles at the TeV scale may cause the mis-

² α_S , α_W and the fine structure constant $\alpha = e^2/(4\pi\hbar c) \sim 1/137$.

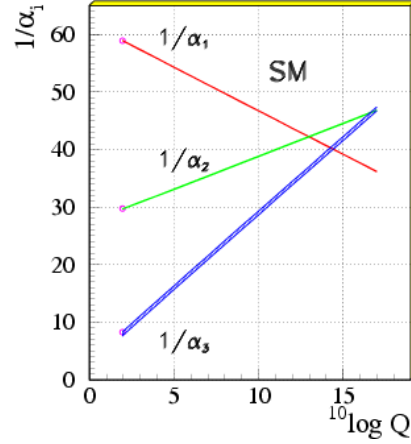


Figure 1.1: Extrapolation at high energies of the three (inverse) SM gauge couplings. They converge, but actually do not meet at an unique point [11].

match to disappear, opening the door for a coherent GUT. This is a strong motivation to go beyond the SM. Some even interpreted it as an indirect evidence for unification.

Let H be the Higgs complex scalar field with the classical quartic potential

$$V = m_H^2 |H|^2 + \lambda |H|^4. \quad (1.2)$$

If we want to satisfy the SM requirement for a non-vanishing vacuum expectation value (VEV) for H at the minimum of the potential, we have to set $m_H^2 < 0$, which leads to $\langle H \rangle = \sqrt{-m_H^2/2\lambda}$. Measurements of the properties of the weak interactions give us the experimental result $\langle H \rangle = 174 \text{ GeV}$, which means that m_H^2 is roughly of order $-(100 \text{ GeV})^2$.

The scale of electro-weak symmetry breaking is very sensitive to two-loop quantum corrections to m_H , and hence m_W , due to their quadratic divergence

$$\delta m_{H,W} \simeq O\left(\frac{\alpha}{\pi}\right) \Lambda^2, \quad (1.3)$$

where Λ is an ultraviolet momentum cutoff used to regulate the loop integral, *i.e.* the scale until which the SM is supposed to be valid. If the SM were to hold unscathed all the way up to the Planck mass $M_P \sim 10^{19} \text{ GeV}$, the radiative correction (Equ. 1.3) would be 36 orders of magnitude greater than the physical values. We can override the problem by postulating a tree-level value of m_H^2 that is approximately equal and of opposite sign to the correction (Equ. 1.3) to obtain the correct physical value. Beyond the mathematical artifact, this fantastically unlikely fine-tuning poses "ethical" concerns among

the physicists, who would naturally prefer a mechanism that keep this correction closer to the physical value. This is known as the *hierarchy problem* [13].

The difference of energy between the Planck scale $M_P = (8\pi G_N)^{-\frac{1}{2}} \sim 10^{19}$ GeV, where quantum gravitational effects *would* arise, and the electro-weak scale ($\lesssim 10^2$ GeV), which is about the energy available in the presently explored events, represents 17 orders of magnitude. *There must be something in between!* As well as the Fermi theory is a lower limit of the electro-weak theory, the SM would be a lower limit of a new (field ?) theory as the ratio M_P/M_W strongly suggests. Then all the parameters and quantum numbers in the SM could be derived from a more fundamental description of nature, leading to the SM as an effective low-energy theory. The scale of the higher level theory can be regarded as a cutoff to the SM. Above this cutoff scale, the SM ceases to be valid and the new physics takes over.

In the next sections, we will review the most popular extensions of the SM, focusing on the models featuring long-lived exotic particles that would decay in the range of the actual accelerator experiments.

1.3 Beyond the Standard Model : Supersymmetry

“The most amazing thing about Supersymmetry is how much we know about it, despite the complete lack of direct observations.”

Heard at the end of a seminar on Supersymmetry.

Supersymmetric theories are nowadays probably among the most popular extensions of the SM. For a complete introduction to the concept of supersymmetry, the reader is kindly referred to [24], a pedagogical paper oriented on field theory and particle physics that provides many tools for the beginner. Many other books and papers have been written on the subject. A personal selection of books may be found in the bibliography [14], [15], [16], [17], [18], [19], [20] and [21].

Supersymmetry, popularly abbreviated as SUSY, is a symmetric conspiracy that relates fermions and bosons by introducing a new operator Q which turns a bosonic state into a fermionic one, and vice versa :

$$Q|Boson\rangle = |Fermion\rangle \quad Q|Fermion\rangle = |Boson\rangle. \quad (1.4)$$

One can of course not restrict oneself to one operator and introduce many other such operators. One talks in this case of N-extended supersymmetries, N being the number of new operators. From Equ. 1.4, it is clear that Q is a fermionic operator, i.e. that carries spin angular momentum 1/2.

The SUSY algebra reads as :

$$\{Q_\alpha, \bar{Q}_\beta\} = -2(\gamma_\mu)_{\alpha\beta} P^\mu \quad (1.5)$$

$$\{Q_\alpha, Q_\beta\} = 0 \quad (1.6)$$

$$[Q_\alpha, P^\mu] = 0 \quad (1.7)$$

$$[Q_\alpha, M^{\mu\nu}] = \frac{1}{2}(\sigma^{\mu\nu} Q)_\alpha \quad (1.8)$$

It is therefore a space-time symmetry, that gives us fundamental relation with general relativity.

The irreducible representations of the SUSY algebra are called “supermultiplets”. Each of them contains the same number of fermionic and bosonic degrees of freedom. An elegant proof of that is to be found in [24]. The single-particle bosonic and fermionic states in such a super-multiplet are commonly known as superpartners. In a supersymmetric extension of the SM, each of the known fundamental particles must fit in a supermultiplet and have a superpartner with spin different by a half unit. Such an arrangement is not possible without resorting to the definition of new particles. The generic nomenclature for a spin 1/2 superpartner is to append a “ino”, higgsino, zino, wino, photino, gluino, gravitino, while prepending a “s” for the scalar spin-0 superpartner : squarks, sleptons, stau, sbottom, etc... The Higgs scalar boson actually resides in at least two supermultiplets, which is the minimum to provide masses to all charged Higgs bosons and to avoid the electro-weak gauge symmetry suffering a triangle gauge anomaly, and therefore be inconsistent as a quantum theory, see [24].

Table (1.1) sums up the particle content of the Minimal Supersymmetric Standard Model (MSSM). MSSM is the minimal model in the sense that it is just sufficient to produce a phenomenologically viable model, without introducing extra fields. A very important feature of the MSSM is that the superpartners are not necessarily the mass eigenstates of the theory, but mixing can happen between the electro-weak gauginos and the higgsinos, and within the various set of squarks and sleptons, and Higgs scalars sharing the same electric charge. After electro-weak symmetry breaking, the W^0, B^0 gauge eigenstates mix to give mass eigenstates Z^0 and γ , so do their SUSY counterparts \tilde{W}, \tilde{B} to give the zino \tilde{Z}^0 and the photino $\tilde{\gamma}$. The charginos and neutralinos are the mass eigenstates of the $(\tilde{W}^\pm, \tilde{H}^\pm)$ and $(\tilde{\gamma}, \tilde{Z}, \tilde{H}^0)$ fields, respectively.

Names	Spin	P_R	Mass Eigenstates	Gauge Eigenstates
Higgs bosons	0	+1	$h \ H^0 \ A^0 \ H^\pm$	$H_u^0 \ H_d^0 \ H_u^\pm \ H_d^\pm$
squarks	0	-1	$\tilde{u}_L \ \tilde{u}_R \ \tilde{d}_L \ \tilde{d}_R$ $\tilde{s}_L \ \tilde{s}_R \ \tilde{c}_L \ \tilde{c}_R$ $\tilde{t}_1 \ \tilde{t}_2 \ \tilde{b}_1 \ \tilde{b}_2$	$\tilde{u}_L \ \tilde{u}_R \ \tilde{d}_L \ \tilde{d}_R$ $\tilde{s}_L \ \tilde{s}_R \ \tilde{c}_L \ \tilde{c}_R$ $\tilde{t}_L \ \tilde{t}_R \ \tilde{b}_L \ \tilde{b}_R$
sleptons	0	-1	$\tilde{e}_L \ \tilde{e}_R \ \tilde{\nu}_e$ $\tilde{\mu}_L \ \tilde{\mu}_R \ \tilde{\nu}_\mu$ $\tilde{\tau}_1 \ \tilde{\tau}_2 \ \tilde{\nu}_\tau$	$\tilde{e}_L \ \tilde{e}_R \ \tilde{\nu}_e$ $\tilde{\mu}_L \ \tilde{\mu}_R \ \tilde{\nu}_\mu$ $\tilde{\tau}_L \ \tilde{\tau}_R \ \tilde{\nu}_\tau$
neutralinos	1/2	-1	$\tilde{\chi}_1^0 \ \tilde{\chi}_2^0 \ \tilde{\chi}_3^0 \ \tilde{\chi}_4^0$	$\tilde{B}^0 \ \tilde{W}^0 \ \tilde{H}_u^0 \ \tilde{H}_d^0$
charginos	1/2	-1	$\tilde{\chi}_1^\pm \ \tilde{\chi}_2^\pm$	$\tilde{W}^\pm \ \tilde{H}_u^\pm \ \tilde{H}_d^\pm$
gluinos	1/2	-1	\tilde{g}	\tilde{g}
gravitino/goldstino	3/2	-1	\tilde{G}	\tilde{G}

Table 1.1: New fundamental particles of the Minimal Supersymmetric Standard Model to be added to the already discovered particles of the SM.

A strong hint of supersymmetry is provided by the measurement at LEP of the strengths of the different gauge interaction couplings, which can be run up to high energy scale using the renormalisation-group equations. In the last section, we came to the troubling result that they do not converge at a single point, but almost ! In the SUSY version of a GUT, there are more particles in the theory which contribute, via loop corrections, to the running of the couplings. This leads to two changes.

Firstly, the coupling constants now do meet at a single point, as can be seen on Fig. 1.2. Indeed, GUTs would require for the value of the effective neutral weak mixing parameter

$$\sin^2\theta_W = 0.214 \pm 0.004, \quad (1.9)$$

whereas the experimental value is $\sin^2\theta_W = 0.23149 \pm 0.00017$ [4]. Minimal supersymmetric GUTs yield the value

$$\sin^2\theta_W \sim 0.232 \quad (1.10)$$

where the error depends on the assumed sparticle masses.

Secondly, the unification scale is shifted to an energy scale which is an order of magnitude larger, at around 10^{16} GeV. This consequently suppresses the probability of proton decay, and moves the predicted proton lifetime beyond current experimental bounds.

Precision electro-weak data from the LEP Electro-weak Group [4] prefer a relatively light Higgs boson, weighting less than about 200 GeV, which is

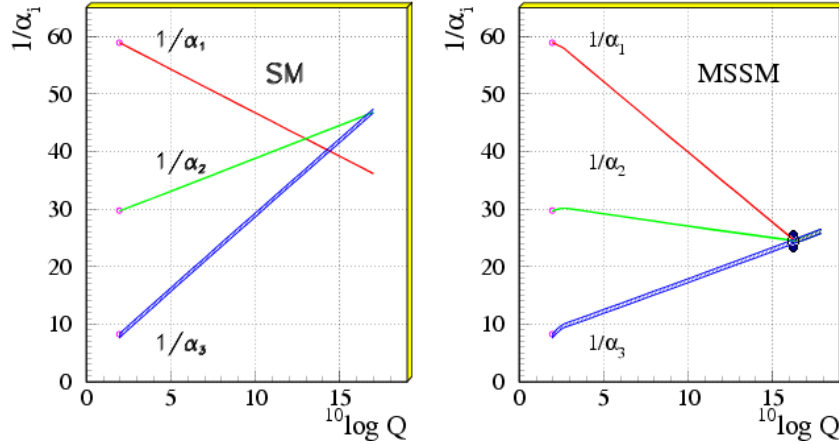


Figure 1.2: Extrapolation at high energies of the three (inverse) SM gauge couplings. In the SM (left), they converge, but actually do not meet at an unique point, while in the MSSM (right) they do [11]. The dark blob in the right plot represents the model dependent corrections.

consistent with calculations in the minimal supersymmetric extension of the Standard Model, predicting a Higgs of about 130 GeV or less [28].

Within the SM, the size of \mathcal{CP} violation is insufficient to drive the cosmological baryon asymmetry. In the MSSM, however, while the Higgs potential is \mathcal{CP} -invariant at tree level, substantial \mathcal{CP} asymmetry can be generated by radiative contributions, e.g. from third generation scalar-quarks [37] to ensure baryogenesis, assuming an initially matter-antimatter symmetric universe.

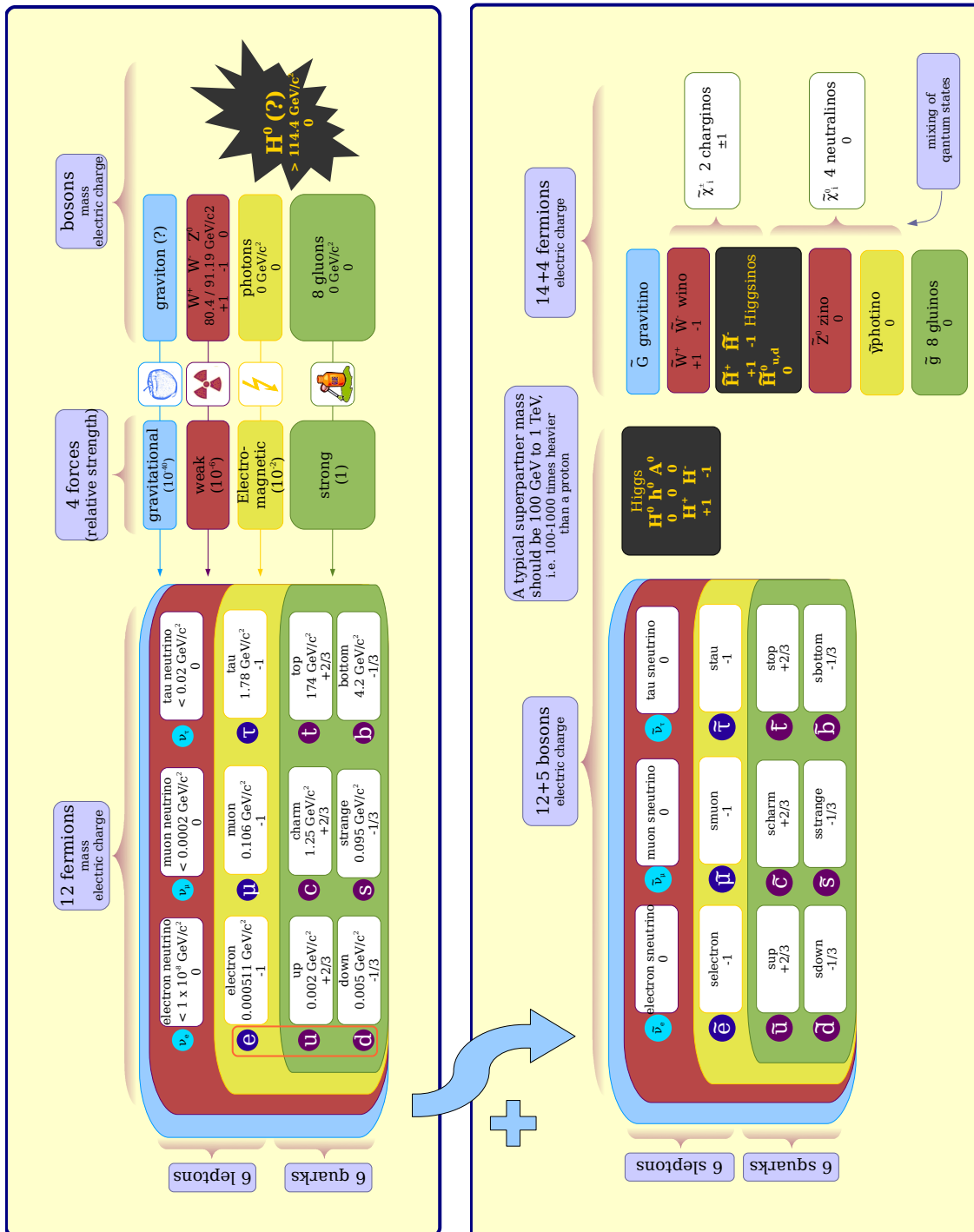
Supersymmetric theories offer a great help to solve the *hierarchy problem*. As mentioned in Sec. 1.2, the hierarchy problem arises when including new structures at higher energies. The Higgs boson is very sensitive to whatever lives at higher energies. This gives very large quantum corrections to the Higgs mass, which needs to be “fine tuned” to an unacceptable degree to obtain a light Higgs mass. Since they have equal numbers of bosons and fermions and since bosonic and fermionic loops have opposite signs, the residual one-loop correction

$$\delta m_{H,W} \simeq O\left(\frac{\alpha}{\pi}\right)(m_B^2 - m_F^2) \quad (1.11)$$

becomes naturally “small” ($\lesssim m_{H,W}^2$) if the supersymmetric partner bosons B and fermions F have similar masses

$$|m_B^2 - m_F^2| \lesssim 1 \text{ TeV}^2. \quad (1.12)$$

If SUSY would be kept unbroken, then all particles that inhabit the same irreducible supermultiplet would have exactly the same mass, weak



isospin and colour degrees of freedom, just because they are the same representation of the gauge group. In that case selectrons with mass equal to $m_e = 0.511 \text{ MeV}$ would have been detected long time ago. Therefore SUSY is clearly a spontaneously broken symmetry in the vacuum state chosen by nature. In other words, a SUSY model should have a Lagrangian density invariant under supersymmetry, but a vacuum state, which is not. In this way, supersymmetry is hidden at low energies in a manner exactly analogous to the fate of the electro-weak symmetry in the SM. The usual approach is to start by writing down the SUSY theory, and then to add by hand all terms consistent with the low-energy breaking of SUSY. In other words, we parametrise our ignorance. The effective Lagrangian of the MSSM is made up from two parts

$$\mathcal{L} = \mathcal{L}_{\text{SUSY}} + \mathcal{L}_{\text{soft}} \quad (1.13)$$

where $\mathcal{L}_{\text{SUSY}}$ preserves SUSY invariance, while $\mathcal{L}_{\text{soft}}$ “softly” violates it, softly in the sense that relation (1.11) is maintained small.

Actually, a great part of our ignorance is confined in $\mathcal{L}_{\text{soft}}$. All of the dimensionless couplings and all but one mass term in $\mathcal{L}_{\text{SUSY}}$ correspond indeed directly to some parameter in the SM. For instance SUSY coupling of gluino to a squark and a quark is determined by α_S .

If we denote m_{soft} as the largest mass scale associated with the soft terms, then the mass splitting between the known SM particles and their superpartners are just determined by this parameter. In order not to loose our successful cure for the mass hierarchy problem, superpartner masses must not stray away from each other by more than about an order of magnitude. In essence, for the MSSM scalar potential to provide a Higgs VEV resulting in $m_W = 80.4$ and $m_Z = 91.2 \text{ GeV}$ without miraculous cancellations, the mass of at least the lightest superpartner (LSP) should be at most about 1 TeV. Without going into too much details, one neutral Higgs scalar has to be lighter than $\sim 130 \text{ GeV}$. This is the main reason why theorists expect supersymmetric particles to be found at the TeV scale.

How SUSY is broken is the very central question on which most of the theorists focus. A whole set of models that do not require the degeneracy of scalar and fermion masses yield effective Lagrangian with such terms for $\mathcal{L}_{\text{soft}}$, providing a way to maintain the cancellation of quadratically divergent terms in the radiative correction of all scalar masses to all order in perturbation theory.

Supersymmetry breaking occurs in a “hidden sector” of particles which have no (or only very small) direct couplings to the “visible sector” supermultiplets of the MSSM. However, the two sectors do share some interactions

which are responsible for mediating supersymmetry breaking from the hidden sector to the visible sector, where they appear as calculable soft terms.

Three main class of models are competing to explain the mediating interactions.

In the gravity-mediated supersymmetry breaking scenario, the mediating interactions are of gravitational nature, where gravity enters at the Planck scale. The most well-known of these models are the minimal supergravity models, abbreviated mSUGRA. They assume universality of the gaugino and sfermion masses at the high scale. Also they always have an extra scalar mass parameter m_0^2 which needs fine tuning so that the sparticle exchange does not generate flavour changing neutral currents (FCNC) effects, at an unacceptable level.

In anomaly mediated supersymmetry breaking (AMSB) models, supergravity couplings that induce mediation are absent and the spontaneous symmetry breaking is caused by loop effects. The conformal anomaly, which is always present, generates the breaking terms and the sparticles acquire masses due to the breaking of scale invariance. This mechanism becomes a viable one for generating only the breaking terms, when the quantum contributions to the gaugino masses due to the “superconformal anomaly” can be large, hence the name Anomaly mediation. The slepton masses in the simplest model of this kind require some other SUSY breaking mechanism to obtain phenomenologically acceptable mass spectrum. One way to fix this problem is to introduce a scalar mass parameter m_0^2 .

In the gauge-mediated supersymmetry breaking (GMSB) scenarios, the MSSM soft terms arise from loop diagrams involving some *messenger* particles. The messengers couple to a supersymmetry-breaking VEV, and also have a $SU(3)_c \otimes SU(2)_L \otimes U(1)_Y$ interactions which provide a link to the MSSM.

A general expectation of this class of models is that the strongly-interacting sparticles (\tilde{q} , \tilde{g}) should be heavier than weakly-interacting sparticles (s , \tilde{B} , \tilde{W} , \tilde{H}) simply because of the hierarchy of gauge couplings $\alpha_3 > \alpha_2 > \alpha_1$. The common feature which makes all of these models very appealing is that soft masses are automatically flavor universal. The masses of the squarks and sleptons depend only on their gauge quantum numbers, leading automatically to the degeneracy of squarks and slepton masses needed for suppression of FCNC effects. But the most distinctive phenomenological prediction of gauge-mediated models is that the gravitino is the LSP. This has crucial consequences for both cosmology and collider physics.

The spontaneous breaking of global supersymmetry implies the existence of a mass-less Weyl fermion, the goldstino. When gravity is taken into ac-

count, supersymmetry becomes a local symmetry and receives the name of *supergravity*. It thus unifies the space time symmetries of ordinary general relativity with local supersymmetry transformations and the spin-2 graviton is assigned a spin 3/2 fermion superpartner named gravitino. Once supersymmetry is spontaneously broken, the gravitino acquire a mass “by eating up” the goldstino, which becomes its longitudinal helicity $\pm 1/2$ components. This mechanism called *super-Higgs mechanism* is entirely analogous to the ordinary Higgs mechanism by which the W^\pm and Z^0 gauge bosons gain mass by absorbing the Goldstone bosons associated with the breaking of the electro-weak gauge invariance.

In the gravity-mediated supersymmetry breaking case, the gravitino mass is comparable to the masses of the MSSM sparticles : $\mathcal{O}(100)$ GeV. Its interactions will be of gravitational strength, so the gravitino will not play any role in collider physics, but it can be very important in cosmology [39].

In contrast, gauge-mediated supersymmetry breaking models predict that the gravitino is much lighter than the MSSM sparticles. \tilde{G} is almost certainly the LSP in this case, and all of the MSSM sparticles will eventually decay into final states that include it. The decay rate of any sparticle \tilde{X} into its SM partner X plus a \tilde{G} is given by

$$\Gamma(\tilde{X} \rightarrow X\tilde{G}) = \frac{m_{\tilde{X}}^5}{16\pi\langle F \rangle^2} \left(1 - \frac{m_X^2}{m_{\tilde{X}}^2}\right)^4, \quad (1.14)$$

where $\langle F \rangle$ is the hidden sector VEV. If $m_{\tilde{X}}$ is of order 100 GeV or more and $\sqrt{\langle F \rangle} \geq 10^6$ GeV, then the decay $\tilde{X} \rightarrow X\tilde{G}$ occurs macroscopically and can be observed in a modern collider detector.

Although a number of consistent mechanisms for soft supersymmetry breaking have been put forward, it remains unknown which one is correct, or whether future experiments can distinguish them. They always involve extending the MSSM to new particles and interactions at very high mass scales, and there is no consensus on exactly how this should be done. This ignorance prevent any concrete predictions for the masses of the superparticles and their couplings.

A careful count reveals that MSSM (or more precisely the supersymmetric breaking part of MSSM) introduces 105 new masses, phases and mixing angles which cannot be rotated away by redefining the phases and flavor basis for the quark and lepton supermultiplets. However, there are some hints of an “organising principle” that governs the soft terms [24]. Most of the new parameters involve FCNC or \mathcal{CP} violation and can be severely constrained by experiments. Minimal supergravity models can be unduly contrived by

actual measurements to only five free parameters: the up-type Higgs doublet mass squared m_0^2 , the gaugino mass at the unification scale $m_{1/2}$, the mass m_{A_0} of the \mathcal{CP} -odd scalar A^0 , the sign of the Higgs mass parameter $\text{sign}(\mu)$ and the ratio $\tan\beta = v_2/v_1$ of the vacuum expectation values associated to the neutral components of the two Higgs fields (v_1 and v_2 couple to up and down fermions, respectively). On the other hand, the parametrisation of GMSB models can be restricted to the scale Λ , the typical messenger mass scale M_{mess} , the integer number N_3 of copies of the minimal messengers, the goldstino decay constant $\langle F \rangle$, $\text{sign}(\mu)$ and $\tan\beta$.

Some theorists feel uneasy with these “aggressive simplifying assumptions”, which reduces the field of BSM investigation. They fear one may pass by important features with deep implications on the possible signatures³. Matt Strassler even speaks of “tyranny of the minimalist models”.

Many other terms could be written down in the *superpotential*, which are gauge-invariant and renormalisable, but are not included in the MSSM because they violate either the total baryon number (B) or the total lepton number (L) :

$$W \supset \underbrace{\mu_i L_i \bar{H} + \lambda_{ijk} L_i L_j E_k^c + \lambda'_{ijk} L_i Q_j D_k^c}_{\text{Violate } L} + \underbrace{\lambda''_{ijk} U_i^c D_j^c D_k^c}_{\text{Violate } B}, \quad (1.15)$$

where L , \bar{H} , E^c , Q , U^c and D^c are the lepton doublet, up-type Higgs doublet, lepton singlet, quark doublet, up-type quark singlet and down-type quark singlet superfields respectively. Gauge indices are implicit. These interactions are allowed by gauge symmetries.

It is not worth adding that B- and L-violating processes have never been observed experimentally. The most obvious experimental constraint comes from the non-observation of the proton decay, whose decay time is measured to be in excess of 10^{32} years. Its decay would violate both B and L by one unit.

We shall recall that in the SM, B- and L-conservation is not *assumed*, but is rather an *accidental* consequence of the fact that there are no possible renormalisable Lagrangian terms which violate B and L. One could just take this conservation as a postulate in the MSSM, but there is a quite general concern to treating B and L as fundamental symmetries of nature, since they are known to be necessarily violated by non-perturbative electro-weak effects. In order to rule out the possibility of B- and L-violating operators in the renormalisable superpotential, while allowing the “good” terms, a new symmetry, more fundamental and *exact*, is added : R-parity (P_R), or

³Consider for example the models with \mathbb{P}_R in Sec. 1.3.1.

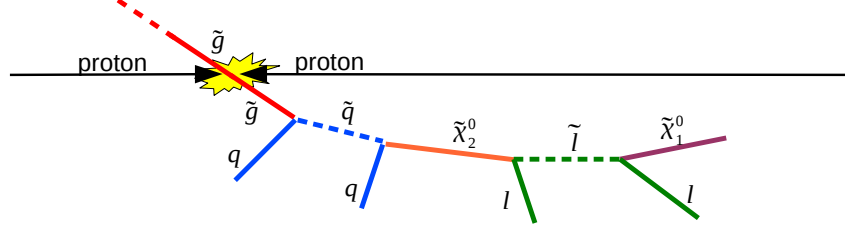


Figure 1.3: Illustration of a typical SUSY *cascade*. The sgluinos decay into SM and SUSY particles till the LSP, conserving P_R .

equivalently “matter parity” (P_M), is a multiplicatively conserved quantum number defined as

$$P_R = (-1)^{3(B-L)+2s}, \text{ or} \quad (1.16)$$

$$P_M = (-1)^{3(B-L)} \quad (1.17)$$

for each particle in the theory, where s is the spin of the particle. All of the SM particles and the Higgs bosons have even R-parity ($P_R = +1$), while all of the sparticles, squarks, sleptons, gauginos and higgsinos have odd R-parity ($P_R = -1$). If R-parity is exactly conserved, then there can be no mixing between the sparticles and particles. If R-parity is conserved, every interaction vertex contains an even number of $P_R = -1$ sparticles. This has the following phenomenological consequences :

- Sparticles can only be produced in even numbers in collider experiments, usually two at a time.
- The LSP is absolutely stable. It is forbidden to decay into SM particles.
- Sparticles other than the LSP must eventually decay into an odd number of LSPs.

Figure 1.3 illustrate the production of a pair of sgluinos from the collision of two protons. The sgluinos *cascade* down to the LSP, here a neutralino, which remains stable. Typical signatures in collider experiments of SUSY cascades are high p_T leptons, high jet multiplicity and missing energy, as the LSP escapes detection.

Astrophysicists are still seeking for a cold non-baryonic dark matter candidate. If the LSP is electrically neutral it will interact very weakly with

ordinary matter and therefore could be an suitable WIMP⁴ candidate for this casting. A neutralino $\tilde{\chi}^0$, alongside with a neutral Higgs, are often cited [30], while sneutrinos and gravitinos are not ruled out. It is a remarkable coincidence that the predicted relic density of a bino-like neutralino LSP obtained after the cool-down of the Universe can be in the right range to make up a significant part of the critical density of the Universe, and perhaps to explain the rotation curves of galaxies [41].

But why should R-parity be conserved, given that the known discrete symmetries in the SM (charge conjugation C, parity P and time reversal T, etc.) are observed to be inexact symmetries ? The MSSM would not suffer any internal inconsistency if matter parity is not imposed. R-parity conservation is in fact not inevitable to preclude proton decay and neutron antineutron oscillations⁵, and can be relaxed. Either L- or B-violating terms are then allowed in the renormalisable Lagrangian, but not both. We could then for instance impose a discrete symmetry which only forbids L-violation, while allowing B-violation.

Such alternative symmetries are discussed in [34]. For a general review of R-parity violation and searches, please consult [35].

R-parity violation (\mathcal{P}_R) has two major consequences for collider phenomenology:

- The LSP is not stable and can decay to SM particles.
Dark matter candidates have to be provided by another theory.
- Sparticles may be produced individually.

Sections 1.3.1 and 1.3.2 present two R-parity violating supersymmetric models featuring a LSP with macroscopic decay length, large enough to be detected in a collider detector.

We can finally close this section by adding that supersymmetry is an essential component of consistent string theories⁶ [40].

1.3.1 mSUGRA with Baryon Number Violation

L. M. Carpenter, D. E. Kaplan and E.-J. Rhee proposed the decay of the lightest neutralino $\tilde{\chi}_1^0$ through B violation (\mathcal{P}_R) into 3 quarks via a virtual squark (see Fig. 1.4) in the framework of mSUGRA models and non-unified gaugino masses [25].

⁴Weakly Interacting Massive Particle.

⁵ $u\bar{d}d \rightarrow \tilde{d}_i d \rightarrow \tilde{g} \rightarrow \tilde{d}_i \bar{d} \rightarrow \bar{u} \bar{d} \bar{d}$

⁶*I.e.* those with fermions and without quantum inconsistencies.

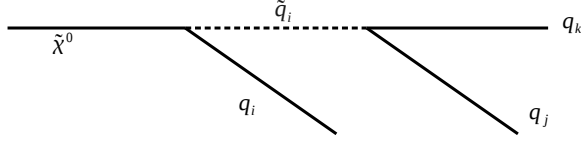


Figure 1.4: Neutralino decaying into three quarks via an off-shell squark.

Gauge mass unification states that the bino and wino mass parameters M_1 and M_2 in the soft SUSY breaking Lagrangian are related according to

$$M_1 = \frac{5}{3} \tan^2 \theta_W M_2 \simeq \frac{1}{2} M_2 \quad (1.18)$$

where θ_W is the weak mixing angle. This constraint comes from renormalisation group running (at one loop) for the grand unified scale under the assumption that

$$M_1 = M_2 = m_{1/2} \quad (1.19)$$

at the GUT scale. However, as the authors state, many of the compelling models of soft supersymmetry breaking in a unified framework either do not guarantee or explicitly violate Equ. 1.19. One compelling mechanism for breaking the grand unified theory is through boundary conditions in extra dimension [47]. If supersymmetry breaking occurs effectively at the GUT breaking boundary, then no relationship is predicted between M_1 and M_2 , while the boundary breaking still predicts gauge couplings unification up to small threshold corrections. Moreover, if the gauginos have Dirac rather than Majorana masses, the one-loop running of gaugino masses leads to a different ratio M_1/M_2 . In the case of non unified gaugino masses, the model can be better parametrised by M_1 , M_2 , $\tan \beta$ and μ .

The experimental bounds on all superpartners masses are weaker than in the case of R-parity conserved MSSM, due to a lack of missing energy in the signal. The current bounds of 300 – 400 GeV on squarks and gluinos from Tevatron searches come from analyses which require significant missing transverse energy cuts [43].

With baryon-number violating interactions, the bounds of all superpartners are below 100 GeV (95% CL), except for the chargino, whose bound remains roughly the same (102.5 GeV) [44]. The gluino or the lightest sbottom do not have a published bound above ~ 10 GeV [45].

Direct searches for neutralinos which decay via baryon number violation have been performed by ALEPH, DELPHI and L3 [42], none of them were

able to put bounds on its mass. The bounds on the lightest neutralino quoted in the particle data book are due to chargino searches and the requirement of gaugino mass unification.

It should be stressed that lighter scalar quarks and other superpartner masses allow to reduce the persistent fine tuning typically required to generate the measured scale of electro-weak symmetry breaking.

The decay length of the neutralino essentially depends on the R-parity violating couplings λ'' , the neutralino mass $m_{\tilde{\chi}_1^0}$ and the squarks masses $m_{\tilde{q}}$. Assuming an universal squark mass at low energies and a single dominant P_R violating coupling, the decay length may be written as :

$$\begin{aligned} L &\simeq \frac{384\pi^2 \cos^2\theta_W}{|U_{21}|^2 \alpha \hbar c \lambda''^2} \frac{m_{\tilde{q}}^4}{m_{\tilde{\chi}_1^0}^5} (\beta\gamma) \\ &\sim \frac{3\mu m}{|U_{21}|^2} \left(\frac{10^{-2}}{\lambda''}\right)^2 \left(\frac{m_{\tilde{q}}}{100 \text{ GeV}}\right)^4 \left(\frac{30 \text{ GeV}}{m_{\tilde{\chi}_1^0}}\right)^5 \frac{p_{\tilde{\chi}_1^0}}{m_{\tilde{\chi}_1^0}}, \end{aligned} \quad (1.20)$$

where $|U_{21}|$ is an element of the neutralino mixing matrix and $p_{\tilde{\chi}_1^0}$ is the neutralino's momentum. Final-state particle masses, Yukawa couplings and QCD corrections have been neglected. Within the allowed parameter space, λ'' is the most relevant parameter for the order of the decay length.

Bounds on the proton decay strongly constrain the combinations of baryon and lepton number violation. Taken separately, however, they are much more weakly constrained. Bounds on the individual λ'' couplings are only stringent from double nucleon decay (in a nucleus) into two kaons⁷ [36], requiring $\lambda''_{112} \lesssim 10^{-7}$ and $\lambda''_{113} \lesssim 10^{-4}$ for 200 GeV squarks and gluino masses. Other couplings are less tightened. Rare hadronic B mesons decays give us limits in terms of products of two different couplings which ranges from $\lambda_{ijk}\lambda_{lmn} < 10^{-2} - 10^{-4}$ [25].

If the λ'' have arbitrary complex phases, they can contribute to direct \mathcal{CP} violation in kaon decays and to $K - \bar{K}$ mixing. The strongest bound in this case is the limit $\lambda''_{313}\lambda''_{323} < 10^{-8}$. There are no significant bounds on the individual λ''_{223} and λ''_{323} couplings.

At the LHC energies, the above bounds would allow for a $\tilde{\chi}_1^0$ decay length long enough to result in a macroscopic displaced vertex.

A spurion analysis of flavour breaking in the SM shows that λ''_{323} would be dominating, thus favouring $\tilde{\chi}_1^0 \rightarrow tbs$ or $\tilde{\chi}_1^0 \rightarrow cbs$ if the $\tilde{\chi}_1^0$ is lighter

⁷The diagram involves having two λ_{dsu} interactions turning u and d quarks into s anti-squarks, which exchange a gluino and turn into s antiquarks; the spectators then form the two kaons.

Model	M_1 [GeV]	M_2 [GeV]	$\tan \beta$	μ [GeV]	$m_{\tilde{\chi}_1^0}$ [GeV]	τ [ps]
BV48	63	250	5	140	48	10
BV48_500	63	250	5	140	48	500
BV38	40	1200	5	1200	38	10
BV98	100	1200	5	1200	98	10
BV198	200	1200	5	1200	198	10

Table 1.2: Theoretical mass of the $\tilde{\chi}_1^0$, its lifetime, and the parameters of the models.

than the top. Neutralino decays dominated by heavy flavour would contain additional displaced vertices.

Decays of neutralino into three quarks give rise to a composite jet with a jet mass related to that of the original sparticle, which is made up of two or more collimated sub-jets [46].

The cross-section of $\tilde{\chi}_1^0$ production through squark decay is particularly interesting in certain region of the allowed parameter space. Three points have been chosen to cover the $\tilde{\chi}_1^0$ mass range of the model. For further referencing, these sets of parameters will be labelled as BV38, BV98, and BV198 for the generated $\tilde{\chi}_1^0$ masses of 38 GeV, 98 GeV and 198 GeV, respectively. We set the lifetime of the $\tilde{\chi}_1^0$ to be 10 ps compatible with the limits on λ'' [48], [35]. This results in a $\tilde{\chi}_1^0$ decaying well inside LHCb’s vertex locator (VeLo) that will be presented later in Sec. 2.3.2.a. The table 1.2 sums up the chosen theoretical parameters, the theoretical mass of the $\tilde{\chi}_1^0$ and its lifetime.

Both electro-weak precision measurements and simple SUSY extensions of the SM prefer a mass of the Higgs boson less than experimental limit of 114 GeV. In their paper, [25] argue that a light Higgs could have been missed by experiments. The quoted lower bound on the Higgs mass comes from analyses assuming a Higgs with SM properties such as a SM cross section for Z–Higgs production and SM branching ratios into bottom quarks and tau leptons. If the branching ratio to SM final states are uniformly suppressed by, for example, a factor of five - and the new decay modes are not picked up by any LEP searches - the 95% CL lower limit on the Higgs mass reduces to roughly 93 – 95 GeV, just around the Z^0 mass.

A significant portion of parameter space allows for the production of $\tilde{\chi}_1^0$ pairs through the decay of the light Higgs bosons h^0 , alongside with the single production through the decay of superparticles. The branching ratio $h^0 \rightarrow \tilde{\chi}_1^0 \tilde{\chi}_1^0$ ranges from 70% to more than 90%.

A point in the parameter space has been chosen and is shown in Table

1.2. It is labelled as BV48, to remember the $\tilde{\chi}_1^0$ theoretical mass of 48 GeV. The corresponding h^0 mass is 114 GeV. A $\tilde{\chi}_1^0$ with a longer $\tilde{\chi}_1^0$ lifetime of 500 ps has also been considered. It is accordingly labelled as BV48_500. As it will be shown later in Sec. 5.2, most $\tilde{\chi}_1^0$ of this scenario escape detection in the VeLo and decay later in the LHCb detector.

How could such a light neutralino with strong enough couplings to dominate the Higgs width not being detected indirectly by its effect on the Z width or directly in searches at LEP II ?⁸ A first reason is that the width of the Z in the SM (~ 2.5 GeV) is three orders of magnitude bigger than the SM width of a 100 GeV Higgs. A second reason is that, in the range of small to moderate bino-higgsino mixing, the Higgs decay rate into neutralinos is roughly proportional to the mixing angle squared (Δ) while the same rate for the Z goes like the mixing angle to the fourth power. The decay width of the Z^0 into the neutralino LSP at tree level reads as

$$\Gamma_{Z^0 \rightarrow \tilde{\chi}^0 \tilde{\chi}^0} = \Gamma_\nu \times \Delta^2 \sqrt{1 - \left(\frac{2m_{\tilde{\chi}^0}}{m_Z^0}\right)^2} \left(1 - \left(\frac{m_{\tilde{\chi}^0}}{m_Z^0}\right)^2\right), \quad (1.21)$$

where Γ_ν is the Standard model Z^0 width into one family of neutrino. The LEP II electro-weak fit [4] requires a branching ratio $\text{BR}(Z^0 \rightarrow \tilde{\chi}^0 \tilde{\chi}^0)$ to be less than 0.1% (1σ). This sets a bound of $\Delta \lesssim 0.1$ for a very light neutralino, and weaker for heavier neutralinos as the phase space gets reduced, constraint satisfied in most of the parameter space.

For a broader view on the general theory and searches made on the SM and MSSM Higgs bosons, please consult [37] and [38]. For details on this class of models, please consult [25].

1.3.2 Bilinear R-parity violating supersymmetric models

Supersymmetric models with bilinear R-parity violation (BP_R) [49] introduce extra “bilinear” allowed terms in the MSSM superpotential :

$$W_{\text{BP}_R} = W_{\text{MSSM}} + \epsilon_{ab} \epsilon_i L_i^a H_u^b \quad (1.22)$$

The additional bilinear contribution contains three parameters ϵ_i , one for each fermion generation. Their smallness may arise from a suitable symmetry, for example a horizontal symmetry [51]. The smallness of ϵ_i could also arise dynamically in models with spontaneous breaking of R-parity. ϵ_i

⁸Paragraph borrowed from [25]

is given as the product of Yukawa couplings times a singlet sneutrino VEV. \mathcal{BP}_R models also possess new soft supersymmetric breaking terms :

$$V_{\text{soft}} = V_{\text{mSUGRA}} - \epsilon_{ab} B_i \varepsilon_i L_i^a H_u^b \quad (1.23)$$

with three new free parameters (B_i). There is no field definition that the bilinear terms get eliminated simultaneously.

Alongside with the two Higgs doublets, the sneutrino fields acquire non-zero VEV. A striking contribution of these VEVs is the appearance of new possible mixing between :

- the neutrinos and neutralinos,
- the charged leptons and charginos,
- the charged Higgs and charged sleptons,
- the \mathcal{CP} -odd and even Higgses and the sneutrino sector,

leading to new effecting couplings. In general SUSY decays are not affected by the new \mathcal{BP}_R interactions, with the notable exception of the LSP, which becomes unstable and decays into SM particles. In the parameter space region where the lightest neutralino is the LSP, the $\tilde{\chi}_1^0$ may undergo fully leptonic decays :

$$\tilde{\chi}_1^0 \rightarrow \nu \ell^+ \ell'^-, \text{ with } \ell = e, \mu \text{ or } \tau, \quad (1.24)$$

as well as semileptonic decays :

$$\begin{aligned} \tilde{\chi}_1^0 &\rightarrow \nu q \bar{q}, \\ \tilde{\chi}_1^0 &\rightarrow \ell q' \bar{q}, \ell = e, \mu \text{ or } \tau, \end{aligned}$$

and finally pure neutrino decay $\tilde{\chi}_1^0 \rightarrow \nu \nu \nu$.

As a consequence of the above-mentioned mixings, if kinematically allowed, these decays may happen via two body decays such as $\tilde{\chi}_1^0 \rightarrow W^\pm \mu^\mp$, $\tilde{\chi}_1^0 \rightarrow W^\pm \tau^\mp$, $\tilde{\chi}_1^0 \rightarrow Z^0 \nu$ or $\tilde{\chi}_1^0 \rightarrow h^0 \nu$.

In AMSB scenario, the lightest chargino has a mass very close to the $\tilde{\chi}_1^0$. As the latter, it may decay via two or three-body decay into SM final states :

$$\begin{aligned} \tilde{\chi}^\pm &\rightarrow \nu q' \bar{q}, \\ \tilde{\chi}^\pm &\rightarrow \ell^\pm q \bar{q}, \\ \tilde{\chi}^\pm &\rightarrow \ell^\pm \ell^+ \ell^-, \\ \tilde{\chi}^\pm &\rightarrow \ell^\pm \nu \nu. \end{aligned}$$

$B\mathcal{P}_R$ supersymmetric models provide the simplest extension of the MSSM to include lepton number violation and have the additional benefit to accommodate neutrino oscillations [8][9]. Neutrino physics data allow consequently to constrain the R-parity violating parameters, actually reducing them to a rather small value, making $B\mathcal{P}_R$ interactions, responsible for the LSP decay, rather weak. As a result, the LSP may become long-lived, with a $c\tau$ as large as a few mm for light neutralino masses. Although the decay length shortens with the increase in neutralino mass, it remains sizable for heavier neutralino, with $c\tau$ of $\mathcal{O}(100) \mu\text{m}$. The same result applies for the $\tilde{\chi}^\pm$ in AMSB scenarios. When the LSP is not the lightest neutralino or chargino, its distance of flight is unfortunately too small to be observed.

In their paper [49], the authors claim that the LHCb experiment can probe a large fraction of the allowed parameter space and explore neutralino masses up to 200-240 GeV. What is more, the discovery potential of LHCb would be rather similar (60% – 70%) of the ATLAS/CMS⁹ one in the low luminosity runs of the LHC.

Five points in the rich parameter space are retained [50] for simulations in LHCb. 4 mSUGRA models yielding a wide range of $\tilde{\chi}_1^0$ masses - from 76 GeV to 252 GeV - and lifetimes. One AMSB model is also considered for chargino studies (see also Sec. 1.3.3), alongside the neutralino. These points are summarised in table 1.3 and labelled for further reference.

To reflect the different possibly interesting signatures - di-jets + ℓ , di-jets + E_T , di-leptons + E_T , we'll later also focus on the decay of the neutralino LSP of model BRpV1 into the following final states :

$$\begin{aligned}
 \text{BRpVmuq} & : \quad \tilde{\chi}_1^0 \rightarrow \mu^\pm qq' \\
 \text{BRpVb} & : \quad \tilde{\chi}_1^0 \rightarrow \nu b \bar{b} \\
 \text{BRpVmu} & : \quad \tilde{\chi}_1^0 \rightarrow \nu \mu^+ \mu^-
 \end{aligned}
 \tag{1.25}$$

1.3.3 Gauge-Mediated Supersymmetry Breaking Models

In gauge-mediated supersymmetry breaking (GMSB) models presented earlier in Sec. 1.3, the next-to-lightest superpartner (NLSP) decays into \tilde{G} typically with a very long lifetime. The standard scenarios put the NLSP as a \tilde{B} or $\tilde{\tau}$ in which case there is a photon or a tau emitted at a displaced vertex.

⁹See Sec. 2.2.

mSUGRA	m_0 [GeV]	$m_{1/2}$ [GeV]	$\tan \beta$	$\text{sgn}(\mu)$	$m_{\tilde{\chi}_1^0}$ [GeV]	τ [ps]
BRpV1	200	200	10	+1	76	71.2
BRpV2	400	300	10	+1	120	5.1
BRpV3	600	400	10	+1	164	1.5
BRpV4	1000	600	10	+1	252	0.4
AMSB	m_0 [GeV]	$m_{3/2}$ [GeV]	$\tan \beta$	$\text{sgn}(\mu)$	$m_{\tilde{\chi}_1^0, \tilde{\chi}^\pm}$ [GeV]	τ [ps]
BRpV5	800	400	15	+1	116	2.2

Table 1.3: Theoretical mass of the $\tilde{\chi}_1^0$, its lifetime, and the parameters of the models. $\tau_{\tilde{\chi}_1^0}$ fixed by the observations of neutrino oscillations.

Models with the $\tilde{\tau}$ as the only NLSP are the most studied models and are particularly appreciated for the search of heavy stable charged particles (HSCPs), see for example [64] and [65]. Sleptons are light ($\mathcal{O}(100)$ GeV) and $\tilde{\tau}$ pairs could be copiously produced at the LHC. Such HSCPs can be distinguished from SM particles by exploiting their unique signature: a low velocity β associated with a high momentum of order a few hundred GeV and a large energy deposit (ionisation) in the silicon trackers. This is clearly beyond the scope of the present document, but had to be mentioned, as this field touches ours : many HSCPs end-up in heavy displaced vertices (e.g. the $\tilde{\chi}_1^\pm$ of Sec. 1.3.2).

Although much of the studied parameter space leads to the creation of displaced leptons, these models are extremely broad in extent. A higgsino or other gauginos are possible in which case the Higgs or Z^0 can be emitted at a displaced vertex giving us a large multiplicity and a high invariant mass.

1.3.4 Split Supersymmetry

Our discussion on theories lying beyond the Standard Model would not be complete without a full section about Split Supersymmetry [58].

We have seen that “standard” supersymmetry helps to relieve much of the incredible amount of fine-tuning of the vacuum energy necessary, such that the resulting cosmological constant is as small as observed. Among other merits, R-parity - if accepted ! - eventually provides a natural dark-matter candidate with about the right properties. Grand unification is achieved by the quantum corrections due to the gauginos and Higgsinos.

However, supersymmetry has weaknesses as well: naturalness is in conflict with experiment, since the non-observation of light Higgs bosons and gauginos at LEP requires large, somewhat fine-tuned, soft-breaking parameters.

Large FCNC effects due to sfermion exchange are generically expected but not observed, a problem that has a natural solution only in gauge-mediated models. It is also possible that dimension-five operators at the GUT scale could mediate proton decay with an unacceptable rate.

Briefly speaking, the split supersymmetry abandons the hierarchy problem and uses unification and dark matter as the only guiding principles.

The cosmological constant problem appears to be very similar to the hierarchy problem of the Higgs mass. If the universe is described by an effective local quantum field theory down to the Planck scale, then we would expect $\Lambda \sim M_{\text{pl}}^4$, where Λ is the cosmological constant in Einstein's equation of general relativity :

$$R_{\mu\nu} - \frac{1}{2}Rg_{\mu\nu} + \Lambda g_{\mu\nu} = \frac{8\pi G}{c^4}T_{\mu\nu}. \quad (1.26)$$

However, the measured value is smaller than this by a factor of 10^{120} . There is here a large *fine-tuning problem*. This discrepancy has been named “the worst theoretical prediction in the history of physics !”.

Present particle physics calculations can be safely performed by setting the cosmological constant to zero and ignore any effect caused by the mechanism ultimately responsible for the solution of the problem (via the anthropic principle¹⁰). Such an “explanation” could also apply to the hierarchy problem in Higgs physics, if you are willing to accept a high degree of fine-tuning for the separation between the weak and Planck scale.

As a result, supersymmetry can be broken near the unification scale, and a low-energy SUSY becomes unnecessary. A decoupling occurs between the gauginos, higgsinos, a single finely-tuned Higgs and the rest of the MSSM zoology, which becomes extremely heavy. Hence the name *split* supersymmetry. Gauge-coupling unification can be achieved with the fermions of the MSSM which can remain light, protected by the chiral symmetry. The pattern of unification is unchanged, if all bosonic superpartners (coarsely called sfermions later on) are heavy, since they form a complete SU(5) representation. With this framework, one cures all the difficulties of the MSSM mentioned at the beginning of this section. Without light sfermions no more FCNC, large \mathcal{CP} violation and proton-decay problem. Also, R symmetry makes a TeV-scale LSP possible.

The low-energy effective theory becomes particularly simple. In addition to the SM including the Higgs boson, the only extra particles are the four neutralinos, two charginos and a gluino.

¹⁰In physics and cosmology, the anthropic principle is the collective name for several ways of asserting that the observations of the physical Universe must be compatible with the life observed in it [59].

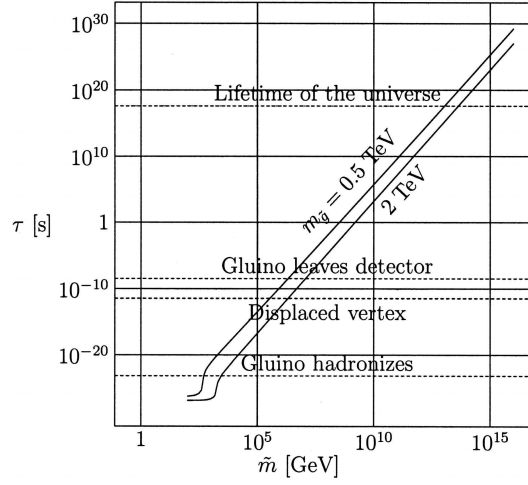


Figure 1.5: Gluino lifetime as a function of the common scalar mass \tilde{m} . Picture taken from [58]

Because the scale of supersymmetry breaking is now high, the squarks are heavy and the lifetime for the gluino to decay into a quark, antiquark and LSP - which is mediated by virtual squark exchange ($\sim \frac{1}{\tilde{m}^2}$ in analogy to Fermi's theory) becomes very long, making it observable in collider experiments.

If sparticles are long-lived, they can hadronise [60]. The gluinos can combine with quark, antiquark and gluons to form new hadronic states R-hadron (carrying one unit of R). Combined with three quarks, quark-antiquark pairs or simply gluons, gluinos lead, respectively, to new bosonic states (R-baryons) and new fermionic states (R-mesons, R-glueballs) which are colour-singlets with a flavour multiplet structure similar to ordinary baryons, mesons and glueballs.

Figure 1.5 pictures the dependence of the gluino lifetime as a function of the sfermion scale \tilde{m} .

- Once $\tilde{m} \geq 10^3 \text{ GeV}$, the gluino hadronises before decaying. It is then sufficiently long-lived to form R-hadrons.
- For $\tilde{m} > 10^6 \text{ GeV}$, weak decays of heavy-flavoured R-hadrons play a role. The gluino typically travels a macroscopic distance.
- For $\tilde{m} > 10^7 \text{ GeV}$, strange R-hadrons can also decay weakly and gluinos typically leave the detector undecayed or are strapped in the detector material.
- For $\tilde{m} > 10^9 \text{ GeV}$, R-hadrons could become cosmologically relevant,

since they affect nucleosynthesis if their abundance in the early Universe is sufficiently high.

- For $\tilde{m} > 10^{13}$ GeV, the gluino is considered stable since its lifetime is longer than the age of the Universe.

If gluino decays can be observed via distant vertices for example, their analysis yields information about the physics at the scale \tilde{m} . The longevity of the gluino is a strictly qualitative prediction of split-SUSY, which is different from the usual MSSM.

In conclusion, the phenomenology of split-SUSY models at the LHC is very dependent on the lifetime of the gluino. If this is smaller than the hadronisation time scale, the signals will be the usual signals for SUSY. If the gluino hadronises, but the lifetime of the R-hadrons products is short enough that they decay inside the detector, we might see additional vertices from the R-hadron decay.

The production of a stable, charged R-hadron will give a signal much like the production of a stable charged weakly-interacting particle, an object that would look like a muon but arrives significantly later at the muon chambers due to its larger mass. In case of production of a stable neutral R-hadron there will be a missing transverse energy due to its escape from detection.

Flavour decomposition of gluino decays mirrors the sfermion mass hierarchy at the sfermion scale \tilde{m} . The reason is that FCNC are absent and also L-R-mixing is suppressed. The ratio of branching ratios $\tilde{g} \rightarrow q\bar{q}\tilde{\chi}_1^0$ and $\tilde{g} \rightarrow Q\bar{Q}\tilde{\chi}_1^0$ is given by $(m_{\tilde{Q}}/m_{\tilde{q}})^4$, so even a weak hierarchy will be greatly enhanced. If the decays of long-lived gluinos can be observed, it is therefore important to identify the flavour.

1.4 Beyond the Standard Model : Hidden Valley models

The SM, as well as SUSY models, can be extended by additional non-abelian gauge groups, that would have been thus far “hidden” by a large energy gap. Unlike the LEP, the LHC would be able to leap over the barrier and access higher dimensional operators at the TeV scale to allow for interactions between SM and new particles [52], as pictured in Fig. 1.6.

Theorists expect the bridge scale to happen at the TeV scale essentially for the same reasons that we would expect supersymmetry to be there : to solve the Higgs mass hierarchy problem.

“Hidden valley” (HV) models offer more liberty than most extensions of the SM, like supersymmetry. They have very few limits on light particles that interact weakly with the SM : no precision constraints, moderate LEP constraints and weak cosmological constraints.

The manifestations of hidden valley models are very broad in extent. Here, we’ll concentrate on one simple example, which exhibits the most features we’re interested in. Following [53], a new sector v is created, which contains two heavy quarks U and C . In a “confining” model, they are close in mass and can combine to form hadrons with either v -charge $v = \pm 1$, denoted as π_v^\pm , or $v = 0$, called π_v^0 .

All SM particles are neutral under the new gauge group G_v , while the v -particles are neutral under G_{SM} .

The v -hadrons with $v = 0$ can decay by tunnelling back through the energy barrier, again via higher dimension operators, to gauge-invariant combinations of SM particles, with observable lifetimes, therefore leaving displaced vertices. If the mass of the spin-less π_v^0 is below the ZZ mass threshold it will decay dominantly into $b\bar{b}$ due to helicity conservation. The details of the decay depend on the properties of the v -flavoured hadrons. The lightest v -particle with $v \neq 0$ is a potential dark matter candidate.

v -particles can be produced directly via a Z' or a loop of heavy particles carrying both G_{SM} and G_v charges. In fact, many such v -particles could be produced in a single event (see for example Fig. 1.7(*left*)). LHC production cross-sections are typically in the 1-100 fb range, though they can be larger.

In their paper [54], Matthew J. Strassler and Kathryn M. Zurek review a class of HV models - including supersymmetric extensions - in which the light Higgs boson would preferentially decay into the heaviest kinematically allowed v -quarks, i.e. into two or more resonances. In many models, the resonances will decay in turn into the heaviest fermion pair available, with branching fractions similar to those of the standard model Higgs. To resume, the Higgs boson would possibly decay with a significant branching fraction into $h^0 \rightarrow \pi_v^0 \pi_v^0 \rightarrow b\bar{b}b\bar{b}$, as shown in Fig. 1.7(*right*). It has good chance to reveal itself through this channel. Unusual combinations of b jets, lepton pairs and/or missing energy may accompany this signal.

It should be added that the same topology can also be achieved in the next-to-minimal supersymmetric standard model (NMSSM) : $h^0 \rightarrow ss \rightarrow b\bar{b}b\bar{b}$, where s is any scalar.

In this thesis, we have chosen three samples of such a decay with $m_{h^0} = 120 \text{ GeV}$, $m_{\pi_v^0} = 35 \text{ GeV}$ and $\tau_{\pi_v^0}$ equal to 1 ps, 10 ps and 100 ps. They will be later referred as HV1, HV10, HV100, for lifetime of the simulated π_v^0 .

This choice should not hide the great richness of possible decays and signatures of the HV models. We strongly recommend the interested reader

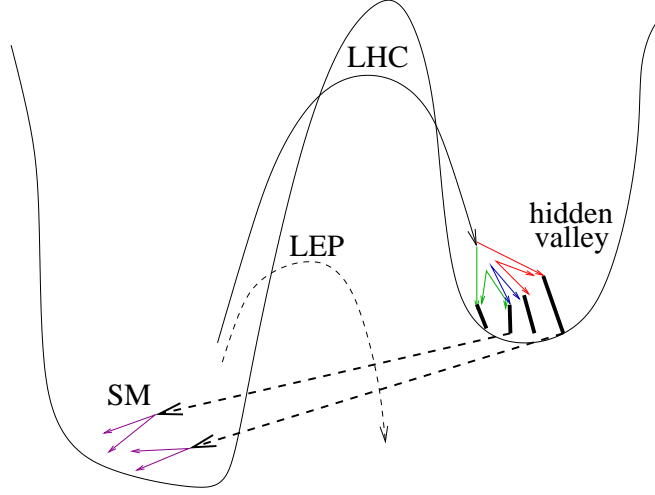


Figure 1.6: While the LEP was unable to penetrate the barrier separating the sectors, LHC may leap over it and produce v -particles. Illustration taken from [55].

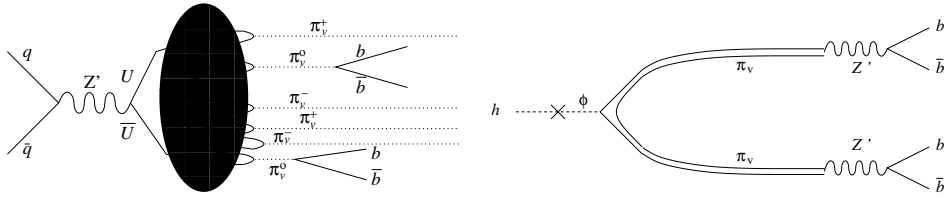


Figure 1.7: *Left:* production of v -hadrons through fusion of quarks and production of a Z' . *Right:* decay of H^0 via a scalar field ϕ into two π_v^0 , that subsequently decay into $b\bar{b}$ jets. Illustration taken from [53] and [54].

to consult the given references.

The hidden-valley scenario appears consistent with most methods for solving the hierarchy problem like supersymmetry, little Higgs models [61], TeV extra dimensions [66], Randall-Sundrum scenarios [57], etc. The phenomenology it describes may go along many other theoretical BSM phenomenologies. This scenario arises naturally in the construction of extra-dimensional models and most particularly in string theories. [55] reviews the impact of a hidden valley sector may have on the classic phenomenology of supersymmetry if the LSP lies in the valley sector. Finally, it should be stressed that dark matter consistent with recent measurements may arise from such “hidden” sectors [56]. These two references are a good example of an harmonic relation between SUSY and HV models.

1.5 Beyond the Standard Model : And Many More...

This list of models presented in the previous sections is of course far from being exhaustive.

We have seen in previous sections that extra dimensions (ED) are compatible with all models presented so far. By themselves, ED accessible to SM fields - so called “universal” ED (UED) - could allow gauge coupling unification, provide new mechanisms for supersymmetry breaking and the generation of sfermion mass hierarchy, and may be responsible for electroweak symmetry breaking. For example, standard model gauge interactions may produce a bound-state Higgs doublet in six dimensions without excessive fine-tuning. According to UED [66], all SM particles uniformly propagate in extra dimensions of size $R^{-1} \sim \text{TeV}$. UED models predict that for all SM particles there exist corresponding so-called Kaluza-Klein (KK) states in extra dimensions, which have the same quantum numbers and spins as their SM partners. Most KK modes are stable, which could cause cosmological problems, unless there exists KK-number-violating interactions, in which case the KK states can decay into ordinary SM particles with macroscopic decay length. Their production and signature are expected to be close to standard supersymmetry.

Little Higgs models with T-parity, conceived to solve the little hierarchy problem, contain a T-odd heavy photon [61] A_H . If the T-parity is slightly violated, this photon can decay with long lifetime to W^+W^- or ZZ , or via loops to $f\bar{f}$ [62]. T-odd partners would be potentially copiously produced at the LHC/LHCb and cascade down to A_H .

Extensions of the SM with extra $U(1)_{B-L}$ feature a Z' and 3 long-lived, heavy neutrinos. The mass of the light ν are generated through see-saw mechanism. The decay width of these heavy neutrinos (ν_H) is proportional to the ratio of light to heavy neutrino masses, hence they could have a macroscopic lifetime [63]. The signatures of the ν_H are similar to the ones of the $\tilde{\chi}_1^0$ from $B\bar{P}_R$ models.

Finally, a quark from a 4th generation might well be another candidate [111]. if the b' quark has a lower mass than the top quark, its dominant decay would be $b' \rightarrow bZ^0$ through loop diagram, leaving us with a displaced Z^0 and a b jet.

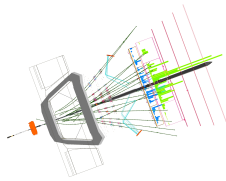
In this chapter, we have introduced the Standard Model of Particle Physics and discussed its limitations. We have then summarised some models built to cure them and complete it in a coherent and more general framework, with a special focus on the ones predicting long-lived particles. It should be stressed

that this list of models is far from being complete. Due to limited time at our disposal, we had to restrict ourselves to the most famous ones. But the imagination of theorists is known to have no limitations. We therefore tried to also include the most promising ideas.

While doing this work, a strong impression came : there is always, in any model, a way to generate long-lived *objects*.

Chapter 2

The LHC and LHCb experiment



This chapter describes the LHC and briefly introduces its experiments. The LHCb detector, its particle identification and tracking systems, as well as the trigger system, are discussed in details. This chapter closes with the presentation of the common software for simulation and analysis of the data.

2.1 The LHC challenge

THE EUROPEAN ORGANISATION for Nuclear Research (CERN) aims at probing the very nature of matter at high energy density, pushing always further and further the frontiers of reachable energy. CERN currently hosts the large hadron collider (LHC). The LHC is a remarkable machine in many aspects and represents probably one of the greatest scientific challenges ever dreamt up and conceived.

The LHC consists of two counter-rotating hadron beams and replaces the previous LEP accelerator in its original 27 km long tunnel situated approximately 100m underground in the Geneva area.

Two parameters are mainly used to describe a collider performance : the energy in the center-of-mass (CM) of the colliding particles and the luminosity. The LHC is designed to operate at an energy in the CM up to $\sqrt{s} = 14$ TeV. This is considerably higher than the LHC's main competitor, Fermilab's Tevatron (USA), which runs at a maximum of 2 TeV. In

comparison, the LEP achieved 209 GeV, the highest CM energy for a lepton collider. At their high energies are created massive particles that are otherwise unobserved in nature.

For the LHC, the luminosity is given by

$$\mathcal{L} = \frac{N_b^2 n_b \nu}{\mathcal{F}} \quad (2.1)$$

where n_b the number of bunches per beam, N_b is the number of particles per bunch (10^{11} !), ν the frequency of revolution and \mathcal{F} is a factor grouping terms describing the beam geometry. The LHC targets $\mathcal{L} = 10^{34} \text{ cm}^{-2} \text{ s}^{-1}$. This can be reached through a large number of bunches, 2808 per beam, and by a large revolution frequency of 11245 Hz, leading to a period of 25 ns between two consecutive bunch crossings. Higher luminosity ensures higher statistics for the phenomena investigated. This cannot be achieved colliding $p\bar{p}$ as done in the Tevatron. It would require a production of antiprotons at a level presently impossible. Tevatron reaches an instantaneous luminosity of $\sim 4 \cdot 10^{32} \text{ cm}^{-2} \text{ s}^{-1}$

The construction and operation of the LHC involves massive engineering and computing challenges, as well as financial ones. The machine and detectors alone have cost around 6 billion Swiss francs (4.5 billion €). From the onset, it was clear that no new dedicated tunnel would be dug for the LHC. Therefore the LEP tunnel was used. The excavation of the LEP tunnel was one of Europe's largest civil-engineering projects before the achievement of the Channel tunnel. To reach the incredible energy density, the magnetic field used to guide the protons around the tunnel had to be increased to 8.3T. Generating such magnetic fields requires huge electric currents in the order of 200 amps. In order to carry such currents superconducting cables are used, which must be cooled to temperatures just a few degrees above absolute zero with liquid helium.

A priori, the thermal energy density stored in the magnet seems quite low. However, the difference in energy density between the magnet cold mass and the ambient air is tremendous. Any thermal insulation weakness can have dramatic consequences. The incident that occurred on the 19th of September 2008 [68] reminds us that keeping the LHC in a safe state is a challenge in itself.

The computing challenges are particularly pressing. High-energy collisions between protons typically generate hundreds of secondary particles. The high luminosity implies the production of a tremendous amount of interesting events per second. Consequently, vast amounts of data must be stored and analysed. It is estimated that around 15 petabytes of data will

be generated per year at the LHC. If stored on compact discs, one year's worth of data would result in a stack as high as the Mount Everest and it would require the equivalent of 10^5 of today's highest performance personal computers to process it. In order to deal with such a huge amount of data, a new concept in scientific computing, known as the "Grid", is employed. The Grid is a global computing infrastructure, based on 60 major computing sites spread across Europe, North America and Asia, and connected by a super-high-bandwidth telecommunication network which will process and store the LHC data. The Grid will allow for computing power around the world to be pooled for the first time, making it possible to perform computations that no single local cluster of computers could ever hope to perform. The Grid team has faced enormous challenge to solve issues concerning the storage, security and accessibility of data, but has overcome most of them.

The Grid could well result in another revolution in computing and telecommunications, just like the World Wide Web.

2.2 The LHC Experiments

CERN hosts 7 main experiments using the LHC facility, found at the four interaction points around the ring :

ATLAS (A Toroidal LHC ApparatuS) [70] is a general-purpose detector devoted to the research and study of the Higgs Bosons, improved measurements of the SM, and of possible physics beyond the SM. ATLAS is the biggest of the LHC detectors : it measures 45m in length and 25m in diameter, as shown in Fig. 2.1(s). It weights about 7000 tons.

CMS (Compact Muon Solenoid) [71] is the second "heavy-weight" of the LHC experiments. It shares with ATLAS the same physics program, and same huge barrel-shaped design, see Fig. 2.1(b). Both are "hermetic" in the sense that they entirely surround the collision point. Although they were designed for pp collisions, these experiments will also operate during heavy ions runs. CMS has a solenoid magnet, unlike ATLAS which has a toroidal magnet. As its name says, it is more *compact*, smaller in size (22m \times 15m), but much heavier than Atlas, weighting 14'500 tons. Its name also suggests that it is optimised for the detection of muons.

TOTEM stands for TOTAl cross section, Elastic scattering and diffraction dissociation Measurement at the LHC [72]. The TOTEM's physics program is dedicated to the precise measurement of the proton-proton interaction

cross section, as well as to the in-depth study of the proton structure which is still poorly understood. It covers the region in the pseudo-rapidity range $3.1 < \eta < 6.5$. TOTEM consists of Roman pots located several hundreds of meters on either side of the CMS interaction point, as well as detectors integrated in the CMS apparatus at about ten meters from the interaction point.

LHCf [73] is an experiment to cover the very forward regions. Located at 140 meters on either side of the ATLAS interaction point, it aims at studying the neutral-particle production cross sections of proton-proton and nucleus-nucleus interactions at very small scattering angles. This could help to improve our understanding of the development of atmospheric showers induced by very high energy cosmic rays hitting the Earth atmosphere.

ALICE [74] is dedicated to the study of strongly interacting matter at extreme energy densities, where the formation of a new phase of matter, the quark-gluon plasma, is expected. For this experiment, the LHC will also collide lead ions with a total CM energy of 1.15 PEV and a luminosity of $10^{27} \text{ cm}^{-2} \text{ s}^{-1}$. The main experimental challenge is to operate in the extreme multiplicity environment anticipated in Pb-Pb collisions. The ALICE detector is depicted in Fig. 2.1(c).

LHCb the LHC “beauty” experiment is firstly intended for the study of \mathcal{CP} -violating processes and rare decays in the B mesons. The experiment is described in more details in Sec. 2.3.

MoEDAL [76] MoEDAL is a passive experiment dedicated to the search highly ionising exotic particles, using plastic track-etch detectors (aka NTDs). The MoEDAL detector is housed in the LHCb cavern and is located around the VeLo, as can be seen on Fig. 2.1(d). The passage of a highly ionising particle through the plastic track-etch detector is marked by an invisible damage zone along the trajectory. The track in the track-etch detector stack can be pointed to the primary vertex (PV) with precision 1 cm. Some of these hypothetical particles are magnetic (Dirac) monopoles with mass up to $\sim 4 \text{ TeV}$ and magnetic charge (g) of up to 3, Dyons with magnetic and electric charge, or exotic, (pseudo-)stable, heavy, single or multiply charged particles, e.g. :

- Charged black hole remnants from ADD models of extra dimensions,
- Doubly Charged Higgs bosons,
- Very heavy stable SUSY particles,

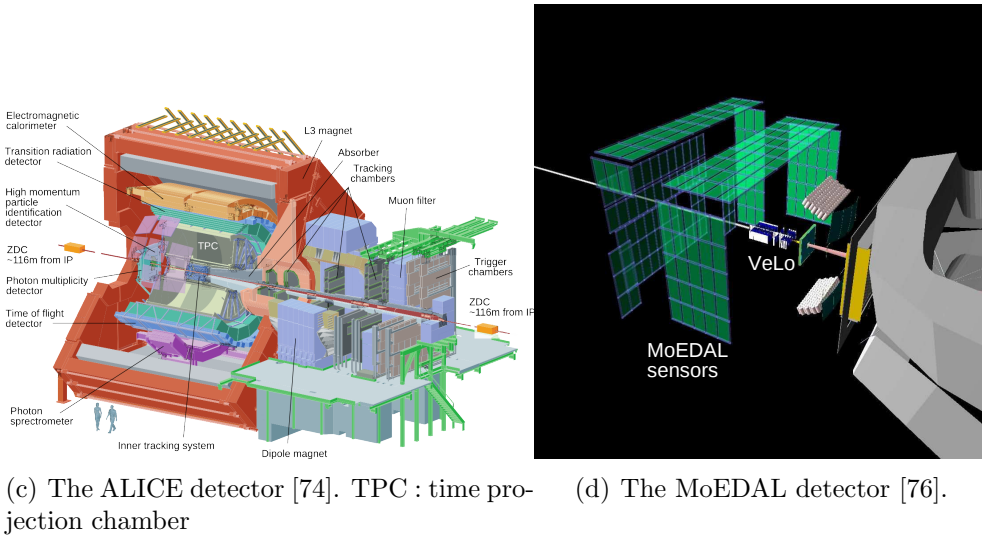
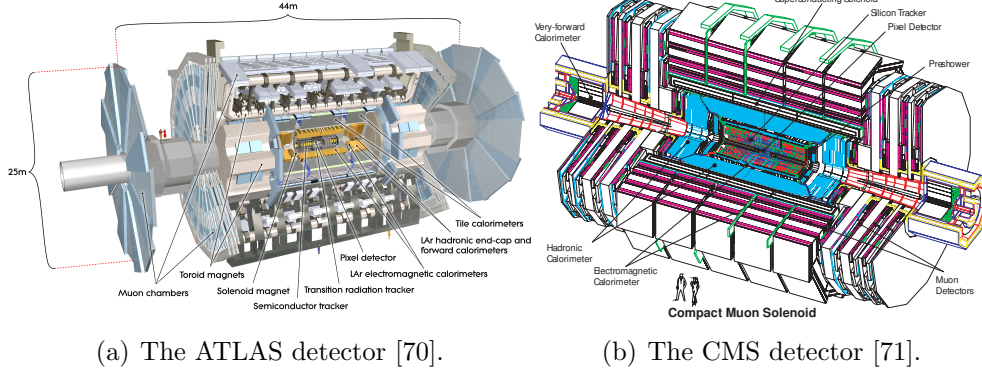


Figure 2.1: Some of the LHC detectors.

Q-balls¹.

The data collected could be of order $\mathcal{O}(\text{fb}^{-1})$.

2.3 The LHCb Experiment

LHCb is an experiment dedicated to heavy flavour physics at the LHC [75]. Its primary goal is to look for indirect evidence of new physics in \mathcal{CP} violation and rare decays of beauty and charm hadrons.

The number of inelastic pp collisions N_{pp} taking place at each interaction

¹Extended balls of electric charge, predicted in non-Abelian gauge theories.

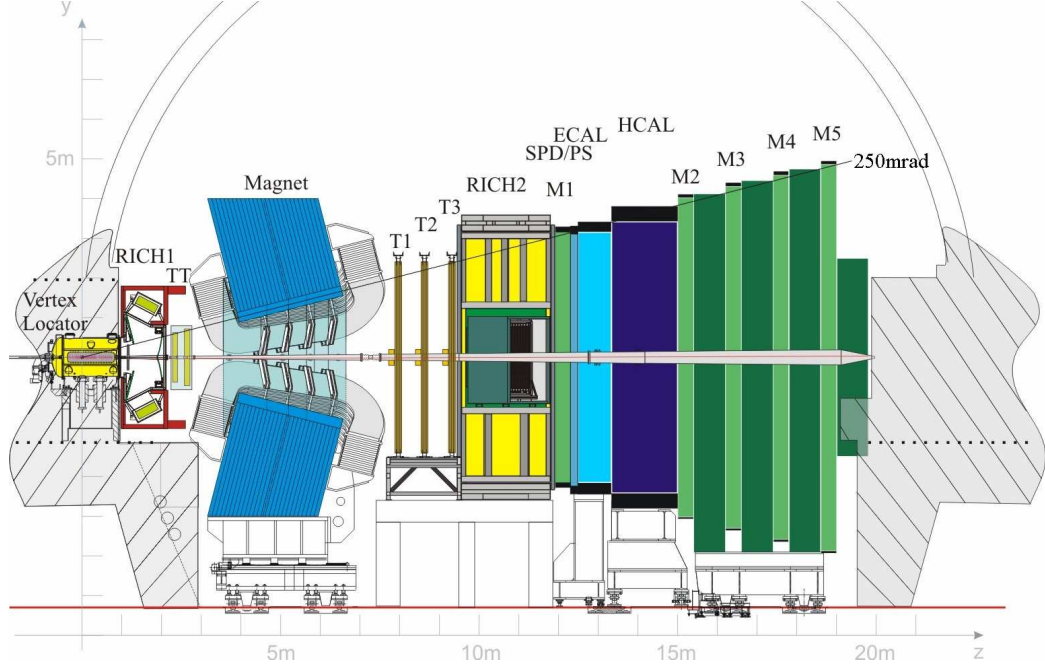


Figure 2.2: View of the LHCb detector [75].

point for a given period can be computed as

$$N_{pp} = \sigma_{pp}^{incl} \int \mathcal{L} dt, \quad (2.2)$$

where $\sigma_{pp}^{incl} = 60$ mbarn is the expected inelastic proton-proton cross-section at $\sqrt{s} = 14$ TeV and \mathcal{L} is the instantaneous luminosity.

The mean number of interactions per bunch crossing is

$$\langle n_{pp} \rangle = \frac{\sigma_{pp}^{incl} \mathcal{L}}{\nu_x}. \quad (2.3)$$

The average crossing rate of two proton bunches ν_x is of the order of ~ 30 MHz at the LHCb interaction point. At the LHC design luminosity, this will lead to $\langle n_{pp} \rangle = 25$ interactions per bunch crossing. This is too large for LHCb's purposes, which require the correct matching of a reconstructed b decay to the primary vertex from which it originated. Events with that many interactions would lead to false matches which will alter the quality of the physics results. At the LHCb interaction point, the beam will be slightly defocalised in order to reduce $\langle n_{pp} \rangle$ to 0.7. The nominal luminosity will therefore be lower in LHCb than in ATLAS and CMS, at about $\mathcal{L} =$

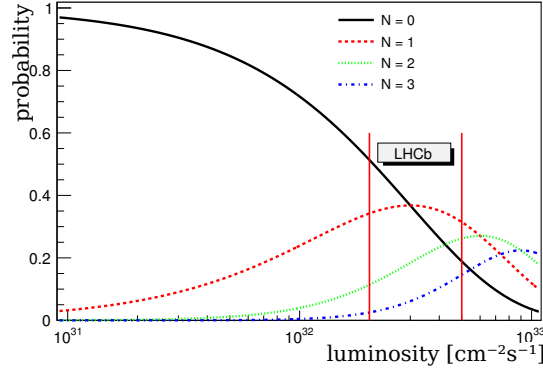


Figure 2.3: Probability to observe $N = 0, 1, 2, 3$ interactions per bunch crossing as a function of the instantaneous luminosity. In the LHCb luminosity region, the probability of 0 or 1 interaction is dominating.

$2 \cdot 10^{32} \text{ cm}^{-2} \text{ s}^{-1}$. Figure 2.3 shows the probability to get $\langle n_{pp} \rangle = 0, 1, 2, 3$ or 4 interactions per bunch crossing as a function of the luminosity.

The LHCb detector is a single-arm spectrometer with a forward angular coverage from approximately 10 mrad to 300 (250) mrad in the bending (non-bending) plane. In terms of pseudo-rapidity ($\eta = -\ln \tan(\frac{\theta}{2})$) the acceptance is $1.8 < \eta < 4.9$. The choice of the detector geometry is justified by the fact that at high energies both the b- and $\bar{\text{b}}$ -hadrons are predominantly produced in the same forward or backward cone. The layout of the LHCb spectrometer is shown in Fig. 2.2. The LHCb coordinate system is centred at the interaction points, which is in the middle of the vertex locator (VeLo). The z axis is parallel to the beam and points downstream, i.e. in the direction of the detector, also called the forward direction. The y axis is vertical and points to the top, the x axis is horizontal, it points outside the LHC ring and defines what is called the left side ($x > 0$) and the right side ($x < 0$) of the detector. The LHCb detector is essentially composed of a tracking system and a particle identification system.

The tracking system, and the VeLo in particular, will be more extensively depicted as they play a central role in our analysis. The inner tracker (IT) sub-detectors will be the object of a complete description in Chapter 3.

2.3.1 The Particle Identification System

The particle identification system is particularly elaborated as the identification of particles is important in B physics. It is essential to determine the flavour of the mother B meson, as well as to distinguish between kinetically

and topologically similar decays.

The identification system is made of the following devices :

Two Ring Imaging Cherenkov detectors (RICH1/2) : RICH1, located between the VeLo and the tracker turicensis (TT), and RICH2 located between the last T stations and the calorimeters. These two detectors are complementary in terms of angular and momentum coverage. The combined system achieves a $K-\pi$ separation of 3σ in the momentum range of 3 to 90 GeV. This separation is required for example to allow a distinction of the $B_s \rightarrow D_s^\mp K^\pm$ decays from the $B_s \rightarrow D_s^\mp \pi^\pm$ decays.

The Calorimeters, situated after RICH2 and the tracking system in the given order of presentation. They are made of three main elements :

First, in order to distinguish between charged particles and neutrals such as photons and π^0 , a layer of scintillators is placed just after the M1 station. This detector is the scintillator pad detector (SPD), which achieves a good separation between electrons and photons. The latter will have identical behaviour downstream in the electromagnetic calorimeter (ECAL). After a 12 mm-thin layer of lead, one finds a layer of scintillators almost identical to the SPD, the preshower (PS). Its purpose is to distinguish between electrons and charged pions. Due to the difference in interaction lengths of electrons and pions in the lead, electrons produce showers that initiate in the lead converter, whereas pions do not. Those two detectors provide identification in a very fast way, to be used by the first-level trigger.

The electromagnetic calorimeter (ECAL) aims at measuring the energy deposit of the electromagnetic showers. It is made of alternating layers of scintillators and lead, optimised for the reconstruction of π^0 from photons conversion.

The hadronic calorimeter (HCAL) identifies hadrons via inelastic interactions in a dense material. The charged products of these interactions, mainly pions, are detected in a scintillating medium. The HCAL is made of a succession of 16 mm-thick iron and 4 mm-thick scintillating tiles which are parallel to the beam. Ionising particles crossing the scintillator produce light in the UV range which is converted to visible light by scintillating dopants. The light is collected at the end of the tile by wavelength shifting fibres. The calorimeters also provide critical information about transverse energy of hadron, electron and photon candidates to the first-level trigger.

The muon chambers, made of five stations labelled M1 to M5. M1 is located between RICH2 and the preshower, whereas M2 to M5 are located

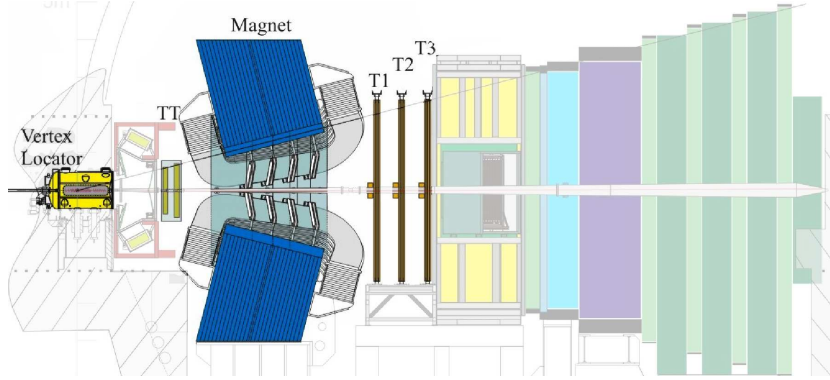


Figure 2.4: The Tracking System of the LHCb detector [75].

after HCAL and whose dimensions follows approximately the LHCb acceptance. Muons are identified by a dedicated system as they are the sole charged particle to go through the calorimeters without being stopped. The muon stations are for the greatest part equipped with multi-wire proportional chambers (MWPC) which allow a full collection of the signal within 20 ns, hence its importance in the trigger.

2.3.2 The Tracking System

To achieve an excellent vertex resolution, it is important to get precise measurements of the track momentum and position as close as possible to the beam-beam interaction region. In this challenge, outstanding detectors and track reconstruction algorithms are needed. This section aims at presenting the key players.

The tracking system, illustrated in Fig. 2.4, consists of several subdetectors. Surrounding the *luminous* region, i.e. the region in which pp collisions occur, one finds the VeLo [77][75][78]. The VeLo is described in details in Sec. 2.3.2.a.

The next tracking subdetector is the tracker turicensis (TT) [78], just before the magnet [79]. The TT consists of two stations separated by a distance of 27 cm. Each station consists of two layers of silicon detectors, for a total of four layers which have a small stereo angle between them to resolve tracking ambiguities. The total silicon surface adds up to 8.4m².

The dipole magnet [79] consists of two trapezoidal coils bent at 45° on the two transverse sides, arranged inside an iron yoke. The magnet is made of aluminium conducting wires (9 km in total). Mainly for cost reason, it is warm rather than super-conducting. The magnetic field is vertical and bends the track in the horizontal x-z plane. To meet the requirements on the track

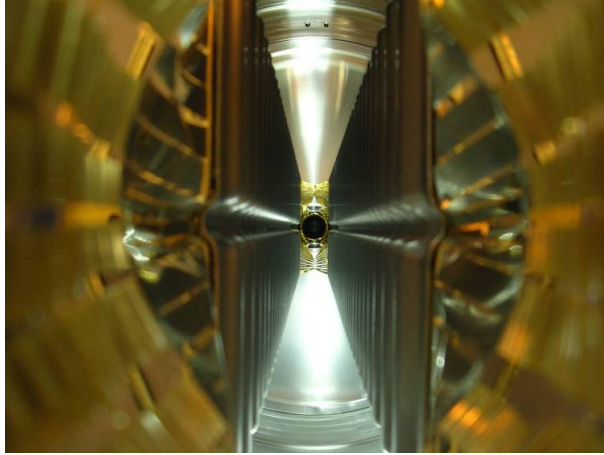


Figure 2.5: Picture of the interior of the VeLo (in open position), as viewed from an incoming proton.

momentum resolution, a 4 Tm integrated magnetic field over the part of the detector dedicated to the tracking is necessary. The magnetic field reaches a maximum at 1.1 T. To control systematic errors and eventually compensate for a possible detector left-right asymmetry, the magnetic field polarity can be reverted.

The charged particles bent by the magnet then reach the T tracking stations, which present themselves as three vertical stations, each covering an area of about $6 \times 5\text{m}^2$. In order to cope with a large particle flux gradient, these stations are made in two parts.

The inner part, surrounding the beam pipe, is referred to as the inner tracker (IT) [80]. The IT covers approximately 2% of the surface but detects about 20% of the tracks passing through the T stations. An IT station consists of four boxes with four layers silicon sensors, placed around the beam pipe in a cross shape. It spans about 125 cm in width and 40 cm in height. The IT subdetector is described in details in Chapter 3.

The outer part, which covers the remaining acceptance, is called the outer tracker (OT) [81]. Unlike the other tracking detectors, based on silicon-strip technology, the OT is a straw tube drift chamber detector. The straw tubes have a diameter of 5 mm and $75\text{ }\mu\text{m}$ -thick walls. The gas filling the cells is an $\text{Ar}/\text{CF}_4/\text{CO}_2$ mixture, which has a drift and collection time of less than 50 ns. The spatial resolution obtained is $\sim 200\text{ }\mu\text{m}$.

2.3.2.a The Vertex Locator

The vertex locator (VeLo) [77][75][78] provides precise measurements of track coordinates close to the interaction region, which are used to reconstruct the PV, where the pp interaction occurred, and to identify the displaced secondary vertices produced by the decay of long-lived particles.

The VeLo is built out of a succession of $300\text{ }\mu\text{m}$ thick silicon half disks arranged perpendicularly along the beam line. The layout has been optimised to minimise the amount of material in the acceptance while providing good geometrical coverage. All tracks inside the LHCb acceptance ($1.6 < \eta < 4.9$) pass through at least three modules, as shown in Fig. 2.6. Each half-disk provides a measurement of either the r or the ϕ (azimuthal angle) coordinate of a track and is called r or ϕ *sensor*. The sensors use single-sided n-implants in n-bulk technology with strip isolation achieved through the use of a p-spray.

The r -sensors are designed with concentric semi-circular microstrips, centred on the nominal LHC beam axis. In order to lower the occupancy and strip capacitance, the strips are subdivided in four 45° regions. The innermost strip lies at 8.2 mm from the beam interaction axis. At that position the pitch between two r -strips is $38\text{ }\mu\text{m}^2$, increasing linearly to $101.6\text{ }\mu\text{m}$ at the outer radius of 41.9 mm . This varying pitch allows measurements along a track to contribute with an equal weight to the impact parameter (IP) measurement, and helps to average the occupancy.

ϕ sensors are divided in two regions, for resolution and occupancy reasons. The strips of the inner region are characterised by an angle with respect to the radial direction of 20° and a pitch between $35.5\text{ }\mu\text{m}$ and $78.3\text{ }\mu\text{m}$. The inner region covers radii from 8 mm to 17.25 mm , while the outer region covers radii from 17.25 mm to 41.9 mm radius with a pitch between $39.3\text{ }\mu\text{m}$ and $97\text{ }\mu\text{m}$. The strips of the outer region make a $\pm 10^\circ$ angle with the radial direction, its sign being opposite to the one of the inner region. To resume, two sensors together in closed position look like a compact-disk of 84 mm in diameter, with a hole of 16 mm in diameter. Figure 2.7 shows a front view of both sensor types in the closed detector position.

A *module* is made of an r and a ϕ sensor held together with a gap of about 2 mm by a carbon fibre structure. The modules are arranged so that two consecutive ϕ sensors have opposite skew orientation. This skewed strip design is motivated by pattern recognition efficiency. Two modules at about the same z position on each side of the VeLo define a *station*, which can be seen as a plane able to measure a 2D point, the third dimension being known from the plane position.

²The minimum pitch achievable using the n-bulk technology is approximately $32\text{ }\mu\text{m}$.

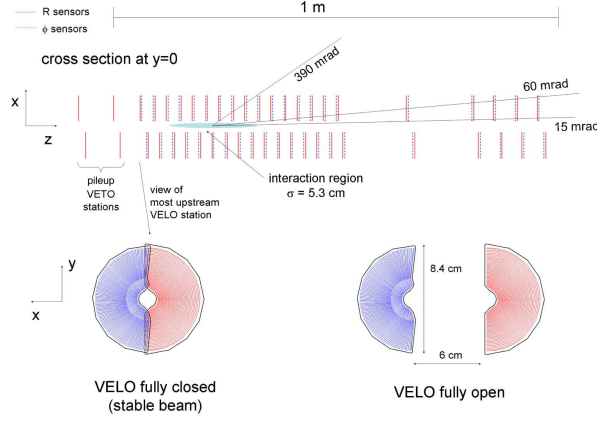


Figure 2.6: Arrangement of the VeLo modules viewed from the top. The interaction region is represented with the shaded elliptic area. The r (red) and ϕ (blue) sensor are displayed below [75].

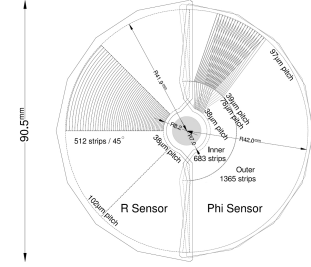


Figure 2.7: Sketch of r and ϕ VeLo sensors in closed position [75].

The choice of the (r, ϕ, z) cylindrical coordinates was motivated by cylindrical geometry, but also to drive fast track reconstruction in the high-level trigger (HLT) (see Sec. 2.3.3). Indeed, the reading of the r -sensors only is sufficient to estimate the IP of a track with respect to the primary vertex. In the r - z projection, forward-going tracks with a high IP with respect to the PV are easily identified, allowing the separation of interesting tracks, not coming from the PV, from prompt products of the collision.

The VeLo comprises 21 such stations and four additional r sensors in the backward region called the VETO stations and used by the Pile-up Veto system.

The two VeLo halves are retractable and the VeLo can be operated at different apertures. This mechanical feature requires that no physical pipe is present. Therefore, the vacuum is ensured by a vacuum vessel surrounding the detector. To minimise the extrapolation of tracks to the beam interaction axis and thus increase the resolution on reconstructed vertices, the innermost strip of the sensors must have a radius as small as possible. During physics running conditions, the RMS spread of the beams will be less than $100 \mu\text{m}$, but for safety reasons, the closest approach allowed to the nominal beam axis is 5 mm. This value is dominated by the yet unknown closed-orbit variations of the LHC and could be reduced in an upgraded detector. To this must be added the thickness of the RF-foil (see later), the clearance between the RF-

	CMS	ATLAS	LHCb
Pixel size	$100 \times 150 \mu\text{m}$	$50 \times 400 \mu\text{m}$	$38 \mu\text{m}$ (r-strips), $35.5 \mu\text{m}$ (ϕ -strips)
Closest dist. to beam	4.4 cm	5 cm	8 mm
nominal \mathcal{L} [$\text{cm}^{-2}\text{s}^{-1}$]	$> 10^{34}$	$> 10^{34}$	$2 - 5 \cdot 10^{32}$
$\langle \frac{\text{interactions}}{\text{bunch crossing}} \rangle$	23	23	0.7

Table 2.1: Some main characteristics of the ATLAS, CMS and LHCb experiments.

foil and the sensors, and the design of about 1 mm of guard-ring structures on the silicon. Taking everything into account, the sensitive area can only start at a radius of about 8 mm in the best stable running conditions (fully closed position, see Fig. 2.7). During beam injection, the two halves are retracted by 3 cm.

As a rough comparison, the ATLAS tracking system (the Inner Detector) features a semiconductor pixel detector, called the “Pixel detector”, for track reconstruction close to the luminous region. The pixel size is about $50 \times 400 \mu\text{m}$ and the first pixels begin at about 5 cm from the beam interaction line. On the other side of the LHC ring, the CMS collaboration is proud to have built the world’s largest silicon detectors, covering an area the size of a tennis court. Surrounding the CMS collision point a pixel detector is also to be found, where some pixels come as close as 4.4 cm from the beam. These pixel tiles span about $100 \times 150 \mu\text{m}$. Table 2.1 resumes the main differences between the ATLAS, CMS and LHCb detectors. LHCb is by far measuring hits the closest to the collisions and achieving the highest granularity in that area, but covers a limited acceptance for track reconstruction of about 390 mrad originating from $|z| < 10.6 \text{ cm}$, as shown in 2.6.

Due to the absence of any physical pipe³, the silicon disks and the front-end electronics must be protected from the beam radio-frequency pickup, while the LHC vacuum needs also to be preserved from out-gassing of the radiated detector modules. This is achieved through a $300 \mu\text{m}$ thick aluminium (AlMg_3) box called the RF-foil. To allow the overlapping of the two sensitive regions, the foil has a complex shape in the yz plane. Figure 2.10 shows a close-up of some of the VeLo sensors with the vertical part of the RF-foil.

The VeLo detector is performing as expected : the cluster finding efficiency reaches 99.7%, while the single hit resolution is as low as $\sim 4 \mu\text{m}$. The module and sensor alignment is better than $5 \mu\text{m}$ and the variation from

³The reason why will be given in 2.3.2.c.

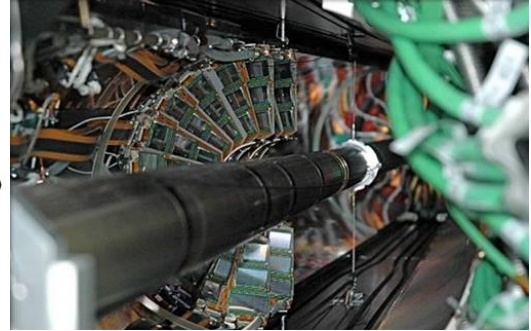
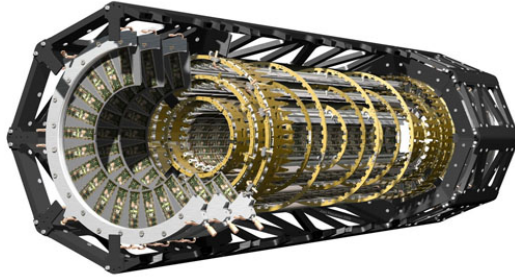


Figure 2.8: Scheme of the ATLAS Pixel detector.

Figure 2.9: A CMS pixel detector “half” wrapping around the beam.

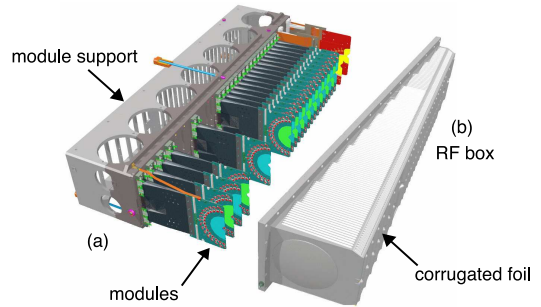
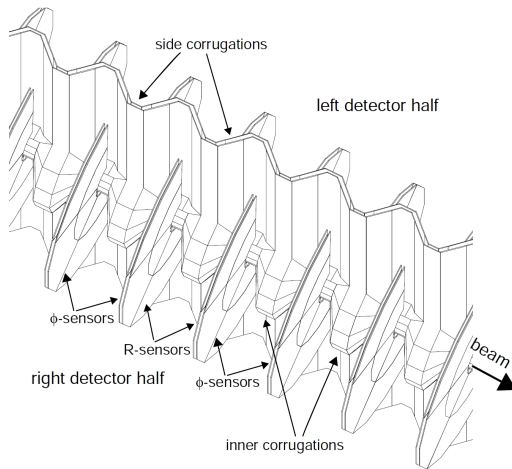


Figure 2.10: Zoom on the inside of Figure 2.11: Exploded view of the an RF-foil, as modelled in GEANT, module support and the modules (a), with the detector halves in the fully and the RF box (b). The corrugated closed position. The edges of the box foil on the front face of the box, which are cut away to show the overlap with forms a beam passage can be seen. Its the staggered opposing half [75]. form allows the two halves to overlap when in the closed position [75].

fill to fill is below $5\,\mu\text{m}$ (opening and closing occurs for each fill).

2.3.2.b The Track Reconstruction

The track reconstruction is the nontrivial operation consisting in connecting the hits left by the charged particles in the tracking subdetectors (VeLo, TT, IT and OT), to reconstruct their trajectory - taking into account the effects of the magnetic field - and estimate their momentum through the bending in the magnetic field. A track reconstructed in a subdetector can be extrapolated in the other subdetectors and thus link the information gathered in those to the corresponding charged particle.

Reconstructed tracks are classified according to their trajectories inside the spectrometer, as illustrated in Fig. 2.12:

Long tracks cross the entire tracking system, from the VeLo to the T stations. These have the most precise momentum resolution and therefore are the most important tracks for the study of displaced vertices.

VeLo tracks are reconstructed only in the VeLo and are typically large angle or backward tracks. They are very useful for the primary vertex reconstruction, as well as for the secondary.

Upstream tracks traverse only the VeLo and the TT. In general those tracks are left by particles that were bent outside the acceptance by the magnetic field. The momentum resolution of the upstream tracks is rather poor. However, since they cross RICH1, they are used to understand backgrounds in the RICH1 particle identification algorithm. They may also be used for b-hadron decay reconstruction or flavour tagging.

Downstream tracks traverse only the TT and the tracking stations. The most relevant cases are tracks produced by decay products of long-lived particles, such as Λ or K_S^0 decaying outside the VeLo.

T tracks are only measured in the T stations. Those tracks are generally produced by secondary interactions. Similarly to the upstream tracks for RICH1, T tracks are useful for RICH2 pattern recognition.

The magnetic field in the VeLo is low enough (see Fig. 2.12) to treat VeLo tracks as straight lines. Aligned clusters of hits in the VeLo sensors are

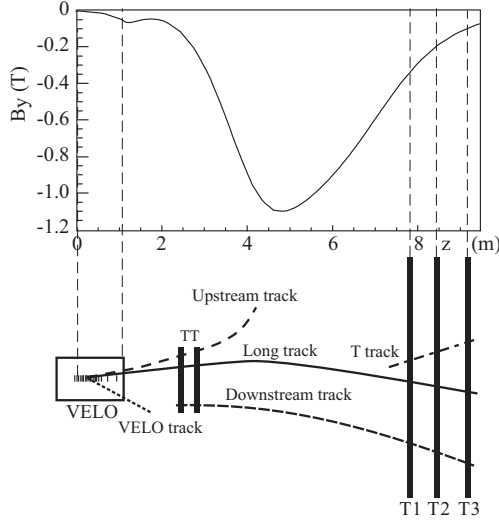


Figure 2.12: Categorisation of the different tracks according to their topology in the LHCb tracking system. The main component of the B -field is also plotted [75].

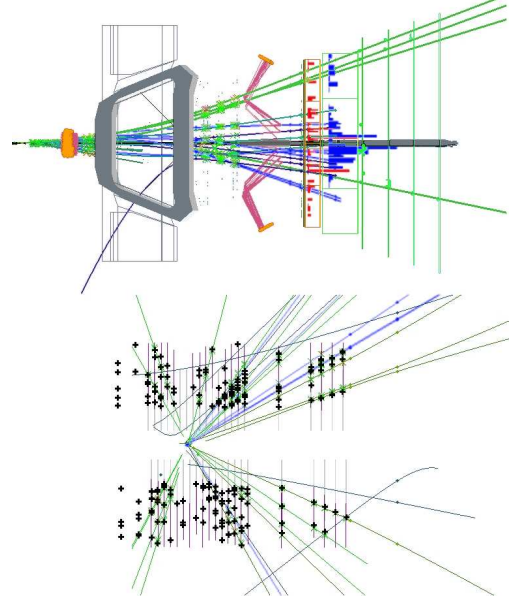


Figure 2.13: Display of reconstructed tracks within the LHCb detector (top), it is an event record on the 11/12/2009 during the first collisions. The reconstruction has a clearly visible PV (bottom) and at least three long tracks.

used to reconstruct straight track segments, that will serve as “seeds” for the LHCb track reconstruction software.

Similarly, an iterative algorithm looks for segments of tracks in the T stations, using both OT and IT clusters of hits, where the magnetic field is also low. Those segments are called T track seeds. The next steps seeds are associated to hits in the other tracking subsystems to form tracks. The procedure to find the Long tracks, defined above, is twofold. First, taking a VeLo seed and a hit in a T station, hits are looked for in the other T stations in a search window around the track candidate trajectory. If hits are found to confirm the track candidate and if its quality is sufficient, it is then classified as a Long track. Hits in the TT corresponding to the track are added to it. Finally, the hits associated with the tracks are removed from the list of hits on which the algorithm has to run. This algorithm, called the forward tracking, reconstructs about 90% of the Long tracks. Secondly, another 4% of the Long tracks are reconstructed by the track matching algorithm. It tries to match pairs of VeLo and T seeds. Each of those seeds is extrapolated

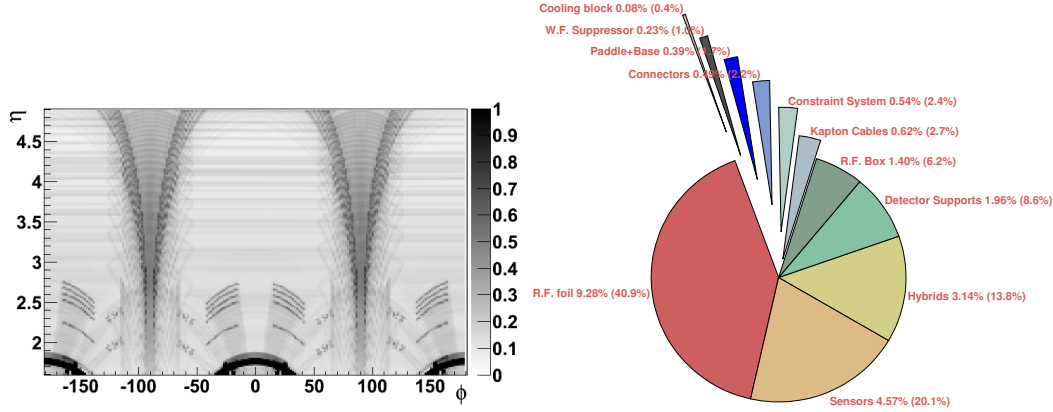


Figure 2.14: *Left*: number of radiation lengths of material in the VeLo as a two-dimensional function of pseudorapidity η and azimuthal angle ϕ . *Right*: the average radiation length per component in the VeLo as a percentage of X_0 , with $1.6 < \eta < 4.9$. The numbers in brackets give this value as a percentage of the average VeLo radiation length. The sum of the segments in the chart gives the total VeLo radiation length as $0.227X_0$ [82].

into the magnet region and their compatibility to form a track is assessed using their position and slopes, as well as the number of compatible clusters in the TT. The TT hits are added to successful candidates. The track reconstruction software fails to reconstruct the remaining 6% of Long tracks. Other algorithms are used to reconstruct the other types of track listed above. It is of course possible for a physical track to be reconstructed by more than one algorithm, resulting in two clone tracks. In that case, only the best out of the two tracks is kept.

After tracks have been found, their trajectories are refitted with a Kalman filter which uses full magnetic mapping and accounts for multiple scattering and corrects for energy loss caused by crossing detector materials.

2.3.2.c Interactions with the Detector

Interactions in the detector material reduce the detection efficiency and multiple scattering of flying particles complicates the pattern recognition and degrades the momentum resolution. Therefore special attention was paid to the amount of material in the VeLo and up to the last station of the tracking system. This motivated the fact of not using a physical pipe to wrap the beam and operate the VeLo sensors directly in the vacuum. (As already outlined in Sec. 2.3.2.a, one had to resort to a protection from the radio-frequencies induced by the beam.)

Investigations of the material budget were performed in simulations by generating straight tracks originating from the interaction point and extrapolating them through the VeLo. The radiation length seen by the tracks was computed for each volume it crossed in the geometry description. The average radiation length is shown as a function of the azimuthal angle ϕ and the pseudorapidity η , with $1.6 < \eta < 4.9$ in Fig. 2.14 (*left*). For a uniform sampling over these coordinates the average contribution of the VeLo to the radiation length is $0.227 \cdot X_0$. The contribution of the components is shown in Fig. 2.14 (*right*). The RF-foil represents a major fraction of the VeLo material in the LHCb acceptance, along with the sensors.

At the end of the tracking, just before entering RICH2, a particle has seen, on average, about 60% of a radiation length and about 20% of an absorption length.

2.3.2.d Performance

The pattern recognition performance is evaluated in terms of efficiencies and ghost rates. The efficiencies are normalised to the reconstructible track samples. To be considered reconstructible, a track must have a minimum number of hits in the relevant subdetectors. To be considered successfully reconstructed, a track must have at least 70% of its associated hits originating from a single Monte-Carlo (MC) particle. The reconstruction efficiency is defined as the fraction of reconstructible tracks that are successfully reconstructed, and the ghost rate is defined as the fraction of reconstructed tracks that are not matched to a true MC particle.

The average number of successfully reconstructed tracks in fully simulated $b\bar{b}$ events is about 72, which are distributed among the track types as follows: 26 long tracks, 11 upstream tracks, 4 downstream tracks, 26 VeLo tracks and 5 T tracks.

The efficiency to find as a long track the trajectory of a particle with momentum larger than 10 GeV is 94% on average. The corresponding average ghost fraction is about 9%, these mostly consisting of low p_T tracks. The momentum resolution ranges from $\delta p/p \sim 0.35\%$ for low momentum tracks ($\mathcal{O}(1)$ GeV) to $\delta p/p \sim 0.55\%$ for tracks with momentum of $\mathcal{O}(100)$ GeV.

2.3.3 The Trigger System

At the nominal luminosity of $2 \cdot 10^{32} \text{ cm}^{-2}\text{s}^{-1}$, the expected rate of pp (visible) collisions is about 10 MHz. Since the average size of an event is about 35 kByte, keeping all data becomes an impossible challenge. And an absurd

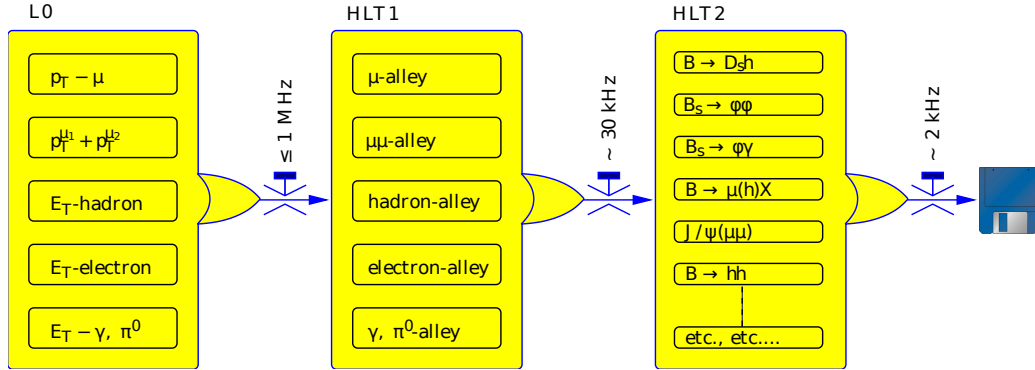


Figure 2.15: Flow-diagram of the different trigger sequences [75].

one, as at the end only a tiny fraction will be exploited for analysis. As an example, about 15'000 B mesons are expected per second.

The essence of a good trigger system is to identify and select *interesting* events while keeping the level of non-desired events - the background - as low as possible, in the limits of the available data storage capacity and computing power.

But what is interesting and what is not? Only an in-depth analysis could help to decide. Keep in mind as well that new ideas for researching new objects come often later on as the knowledge about a specific phenomenon increases. This is particularly true as the LHC brings us at the border a large unknown territory. All events put aside by the trigger are irremediably lost for analysis. The quintessence of a good trigger is to leave open doors for the unexpected...

The LHCb trigger system is implemented as a two-level architecture. The level-0 trigger (L0) operates at hardware level synchronously with the 40 MHz bunch crossing frequency whereas a second level, the high-level trigger (HLT), is run asynchronously on a computer farm of about 16'000 CPU cores (20'000 in 2011). The HLT is fully implemented in software, which makes it a very flexible tool, capable of evolving with the knowledge of the real data as the luminosity and energy increase and can be subjected to developments and adjustments of the event reconstruction and selection software.

The HLT is further subdivided into the HLT1 and HLT2 stages.

Constraints set the output rate at each trigger level. The maximum global detector data readout sets an upper limit of $\sim 1 \text{ MHz}$ the L0 has to respect. The HLT1 gets constrained to $\sim 30 \text{ kHz}$ by the full event reconstruction necessary for HLT2, which in turn is limited to $\sim 2 \text{ kHz}$ by offline analysis computing resources.

The following subsections show in more details how these goals are achieved. The trigger logical flow, together with the approximate output rate after each level, is illustrated in Fig. 2.15.

2.3.3.a The Level-0 Trigger

The level-0 trigger (L0) is designed to achieve a reduction of the data flow to ~ 1 MHz, which is the maximum readout frequency of the data acquisition system.

The L0 is hardware implemented with custom made embedded electronics. Partial information from the different sub-detectors is used to accept events with high activity.

The L0 attempts to reconstruct the hadrons, electrons, neutral pions and photons clusters with highest transverse energy E_T in the calorimeters and the two muons with highest transverse momentum p_T in the muon chambers. In addition, a pile-up system in the VeLo estimates the number of pp interactions in each bunch crossing. The calorimeters calculate the total observed energy and an estimate for the number of tracks, based on the number of hits in the SPD. With the help of these global quantities events with poor activity may be rejected.

The level-0 trigger (L0) is subdivided into three components: the pile-up system, the L0 calorimeter trigger and the L0 muon trigger.

The L0 Calorimeter trigger looks for high E_T electron, photon, neutral pion or hadron candidates. It forms clusters by summing the E_T of 2×2 cells and selects the highest E_T clusters. Then the information from the SPD/PS, ECAL and HCAL tags the clusters as electron, photon or hadron. Besides the total E_T in the HCAL is used to reject crossings without any visible interaction and to reject events triggered by halo muons. Finally the numbers of hit cells of the SPD is used to evaluate the charged track multiplicity.

The L0 Muon trigger selects the two muons with the highest p_T for each quadrant of the muon detector. The muon chambers allow stand-alone muon reconstruction with a p_T resolution of $\sim 20\%$. Track finding is performed by processing elements which combine the strip and pad data from the five muon stations to form towers pointing towards the interaction region.

The Pile-Up System aims at distinguishing between the single interactions from multiple ones. Four r-sensors of the same type as those used in the

VeLo, are located before the interaction region to measure the radial position of the backward tracks. The Pile-Up system delivers informations about the positions of the PVs and the backward charged track multiplicity. It is not presently used in the final decision.

Each L0 component is connected to one specific sub-detector and to the L0 decision unit (L0DU) which collects all information calculated by the trigger systems to evaluate the final decision. The L0DU has to release its decision in the $4\mu\text{s}$ after a collision, this corresponds to the buffer width implemented in the front-end read-out chips. Furthermore, the time-of-flight of the particles, plus the cable delays, plus the electronics delay already corresponds to $2\mu\text{s}$, leaving only $2\mu\text{s}$ to the L0 system to deliver a decision.

The value of the cuts on E_T and p_T varies depending on the running conditions of the LHC. Typical thresholds for running at a luminosity of $2 \cdot 10^{32} \text{ cm}^{-2}\text{s}^{-1}$ demand having at least one cluster in the HCAL with $E_T^{\text{hadron}} > 3.5 \text{ GeV}$, or the ECAL with $E_T^{e,\gamma,\pi^0} > 2,5 \text{ GeV}$, or a muon candidate in the muon chambers with $p_T^\mu > 1,2 \text{ GeV}$, or $p_T^{\mu_1} + p_T^{\mu_2} > 1 \text{ GeV}$, where μ_1 and μ_2 are the two muons with the largest p_T .

The decision criteria are essentially based on the need of the B physics program. The decay of B mesons produces tracks with large transverse momentum p_T and large transverse energy E_T . This is hopefully the case for all new physics scenarios, which should not suffer from the L0 policy.

2.3.3.b The High-Level Trigger : HLT1

At this stage, the output rate is sufficiently low to allow for an entire read-out of the detector. The HLT1 has access to all data of an event and aims at reducing further the rate to $\sim 30 \text{ kHz}$ to make a full pattern recognition of the event by HLT2 possible.

In brief, the purpose of HLT1 is to reconstruct particles in the VeLo and T-stations corresponding to the objects that triggered the L0 (L0 objects), or, in the case of L0 γ and π^0 candidates, to confirm the absence of a charged particle which could be associated to these objects. This is called Level-0 confirmation.

The HLT1 is organised in several parallel sequences of algorithms, called trigger “alleys”. Each of them confirms a specific Level-0 object. An HLT1 alley is a logical structure, consisting of multiple HLT1 “lines”, which are the physical classes to define the sequence of algorithms to run and set the trigger decision. The “lines” are the structural unit of the whole HLT software. Although each HLT1 line decision is independent of all other HLT1 line decisions, they may share reconstruction steps, executed at most once per event. For instance, the tracks and vertices are reconstructed only once and

this information is available for all.

The HLT1 is based around a single track trigger [116] searching for a single track with high momentum, a large impact parameter with respect to all primary vertices (PVs) in the event, and good track quality. In addition to this, lifetime unbiased muon [114] and electron lines are used for analyses such as the β_s measurement from $B_s \rightarrow J/\psi\phi$; such measurements are sensitive to the presence of lifetime biases. These triggers are based around confirming the L0 trigger decision by matching tracks reconstructed in the HLT to the objects (muon segments or calorimeter clusters) used in the L0 trigger decision. The final decision on the event is an or between all alleys.

HLT1 takes ~ 15 ms to process a L0 accepted minimum bias event and has a retention of $\sim 5\%$ on these events. The relative bandwidth of the different alleys is not fixed and is adapted to the evolution of the LHCb physics goals. It is more than 80% efficient on signal events for the majority of LHCb's benchmark B decay modes.

2.3.3.c The High-Level Trigger : Hlt2

The bulk of the uninteresting events is now removed and the combined output rate of events accepted by the HLT1 alleys is sufficiently low to allow to perform reconstruction that is very similar to what is done offline. This allows the HLT2 to use event-selection criteria that are more in line with those used in offline analyses.

Certain aspects of the reconstruction are simplified for reasons of speed. For example, a simplified detector geometry is used in the Kalman fit, and the RICH reconstruction is only performed on-demand for a small subset of the events. To save time in the HLT2 reconstruction, only tracks with $p_T > 500$ MeV and $p > 5$ GeV are fully reconstructed and fitted with a Kalman filter to obtain a full covariance matrix. To reduce the background rate due to ghosts, all tracks are required to have a track χ^2 value less than 5. From these reconstructed tracks, the basic particles, such as the e^\pm , μ^\pm , p , γ , π , are made using the particle identification (PID) hypothesis. The most common composite particles like some D mesons and kaons, are also reconstructed to avoid multiple reconstructions by different lines.

To the contrary of the previous triggers, the HLT2 is specifically driven by the physics analyses. The HLT2 is split into “inclusive” and “exclusive” lines to cover the whole physics program.

As its name indicates, the inclusive lines aim at selecting decays with the same topology. The most famous ones are the so-called “topological” triggers for B and D decays into hadrons [115]. The exclusive lines are dedicated to decays in specific channels.

Each HLT2 line decision is independent of any other HLT2 line decision, but a HLT2 line may depend on a L0 or HLT1 line decision (confirmation). HLT2 lines share the event reconstruction and intermediate particles (K^* , D , ρ ,...), which are made once per event, when first asked for.

The final trigger is the logical OR between all lines and should produce a final output rate no more than ~ 2 kHz, a rate at which the data can be reasonably stored for off-line analysis.

2.3.3.d Global Event Cut

In order to protect the reconstruction strategy outlined in subsequent sections against saturated events, it is necessary to begin by removing events with too high an occupancy in the VeLo, OT, and IT. In the case of the OT and IT, events are rejected if they contain above 10'000 and 3'000 clusters respectively, corresponding to an occupancy of about 20%. In the case of the VeLo, events are rejected if they contain more than 3000 clusters, a value chosen by observing that above this occupancy the number of tracks reconstructed in the VeLo ceases to have a linear dependence on the number of clusters, indicating an increasing ghost rate. Out of the three, the cut on the number of VeLo clusters is the least critical to the performance, since the timing of the VeLo reconstruction is quite stable with detector occupancy. The effectiveness and importance of global event cuts (GEC) depends strongly on the LHC running conditions and the rate at which high occupancy events are generated.

Exotic events may produce a higher occupancy, especially coupled with a high visible interaction multiplicity, and get eliminated. As GEC are motivated by machine limitations, there's nothing we can do to by-pass those rules.

2.3.4 The Stripping Framework

To avoid running specific analysis too often on large datasets, the data stored on tape is stripped into smaller datasets, called "streams", for an easier access. The idea is that no analysis should be run on more than about 1 to 10M events.

This "stripping" process is carried out within the stripping framework regularly according to the physical needs, the amount of data stored, progress in the event reconstruction and in the detector alignment.

The stripping framework uses a similar software architecture than the HLT, with the difference that it is using all available offline tools and resources. It consists of a large set of lines, which are offline mini-analysis or

preselections. Lines reconstructing similar candidates and saving the same kind of events are grouped together and their selected events, as well as the reconstructed candidates, are written in a common stream. Each line must obey to a minimum reduction factor of $\mathcal{O}(1000)$ with respect to the HLT2 output rate.

In the early 2010 LHC runs, as the low luminosity was still permitting it, both HLT1 and HLT2 were configured in pass-through mode to provide large available datasets to be stripped for offline studies. Since summer 2010 both trigger are set to rejection mode to fulfil the allowed bandwidth. Without a dedicated line, potential signal is irremediably lost for the stripping level, and therefore for analysis.

2.3.5 The LHCb Software

The LHCb experiment softwares are developed within the GAUDI framework [83], which provides a common C++ object-oriented architecture, withstanding evolutions in both software and technology over the life of the experiment. The LHCb software chain, from generation of Monte-Carlo (MC) simulated data, via the full event reconstruction, to the physics analysis is briefly described below.

Gauss [84] steers the Monte-Carlo data simulation, used to assess the performance of the reconstruction, trigger and offline selection and analysis. This simulation is done in two phases.

The first phase is the generation of the physics events. For that purpose, Gauss is interfaced to various standalone event generators, such as PYTHIA, Herwig, Sherpa, etc.. PYTHIA [86] 6.X (Fortran 77) is the most widely used to produce the collisions, generate the resulting particles and their corresponding momentum four-vectors, and to perform the hadronisation process. The number of pp collisions can be set by the luminosity.

PYTHIA contains theory and models for a large number of physics aspects, including hard and soft interactions, parton distributions, initial- and final-state parton showers, multiple interactions, fragmentation and decay. It is capable to generate the mass spectrum and decay properties and process the generation of events for some models beyond the SM, such as mSUGRA. Mass spectrum and decay files generated by an external dedicated program can also be passed to PYTHIA to perform the simulation. A few years ago a rewriting from Fortran 77 to C++ was begun, and is available under the 8.X versions. It will gradually be pulled ahead as being fleshed out and validated.

The decay of B hadrons and other long-lived particles can be carried out by dedicated programs, like Sherpa, Photos, Tauola and EvtGen. The

EvtGen [87] package is the default. All generators are tuned for the LHCb environment.

The second phase is the tracking of the generated particles (4-momenta) through the detector and the simulation of the physical processes that those particles undergo when travelling through the experimental setup. This is achieved with the Geant4 [88] program, which can take into account the effect of the magnetic field on the charged particles (transport), the energy loss through radiation and interaction with material, as well as multiple scattering effects. Particularly, the interaction of the particles in the sensitive materials is crucial for the next step. A full description of the detector geometry and materials is stored in a database, including the mapping of the magnetic field.

Boole [89] performs the digitisation of the energy depositions, taking as input the MC hits previously generated in sensitive detectors by the Gauss simulation application. The digitisation simulates the subdetectors and the response of the readout electronics chain to those hits, taking into account the electronics efficiency and the known biases, as well as the “spillover”, that is to say the possible pollution to the electronic signal coming from the two preceding and the one following bunch crossings. The Level-0 trigger is also simulated. After this point, the MC simulated data completely mimics the real data and can be reconstructed as if it was raw data produced by the detector.

Brunel [90] proceeds from the hits collected in the detector to reconstruct the tracks and compute their momenta. It extracts the PID informations using the data from the RICHes, the calorimeters and the muon chambers. The output is stored as data summary tape (DST) files for usage in offline analysis.

DaVinci [91] is a complete physics analysis framework, hard-coded in C++. It provides the end-users with the full set of tools to perform analysis of the data, like filters and vertex filter. Reconstruction of the primary vertices is done by default.

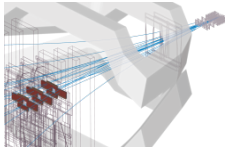
Panoramix provides a complete graphical display for the detector geometry and event data.

GaudiPython [93] provides the users with a full interface in Python to Gaudi and related programs. It takes advantage of the flexibility of the

Python scripting language to arrange the pieces of codes of interests - classes, algorithms, functions, tools, ... - according to the needs. Since it delegates time consuming tasks to the C++ functions, almost no computing time penalty arises from using this non-compiled language. It offers the possibility to have access to everything in a single script, comprising all other environment interfaced in Python, like the ROOT framework for high energy physics data analysis. Most of the work in this thesis has been carried out using GaudiPython.

Chapter 3

Assembly of the Inner Tracker



As part of the LHCb tracking system, the Inner Tracker provides information about the passage of charged particles after the magnet in the region close to the beam pipe, where there is a high flux of flying particles. The testing of the sensor modules and the assembly of the detector boxes are detailed in this chapter.

THE LATEST TRACKING STATIONS (T1-T3) are about 10m far from the interaction point and thus, considering the LHCb acceptance, covers a large area of $\sim 27\text{m}^2$. As already outlined in section 2.3.2, there exists a large variation of the particle flux between the central region, where the flux is maximal, and the peripheral region of such a tracking station, where it is very small in comparison. To deal efficiently with this gradient, two different detector technologies are used. Straw-tube drift chambers were chosen for the outer part, where the flux is smaller, and which are forming the outer tracker (OT), while silicon microstrips detectors are more able to cope with a higher flux and were elected for the design a the inner tracker (IT).

The design of the inner tracker detector has been constrained by the following requirements and considerations:

Minimisation of the material : The IT detector boxes, as well as their front-end electronics, their mechanical support and part of the cooling are located inside the experiment acceptance. The LHCb physics program requires an excellent momentum resolution of about $\delta p/p \approx 0.4\%$ for long tracks. However, the momentum resolution is dominated by multiple scattering up to 80 GeV. That's why minimisation of the material budget is the

driving consideration. The mechanical support of the IT has been designed to minimise the material while keeping the support sufficiently precise, steady and rigid. As the silicon of the sensors is an important contributor to the material budget, the thickness of the sensor has to be as small as possible. Reducing the silicon thickness worsens the signal-to-noise ratio, which needs to be larger than 12 for a good hit efficiency [98][99]. A silicon sensor thickness of $320\text{ }\mu\text{m}$ for the one-sensor modules and $410\text{ }\mu\text{m}$ for the two-sensors modules were found to be the best compromise [97].

Spatial resolution : The required momentum resolution translates into a spatial resolution of $70\text{ }\mu\text{m}$ for the IT. Considering one-strip clusters this would call for a strip pitch p of $240\text{ }\mu\text{m}$ ($\sigma_{\text{hit}} = \frac{p}{\sqrt{12}}$). To take into account a ballistic charge deficit effect for particles crossing the silicon between two strips, the pitch had been lowered to $198\text{ }\mu\text{m}$. The same charge loss effect drove the choice of the strip implantation width, w , to be $w/p \approx 0.25$.

Hit occupancy : the mean charged particle density is expected to be $1.5 \cdot 10^2\text{ cm}^{-2}$ close to the beam pipe and $2 \cdot 10^3\text{ cm}^{-2}$ in the outer regions [80]. Keeping the maximal strip occupancy below a few percent, conditions the product of the pitch and the length of the strips.

Resistance to radiation damage : A 1 MeV neutron equivalent fluence of $9 \cdot 10^{12}\text{ cm}^{-2}$ is expected in the innermost region of the IT for the ten years of operation that are foreseen. The radiation damage to the silicon causes leakage currents. What is more, the leakage currents grow with the temperature, and above some threshold a thermal runaway process occurs, leading to the destruction of the sensor. Due to the front-end electronics power dissipation, an active cooling of the IT is necessary to keep the sensor below a safe 5°C . This cooling is achieved with the help of liquid C_6F_{14} at -25°C . To avoid dew or even ice, the humidity in the detector enclosure has to be strictly controlled by a constant flow of nitrogen and good air tightness of the box envelope.

The average occupancy of the OT modules where the particle flux is the highest should not exceed 10% at the nominal luminosity. The overall IT area should be minimal, as silicon sensors are expensive, in terms of both financial and material budget. To prevent gaps in the acceptance, an overlap of 1 cm between the IT and OT areas is needed. The modularity of both detectors, defined by the dimensions of their modules, must be respected. These considerations have lead for the arrangement illustrated in Fig. 3.1. In each of the three T stations, the IT is broken down into four independent detector

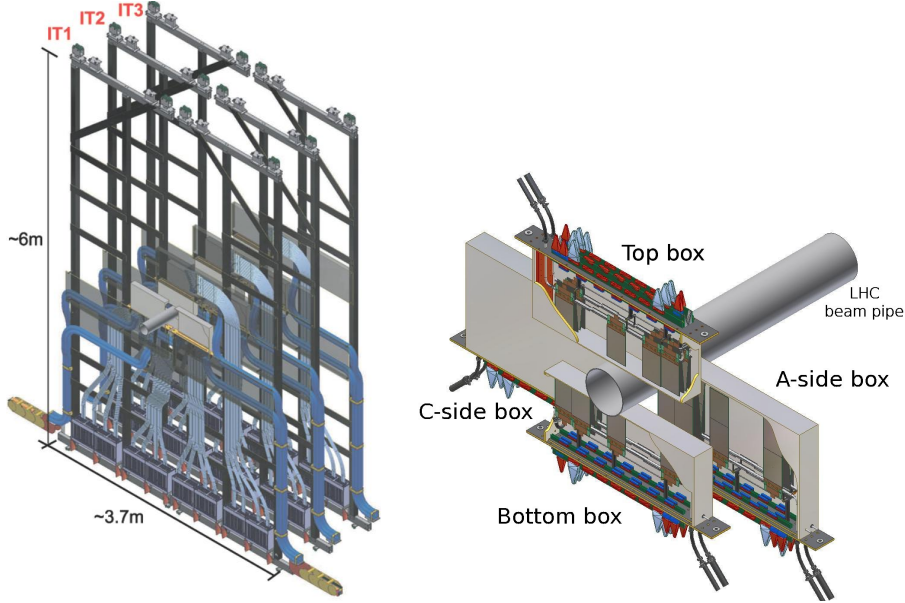


Figure 3.1: The IT detector consists of three stations IT1, IT2 and IT3 (*left*), each broken down into four independent detector boxes located around the beam pipe (*right*). The boxes above and below the beam pipe are called Top and Bottom central boxes and contain one-sensor modules, whereas the boxes on the side of the beam pipe, called Access and Cryo side boxes, contain two-sensors modules.

“boxes”, covering a roughly 120 cm wide and 40 cm high cross-shaped area around the beam pipe.

The boxes above and below the beam pipe are called respectively Top and Bottom central boxes, whereas the boxes on each side of the beam pipe are called Access and Cryo side boxes, following the LHCb naming convention. Each detector box contains four layers of seven detector “modules”, the external layers with vertical strips, the inner layers with strips oriented at $\pm 5^\circ$ with respect to the vertical ones. The active region of a module consists of either one or two $110 \text{ mm} \times 80 \text{ mm}$ silicon microstrip detectors.

The central boxes are composed of one-sensor modules, while the side boxes are composed of two-sensors modules.

This chapter addresses our contribution to the testing of the modules and the assembly of the detector boxes. It is organised as follow.

Section 3.1 will detail the preparation of the various elements entering the assembly of an IT detector box, with a special emphasise on the different tests carried on the modules : the burn-in tests in Sec. 3.1.1.a and the metrological survey in Sec. 3.1.1.b.

Section 3.2 will then describe the assembly procedure of the detector boxes. The assembly of the detector boxes was done in the hall of the PH Department Silicon Facility in building 186, at CERN, in a custom-built controlled environment. The details of the box assembly procedure are published in [96].

3.1 Preparation of the different Components

In this section, the various components entering in the assembly of an inner tracker box are described. We indicate how each of them was prepared for the final assembly, in section 3.2. For the full details, please refer to [96].

3.1.1 The Detector Modules

The design and production of the detector modules are documented in [100]. The detector modules consist of one or two silicon sensors bonded via a pitch adaptor to a front-end hybrid, which contains, in particular, a radiation hard readout chip, called “Beetle”. The support structure is made of a layer of Airex foam sandwiched between two sheets of high thermal conductivity carbon fibre; a Kapton sheet is glued on top of this structure for electrical insulation. The balcony, a small aluminium insert, is embedded into the module support at the location of the readout hybrid. It provides a direct heat path between the front-end chips and the aluminium cooling rod onto which the modules will be mounted. It is also in the balcony that are drilled the alignment holes that allow for a precise positioning of the module on the cooling rods.

The different pieces were produced and assembled in various places before being brought to CERN for the final bonding of the modules and thorough testing before their final assembly. The full module production steps and quality assurance tests are listed in [101].

To give an idea of the work : 336 modules are needed, if we request 15% spares, this amounts to 386 modules to produce and test...

3.1.1.a Burn-in Tests

An efficient detection scheme of potential defects on the bonded modules has been developed to ensure the quality of the module after the production.

Each module is subjected to temperature cycling between -5°C and $+40^{\circ}\text{C}$ and electronic burn-in for about 48-hours, during which the quality of the read-out is tested. For that purpose, the modules (up to 6 at a

time) are placed in a dedicated hermetic box, from which it is possible to control precisely the temperature and operate temperature cycles between -5°C and $+40^{\circ}\text{C}$ in about one hour and a half.

During the whole time of the temperature cycling, 500 V bias voltage is applied to the sensors. An extensive readout of the module is performed at 5 different temperatures (-5°C , 0°C , 10°C , 20°C , 40°C). The readout hybrid is powered only for the actual time of the readout while it is switched off during the cooling and warming up periods. This is necessary as the cooling power is not sufficient to cool down the box within a reasonable time while the hybrids are powered.

The various steps are:

- Current versus voltage (I-V) measurement before burn-in (up to 500 V bias voltage),
- temp-cycling (30 cycles between -5°C and $+40^{\circ}\text{C}$) with one readout from the hybrid per cycle at varying temperatures of -5°C , 0°C , 10°C , 20°C , 40°C .

One readout includes :

- pedestal and noise measurements
 - pulse-shape scan performed with an internal test-pulse signal injected to all Beetle channels at the same time.
 - test-pulse scan at the peak of the pulse-shape with one channel being simultaneously injected with pulse charge. This test aims to find open and shorted channels.
- pinhole test. The pinhole test consists of taking pedestal data without sensor bias and a 25W light bulb shining (infrared-)light onto the sensors. The induced photo current saturates the Beetle preamplifier in case of pinholes which then results in very low noise signal for the respective readout channel.
 - I-V measurement after burn-in

All I-V measurements are done at ambient room temperature and humidity which is typically about 20°C and some 40% relative humidity. If the I-V measurement has been done at slightly elevated temperatures, we note the temperature and perform afterwards a temperature correction of the recorded leakage current. The leakage current during the temperature cycling is also recorded at intervals of about 5 min. However the resolution of the CAEN high voltage (HV) supply used for biasing the modules during

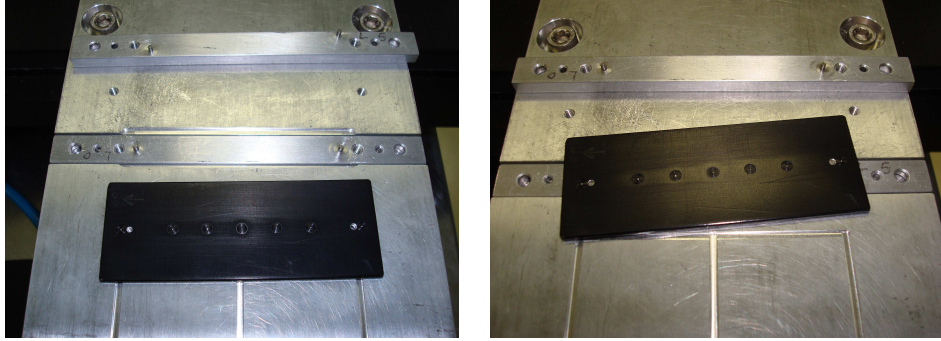


Figure 3.2: The support used for the metrology measurements of 0° modules (*left*) and 5° stereo modules (*right*). The black piece has precision holes that fit onto the positioning pins and small markers that are used to determine the position and orientation of the positioning pins on the support, defining the coordinate system for the metrology.

the temperature cycling has a minimal resolution of 100 nA only and does not seem to give very precise and reliable measurements for very low current readings. A more detailed description of these tests is given in [100].

Fraction of bad channels stayed within 0.1%.

3.1.1.b Metrological Survey

Each single module produced has undergone an individual metrological survey to know the position of the sensors on the module. This is achieved with the help of an x-y table under a microscope. According to their type, 0° or 5° stereo angle, the modules can be fixed in the very same way as they are fixed on the cooling rods, on a dedicated support on the table, support which contains positioning pins that fit the positioning holes on the module.

The survey is performed with respect to the positioning holes of each module. As they are too large to measure their position directly with the microscope, their position is first measured using an aluminium piece which fits precisely onto the positioning pins and contains 7 markers perfectly aligned with respect to the positioning holes, as shown in Fig. 3.2.

The module is then placed on the support. Each sensor is marked with eight “targets”, at each corner and in the middle of each side. The “metrology” is done in the following way. The position of the markers is measured by moving the x-y table from one reference point to the target. The z-coordinate is also recorded using the focusing of the microscope and a distance read-out attached to the z-axis of the microscope. First the reference system

is determined from the measured positioning pins. For easier comparison with the nominal sensor position when plotting, all measurements are then transformed into the nominal reference system, i.e. the one where the actual positioning pins are at nominal positions. The various steps are illustrated in Fig. 3.3.

All deviations from the nominal positions are multiplied by a factor of 100 for illustration purposes. On the left, the nominal sensors and positioning pins (straight line on top of the sensors) are displayed in black. The raw measurement is shown in green. Because the whole setup is not perfectly aligned, the positioning pins are originally not perfectly in the nominal position. The transformation that aligns the positioning pins best to their nominal position is determined by using a fit with three degrees of freedom, shifts in x, y and a rotation around the centre between the two pins. This transformation is then applied to both, the measurements of the positioning pins and the sensors. The result is shown in red. The actual misalignment is now the difference between the red plot and the black one. It is determined by fitting the red sensors to the nominal (black) positions. As a cross check, the resulting transformations are then applied and the result plotted in blue. Comparing the blue rectangles with the black ones gives a feeling for the precision of the measurements and the orthogonality of the x - y table. As the relative position of these 8 points is not changed in the fit, if the x and y axis of the table were not perfectly orthogonal, the “measured” sensor would have the shape of a parallelogram. This also tells that the measurement accuracy of the individual targets on the sensor is much better than the actual misalignments, as the differences between the fitted sensors and the nominal one is much smaller than the original misalignments.

While the precision of the survey process is very good, there are larger uncertainties associated with the results originating from the actual positioning of the module on the positioning pins. As here there is a small amount of play between the positioning pins and holes repeated measurements on one and the same module resulted in variations considerably bigger than the measurement tolerances. However, these variations are fortunately smaller than the measured misalignments. Anyway, these variations are of the same order of the ones encountered when placing the module on the cooling rod. Hence a more precise measurement would not be usable anyhow.

As a final word, one could say that the gluing of the sensors on the module has been performed with great care, as no shift larger than $\mathcal{O}(200) \mu\text{m}$ have been observed.

Metrology for Ladder 100

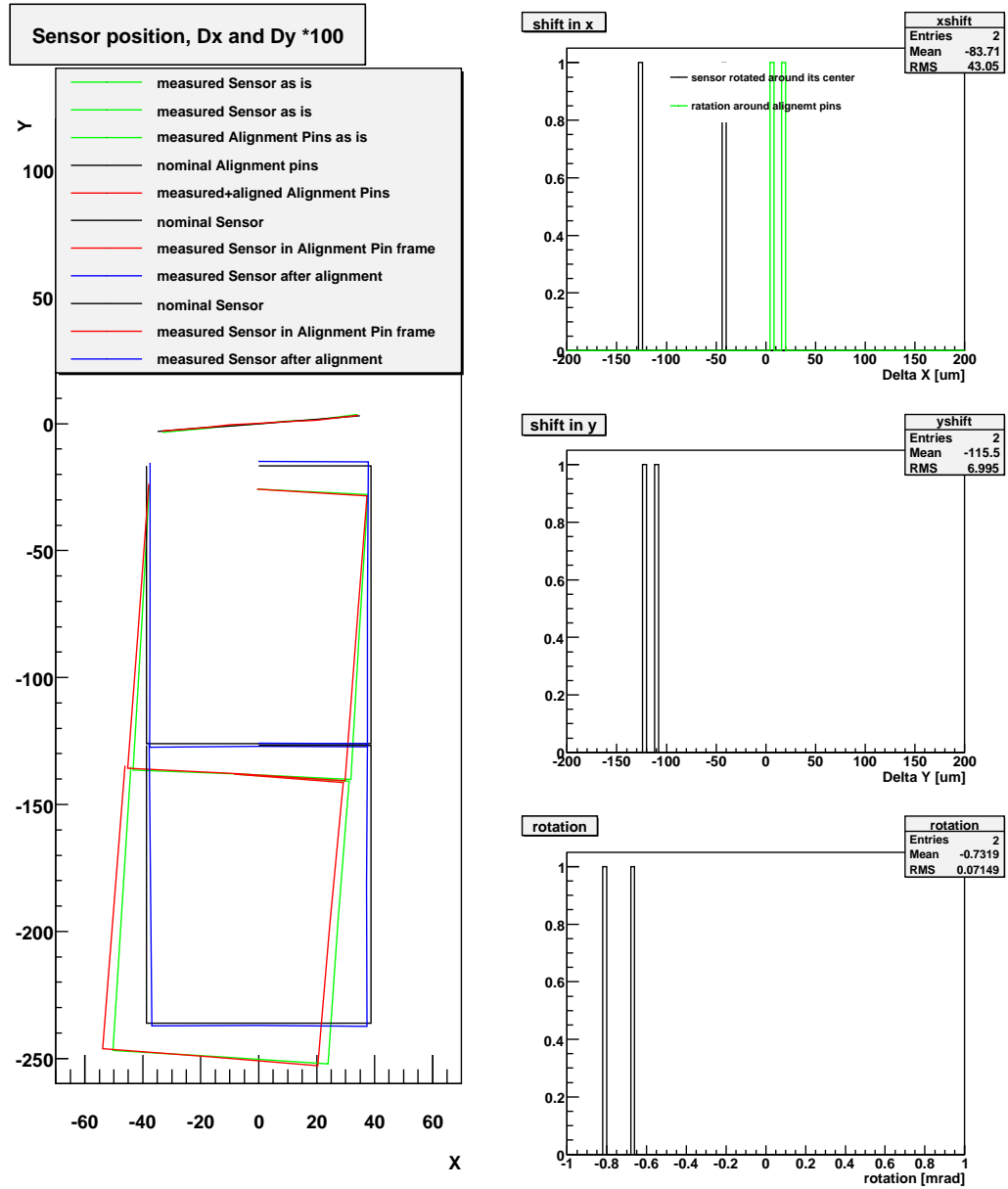


Figure 3.3: *Left*: nominal, measured and aligned sensors positions. The misalignments are amplified by a factor of 100 for illustration purposes. *Right*: misalignment values for both sensors on the module.

3.1.1.c Preparation

Inside an IT detector box, the sensor modules are partitioned in groups of four modules. The modules within a group are supplied with sensor bias voltage from a single HV channel. The main criterion used for the positioning of individual modules in a box is therefore based on the depletion voltage. Hence groups of four modules with close depletion voltage are formed.

An other criterion is the overall quality of the sensor in terms of shorted, open or pinholed channels. The sensor specifications, which we adopted also for the modules, demanded $< 1\%$ of faulty channels. On the installed modules, we have in total 111 faulty strips out of 129k. Modules with a small fraction of faults are placed where the particle density is expected to be the least.

The modules are cleaned with air to remove residual dust on the sensors. The bonds around the beetles, between the pitch adaptor and between two sensors are checked visually with a magnifying glass to ensure none of them have been broken during the storage and transport and that there is no dust nor carbon fibre filament between them.

For the external layers (X1 and X2), there is a risk that the sensors, or the bonds, would touch the inner container wall. To prevent this, a foam buffer is centrally glued with double-faced adhesive tape on top of the forward sensors (Fig. 3.4, *left*).

To have complete spatial coverage, the modules within a layer are staggered in the z direction by four millimetres. Thus, to prevent the back of one module from touching the sensor behind, foam buffers are glued at the rear of the forward modules (Fig. 3.4, *right*).

3.1.2 The Cover

The cover fulfils several roles. It provides a mechanical interface between the IT support frame (Fig. 3.1, *left*) and the detector modules inside the box (Fig. 3.1, *right*), as well as an electronics and power interface between the cables and the front-end hybrid (see Sec. 3.1.1). Being part of the whole box envelope, the cover provides a thermal insulation, as well as electric and light shielding.

Subdetectors are required by the detector safety system (DSS) [103] to use environmental sensors in critical areas to act as safeguards for the experiment, detecting serious dysfunctions. Among general status signals, smoke detection and water leak detection, important inputs for the DSS system are thermostats, which detect over-temperature situations. Thermostats were tested for operation in high magnetic field up to 0.5 T [95]. The mag-

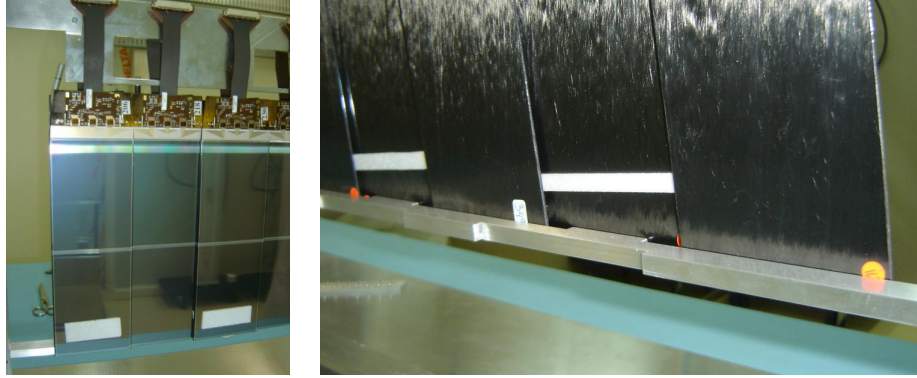


Figure 3.4: Pictures of the foam protections glued on forward sensors of the external layers to prevent them from touching the inner walls of the IT detector boxes (*left*) and at the rear of all the forward modules to protect the backward sensors from being touched by those (*right*).

netic field inside an IT detector box is expected to be 0.35 T. Within the measurement errors, no obvious deviations on either nominal and resetting switching temperatures (60° C and 45° C, respectively) with respect to their zero-field values were observed. The Thermik CO 60 has been elected mainly for practical reasons.

As the presence of these thermostiches was not foreseen in the initial design, no line was available in the interface printed circuit boards (PCBs). A small hole is therefore drilled in the sandwich structure of the cover to allow for the thermostich circuit wires to cross it and get connected to a mini patch-panel added on the cover. One thermostich is glued to the bottom side of each cover to prevent it from touching the sensors (Fig. 3.5). The hole in the cover is then filled with glue from both sides.

3.1.2.a The Cover Preparation

The cover is first mounted on its support, taking care that the latter is adapted to the kind of boxes, side or central boxes, as they do not have the same dimensions. Figures 3.6, 3.17 (*left*) and 3.18 (*right*) show the whole set-up with a mounted cover. A screw at each end keeps a small pressure on the cover to prevent it from moving. A piece of plastic is placed between the cover and the screw to prevent it from damaging the cover (Fig. 3.12). The support allows the cover to be moved up and down, a vertical screw controlling this motion.

The cover is then carefully cleaned with compressed air and alcohol to

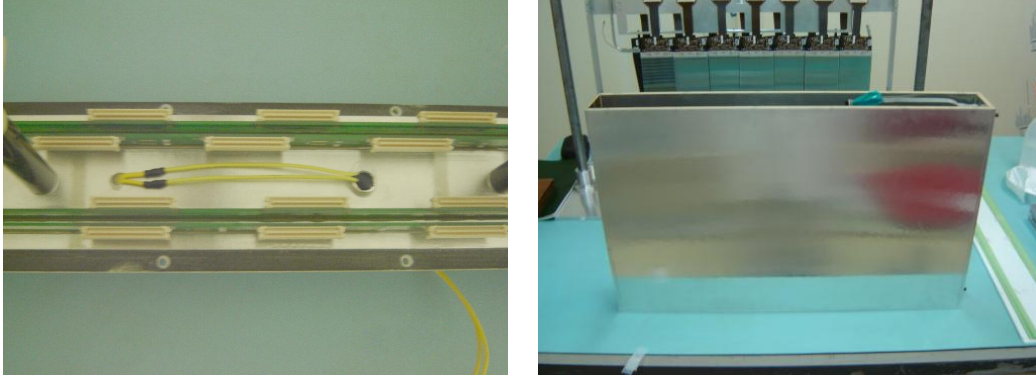


Figure 3.5: The thermoswitch is glued under the cover to prevent it from touching the sensors (*left*). An empty box container (*right*).

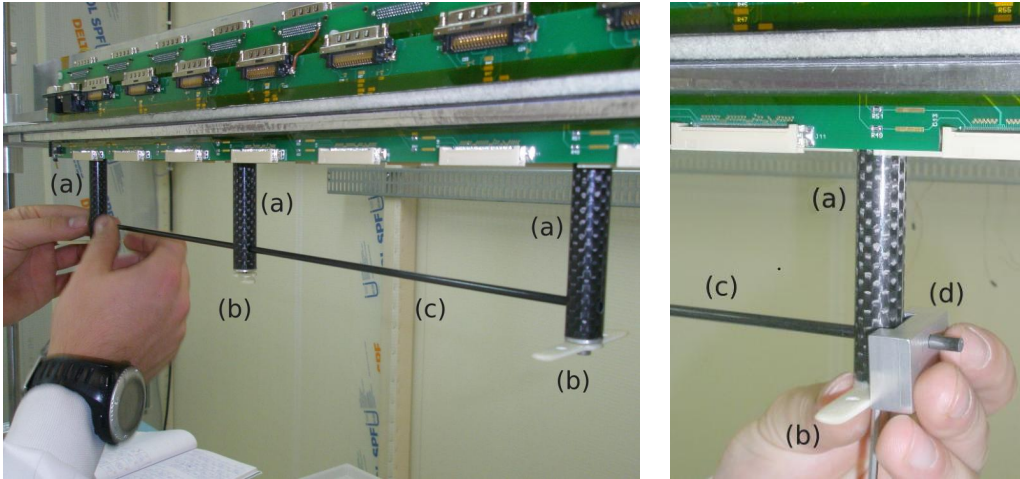


Figure 3.6: A cover mounted on its support. (a) columns, (b) fork, (c) bar, (d) special piece to control the position of the fork while it is being screwed tight.

remove the residual dust. As shown in Fig. 3.6, the columns (a) are fixed to the cover, using screws and hard-paper collars, in order not to damage the thin aluminium film that allows the cover to act as a Faraday cage.

A stesalite transverse piece (b), called a fork, is screwed to each column. The fork connects the columns to the two little columns, called “colonnettes” (Fig. 3.7), the whole having the form of a fork. The dimension of this piece is larger than the distance between the two cooling rods. The extremities of the forks are 0.5 mm away from the container wall. This is done to prevent any damage to the detector modules in case of shock to the box,

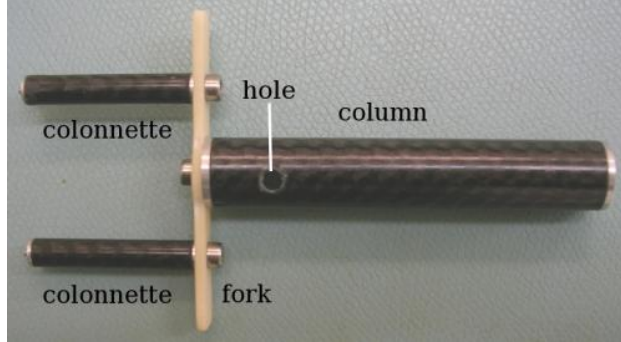


Figure 3.7: Details of the assembly of a column, a fork, and two colonnettes. The hole in the column tube through which the carbon fibre bar is inserted when the fork is aligned can be seen.

the extremities of the forks stopping the movement before the sensors could touch the container wall. Each extremity of a fork has a beveled edge to be placed downwards to avoid potential damage to the inner walls of the box when the cover is moved downwards into the box. There are holes at the bottom of each column to allow a thin carbon fibre bar (c) to be inserted through the three columns (a). This bar is used only to align the three forks while they are screwed in place. For this a special piece (d) is used to get the forks perpendicular to the carbon fibre bar. The thin bar (c) is then removed.

3.1.3 The Box Container

The box container is made of a sandwich of glass fibre and PIR-foam covered with aluminium shielding on the inside and outside. The foam part of the walls is 8 mm thick, except for the walls close to the beam-pipe, which are 3 mm thick to allow the sensitive parts of the detector to lie closer to the beam-pipe. The box enclosure will be continuously flushed with N_2 to prevent condensation inside the box. The humidity has to be such that the dew point remains above the temperature of the coldest element in the box (which is at the coolant temperature). The incoming N_2 flow is spread within the box volume using a perforated channel made out of glass fibre.

Before using the box container in the assembly, several tasks are performed :

Depth measurement The depth of the container is measured with a depth gauge. The depth is measured from the lip of the container to its inside bottom, at six places along the container length. The measurement locations are defined by the position of the screw holes on the container lip. Conservatively, the minimal depth is considered when assessing whether the

detector modules will fit the container, as for central boxes, they are really close ($\sim 0.5\text{ mm}$) to the bottom of the box container. For side boxes, this distance is not as small, but the container depth is measured anyway.

Temperature probes Four PT1000 temperature probes are placed inside the box container in addition to the probe installed on each readout-hybrid. These measure the temperature of the box environment. Three of them are located at the bottom of the box and one on the side wall facing the beam-pipe (side boxes) or the opposite of the N_2 inlet (central boxes).

Inner shield grounding The inner and outer shielding of the container are connected to the ground by a wire glued onto the aluminium shielding. To glue the wire on the shielding using conductive glue, the insulation of the wire is removed on approximately 2 cm. After two days of drying, a protective layer of Araldite is applied on top. The grounding of the inner shielding is soldered to the ground of the temperature probes, which is connected to the ground of the cover during the assembly process. The grounding of the outer shield (Fig. 3.8, *right*) connects to the ground line on one of the PCBs via a small connector.

Verticality control As the containers are standing on the base plate during the sensor modules insertion procedure, their verticality is important. Therefore, it is carefully checked and, if needed, corrections are brought by applying $100\text{ }\mu\text{m}$ thick layers of Kapton tape on the appropriate side of the container bottom.

RMS support The radiation monitoring system (RMS) detector [104] is supported by the IT container boxes for three (Top, Access, Cryo) out of the four detectors of station T2. Therefore, stesalite pieces to fix the RMS detector are glued onto the wall of appropriate containers. To maximise the adherence of the glue, the aluminium shielding is locally removed, the glass fibre surface is scratched and three small holes are cut into the glass fibre surface. A dedicated jig is used to constrain the relative position of the RMS support pieces with one another during the glue drying process.

Beam pipe Approach Monitoring System (BEAMS)

The BEAMS is a safety device that raises an alarm in case a detector box is too close to the beam pipe in order to avoid possible damage. The nominal distance of the detector boxes to the beam pipe is 7 mm, and anything closer to 5 mm is supposed to trigger the alarm. It consists of two gold plated

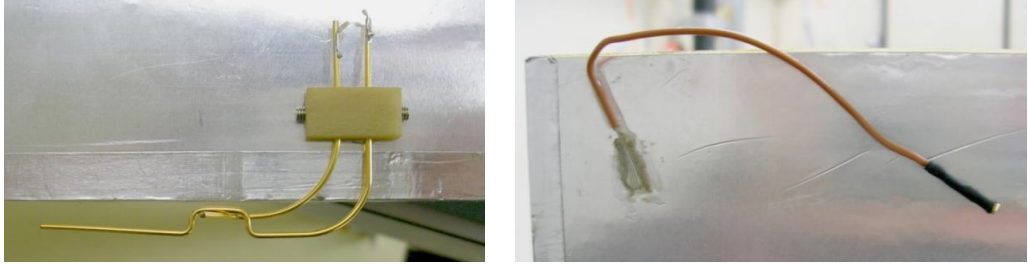


Figure 3.8: A BEAMS device (*left*) and the ground wire of the box external shield (*right*). This particular BEAMS device is located on the long edge of a central box, in such a position that it will lie just above or below the beam pipe, once the IT station closed. This picture allows to understand how the BEAMS electric circuit opens if something pushes the lower finger up.

metallic fingers which are in contact with each other in their nominal position (Fig. 3.8, *left*). The touching fingers are part of an electric circuit which is closed in nominal position. If the outermost finger touches the beam pipe, the fingers would separate from each other and consequently open the circuit. There are six BEAMS devices per station, distributed as follows: two of them on each central detector box, and one on each side box. On the central boxes, one BEAMS device is located in front of the edge of the container which passes close to the beam pipe during the closure procedure of each half-station, like a bumper. This device is only useful during the closure of the half station, preventing a collision of the top or bottom boxes with the beam pipe. The other BEAMS device is located on the wall that is close to the beam pipe, so that it faces the beam pipe when the station is completely closed (the device in Fig. 3.8 is of that type). On the side boxes, there is just one BEAMS sensor such that the sensitive finger is at the level of the beam pipe 5 mm away from it. The BEAMS system is fixed on the box containers. The stesalite pieces that support the fingers (Fig. 3.8, *left*) are glued to the container wall using a similar procedure as the RMS support. Their location is given by a dedicated jig.

3.1.4 The Cooling Rods

The cooling rods provide mechanical support, cooling, and grounding to the sensor modules. They consist of an aluminium part with a complex crenelated design which is glued to a pure aluminium tube (external diameter 6 mm, wall thickness 0.3 mm) in which flows the coolant liquid (Fig. 3.9 and 3.10). Pure aluminium is highly ductile. Aluminium was chosen as it has a

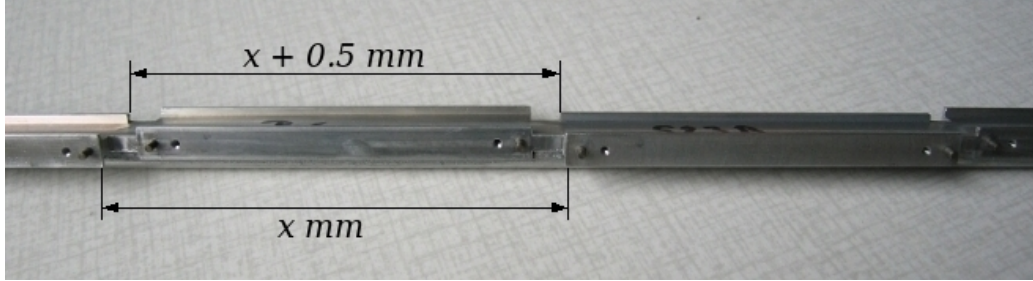


Figure 3.9: The length of the interval between two crenels is about 0.5 mm longer on the U and V layers than on the X1 and X2 layers.

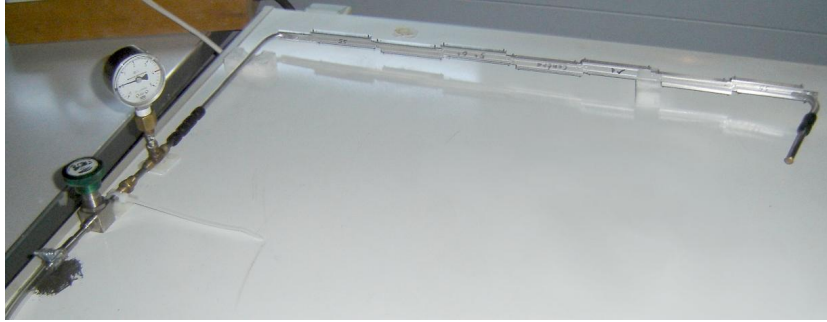


Figure 3.10: A cooling rod under pressure test.

relatively low radiation length ($X_0 = 24.3 \text{ g cm}^{-2}$) and can easily be bent into the desired shape without inducing cracks in the thin walls of the tube. Due to their extreme fragility, the cooling rods have to be manipulated with great care.

To measure the path of a particle in 3 dimensions the IT is made of four sensitive layers in a typical stereo layout. The two external layers, called X1 and X2, are made of sensors with microstrips aligned vertically, whereas the two internal layers, called U and V, have strips which form a 5° angle with the vertical axis. A cooling rod supports two layers of 7 modules. There are therefore two different types of cooling rod: the type A supporting V-X2 layers and the type B supporting X1-U layers.

The crenellated structure (Fig. 3.9) induces a slight staggering between a module and its neighbours and consequently ensures an overlap of the sensitive area. Thus, there is no dead space between two sensors, preventing the existence of gap in the sensitive surface. The gap between two crenels is measured to check the type, A or B, of the cooling rod, as the length of

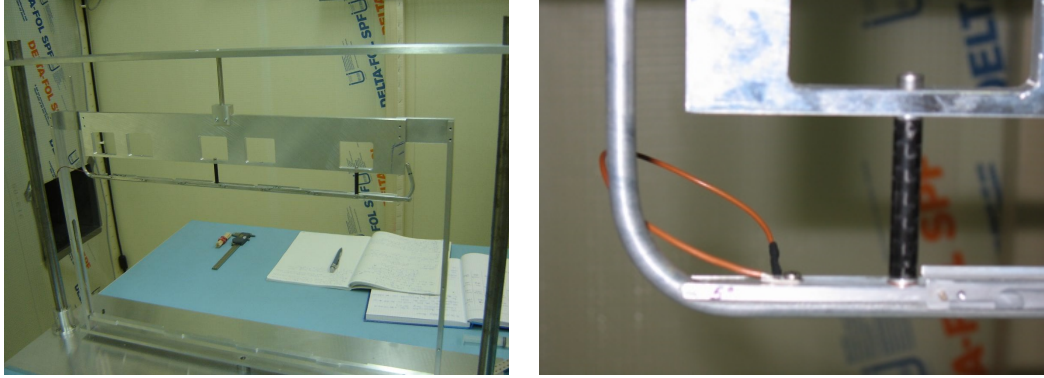


Figure 3.11: View of a cooling rod mounted on its support (*left*) with the help of the three colonnettes of screwed on it (*right*). The thread for the grounding is also visible (*right*).

the interval between two crenels is about 0.5 mm larger for the U or V layers than for the X1 or X2 layers, as explicited in Fig. 3.9. Thus, orientating the cooling rod so that the long tube (the part that exit the cover) is on the left-hand side in front of us, a B type (X1-U) cooling rod will have the longer interval on the side close to us.

Within the support structure of the sensor modules, there is an aluminium piece called the “balcony”. This piece provides stiffness and acts as a thermal bridge. The precision holes that govern the positioning of the module are machined in the balcony. The back of the front-end chips are glued on the balcony with conductive glue and the balcony is in direct contact with the cooling rod. The precise positioning of the sensor modules is achieved by the use of pins fixed to the cooling rod, which are inserted in the holes of the balcony. While mounting the first modules, it was noticed that the distribution of the angle of the module with respect to the vertical direction was very broad. Consequently, most of the modules are neither vertical, nor parallel with each other. The cause was traced back to the alignment pins of the cooling rod. Although they were machine-inserted into the cooling rod, their orientation was found to be inaccurate. Therefore, each pin has to be straightened using a small lever.

The cooling rods are individually tested for leaks. The procedure consists in blocking one end of the cooling tube and connecting the other end to a manometer. The cooling rod is filled with Argon up to about 4.8 bars and the circuit is closed (Fig. 3.10). After two days, the pressure is checked again. If any significant variation of pressure (more than a few tenths of bars) is noted the test is redone. A cooling rod would be rejected if the second test

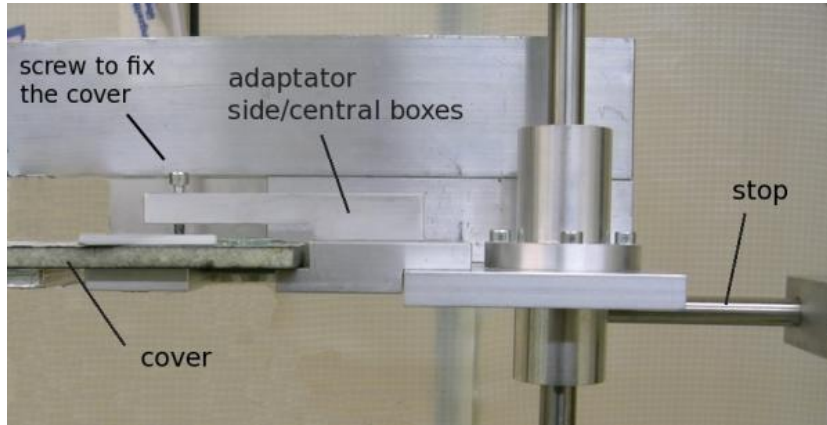


Figure 3.12: The cover is just laid on the set-up, while a screw keeps a small pressure on the cover. A piece of plastic is inserted between the cover and the screw to prevent it from damaging the cover. On the right, a stop is visible.

failed, too; this fortunately did not happen. Finally, a ground wire is screwed on each cooling rod (Fig. 3.11, *right*). The three colonnettes are also screwed and glued to the cooling rod (Fig. 3.11, *left*).

3.1.5 The Assembly Set-ups

Two set-ups are used in the assembly process. The first set-up is called the cooling rod station (Fig. 3.11, *left*). Its function is to hold a cooling rod during the mounting of the modules. The second set-up, called sliding set-up, allows to hold the cover while the cooling rods are mounted on the cover and to control the sliding of the modules into the box container (Fig. 3.18, *right*).

The cooling rod station consists of an aluminium frame on which a cooling rod can be fixed with three screws the same way it would be with an actual cover. The whole frame can be rotated along a vertical axis, so that the operator can access both sides of the cooling rod without moving the set-up base plate. An aluminium bar with specially designed crenellated shapes on both sides can be inserted in the frame. The bar acts as a stop, preventing the back of outer modules from touching the sensors or the bonds of the inner modules during the mounting of the modules (Fig. 3.4, *right*). Two different bars are used, one for the X1-U cooling rods, and one for the V-X2 cooling rods.

The sliding set-up consists of two vertical round bars held at the bottom

by a heavy stable base-plate and at the top by a bar. Two trolleys, one on each vertical bar on which they can slide, are linked together by an horizontal bar, whose vertical position can be controlled by a long vertical screw. The sliding trolleys have to be adapted to either central or side boxes, since the overall length of the cover is different according to the type of the box, as shown in Fig. 3.12. Thus, the correct adaptor piece has to be screwed in place. The horizontal bar linking the trolleys is bulky and limits the working space. Thus, the set-up is oriented so that the main operator of the assembly works with this bar away from him.

Before each use, the surfaces of the set-ups are cleaned with an alcohol soaked tissue. The cleaning of the upper bar of the sliding set-up is important, because dust could fall from there directly on the modules. Particularly, attention is paid to the brass piece holding the vertical screw. At this location, tiny metal chips from the screw are produced when the screw is used. A careful cleaning is needed there to prevent any of those metal chips to fall on sensor bonds or into open connectors.

3.2 Assembly Procedure of an Inner Tracker Detector Box

Once the various elements of the detector boxes are all prepared and the plan of the different modules to be used is defined, the assembly process can begin.

This procedure can be broken down into the following sequence:

- Mounting of the cover on the sliding set-up;
- Adjustment of the detector box container position;
- Mounting of two layers of modules on each side of the first cooling rod;
- Mounting of the cooling rod on the support below the cover;
- Mounting of two layers of modules on each side of the second cooling rod, and mounting of this cooling rod on the support;
- HV test of the modules;
- Closing of the cooling circuit by connecting the two cooling rods;
- Cooling circuit leak test;
- Survey of the visible layers X1 and X2;

- Full electrical tests;
- Test of the height of the modules;
- Final insertion of the detector into container.

Those assembly steps are detailed in the following sections.

3.2.1 Mounting of the Cover on the Sliding set-up

We took the convention to orientate the cover on the sliding set-up so that the cooling pipe exit holes lie on left hand when one faces the set-up, as illustrated in Fig. 3.17, *left*. The cover is maintained by a small pressure from a screw on each side. A piece of plastic is placed between the screw and the cover to protect the aluminium shield integrity, as can be seen in Fig. 3.12.

With this convention, the type B (V-X2) cooling rod is behind the type A (X1-U) and thus has to be mounted first.

3.2.2 Adjustment of the Detector Box Position

On the base plate of the sliding set-up, stops can be adjusted in order to maintain the box container at a precise location when the modules are slid down into the box container. The precise location of those stops have to be set before the assembly process of the detector box. The empty box container is placed on the base plate so that the cover, slid down, fit into it. When the box container is at the correct location, the stops are adjusted and screwed in place. The stop on the back of the box container and the stops on each side of the container are used. The stops on the front side of the box container would be in the way when manipulating the container, consequently they are removed and never used. For the side boxes, the position of the right-hand stop is set in order to have about 1 cm between the stop and the box wall. This precaution is needed because the distance between the edge of the module and the box inner wall is only 0.5 mm on this side. Thus, during the module insertion, this distance is increased for safety reasons. Once the stops are adjusted, the cover is moved up and the box is removed.

3.2.3 Mounting the first Cooling Rod (type B or V-X2)

The first cooling rod to be populated with sensors is a cooling rod of type B (supporting the V-X2 detection layers), following the convention explained

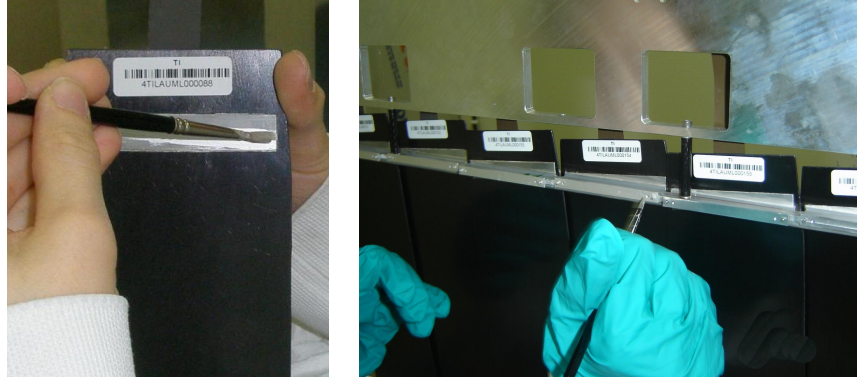


Figure 3.13: *Left* : the operator is applying thermal grease on the module balcony in preparation of the mounting of the module. A sticker is glued at the rear of the detector modules allowing their identification. *Right* : the thermal and electric conductive grease is spread on the cooling rod where the modules are intended to be fixed.

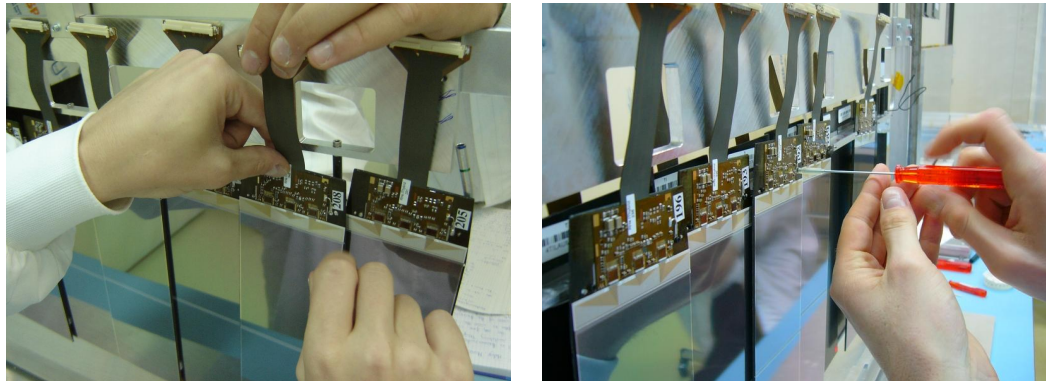


Figure 3.14: View of the fixing of the modules on the cooling rod, by starting with the backward modules and finishing with the forward modules.

in section 3.2.1.

The cooling rod is prepared as detailed in section 3.1.4. A latest cleaning with alcohol is performed, specially for the surface that will be in contact with the modules. The cooling rod is fixed to the cooling rod station set-up (Fig. 3.11, *left*).

To maximise the thermal transfer between the cooling rod and the back of the detector modules, a layer of thermally and electrically conductive grease is spread on the contact surfaces. Thinner is used to control the viscosity of the grease, which have to be such that it could be spread effortless with

a paintbrush. It is important not to use any force to spread it, due to the fragility of the modules. The grease is spread on the contact surfaces on each side of the cooling rod (Fig. 3.13, *right*), as well as at the rear of each module on a line linking the two alignment holes (Fig. 3.13). The modules are placed starting with the ones located behind and then with the ones located affront (Fig. 3.14). They are fixed with one electrically conductive¹ screw at each side of the alignment pins (Fig. 3.14, *right*). This has to be done with great care, in order not to damage the aluminium screw threads. The bonds of each module are inspected with the help of a magnifying glass before and after the mounting procedure. Several damaged HV bonds were observed². Usually, these could be pulled and replaced by new ones, as the HV bonds pads are quite large.

3.2.4 Fixation of the first Cooling Rod under the Cover

The cooling rod, populated with modules, is handled carefully by a first person, who held it at both ends. This person has to control the pressure applied on the aluminium tube, since he could crush it quite easily. A second person helps the cooling pipe to enter the cover properly and screws the colonnettes of the rod to the fork.

3.2.5 Mounting of the second Cooling Rod

The procedure described in sections 3.2.3 and 3.2.4 is repeated for the type A cooling rod. At the end of the step, the two cooling rods are fixed on their support.

Once the two cooling rods are screwed in place, the detector modules could be connected to the inside connectors on the cover. The ground thread of each cooling rod is also connected to the cover, and the thread is secured to the vertical cooling pipe with a little band of Kapton tape. Bubble wrap is used to prevent the Kapton tails from touching one another, which is potentially a source of noise.

At this stage, we did not complete the cooling circuit. Closing/disconnecting the cooling circuit are delicate, accident-prone operations. Thus, to minimise the number of those operations, a high voltage test is performed, as described below, to detect and replace the possible faulty modules before to close the cooling circuit.

¹Since the screws are important in the grounding scheme they have to be electrically conductive rather than passivated.

²The HV bonds are the outermost bonds and as such are more likely to be damaged during module manipulations.

3.2.6 High Voltage Test of the Modules

After the assembly of the cooling rods and their mounting on the cover plate (just before connecting the cooling rods together), a high voltage test of the modules is performed. HV-problems are the most frequent disturbances during the module production and the HV-bond wires are the bonds closest to the edges of the modules and hence more prone to accidental damages. Therefore, one checks for HV-problems before the cooling rods are connected to each other, in case a module would have to be exchanged. For the HV-test, no cooling is necessary.

The test is done by inserting the assembly into a large aluminium test box, which provides light shielding for the modules. This box allows for easy placement of the assembly without the insertion set-up needed for the real detector boxes where the box walls are much closer to the modules. Furthermore, this box has windows that can be opened to access to the readout hybrids which is helpful to trace possible problems. The HV-connectors are then connected to the HV-modules as described in the full module test (section 3.2.10). The modules are slowly ($\simeq 3$ min) ramped to 500 V and the test is passed if none of the modules shows signs of a breakdown. Typical leakage currents of the sensors are 200 nA and 400 nA for short and long modules, respectively. The leakage currents rarely exceeds 1.5 A.

3.2.7 Closing of the cooling Circuit by connecting the two cooling Rods

Once the modules are HV tested and the faulty modules exchanged, the cooling circuit can be completed. The missing piece of the circuit is a steel tube bended in a U-shape. The use of steel is motivated by the observation that it is not possible to bend an aluminium tube to such a small radius without crushing it. For the same reason it is not possible to use plastic tube either.

It is difficult to insert the U-shaped tube into the Legris connectors, mainly because the ends of the cooling rods are usually not parallel to each other. A considerable strength is required but the cooling rods are fragile. To ease the process, the best way is to measure the distance between the connectors and to adjust the bend of the U-shaped tube accordingly. Using two screwdrivers, inserted into each end of the tube, and grasping them as pliers, the shape of the tube could be adjusted.

It is not straightforward to take notice whether the U-shaped tube is inserted home in the Legris connectors or not. Thus, inserting a Legris connector in each end of the tube, a line is drawn on the steel tube with a

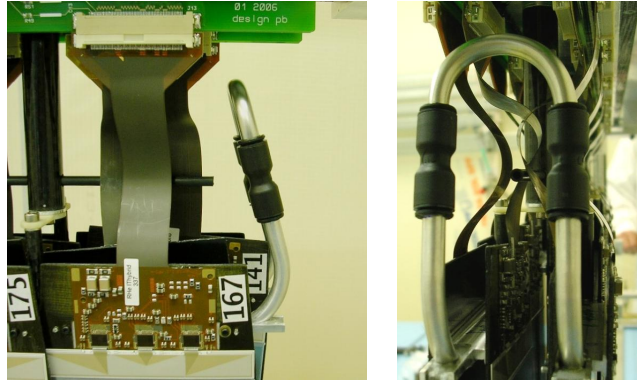


Figure 3.15: The cooling circuit is closed when both cooling rods are connected via the steel U-shaped tube.

permanent marker.

Even with the U-shaped tube adjusted, the closing of the cooling circuit is still the most delicate step of the box assembly. Two people have to slowly insert both ends of the tube simultaneously, and to push it until it reaches the marker line on the tube, meaning it is home. During the operation, both cooling rod ends have to be held tightly to minimise the strain applied on them. Figure 3.15 shows the steel U-shaped piece in its final position.

Once the cooling circuit closed, the distance between the cooling rods is measured. If the measured distance is found smaller than the nominal one, a spacer is inserted at the right length in a carbon fibre rod. This spacer is secured in place with Kapton tape.

3.2.8 Cooling Circuit Leak Test

An electronic device is designed to read out a pressure probe and to display the measured pressure. The test set-up consists of a bottle of argon (Ar), the pressure probe, a valve on one side, and a brass plug on the other side. The tests consists in putting the cooling circuit under pressure for some time and to record any pressure drop. The Ar bottle, pressure probe and valve are connected to one end of the cooling circuit with a Legris connector and the air it contained is flushed away with some Ar. Then, the other end of the circuit is blocked out with the brass plug via a Legris connector. This is secured with Kapton tape, preventing it from flying around in case the Legris connector is faulty. The circuit is pressured up to about 5 bars, the valve is closed, isolating the cooling circuit, and the Ar bottle is disconnected. To compute a leak rate, one took down the current pressure in the circuit, the temperature

and pressure of the room, and the time. After about two days, the same physical quantities are measured again. These data allows to compute the leak rate of C_6F_{14} in cubic centimetres per year. This computation and the conversion from Ar leak rate to C_6F_{14} leak rate is based on the method used for the ATLAS TRT and documented in [105].

If the leak rate is found to be higher than tolerated, which happened a few times, two actions are taken: the connectors of the pressure set-up are tightened, the set-up itself is retested and the four Legris connectors composing the cooling circuit are exchanged with new ones. Eventually, all the twelve detectors boxes are found to be fine. Once the cooling circuit is validated as leak free, it is possible to circulate coolant. It is then safe to power up the beetles and a full electric test is possible.

3.2.9 Survey of the visible Layers X1 and X2

The goal of the survey is to provide first estimates of the position of the sensors. No hardware correction can be performed to correct imperfect positioning, the alignment will be done by software using tracks. However, the more accurately the position of the modules is known the best is the result of the software alignment. Cross-shape fiducial marks engraved on each silicon sensor are surveyed by theodolite. Their coordinates are calculated with respect to targets located on the cover of the detector box, which are still visible once the box is closed and installed in the LHCb cavern. The details of the survey procedure can be found in another LHCb note [106].

3.2.10 Full electrical Tests

A full readout test of a cooling rod assembly with 28 modules is carried out before the assembly is placed in the final detector box container. This is done in the large aluminium box used for the HV-test (section 3.2.6) which provides an easy access to the hybrids. The readout test is described in details in [96].

3.2.11 Test of the Height of the Modules

The goal of this operation is to check whether the sensor modules fit in the box container, such that they do not touch the bottom of the container. For this, we measure the distance between the lower edge of the modules and the lip of the cover and compare this value with the depth measurement of the container to be used, as explained in section 3.1.3. For the central boxes, the nominal space between the bottom edge of the modules and the bottom

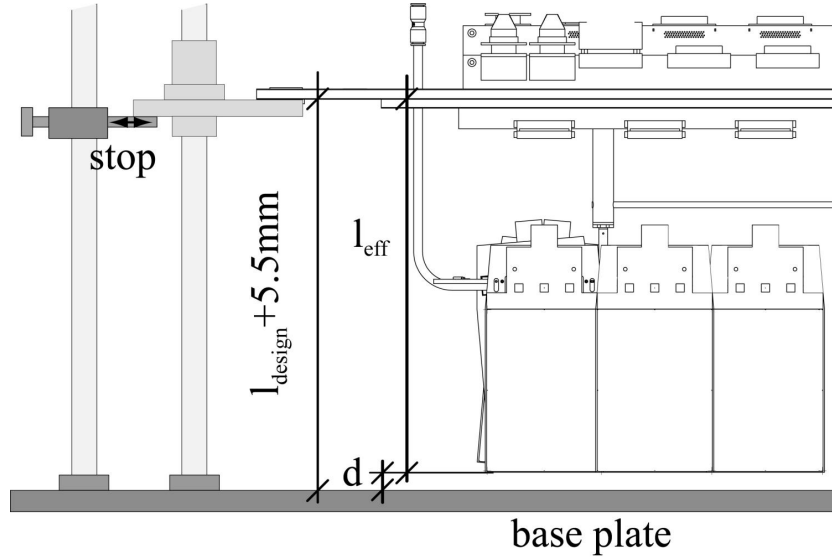


Figure 3.16: Scheme of the different distances involved in the measurement of the distance between the cover and the tip of the sensor modules.

of the box container is 0.5 mm. The motivation for such a tiny distance is to have the sensitive area as close to the beam pipe as possible. For side boxes, the space underneath the tip of the modules is not critical in term of acceptance and hence the space is much larger (≈ 5 mm). The minimal distance is found between the lateral edge of some modules and the container side wall facing the beam pipe which is only 0.5 mm, for the same acceptance reason.

It is not straightforward to measure the distance from the bottom of the lip of the cover to the bottom tip of the module support, l_{eff} , as defined in Fig. 3.16. The solution consists in the permanent installation, on the sliding set-up, of two pairs of stops, one pair for the central boxes and one for the side boxes. Those stops can be engaged or disengaged. When a pair of stops is engaged, the sliding bar of the set-up can rest on it, as shown in Fig. 3.12, and the cover-module ensemble is maintained. The stops are positioned so that, when the sliding bar rests on the stops, the distance between the tip of the module supports and the base plate is 5.5 mm, nominally. This means that the bottom lip of the cover lies at $l_{\text{design}} + 5.5$ mm from the base plate. The positioning of the four stops is performed using an electrical height gauge to control the distance to the base plate. Thus, by measuring this distance, we measure the deviation of the actual assembly from the nominal design. This distance d is measured using calibrated wedges and precision blades

(Fig. 3.17, *right*). The simple arithmetic of equation 3.1 allows to get the effective distance l_{eff} .

$$l_{\text{eff}} = l_{\text{design}} + 5.5 \text{ mm} - d \quad (3.1)$$

Conservatively, we consider the minimal depth measurement of the box container from which the maximal l_{eff} value is subtracted to assess whether the modules fit into the box container.

If it is not the case, an appropriate number of 0.2 mm thick glass fibre frames are added between the cover and the top of the box container. To raise its upper lid is equivalent to increase the depth of the container. The eventual glass fibre frames are fixed using Kapton tape. A strip is centred on the frame and secured on the inside and outside wall of the container on each four sides of the container lid. The result of this operation is a flat lid, without any ripple, enhancing the air-tightness of the detector box. The Kapton covering the screw holes is removed with a lancet blade.

3.2.12 Final Insertion of the Detector into the Container

The verticality of the box container and the height of the module have been checked before. The box container is placed under the cover according to the stops set on the base plate as mentioned in section 3.2.2. The detector box is then ready to be closed (Fig. 3.18, *right*). The ensemble composed of the cover and the detector modules is slowly moved down into the container, actioning the vertical screw on top of the set-up. One person actions the vertical screw while another person supervises the process. Critical moments are when the bottom of the modules, then the inter-sensor bonds (for side boxes), and then the sensor-hybrid bonds enter the container. The descent is not perfectly smooth and the modules could slightly shake. This is mainly due to the screw and is negligible at low descent speed. At each of these moments, the second person checks that the container is properly placed and that there is no danger of collision.

For the side boxes, one of the lateral wall of the container is only at 0.5 mm from the edge of the modules. Thus, for the delicate insertion operation, the container is shifted laterally so that this distance is increased to a safe value of 1–2 cm.

A few centimetres before the completion of the insertion process, the temperature probes and the inner shield ground thread (figure 3.5, *right*) have to be connected to one PCB. The bundle of wire is secured to one of

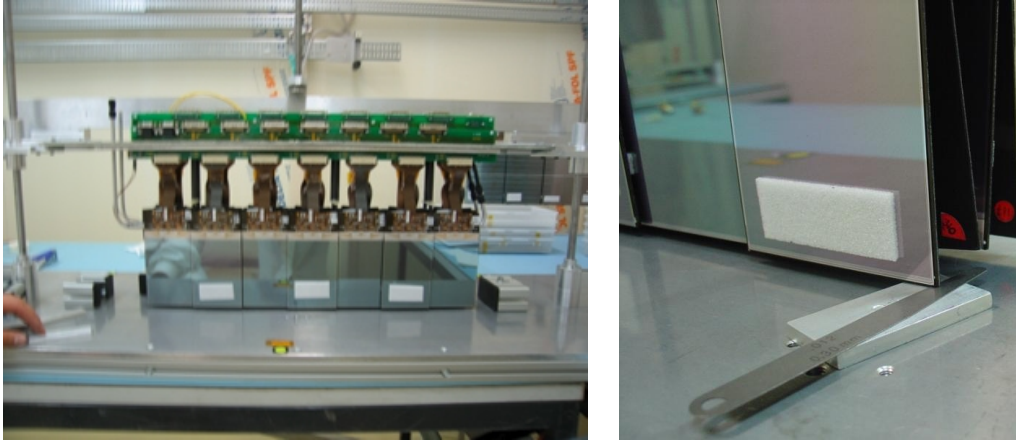


Figure 3.17: Resting on the dedicated stops, an assembly is ready for the test of the height of the sensor modules (*left*). On the right, one measures the distance, d , between the base plate and the bottom of the module supports, as shown on the drawing of Fig. 3.16, using a calibrated wedge and precision blades.

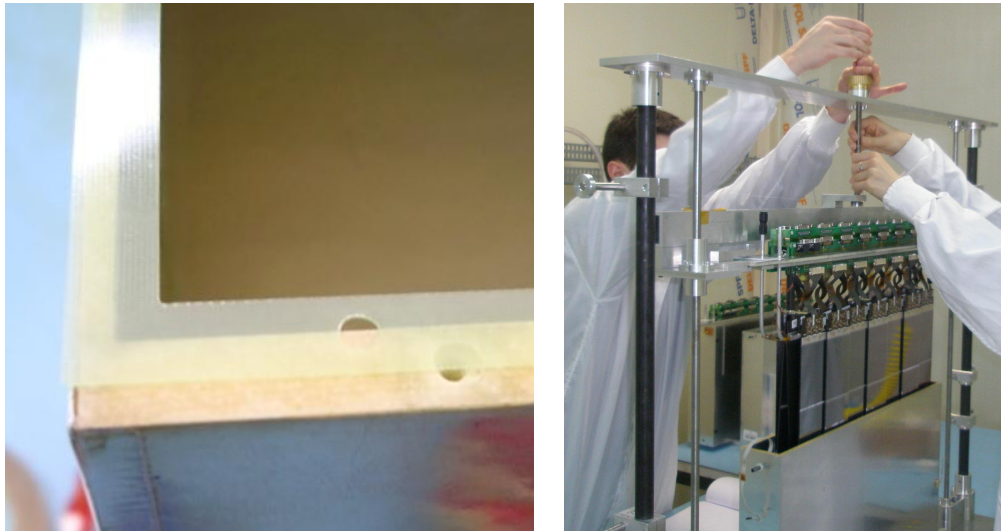


Figure 3.18: A glass frame used to adapt the depth of the container (*left*). The sliding set-up and a box being closed (*right*).

the cooling pipe to prevent any constraint on the connector, which could lead to a disconnection.

A part of the cover has to enter in the container. So, just before the inside of the cover reaches the lip of the container, one could readjust its position to allow a smooth entry of the cover in the container. With certain covers, this is not straightforward and one has to help by slightly opening further the container mouth. Particularly, for the side boxes, it is also time to shift the container back at its nominal position. This operation should be performed very carefully, because of the tiny distance from the wall to the modules.

Once the box is closed, and before the screws are inserted in their holes, a large band of Kapton tape is glued on the cover so that it covers the screw holes and so that a larger part is in the air, not glued to anything. Then, the screw holes are pierced in the Kapton and the cover is screwed to the container with 12 plastic screws. When the screws are tightly screwed, the free part of the Kapton tape is glued to the container wall. In the process, the Kapton band also covers the foam section of the cover. The motivation for the Kapton seal is to maximise the air tightness of the detector boxes. The air tightness is crucial to minimise the transfer of humidity to the inside of the box.

3.3 Performance of the Inner Tracker

The assembly of the twelve IT detector boxes took about one year and a half to be completed. The assembly process is an incredible amount of tiny details. The negligence of one of them could drive disastrous effects. Because of this fact, the process was continuously stopped for checking and thinking, for every true or supposedly default, requiring infinite patience. Due to the extreme fragility of the system, any hurry could be fatal. And disassembling some part of a box might generate even more risks.

The installation of the last box in the LHCb cavern was achieved and put into operation in early summer 2008, before the start of the commissioning phase.

At the beginning of June and October 2009, the LHC carried out several synchronisation tests [109]. Data were recorded where a beam of 450 GeV protons extracted from the super proton synchrotron (SPS) was dumped on to a beam stopper located 350 m downstream of LHCb. The subsequent spray of particles gave a clear signal in the detector that allowed time and spatial alignment to be made. The resulting occupancy in the detector was about twenty times the expected one during running at the nominal luminosity. This allowed each channel to have the chance to detect some particle.

The active fraction of the detector is 99.72% , while the overall efficiency of the IT detector is measured to be 97.6% [110].

Presently, the inner tracker is perfectly aligned and fully operational. In the 2010-2011 LHC runs at 7 TeV, it is showing the great stability and efficiency that were expected from a LHC subdetector.



Chapter 4

Generation and Simulation of the Data Samples



This chapter details the adaptations to the LHCb software chain that were necessary to properly simulate the data samples presented in Chap. 1. It also presents the new event type numbers and various options files created for the simulation of the selected models.

THE NECESSARY ADAPTATIONS concentrate on the Gauss software [84] of the LHCb simulation software chain, presented in Sec. 2.3.5.

Quite some development has been necessary to achieve an appropriate and correct simulation of the desired topologies. The description of this lengthy process can be useful to the others wishing to add new exotic particles to the simulation packages, to avoid being trapped in the same problems we encountered, and be able to benefit from the tools that have been designed.

4.1 The Interface to Pythia : PythiaProduction

The PYTHIA [86] generator has a complete internal machinery to compute the mass spectrum and decay properties and to process the generation of events for the Higgs sector and some models beyond the Standard Model, such as mSUGRA. In particular, mass spectrum and decay files generated

by an external dedicated program can also be passed to PYTHIA to perform the simulation. For these reasons, PYTHIA has been chosen to generate the events.

For that purpose, the Gauss interface to PYTHIA PythiaProduction¹ had been updated to accept external SLHA² mass spectrum and/or decay files and deal with the various supersymmetric switches and parameters PYTHIA possesses.

Below is an example how to set the parameters for the generation of 48 GeV massive $\tilde{\chi}_1^0$ (BV48) :

```

Generation.SampleGenerationTool = "Special";
Generation.Special.ProductionTool = "PythiaProduction";
//Provide a SLHA decay file for the neutralino into 6 quarks,
//There decay length and branching ratios are defined.
Generation.Special.PythiaProduction.SLHADecayFile = "Kaplan_hkk_10ps.LHdec";
//If no list of particles to decay are provided, all particles from the file are decayed
Generation.Special.PythiaProduction.PDecayList = {1000022};
//Provide Pythia with the desired SUSY parameters
Generation.Special.PythiaProduction.Commands += {
  "pymssm imss 1 1",    //switch on SUSY MSSM input from hand.
  //light higgs production
  "pysubs msel 0 0",    //full user control MSUB(ISUB)=1
  "pysubs msub 3 0",    // fermion fusion
  "pysubs msub 102 0",  // gluon fusion
  //Set SUSY parameters for BV48
  "pymssm rmss 1 80",   //M1
  "pymssm rmss 2 300",  //M2
  "pymssm rmss 4 150",  //mu
  "pymssm rmss 5 2.0",  //tanbeta
  "pymssm rmss 9 1000", //right sqark
  "pymssm rmss 10 1000", //left sqark for third gener.
  "pymssm rmss 12 1000", //right stop mass
  "pymssm rmss 16 1000", //top trilinear coupling or common trilinear cplg A
  //Force Higgs decay into neutralinos LSP
  "pydat3 mdme 156 1 0",
  ...
  "pydat3 mdme 173 1 1",
  ...
  "pydat3 mdme 234 1 0"
};

```

During the initialisation process, PythiaProduction updates the particle properties according to the Particle Property Service. If the decay width of a particle is below the default WidthLimit= $1.5 \cdot 10^{-6}$ GeV, its width is set to 0 to ease the simulation. To accommodate the $\tilde{\chi}_1^0$ width (i.e. in BV48), a new parameter is provided :

```

Generation.Special.PythiaProduction.WidthLimit = 1.0e-16 * GeV;

```

In the case a mass spectrum or decay file is provided, PYTHIA does not update the particle properties and this option is not needed.

¹To be found in the Gen/LbPythia package.

²Supersymmetry Les Houches Accord : defines a unique set of conventions for supersymmetric extensions of the Standard Model.

Hereunder follows an example how to pass an external supersymmetry Les Houches accord (SLHA) mass spectrum to PYTHIA, for example for the BRpV1 model.

```
//Provide an external SLHA mass spectrum file
Generation.Special.PythiaProduction.SLHASpectrumFile = "mSUGRA_m0200_m12200.LHspc";
//Provide Pythia with the desired SUSY parameters
Generation.Special.PythiaProduction.Commands += {
    "pymssm imss 1 11", //Switch on SUSY MSSM input from an SLHA file.
    //Switch on the desired SUSY processes
    "pysubs msub 201 1",
    ...
    "pysubs msub 296 1"
};
```

4.2 A new Selection Tool : PythiaLSP

A “Cut Tool”, the PythiaLSP algorithm³, has been written for keeping only the interesting events. The following example selects events with at least one $\tilde{\chi}_1^0$ - the mother⁴ - with a daughter muon in the $1.8 < \eta < 4.9$ range:

```
Generation.Special.CutTool="PythiaLSP"; //Select our tool
//Select which conditions to apply to the mother
//LSPCond = 1~: mother in acceptance,
//          = 2~: all daughters from the DgtsInAcc param in acceptance
//          = 3~: all daughters in acceptance
Generation.Special.PythiaLSP.LSPCond = 2 ;
//If LSPCond = 2, desired daughters of the mother required to be in acceptance
//In our example, we wish to have the muon (13)
Generation.Special.PythiaLSP.DgtsInAcc={13} ;
//Nb of mothers that must satisfy the LSPCond criteria
Generation.Special.PythiaLSP.NbLSP = 1 ;
//ID of the mother, here the neutralino LSP (1000022)
Generation.Special.PythiaLSP.LSPID = { 1000022 };
//Set if at least NbLSP must fulfill LSPCond
Generation.Special.PythiaLSP.AtLeast = true ;
//Define the detector acceptance
Generation.Special.PythiaLSP.EtaMax = 1.8 ;
Generation.Special.PythiaLSP.EtaMin = 4.9 ;
//Some other parameters that can be useful
//Min/max distance of the decay vertex to the primary vertex
//Generation.Special.PythiaLSP.DistToPVMIn(Max) = 5*mm ;
//Min/max position of the decay vertex on the z axis
//Generation.Special.PythiaLSP.ZPosMin(Max) = 200*mm ;
```

Note that PythiaLSP can be used not only for SUSY particles, but for any particles. For instance, to keep the top quarks decaying with both b and W in acceptance. PythiaLSP exists also as “FullGenEventCutTool”, that is to say the selection is applied not only on the “special” pp collision generated, but on all pp collisions of the event. It may be useful for requiring 4b quarks in acceptance, in the full event, including the pile-up.

³To be found in Gen/LbPythia/src/component.

⁴For historical reasons, the mother is called the LSP in the program.

4.3 A new Interface to Geant4 : GenerationToSimulation

The way particles and vertices out of the PYTHIA generation are passed to Geant4 for simulation through the detector structure has been completely revamped. The new interface can deal with any complicated particle tree, like for instance $\tilde{\chi}^0 \rightarrow h^0 \nu \rightarrow b\bar{b}\nu$. In the HepMC format - the structure in which particles are saved after the generation - the $\tilde{\chi}_1^0 \rightarrow 3 \text{ jets}$ decay is represented as the $\tilde{\chi}_1^0$ with pointers to the daughter quarks and gluons, each of the latters pointing in turn to the same string object, containing pointers to the various stable and unstable particles of the hadronisation. When looping on the daughters, and from each of them on their respective daughters, the original interface was simulating the $\tilde{\chi}_1^0$ strings as many times as the number of daughter quarks and gluons !

GenerationToSimulation is simulating all particles with non-negligible flight distance in the event, including the $\tilde{\chi}_1^0$, $\tilde{\chi}^\pm$, π_ν^0 , etc. Prior, the original interface was taking the primary vertex as the origin and sweeping away a possible long-lived particle (LLP). With the new implementation, the whole supersymmetric or Higgs decay chain for instance can be found in the Monte-Carlo simulated data. Everything is saved except the parton information, the gluons and quarks, the strings and the information lines.

4.4 Simulation in Geant4

As already said in the previous section, all particles with a non-zero flying distance are passed to Geant4 for simulation, the other ones are directly saved or not, according to their status, in the final MC structure. That means that the long-lived exotic particles must be known by Geant4. Presently, the $\tilde{\chi}_1^0$, $\tilde{\chi}_1^\pm$, $\tilde{\chi}_2^0$, h^0 , H^0 and A^0 are defined in the Gen/GaussPhysics package and interfaced to Geant4. Note that no physics lists have been defined. That means that these particles have no interactions with the material of the detector. The *simulation* is thus limited to the production of a G4Particle at such given point, which will fly to the given decay vertex position. A chargino will not undergo multiple scattering and deposit energy by ionisation.

4.5 New Event Type Numbers for Supersymmetry

In LHCb, each simulated process is identified by a unique number, called the “EventType”. The general idea is that event types should describe the way a sample was produced, and classify the specific decay channels according to their global features (topology, number of particles of different types, ...). This scheme is based on 8 digits : GSDCTNXU. See [107] for all details.

It was decided to add the following types :

- G(eneral) is kept to 4, corresponding to non-flavour physics with special generator settings.
- S(election)
 - S = 3 for Hidden-Valley $h^0 \rightarrow \pi_v^0 \pi_v^0$ decays (HV).
 - S = 4 for Hidden-Valley multi π_v^0 from Z' production.
 - S = 5 for baryon number violating SUSY models (BV).
 - S = 6 for bilinear R-parity violating SUSY models (BRpV).
- X(tra) : for the various classes of parameters.
- U(ser) : Additional parameters such as τ (BV), specific decay of the $\tilde{\chi}^0$ (BRpV), h^0 , Z' , π_v^0 masses and $\tau_{\pi_v^0}$ (HV).
- The other digits are not used. For some historical reason, the SUSY models have D(decay) = 0, while HV models have D = 9 : the selected particle(s) is(are) forced to a decay chain containing some inclusive decays.

4.6 New Option Files

The various option files dedicated to the production of exotic long-lived particles are listed in table 4.1 and defined in the Gen/DecFiles package. This list does not comprise the HV multi π_v^0 production through Z' decay, as these files have been written years before the general revamp of Gauss and have remained since then untested. The Gen/DecFiles package has been adapted to welcome the presence of the newcomers. The lhfiles repository contains all the SLHA mass spectrum and decay files, while the ppfiles repository collects the various particle property tables.

How to add a new option file in Gen/DecFiles ?

- Write a particle property table (*.tbl) to be put in ppfiles/

Name	Event type
KaplanNeutralino,mN=48GeV,tN=10ps.dec	45000010
KaplanNeutralino,mN=48GeV,tN=500ps.dec	45000011
KaplanNeutralino,mN=38GeV,tN=10ps.dec	45000020
KaplanNeutralino,mN=98GeV,tN=10ps.dec	45000030
KaplanNeutralino,mN=198GeV,tN=10ps.dec	45000040
BRpVNeutralino_m0200_m12200.dec	46000010
BRpVNeutralino_m0200_m12200_nubbar.dec	46000011
BRpVNeutralino_m0200_m12200_numu+mu-.dec	46000012
BRpVNeutralino_m0200_m12200_lqq.dec	46000013
BRpVNeutralino_m0200_m12200_muqq.dec	46000014
BRpVNeutralino_m0400_m12300.dec	46000020
BRpVNeutralino_m0600_m12400.dec	46000030
BRpVNeutralino_m01000_m12600.dec	46000040
BRpVGaugino_m0800_m324000.dec	46000050
Higgs_AA_bbbb,mH=120GeV,mA=35GeV,tA=1ps,HidValley.dec	43900001
Higgs_AA_bbbb,mH=120GeV,mA=35GeV,tA=10ps,HidValley.dec	43900002
Higgs_AA_bbbb,mH=120GeV,mA=35GeV,tA=100ps,HidValley.dec	43900003
Higgs_AA_bbbb,mH=180GeV,mA=35GeV,tA=100ps,HidValley.dec	43900004
Higgs_AA_bbbb,mH=180GeV,mA=50GeV,tA=10ps,HidValley.dec	43900005
Higgs_AA_bbbb,mH=180GeV,mA=70GeV,tA=1ps,HidValley.dec	43900006

Table 4.1: The dec files steering the various option files for the production of exotic long-lived particles, and their EventType number.

- Put eventual slha (*.LHdec or *.LHspc) in lhafiles/
- Read the the DecFiles User Guides from Gauss main page.
- Have a look at the presented dec files !
- Write a *.dec file to be put in dkfiles
- Commit Gen/DecFiles !

4.7 Choice of the generator cuts

To remove non-interesting events and speed up simulations and analysis, cuts on the long-lived particle (LLP) have been applied⁵. Figure 4.1 (*left*) shows

⁵See Sec. 4.2 for the tool used.

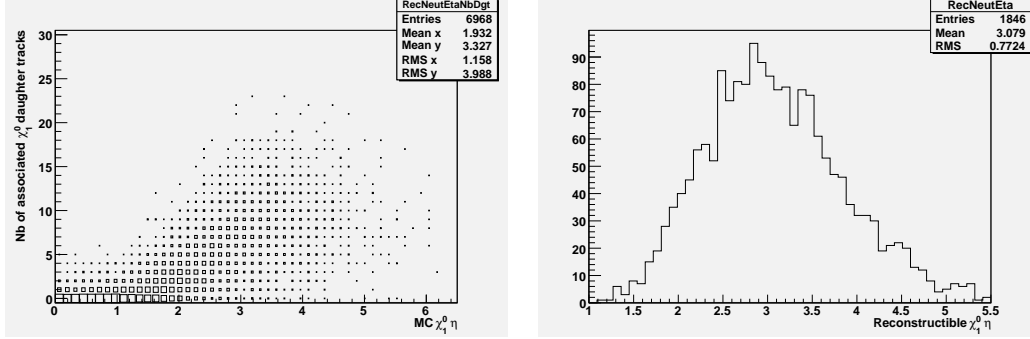


Figure 4.1: *Left*: number of “reconstructible” tracks for a 48 GeV massive $\tilde{\chi}_1^0$ (BV48) with respect to its η . *Right*: η distribution of $\tilde{\chi}_1^0$ having at least 5 reconstructible daughter tracks.

the number of “reconstructible” tracks for a 48 GeV massive $\tilde{\chi}_1^0$ from the BV48 model with respect to its pseudo-rapidity. A simulated track is said to be “reconstructible” if it has left hits in at least 3 r and 3 ϕ VeLo sensors. The η distribution of $\tilde{\chi}_1^0$ having at least 5 reconstructible daughter tracks (Fig. 4.1, *right*) tells us that keeping LLPs with $\eta > 1.8$ - the commonly-agreed VeLo acceptance - is a reasonable choice. No maximum limit on η has been retained as a LLP flying with a radial distance to the beam line and a small θ angle may be well reconstructed.

All Monte-Carlo samples have been generated with the requirement of having at least one particle of interest with $\eta > 1.8$. The particle of interest is the $\tilde{\chi}_1^0$ for the supersymmetric models (BRpV and BV) with the exception of the BRpVmuq sample, where rather the daughter muon is requested to have $\eta > 1.8$. In the HV samples having at least 3 daughter b quarks in the LHCb acceptance was preferred for b-jets dedicated studies. Without any specific notification, this cut is assumed in the following MC plots and analysis.

Chapter 5

Characteristics of the Selected Models. Studies at Generator Level



This chapter exhibits the features at generator level of the selected models that would allow to bring to light the existence of long-lived “exotic” particles. In particular, the attention will be given to the case of the decay of a Higgs-like boson into two such long-lived particles.

THE NEXT SECTIONS show the striking topological features of the long-lived “exotic” particles, such as a high reconstructed mass and a large radial distance to the beam interaction line of the decay vertices, a possible high track multiplicity and large transverse momentum distribution of the daughter tracks. Section 5.6 in turn presents the mother, in the case of its decay into two LLPs. Finally, Sec. 5.7 tables the number of expected events for the selected models.

5.1 LLP and the LHCb Acceptance

A first feature of all the selected theoretical models is the non-negligible portion of long-lived particles and Higgs bosons produced in the LHCb acceptance¹.

¹The η distributions of the LLP determined at generator level for some selected models can be seen in Fig. F.1.

Table 5.1 presents the efficiency of the chosen generator cuts (described in Sec. 4.7) for both the 2010 and designed center-of-mass energy of 7 TeV and 14 TeV, respectively.

For an energy of 7 TeV in the CM, the percentage of $\tilde{\chi}_1^0$ from the BV48 model from generic SUSY production falling in the detector acceptance is 26%, while it gets a bit higher to 28.8% for $\tilde{\chi}_1^0$ decaying from a h^0 . As already stated in Sec. 1.3 supersymmetric particles are produced by pairs. The probability to have at least 2 $\tilde{\chi}_1^0$ in the acceptance is 10%, 16% for the two daughter $\tilde{\chi}_1^0$ of a mother h^0 . The probability for the 114 GeV massive h^0 being in the acceptance is around 33%. These figures improve for a center-of-mass energy of 14 TeV, because of the increased forward boost.

5.2 Distance of flight and radial distance

Until otherwise specified, all plots presented have been done with MC events generated at the center-of-mass energy of 7 TeV.

Figure 5.1 to 5.4 show different distributions relative to the distance of flight for the LLP of the various selected models. Figure 5.4 shows the distribution of the decay position on the z axis. For baryon number violating SUSY models (BV) and hidden valley (HV) models, the lifetime of the LLP is a free parameter within certain bounds (see Sec. 1.3.1 and 1.4, respectively). In bilinear P_R violating SUSY models (see Sec. 1.3.2), the lifetime τ_{LLP} is linked to the mass : the heavier the LLP, the shorter the lifetime. As a reference the B mesons are also shown in the plots. We will refer as B mesons, particles with $500 \leq \text{PID}^2 < 600$ and a decay vertex separated by at least 0.1 mm from the PV.

We can separate τ_{LLP} in 3 classes :

- For $\tau_{\text{LLP}} < \mathcal{O}(1)$ ps, a majority of decay vertices would happen very close to the primary vertex (< 1 mm), making difficult any reconstruction.
- For $\mathcal{O}(1)$ ps $< \tau_{\text{LLP}} < \mathcal{O}(10)$ ps, the LLPs decay in the VeLo z acceptance and could potentially be reconstructed with precision. The VeLo region is roughly a cylinder of radius 82 mm stretching from $z \sim -250$ mm to ~ 750 mm.
- For $\mathcal{O}(100)$ ps $< \tau_{\text{LLP}} < \mathcal{O}(1)$ ns, the majority of LLP escapes the VeLo and decays before the T stations, resulting in the production of

²We use PIDs as defined in the particle data group (PDG) [12].

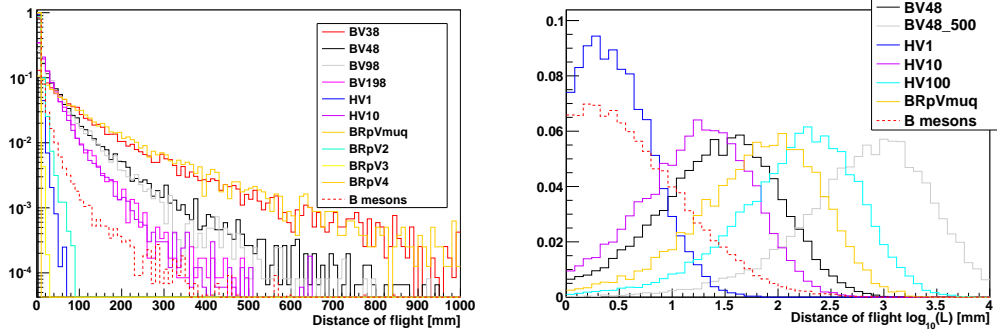


Figure 5.1: Flight distance of the LLP for some of the models. For reference, B mesons are also displayed. Log abscissa in the right plot.

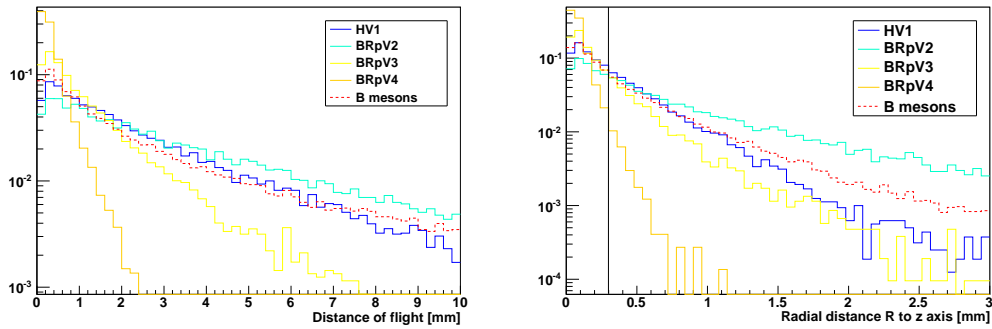


Figure 5.2: *Left:* Flight distance of the LLP for some of the models. *Right:* Radial distance of the LLP decay vertex to the z axis. In the 2010 runs, more than 99% of the reconstructed PVs are found within a radius of 0.3 mm around the beam line (indicated by a vertical bar). For reference, B mesons are also displayed.

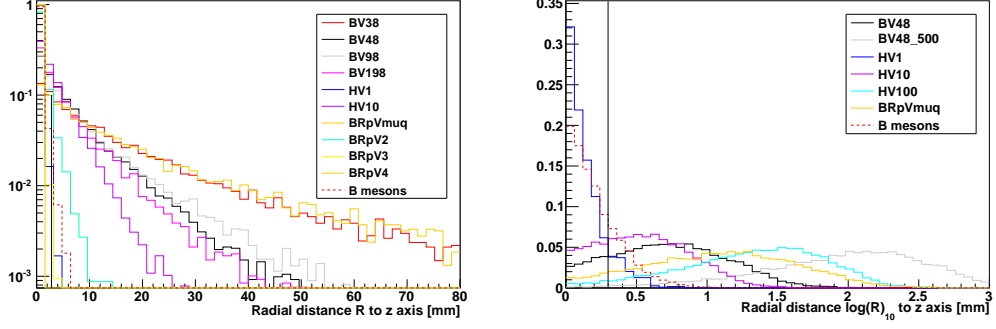


Figure 5.3: Radial distance to the z axis of the LLP and B mesons decay vertex. As a comparison, the outer radius of the VeLo sensors is 82 mm (indicated by a vertical bar). Log abscissa in the right plot.

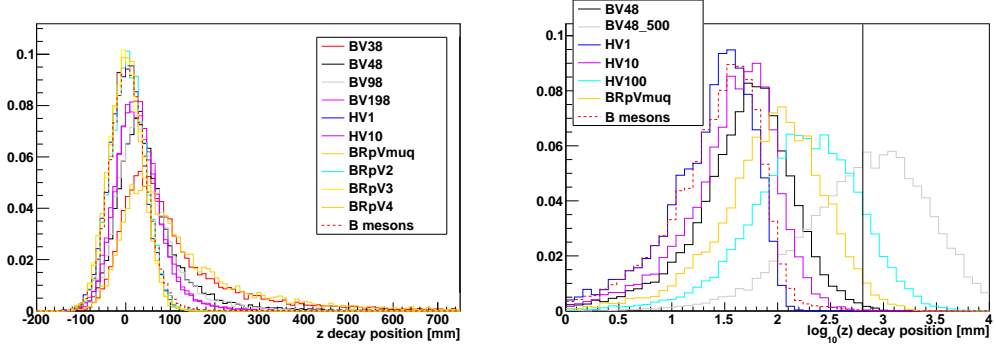


Figure 5.4: Decay position in z of the LLPs and B mesons. Notice that the VeLo sensors cover from $z \sim -250$ mm to ~ 750 mm (indicated by a vertical line). Log abscissa in the right plot.

downstream and T tracks. For HV100, the percentage of LLPs with a decay position $z > 750$ mm is 9%, increasing to 51% for BV48.500.

The decay vertices for $\tau_{\text{LLP}} > \mathcal{O}(1)$ ps will be found at some radial distance from the beam axis. A large enough radial distance would allow to distinguish the candidates from the multiple primary vertices and b-hadron decay. It will be shown in Sec. 6.2.2 that in the 2010 runs, more than 99% of the reconstructed PVs are found within a radius of 0.3 mm around the beam interaction line. Figure 5.2 (*left*) and 5.3 show the distribution of the radial distance R of the LLP decay vertex to the z axis, which can be assimilated with the beam line in the MC simulations. With 98% of decay with $R < 0.3$ mm, LLPs from the BRpV4 models are completely drowned in the sea of beam gas and proton-proton interaction vertices and will be hard to distinguished from.

On the other side, LLPs with $\tau > \mathcal{O}(100)$ ps, face the problem of decaying outside the radial acceptance. For instance, 89% and 42% of LLPs from HV100 and BV48.500 respectively are found with $R > 82$ mm, which is about the outer radius of the VeLo sensors.

5.3 Track multiplicity

The number of stable charged daughter tracks produced in the decay of SM long-lived particles rarely exceed 4 to 5 tracks. This is a potential discriminant if the decaying LLP has a large track multiplicity.

In order to get closer to the experimental conditions in this study at generator level, we count the number of stable charged daughter tracks found in the acceptance and compatible with the LLP decay vertices. For this we select all the tracks with a small impact parameter (IP) to the true decay position.

Figure 5.5 (*left*) shows the distribution of the number of daughter charged stable tracks within the VeLo acceptance for 3 values of the maximum impact parameter, $IPMax$, for the HV10 sample.

Because the LLP is neutral, when all the charged particles from the decay are properly considered, we expect only the even bins to be filled in. The counts in the odd bins happen when an odd number of tracks is lost because falling outside acceptance or when produced from tertiary vertices falling outside the $IPMax$ window.

For $IPMax = 0.1$ mm, essentially only the daughters produced at the decay position will be counted. On the other hand, during the hadronisation of the decaying LLP, an important part of the available energy may be taken for the production of SM long-lived particles, like b-hadrons. It is thus

very important to increase $IPMax$ to catch the daughter tracks produced in their decay. Of course, a too large $IPMax$ value may cause a possible contamination from the underlying event.

In conclusion, for this generator-level study, we will consider a $IPMax = 2$ mm, which will be justified by the actual procedure for the reconstruction of the LLPs (see Sec. 6.2.1).

From Fig. 5.6 (*left*), obtained with $IPMax = 2$ mm, we see that a cut on the minimum number of tracks composing the reconstructed vertex may be quite efficient on the selected models to reject SM particles. For comparison, the number of tracks in the decay vertices of B mesons is also displayed. 2.7% of them were found with ≥ 4 tracks.

By looking carefully at Fig. 5.6 (*left*), one can note a peak at 1 in the BRpVmuq distribution (*orange*), where the μ daughter is requested to be in the acceptance. This fact indicates that the μ may be so isolated that in some cases the sister quarks decay outside the acceptance.

5.4 Reconstructed mass from charged particles

The reconstructed mass of the decay vertex is correlated with its track multiplicity, and is in the same measure dependent on the reconstruction procedure. Figure 5.5 (*right*) shows the distribution of the reconstructed mass from the charged stable daughters in the acceptance of the HV10 35 GeV massive π_v^0 for different values of $IPMax$. Again, a too small value of $IPMax$ would result in the loss of some precious long-lived daughters. The challenge of the reconstruction procedure will be to find the right balance between catching the most possible part of the daughter tracks and keeping the track contamination from the underlying event negligible.

Figure 5.6 (*right*) presents the distribution of the reconstructed mass for $IPMax = 2$ mm for various models. Due to the loss of the neutral particles and tracks outside the acceptance, the distribution has a mean value much lower than the LLP's theoretical mass, only its tail is pointing to it. However, the distributions extend to much larger mass values than the heavier SM long-lived particle, with mass of ≈ 5 GeV (see Fig. 5.7, *right*). The percentage of LLP with $m_{\text{rec}} > 6$ GeV ranges from 47% to 70% for decreasing $\tilde{\chi}_1^0$ mass (BV198 to BV38). With three daughter b quarks in the acceptance, 73% of HV π_v^0 have $m_{\text{rec}} > 6$ GeV for a $m_{\text{th}} = 35$ GeV. It is interesting to compare the distributions of the track multiplicity and the reconstructed masses for $\tilde{\chi}_1^0 \rightarrow \nu b \bar{b}$ (BRpVb) and $\tilde{\chi}_1^0 \rightarrow \mu^\pm q q'$ (BRpVmuq). The part of the total

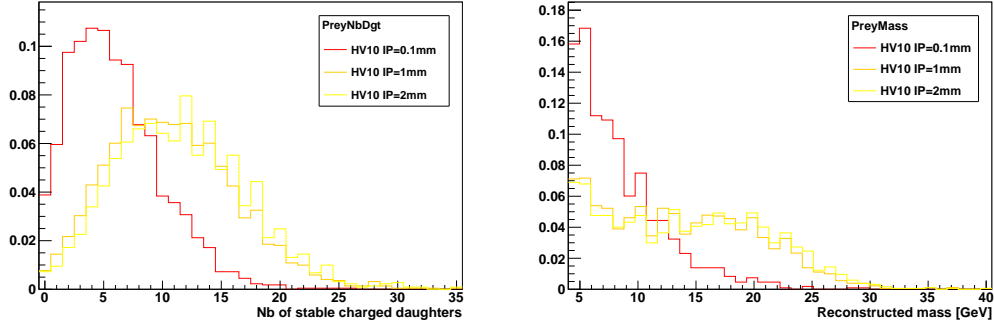


Figure 5.5: Number of daughter charged stable tracks within the VeLo acceptance (*left*) and reconstructed mass (*right*) for different maximum impact parameters IP_{Max} (IP in the legend). Only the HV10 model is shown.

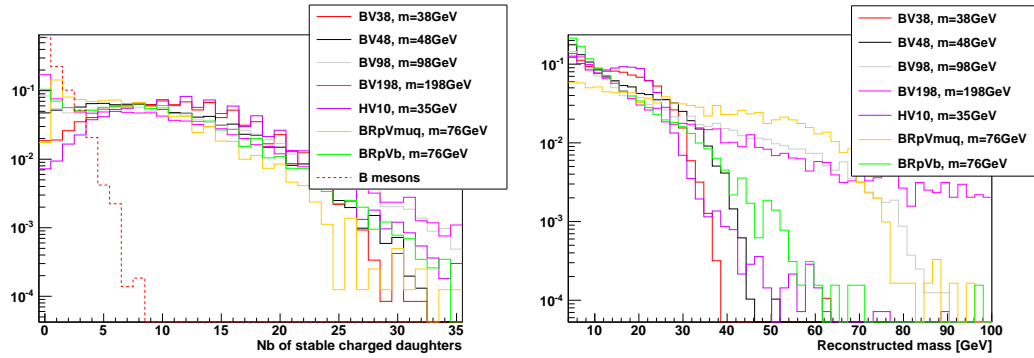


Figure 5.6: Number of daughter charged stable tracks within the VeLo acceptance and with an impact parameter to the decay vertex $IP < 2$ mm (*left*) and reconstructed mass (*right*). B mesons and some selected theoretical models are shown.

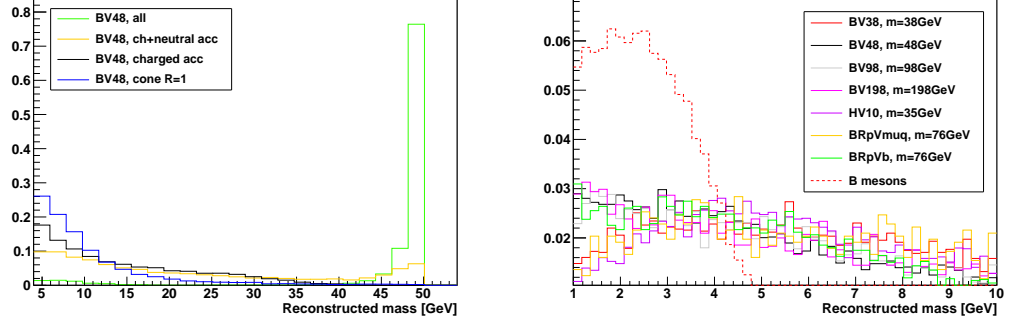


Figure 5.7: *Left* : reconstructed mass from all stable daughters (except ν), stable charged and neutral daughters in the acceptance, stable charged in the acceptance only and from all daughters in a cone of radius $R=1$, for the BV48 model. *Right* : reconstructed mass of B mesons and of the LLP of some selected theoretical models.

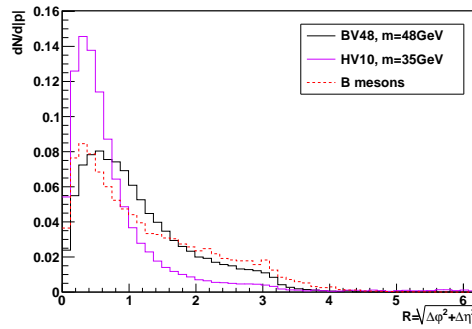


Figure 5.8: Distance in the $\eta - \varphi$ plane of the daughters to the LLP for the B mesons and some selected theoretical models. A weight on $|p|$ has been applied.

available energy taken by the neutrino is by far non negligible, resulting in the loss of about 20 GeV in m_{rec} , on average.

As a contrast, Fig. 5.7 (*left*) shows the reconstructed LLP mass in BV48 when all stable charged and neutral daughter particles - except neutrinos - can be reconstructed (*green*). If one takes into account the detector acceptance (*orange*), the peak at the χ 's mass of 48 GeV fades out to the benefit of a long tail.

Figure 5.8 presents the distance in the $\eta - \varphi$ plane of the stable (charged and neutral) daughters in the acceptance to the LLP, weighted by the momentum of the tracks. We can see that the width of the distribution is roughly proportional to the mass, as expected. The reconstructed mass from all those particles within a cone of radius

$$R = \sqrt{\Delta\eta^2 + \Delta\varphi^2} = 1,$$

shown in Fig. 5.7 (*left*, *blue*) for BV48, is much worse than the mass reconstructed from the charged tracks only. This is due to the relatively large mass of the LLP, and its decay into several partons. A sub-jet reconstruction approach will be tested in the future (see [27]).

Nevertheless, we can assume that a radially distant vertex with a high reconstructed mass might well be the smoking gun for some exotic physics. A precise mass estimation would require dedicated methods adapted to the topology of the decay, like a sub-jet reconstruction approach.

5.5 Transverse momentum of the daughters

A last feature worth mentioning is the large distribution of the transverse momentum of the daughter particles, inherent to the decay of very heavy particles (see Fig. 5.9 (*left*)). For comparison, the distribution of the B mesons daughters is also plotted.

Figure 5.9 (*right*) shows the transverse momentum distribution of the daughter muon in the $\tilde{\chi}_1^0 \rightarrow \mu^\pm \text{qq}'$ decay (BRpVmuq). It is much larger than the distribution of the muon with the highest p_T in the decay of B mesons. For the selection of this channel, it could be worth to request at least a muon candidate with $p_T > 5 - 10$ GeV in the reconstructed vertex.

It was also found that 33% of the daughter muons have a total energy collected in a cone of radius

$$R = \sqrt{\Delta\eta^2 + \Delta\varphi^2} = 0.4$$

which is less than 30% of the energy of the muon. Some isolation criteria could show very helpful.

5.6 The Mother

For the models featuring a Higgs boson decaying into two LLPs, namely BV48 and HV, Fig. 5.10 shows the Higgs mother generated p_T (*left*) and its mass (*right*) calculated by combining the LLP candidates. The boson is produced in the forward direction with a transverse momentum which is in general quite low: below 10 GeV.

5.7 Expected Number of Events

Table 5.1 summarises for the selected channels their total production cross-section, branching ratio and the expected number of events at $\sqrt{s} = 7$ TeV for the 37 pb^{-1} of data taken in 2010, for 1 fb^{-1} of data, which is hoped to be collected during the runs foreseen in 2011, and finally for one year of data taking at the design luminosity and energy at 14 TeV, which is estimated to be roughly 2 fb^{-1} .

For the models featuring a Higgs boson decaying into two LLPs, the Table 5.2 gives the Higgs production cross-sections and the expected number of events with at least one and at least two LLP flying in the detector acceptance, for 2 fb^{-1} at 14 TeV and for the 37 pb^{-1} at 7 TeV of 2010.

The total production cross-sections have been computed by PYTHIA (6.424) at leading order only. Please consult [113] for the Higgs bosons cross-sections (both SM and MSSM) at the next-to-leading orders. A detailed analysis of the uncertainties entering the h^0 cross-sections and decay branching ratios, including all relevant higher order QCD and electroweak corrections, is presented. The total uncertainties rise up to 30% of the cross-section.

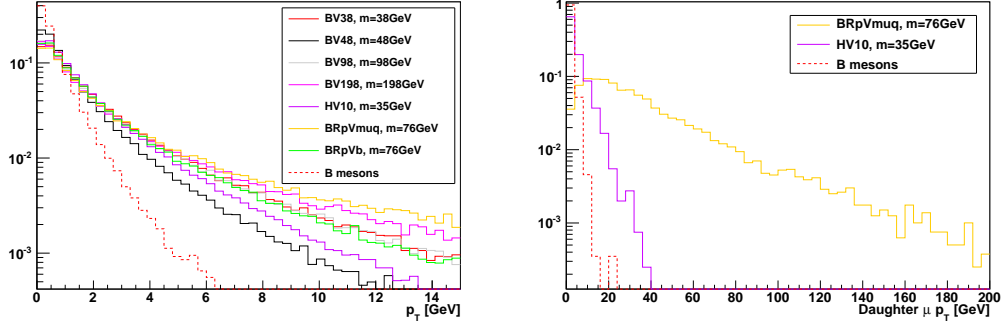


Figure 5.9: *Left*: p_T distribution of the daughter tracks for B mesons and some models. *Right*: p_T distribution of the daughter muon in the $\tilde{\chi}_1^0 \rightarrow \mu^\pm qq'$ decay (BRpVmuq) and the muon with highest p_T from HV10 and B meson decays.

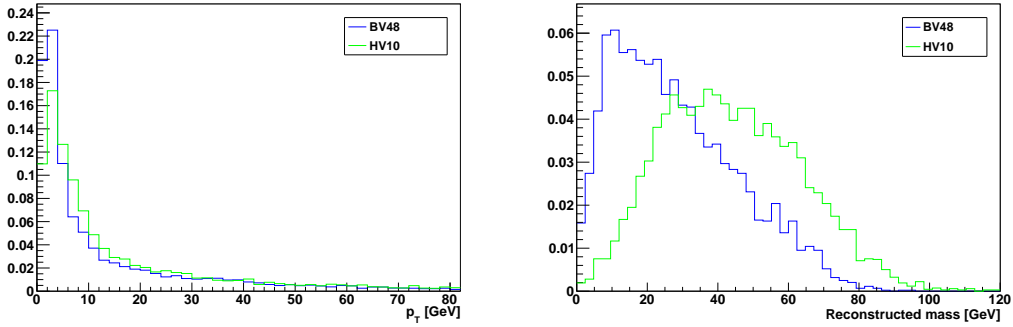


Figure 5.10: Parent generated p_T (*left*) and reconstructed Higgs mass (*right*), obtained by combining the two LLP candidates reconstructed from charged particles. BV48 features a 114 GeV massive Higgs bosons, while $m_{h^0} = 120$ GeV for HV.

Model	7 TeV		1 fb ⁻¹	37 pb ⁻¹
	GC [%]	$\sigma \times \text{BR}$ [mbarn]	# evts	# evts
HV	11	$1.7 \cdot 10^{-08}$	2k	74
BV48	29	$2 \cdot 10^{-08}$	5.7k	211
BV38	17	$2 \cdot 10^{-08}$	3.4k	124
BV98	21	$1.5 \cdot 10^{-08}$	7k	258
BV198	19	$1.5 \cdot 10^{-09}$	270	10
BRpVmuq	11	$1.2 \cdot 10^{-08} \times 0.02$	20	1
BRpVb	13	$1.2 \cdot 10^{-08} \times 0.36$	550	20
BRpVm	15	$1.2 \cdot 10^{-08} \times 0.003$	5	< 1

Model	14 TeV		2 fb ⁻¹
	GC [%]	$\sigma \times \text{BR}$ [mbarn]	# evts
HV	11	$6.5 \cdot 10^{-08}$	15k
BV48	30	$8.1 \cdot 10^{-08}$	48k
BV38	20	$1.1 \cdot 10^{-07}$	45100
BV98	25	$9.2 \cdot 10^{-08}$	45000
BV198	24	$1.2 \cdot 10^{-08}$	5700
BRpVmuq	15	$1.1 \cdot 10^{-07} \times 0.02$	470
BRpVb	17	$1.1 \cdot 10^{-07} \times 0.36$	12800
BRpVm	17	$1.1 \cdot 10^{-07} \times 0.003$	110

Table 5.1: Percentage of events passing the generator cuts (GC), production cross-section times branching ratios and expected number of events at $\sqrt{s} = 7$ TeV for $L = 37 \text{ pb}^{-1}$ (2010 runs), $L = 1 \text{ fb}^{-1}$ (2011 runs) and at $\sqrt{s} = 14$ TeV for $L = 2 \text{ fb}^{-1}$ (design luminosity) for all selected models.

Model	37 pb ⁻¹ @7 TeV			2 fb ⁻¹ @14 TeV		
	σ [mbarn]	N ₁	N ₂	σ [mbarn]	N ₁	N ₂
HV10	$1.74 \cdot 10^{-08}$	163	54	$6.5 \cdot 10^{-08}$	36000	14150
BV48	$1.57 \cdot 10^{-08}$	167	94	$5.75 \cdot 10^{-08}$	36800	22570

Table 5.2: Estimation of the cross-sections and number N₁ (N₂) of events with at least one (at least two) LLPs in the LHCb acceptance, for 37 pb⁻¹, at $\sqrt{s} = 7$ TeV, and for 2 fb⁻¹ (one nominal LHCb year) at 14 TeV. The models have a Higgs parent decaying into 2 LLPs.

Chapter 6

Inclusive Selection of Events with Displaced Vertices



We present the algorithms and their optimisation used to select events with displaced vertices. Key features of the candidates for the selected models are shown, leading to the design of trigger and stripping selections.

THE EVENT SELECTION requires a search for vertices consistent with the decay of a LLP. Following the general features of exotic LLPs outlined in chapter 5, a sufficient number of tracks, total p_T and invariant mass and long flight distance are key ingredients in the selection.

The selection of events with at least one candidate is achieved in 3 main steps :

1. Reconstruction of all vertices in the events. This operation gathers the primary vertices (PVs) of the pp interactions, vertices created by the subsequent decay of the particles produced, vertices from interaction with matter, etc.
2. Preselection of the interesting vertices, to separate the PV candidates from the secondary vertices, which for simplicity will be called displaced vertices (DVs).
3. Selection of the candidates consistent with some physical expectations ($\tilde{\chi}_1^0$, π_v^0 , ...).

Section 6.1 presents the different algorithms and tools that have been developed and used to achieve these three steps, at both on-line and off-line level. The optimisation of these algorithms is described in Sec. 6.2, while the properties of the selected candidates for different models are shown in Sec. 6.3. This leads to the design of trigger and stripping selections that are presented in Sec. 6.4.

6.1 Presentation of the Algorithms

6.1.1 Reconstruction of the Vertices

The reconstruction of all vertices in the event is performed in two steps, the seeding followed by the fitting. The purpose of seeding is to search for vertex candidates and produce a list of seeds. In the second step each seed is used as a starting point for the fit. The candidates which fulfil the quality conditions are accepted, otherwise the tracks used in the fit are removed from further vertex search. The seeding and fitting are repeated until no new vertex is found.

Vertex seeding The tracks that have a segment in the VeLo and fulfil minimal quality criteria are collected. The search for the accumulation of tracks is performed. For each track the distance of closest approach (DoCA) to another track is calculated. If their DoCA is smaller than a parameter (called *TrackPairMaxDistance*), we compute the position of the point of closest approach.

Then the truncated mean position of such points is calculated by removing outliers iteratively until all points are within a radius of dubbed *zMaxSpread* around the mean value. The seed is accepted if enough (*MinCloseTracks*) tracks are left. The seeds are sorted according to the multiplicity of tracks, from highest to lowest one.

We will later refer to this procedure by using the name of the algorithm : PVSeed3DTool, which indicate the “3D” nature of the calculation.

Vertex fitting The fitting algorithm starts by collecting tracks passing close to the seed point. A relatively wide window is used since the seed position is known with limited precision. An adaptive least square fit is then performed. In each iteration the track’s χ^2 contribution gets a weight defined

as follows :

$$\begin{aligned} & \left(1 - \frac{\chi^2}{c^2}\right) \quad , \text{ if } \chi^2 < c^2 \\ & 0 \quad , \text{ if } \chi^2 > c^2 \end{aligned} \quad (6.1)$$

where c is Tukey's constant, set to 3. This constant defines the threshold of IP significance (χ_{IP}^2). χ_{IP}^2 must be lower than $\chi_{IP,max}^2$ (*trackMaxChi2*) for the tracks to be included in the fit. One of the advantages of the adaptive fit is that the tracks of bad quality, suffering from large multiple scattering effects or being poorly reconstructed, do not influence much the position of the vertex.

In addition, bias coming from the SM LLPs decay products included in the vertex reconstruction is minimal. During the iteration the tracks with weights equal zero are not discarded permanently from the initial set of selected tracks. They can get non-zero weight at next iteration when calculated with respect to an adjusted vertex position. The iteration stops when the change in z position of the vertex is less than $0.5 \mu m$ or if the change in χ^2 per degree of freedom is appropriately small. The vertex is accepted if the number of tracks used in the last iteration is greater than or equal to a parameter (*MinTracks*).

For high multiplicity candidates, a relatively large number of tracks is not included in the fit (bad quality tracks with $\chi_{IP}^2 > \chi_{IP,max}^2$). The accumulation of such tracks can satisfy the conditions for another candidate and can be reconstructed as a false vertex. To avoid this, some separation has to be ensured. It is done by removing tracks with $\chi_{IP,max}^2 < \chi_{IP}^2 < \chi_{IPR,max}^2$ (*trackMaxChi2Remove*) around the properly reconstructed candidates. In the standard procedure for the reconstruction of PVs, this separation condition protects also genuine secondary vertices of B meson decays to be reconstructed as PV.

There are two versions of the fitting algorithm : one is meant for the HLT context and the other one for off-line analysis. The main difference is that in the HLT the VeLo tracks are used. Because VeLo tracks do not have any momentum assigned, a special track error parametrisation is used. In addition the algorithm contains a cut on the IP of the track to the seed : if it is greater than a maximum value (*maxIP2PV*), the track is removed from the selection before the adaptive least square fit is performed.

In the off-line case proper IP errors from the track's covariance matrix are calculated.

By default, a separation $-\chi_{1,2}^2 = \frac{(z_1 - z_2)^2}{\sigma_{z_1} + \sigma_{z_2}}$ is calculated on all reconstructed vertices (RVs). For a vertex to be saved, it is required to have a small $\chi_{1,2}^2$

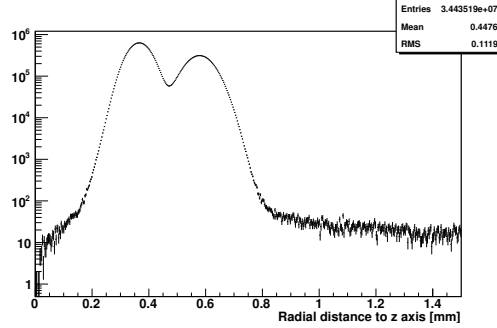


Figure 6.1: Radial position in the global frame of the reconstructed primary vertices for the 2010 data.

($<PVsChi2Separation$) with respect to all previously saved vertices. This requirement is increased (to $PVsChi2SeparationLowMult$) if the candidate vertex has less than 7 tracks. This is intended to avoid taking the secondary vertices from SM particle decay and eventually PVs that are too close to each other.

6.1.2 A Beam Line Position Algorithm

The selection of the PVs will make use of the distance to the beam line which is known to move in time. An algorithm, CalibrationIP, has been specifically written for providing information about the beam interaction line position and width. It loops over all PVs, as reconstructed by the standard procedure, in every events, and averages the position of the selected PVs to get the mean interaction point. By default, at least 10 tracks are required in the vertex, from which at least 6 Long tracks.

From the diagonalisation of the covariance matrix of the positions, it yields an estimation of the beam line direction through the eigenvectors and its “width” through the eigenvalues. This information - mean interaction point, direction and width - allows to estimate the beam line.

The diagonalisation process is repeated at a given frequency on the subset of PVs. If the reconstructed beam line differs by more than $50\text{ }\mu\text{m}$ from the previous estimate, all the statistics accumulated so far is reset and the new estimate kept. On the contrary, if the beam line is found stable, the subset of PVs is incorporated to the accumulated data, and an estimate of the beam line is performed over the whole set. On the 2010 data, the frequency has been set to 30 events, which proved to be safe. The statistics are automatically cleared if the run number is different from the one of the previous event. Figure 6.1 shows a quite small radial variation of the order

of 0.3 mm over the whole processed data.

6.1.3 Preselection of the LLPs

The LLP preselection algorithm loops on all reconstructed vertices (RVs) in the event :

- The RV with lowest z position can be considered to be a PV and can be skipped.
- RVs with at least one backward track are removed.
- A minimal number of tracks ($NbTracks$) in the RV is requested.
- RVs close to the beam line are eliminated.
- Candidates originating from regions with detector material (Sensors, RF-shield) can be rejected.
- The reconstructed mass and the sum of the p_T of all the daughter tracks ($\sum_{trks} p_T$) of the remaining candidates are estimated. Minimal values are requested ($MinMass$ and $MinSumpt$).

In parallel, it is also responsible for the selection of the primary vertices that will be used later in the analysis. If none are found, the execution of the algorithm stops before the search for secondary vertices¹.

6.1.3.a Estimation of the Track Momentum

In the HLT2 context, the vertex reconstruction process is performed from “VeLo” tracks, reconstructed from hits in the VeLo only. As it is (almost) free from magnetic field, they can therefore be approximated as straight lines, simplifying the calculation and reducing the processing time. On the other hand, they do not possess any momentum information.

Hence, (in Hlt2PreSelDV) a map is created between the VeLo tracks participating to the vertex and the reconstructed “long” tracks². All tracks are assumed to be pions. The efficiency can be quite low for some candidates, as can be seen in Fig. 6.2 (*left*). When no related long track is found, the

¹The implementation is done in the Hlt2PreSelDV algorithm for the HLT2 project, and RecVertice2Particles for off-line analysis.

²In the HLT context, they are called the forward tracks, because they are the result of the forward tracking procedure.

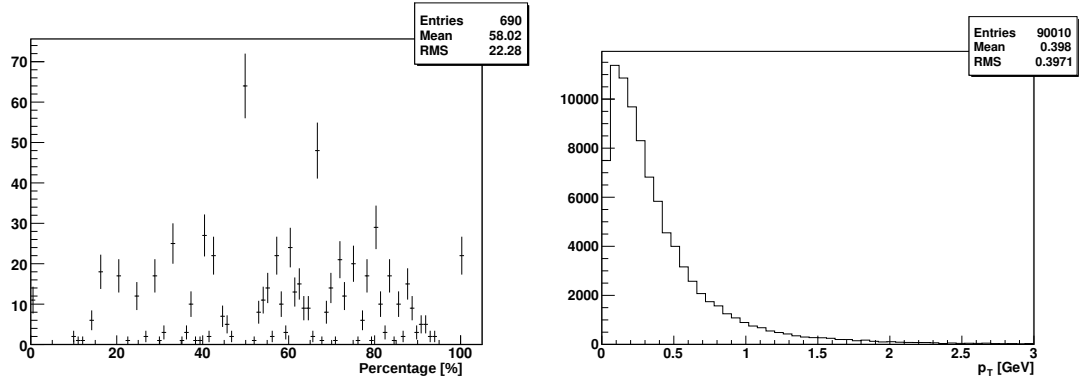


Figure 6.2: *Left* : distribution of the percentage of VeLo tracks that have a related “long” track. *Right* : p_T distribution of pions, from MC.

VeLo track is assumed to be a pion with a p_T of 0.4 GeV. Although this does not give an accurate estimate of the kinematics of the RV, we have found a gain of $\sim 6\%$ of signal rate for the same background rejection. Discarding VeLo tracks, many vertices would not have enough tracks - and mass - to be distinguished from SM particles. This is particularly important for the BRpVb model, where each track counts.

In the off-line context the idea remains basically the same but the implementation differs. Here, all reconstructed tracks in the event are available with full PID information and the reconstruction is done with all tracks possessing a segment in the VeLo. We then form particles with the most probable PID. Also in this case, VeLo tracks become by default pions with a p_T of 0.4 GeV.

6.1.3.b Track Quality Check

The tracking stations measure the charge over momentum (q/p) of a track. The higher the momentum, the smaller the q/p factor and the larger the error $\sigma(q/p)$. Therefore, very high momentum tracks cannot be distinguished from straight lines. The LHCb has a poor resolution beyond a momentum value of 100 GeV.

Another problem is the presence of ghosts, false tracks, reconstructed by wrong associations of hits in the VeLo and T tracks. The momentum distribution of ghost tracks is rather arbitrary: the q/p distribution is almost flat, so ghosts populate the high momentum region where we expect very few physical tracks. As a matter of fact, at very high momenta, almost every track is a ghost! As wrong associations depend on the multiplicity, they are more frequent in jets.

Ghosts with large momentum may yield to an arbitrary very high estimate of the vertex mass, causing it to pass the kinematic cuts. The way to remove them is two-fold. First, a cut on the large values of the track's $\chi^2/ndof$ (*TrackMaxChi2oNDOF*) is performed. Then $\frac{|q/p|}{\sigma(q/p)}$ is computed. If it is less than 20 - errors of the same order as the measure - the track is said to have infinite momentum and therefore rejected. This cut is not applied to the VeLo tracks, as by construction, their momentum is imposed.

Once all preselection cuts are passed, the candidate vertex is saved for further selection by dedicated trigger/stripping lines or off-line analysis. The various cuts, as well as the methods to reject RVs close to the beam line and detector material will be presented in Sec. 6.2.3.

6.1.4 The Selection of the Displaced Vertices

An algorithm has been written which provides a wide range of kinematic and geometrical cuts to apply on the candidate particles. It is named *DisplVertices* in the off-line context and *Hlt2SelDV* for the trigger (HLT2).

It contains all the cuts defined in the preselection algorithms and introduces new ones, like maximum values for the reconstructed mass (*PreyMaxMass*) and the radial distance to the beam line (*RMax*), as well as cuts on the position of the decay vertices. Maximum values for the radial and z estimated errors on the decay vertex positions, σ_r and σ_z , can be requested (through the *SigmaR* and *SigmaZ* parameters). A high p_T muon can be requested in the decay product by a cut (*MuonpT*) set to the value of the minimum desired transverse momentum.

Finally, a certain minimal number of successful candidates may be requested (*MinNBCands*). Specific methods to reject the PVs and RVs from interaction with matter will be presented in Sec. 6.2.3.

6.2 Optimisation of the Algorithms

6.2.1 The Reconstruction Procedure

The default parameter values for the vertex reconstruction, presented in Sec. 6.1.1, are optimised for the reconstruction of the primary vertices (PVs) of the pp interactions. The standard procedure, originally implemented for B physics, asks for vertices that are well separated spatially, (*PVsChi2Separation* and *PVsChi2SeparationLowMult*), and have a high track multiplicity, presently more than 5 tracks. This number is likely to increase in the future to 7 or even more, in case of a larger instantaneous luminosity. This is intended to remove vertices from the decay of SM particles.

The idea is to take advantage of the high number of tracks that have a low χ^2_{IP} to the seed, keep a tight $\chi^2_{IP,max}$ requirement (*trackMaxChi2*) and remove all tracks in a certain $\chi^2_{IPR,max}$ window around the seed (*trackMaxChi2Remove*). Those tracks have either large errors or are likely to come from long-lived SM particle decay. They may form unwanted satellite seeds in the vicinity of the PVs. In some cases, they may attract some tracks produced at the PV and split the PV in two or more PV-like pieces. These satellite vertices and split PVs represent a risk for B physics analysis, especially for the lifetime measurements. Those vertices can worsen the PV resolution and lead to wrong PV-candidate associations.

In our study, we are aiming at a somehow different idea:

- Reconstruct all vertices in the event, with a very good separability. It is important for short lifetime candidates which may decay very close to the PV.
- Reconstruct also vertices with quite low track multiplicity, i.e. ≥ 4 tracks.
- As already stressed in Sec. 5.3, we wish to include the tracks from the decay of SM long-lived daughters, originated by the LLP decay into b or c quarks (tertiary vertices).

As a consequence we have optimised the vertex reconstruction procedure on MC events, considering the following criteria :

- High efficiency to reconstruct the wanted exotic long-lived particles that have at least 4 associated reconstructed tracks in the VeLo. This also with respect to the distance to the PV.

- High purity of the reconstructed candidates.
The purity is defined as the percentage of tracks that are really coming from the LLP (from MC-truth).
- Low probability to split the PV and the RVs.

The optimisation of the reconstruction efficiency and purity has been performed on the BV48, HV10 and HV1 MC samples. π_b^0 decays in b quarks with many tertiary vertices, while BV48 has light quarks attached to the $\tilde{\chi}_1^0$ decay. HV1 is used to check the efficiency for shorter lifetime, closer to the PV. To get the best chance to catch candidates with low track multiplicity distribution, like for instance in the model BRpVmuq, the optimisation is performed with *MinCloseTracks*= 3 and *MinTracks*= 4.

We have iteratively varied the different cuts on :

- *TrackPairMaxDistance* and *zMaxSpread*,
- $\chi_{IP,max}^2$ (*trackMaxChi2*) and $\chi_{IP,max}^2$ (*trackMaxChi2*).

The “best point” in this large parameter space correspond to a large efficiency, while keeping parasitic effects low.

Figure 6.3 shows the LLP MC candidate reconstruction efficiency for BV48 and HV10 for different parameters, and Fig. B.1 gives the percentage of MC LLP decay vertices that have been artificially split into 2 or more RVs. This percentage is higher for HV10 due to the higher frequency of daughter B mesons.

Chapter B in the Appendix gives more details on the optimisation process.

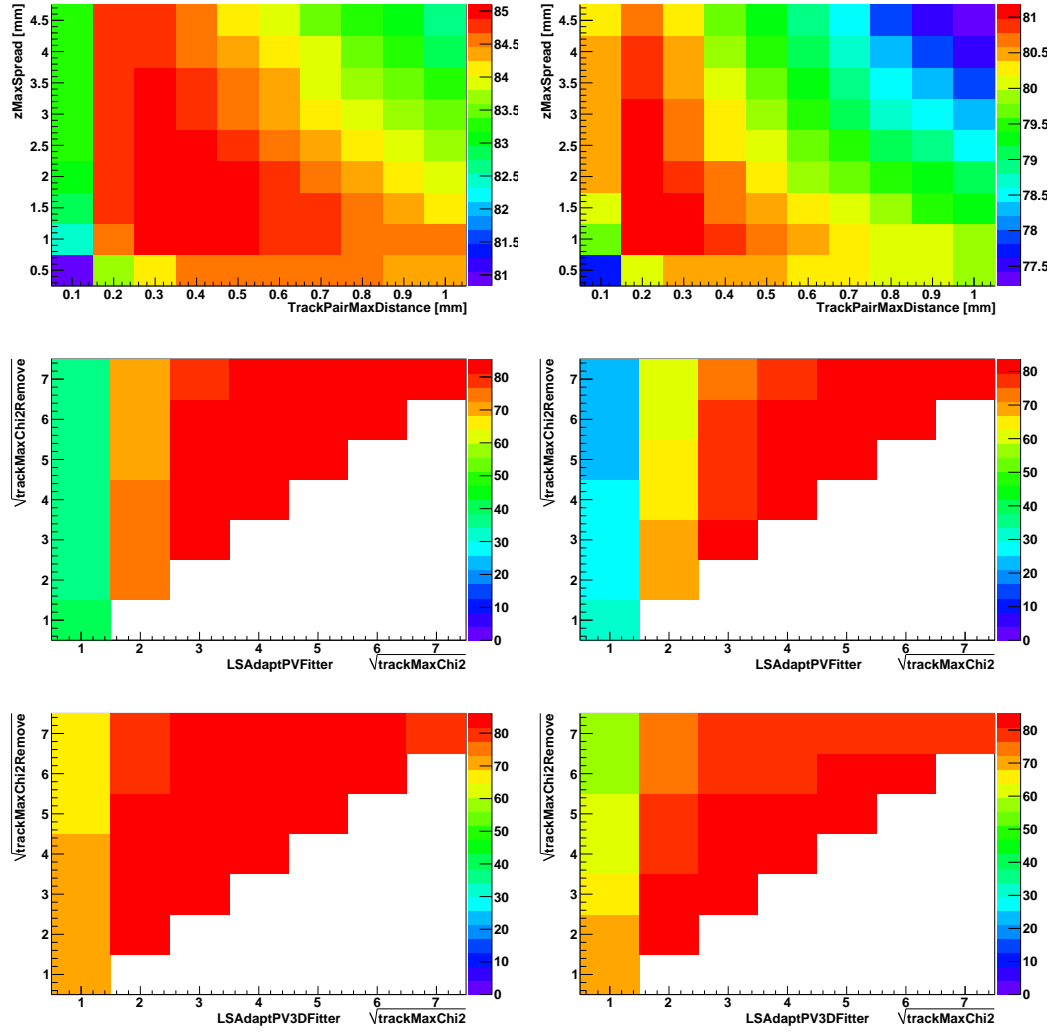


Figure 6.3: LLP MC candidate reconstruction efficiency for BV48 (*left*) and HV10 (*right*), as a function of some the reconstruction parameters.

6.2.2 Selection of the Primary Vertices

This section addresses the selection of the primary vertex candidates in general.

Figure 6.4 shows the position of the upstream “PV” from standard reconstruction from some data taken in early 2010. In the X-Y plots, we can see a peak corresponding to the beam line mean position. The width of the distributions are the results of the combination of the size of the beam line and the vertexing resolution. In this run, the mean X position is slightly shifted from the 0 position in the global frame. In the Z position plot, the distribution has a large tail towards negative z. As about 50% of the RVs in the tail come from beam-empty collisions, we can deduce that they are due to beam-gas interactions.

To reduce the effect of beam-gas, “PV” candidates are selected in the restricted region $|x|, |y| < 1.5 \text{ mm}$ and $|z| < 400 \text{ mm}$. These requirements are quite large to take into account that the beams move and change in size during and between the runs. The VeLo is expected to be re-aligned if the beams are radially moving more than $500 \mu\text{m}$.

A simple way to exclude beam-gas interactions from PVs is to request at least one backward and one forward tracks in the vertex. Beam-gas vertices have all daughter tracks in the same direction.

It is very important to select PVs with good resolution, especially when the upstream PV candidate is used as the reference to evaluate the proximity of a RV to the beam interaction region (see Sec. 6.2.3.a). If a reconstructed PV is radially shifted, it may cause another PV in the event to be selected as LLP.

It was found that the best and most simple way to remove PV candidates with large resolutions (and large x positions - they are in fact correlated, see Fig. A.10), is to request at least 10 tracks in the vertex, as can be seen in Fig. 6.6.

In the first months of 2010 data taking, the standard PV reconstruction was following a very loose policy to allow for some sidebands, asking for instance only for 2-3 tracks in the RV. In this case, the number of PVs per event was very large including several vertices with bad resolution and even not originating from the primary interaction. This was modified afterwards.

Table 6.1 shows the percentage of MC events with at least one DV candidate with $M > 3 \text{ GeV}$ that have the reconstructed (true) PV as a function of the minimum number of tracks. The condition “one backward and forward” tracks is also indicated. Results are shown for PVs taken from the standard procedure (STD) and our own optimisation (OPT). These numbers are essentially the same for all MC signal samples.

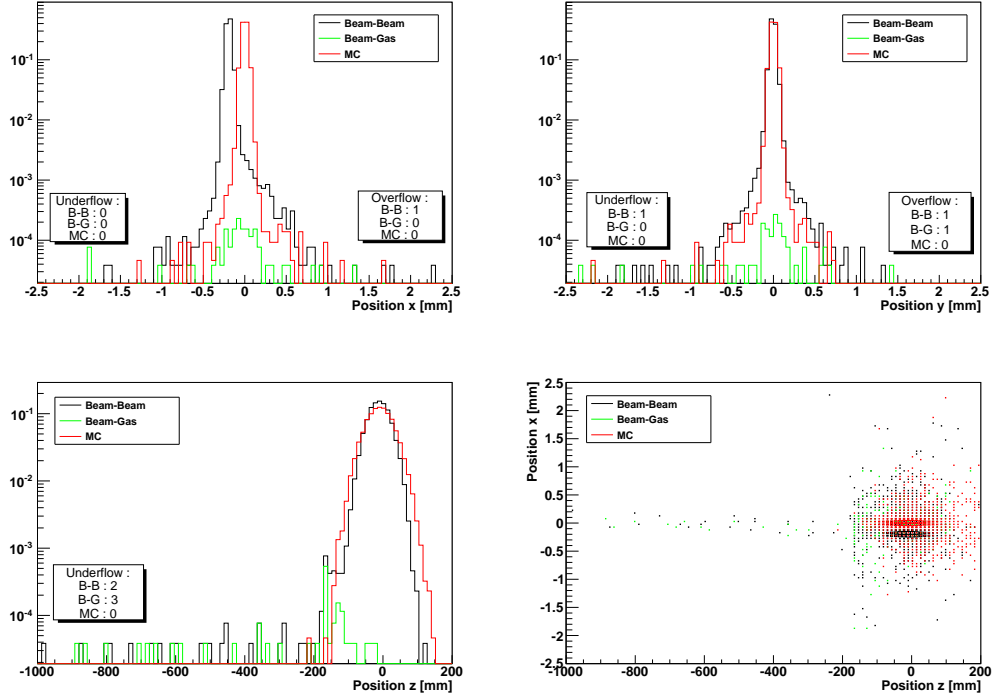


Figure 6.4: Position of the upstream PV from the standard reconstruction. Done on early 2010 data.

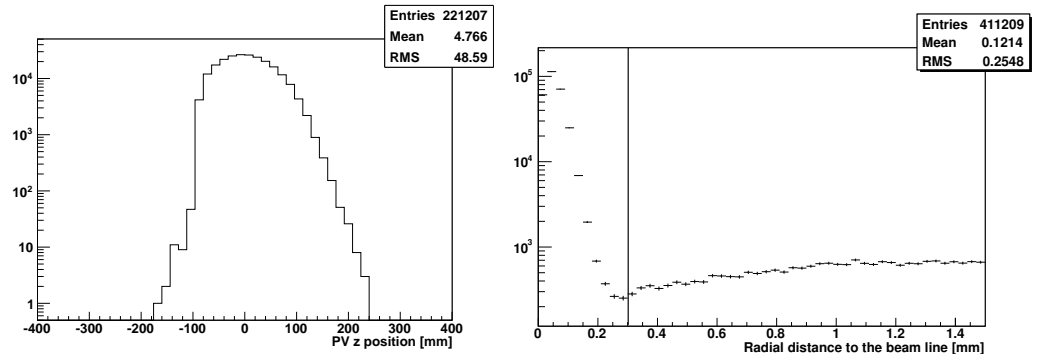


Figure 6.5: *Left* : longitudinal position of the PVs candidates. *Right* : radial position w.r.t. the calculated beam axis. The vertical bar indicates the regions considered for primary vertices, $r < 0.3$ mm.

	BF	NT ≥ 5	NT ≥ 10	NT ≥ 15	NT ≥ 20	BF+NT ≥ 10
STD	99.6%	100%	97.7%	91.2%	82.4%	97.6%
OPT	95.4%	100%	98.3%	93.1%	85.6%	94.8%

Table 6.1: Percentage of MC signal events with at least one displaced candidate with $M > 3$ GeV that have the reconstructed (true) PV fulfilling the requirements. Results for PVs from the standard procedure (STD) and our own optimisation (OPT). BF stands for at least 1 backward and forward track, while NT for number of tracks.

Our analysis is performed with PV candidates having at least 10 backward and forward tracks, from the standard procedure. Moreover, we keep only PVs that fit into a radius of 0.3 mm around the reconstructed beam interaction line (see Sec. 6.1.2). The value of the radius is justified by Fig. 6.7.

The Section A in the Appendix shows some general properties of these PV candidates.

6.2.3 Preselection and Selection of the LLPs

The undesirable vertices (background) come mainly from multiple pp collisions producing extra primary vertices, decays of SM long-lived particles (B, D,...) and vertices created by the interactions of a flying particle with the detector material or with gas residuals (mainly strong interactions of highly energetic pions, protons and neutrons).

6.2.3.a Primary Vertices

Primary vertices from pp collisions are forming the major part of the background and the easiest one to reject. The upstream RV is not taken by default, as it is either a PV or comes from the decay of a backward flying particle³. We also check that the candidates don't have any backward tracks as 95% of PVs have at least one backward track.

Then we remove any candidate that is close to the interaction region. Two methods are used to achieve this goal and are discussed here :

"FromBeamLine" applies a cut (R_{Min}) to the radial distance R to the beam interaction line (see Sec. 6.1.2). Figure 6.7 (*left*) shows the distribution of the radial distance of the RVs to the beam line. One backward track is

³This can be turned off (by setting *KeepLowestZ*=True) in the options. It is particularly useful for analysis of MC data from "particle guns", which do not possess any PV.

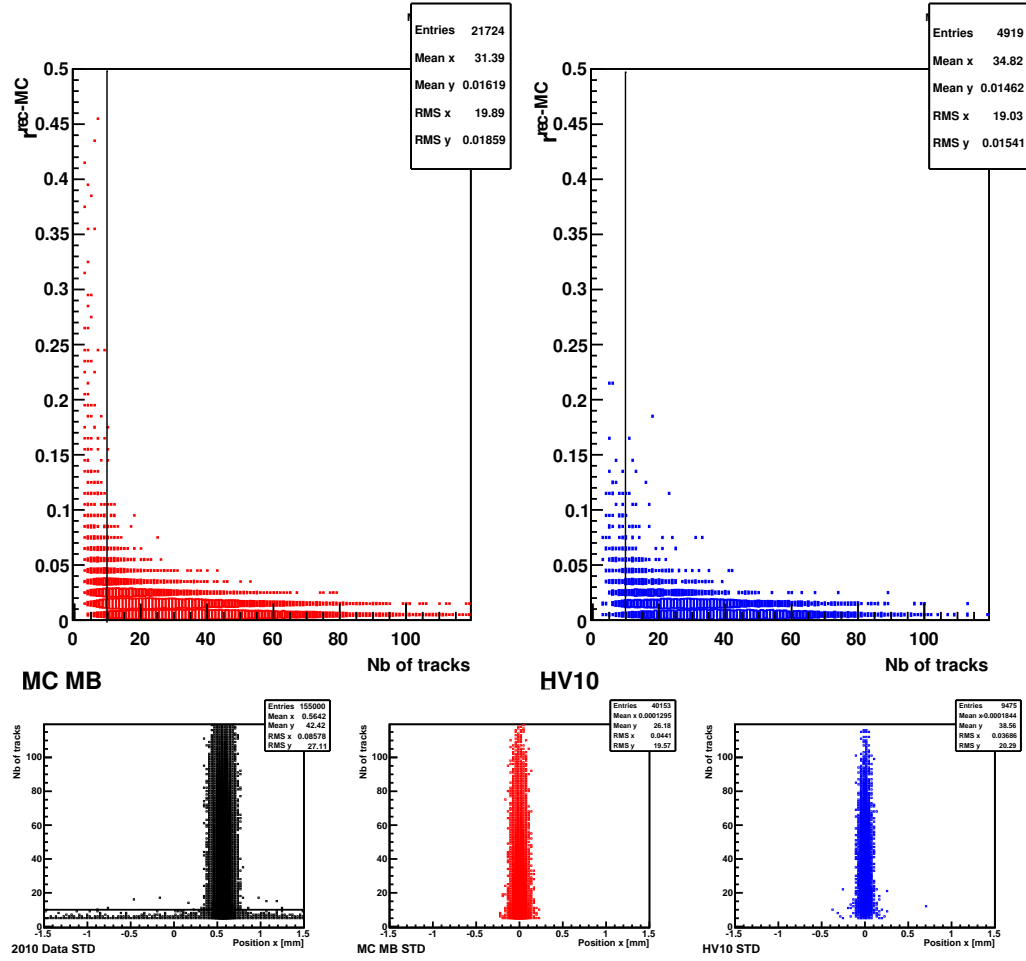


Figure 6.6: Radial distance between the reconstructed and MC-true position (*top*) and X position (*bottom*) of PVs with respect to the track multiplicity. Requesting at least 10 tracks in the vertex eliminates a vast majority of candidates with large r^{rec-MC} and radial positions (horizontal line in the data plot).

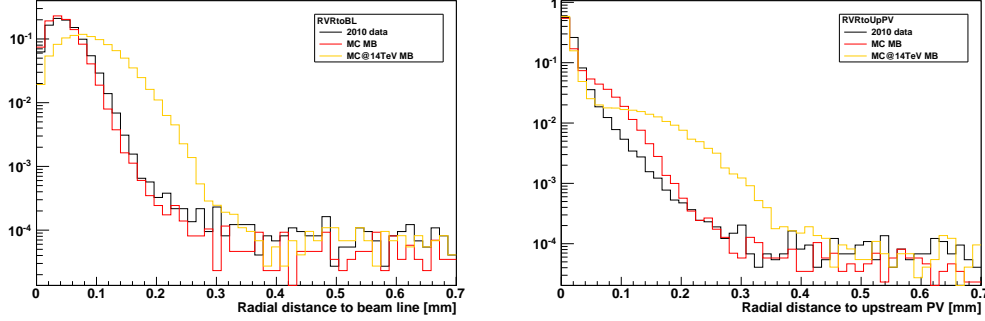


Figure 6.7: Radial distance of RVs to the beam line (*left*) and to the upstream PV (*right*). One backward track is requested on these RVs to identify them as PVs.

requested on these RVs to identify them as “PVs”. The vast majority of these PVs from the 2010 data can be rejected with $RMin = 0.3$ mm. For comparison, the plot also shows the distribution for MC minimum bias data at $\sqrt{s} = 14$ TeV and $\mathcal{L} = 2 \cdot 10^{32} \text{ cm}^{-2}\text{s}^{-1}$ (MC@14TeV MB). In this case, $RMin = 0.4$ mm should be considered at minimum.

”**FromUpstreamPV**” assumes that the upstream reconstructed vertex is a primary one and a radial cut $RMin$ is applied with respect to it.

This assumption is not true for the reconstructed vertices from our reconstruction scheme. The upstream primary vertex (upPV) could indeed be a backward flying long-lived particle from the Standard Model. In this case, the true PV could become candidate for a massive radially distant vertex, difficult to remove with simple cuts. This happens in $\sim 10\%$ of the events.

Therefore, the RV of reference is taken among the vertices reconstructed by the official PV reconstruction procedure.

The upPV is set as the upstream PV candidate from the selection presented in Sec. 6.2.2, but without the radial cut to the beam line. On MC data, the selected upPV is in 99.94% of the cases from a primary interaction.

Figure 6.7 (*right*) shows the distribution of the radial distance of the “PVs” from our reconstruction scheme to the upPV. Again, the vast majority of these PVs from the 2010 data can be rejected with $RMin = 0.3$ mm, while for data at higher luminosity - look at the distribution for MC@14TeV MB - one should consider applying tougher cuts, $RMin = 0.4 - 0.5$ mm.

A few effects explain the tails in both plots of Fig. 6.7. Firstly, the distribution of PV positions also shows a tail in the same proportion, of

$\mathcal{O}(10^{-3} - 10^{-4})$ ⁴. By looking into MC truth on simulated data, one can show that true reconstructed PV with radial position larger than ≈ 0.3 mm have a distance to the MC-truth of the same order. Various reasons due to the nature of the PV or its immediate environment may generate errors in the reconstruction. “Long-lived” SM particles may cause bias. Then there is the possibility to select a candidate as upPV that is not a “real” PV, for instance a vertex from a beam gas interaction. The presence of a long-lived SM particle is also not completely ruled out.

6.2.3.b Problem with LHCb MC Simulation

Figure 6.8 shows the position of the RVs in the X-Z plane for the 2010 data (*top*) and MC MB (*bottom*). We immediately notice the presence of RVs in the $z > 300$ mm and $R \sim \mathcal{O}(\text{mm})$ region in the MB plot, while nothing is visible in the 2010 data (Fig. 6.8, *top*).

After investigation, the following explanation was found. The vacuum tank inside the VeLo is simulated with air at 1 atm. This is due to the way the VeLo geometry needs to be passed to GEANT in order to accommodate open and close position. What we see in the MC MB plots are interactions of particles from the simulated pp collisions with air.

A very simple recipe has been used to identify these spurious interactions, by using the GEANT information which tags interactions with matter. When the interaction does not belong to any solid part of the detector, it is identified as interaction with air.

The effect of this filter is shown in Fig. 6.9. Particularly in the right plot, one can see the drastic reduction of the discrepancy. To get an order of the reduction, the filter removed 21.6% of the candidates with $m > 6$ GeV, nb of tracks ≥ 6 and $r > 0.3$ mm, in the MB sample. We see that the corrected MC distribution well matches the data.

The remaining vertices at $r \sim 0$ are due to a failed association of the reconstructed vertex with its MC counterpart.

We have tested and found that this procedure does not affect the analysis of MC signal.

6.2.3.c Particle-gas Interactions

As a “spin-off” of the previous section, we can perform a rough estimation of the rate of interactions of flying particles with the gas inside the vacuum tank, leading to a LLP candidate.

⁴This is true for both procedures : the standard one and the optimised one for all RVs. The resolution is a bit larger for the latter.

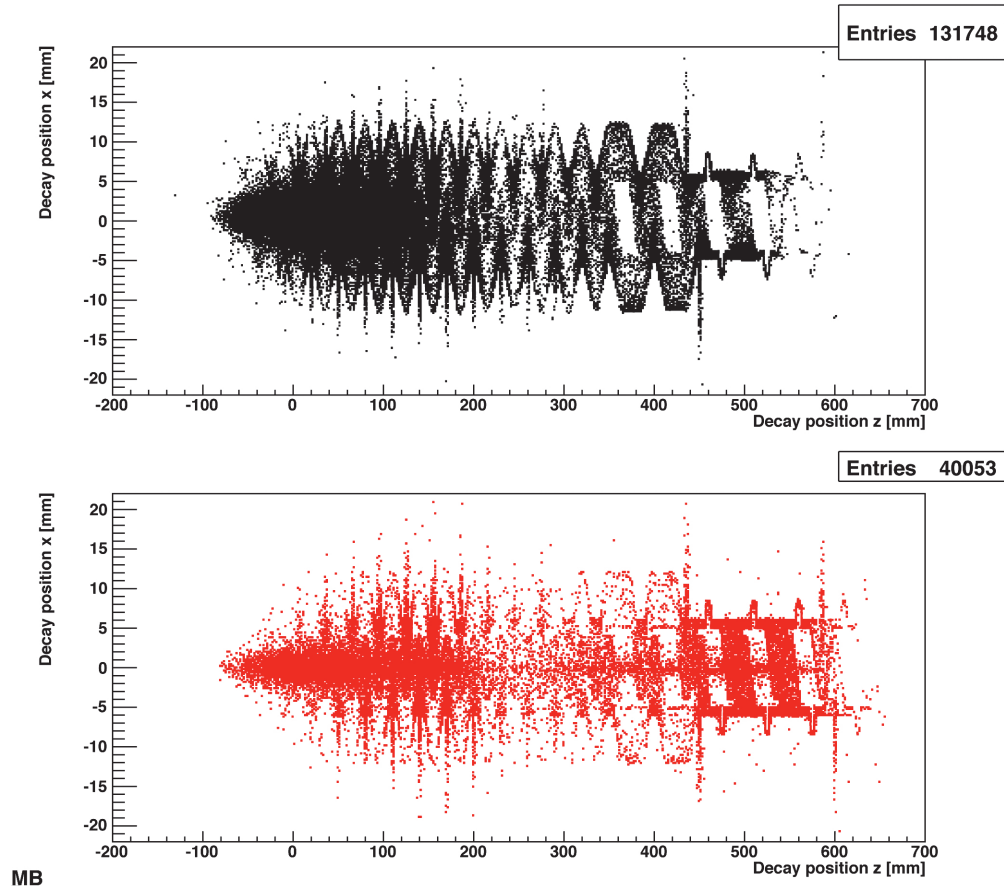


Figure 6.8: Positions of the RVs in the X-Z plane for the 2010 data (*top*) and MB (*bottom*). Note the excess of RVs at large z and $r \sim 0$ mm in the MB sample.

The “vacuum” in the simulation is at 1 Atm, which is $2.7 \cdot 10^{19}$ molecules/cm³, while the pressure in the LHC is about 10^{-10} Torr or $3.5 \cdot 10^6$ molecules/cm³. From this we can deduce that the probability to have such an interaction is lower by factor of $F \sim 10^{-13}$ in the real experiment than in the simulation.

The filter for particle-gas interactions mentioned above selects about 2000 events (N_{MB}^{sel}), with at least one candidate ($m > 6$ GeV, nb of tracks ≥ 6 and $r > 0.3$ mm) on a MB sample of $N_{MB}^{tot} = 69$ M events ($\nu = 1$). Note that this sample has been simulated with a mean interaction per bunch crossing $\nu = 1$.

This allows to estimate the number particle-gas event (N_{PG}) in the 2010 data for those cuts :

$$N_{PG} = N_{MB}^{sel} \times \frac{\sigma_{MB} \cdot L}{N_{MB}^{tot}} \times F \quad (6.2)$$

$$= 2000 \times \frac{3.4 \cdot 10^{12}}{69 \cdot 10^6} \times 10^{-13} \ll 1. \quad (6.3)$$

Even if we correct this relation to account for the higher ν in the real data (~ 2.5), this number is much lower than zero. However, this computation supposes that the GEANT simulation can be fully trusted and the vacuum is as deep as expected.

6.2.3.d Interactions with Detector Matter

Vertices from the interactions of particles with the detector material are forming a very “interesting” part of our background.

Figure 6.8 shows the positions of the reconstructed vertices in coordinates X versus Z in the laboratory frame, for both the 2010 data and MB MC. This distribution compares well with the description given by the LHCb database (see Fig. 6.10), the RF-Foil and the sensors, presented in Sec. 2.3.2.a and in Fig. 2.10, are clearly identifiable.

A total of 1 million e^\pm , π^\pm , p, n have been injected into the LHCb acceptance with $p \in [1, 10^3]$ GeV at generator level and underwent the full simulation chain, a process called particle gun (PG). Events with at least one reconstructed vertex with $M > 1$ GeV and nb of tracks > 4 have been selected (referred as PG).

By looking at the MC truth, only the protons, neutrons and pions created a displaced vertex. Some deuterium, tritium and α particles were seen. In addition, some strangeness was produced, e.g. Kaons, Σ^0 , Σ^\pm ($c\tau = \mathcal{O}(1)$ cm), Λ^0 ($c\tau = 7.9$ cm), but no heavy flavour. It should be noted, however, that it

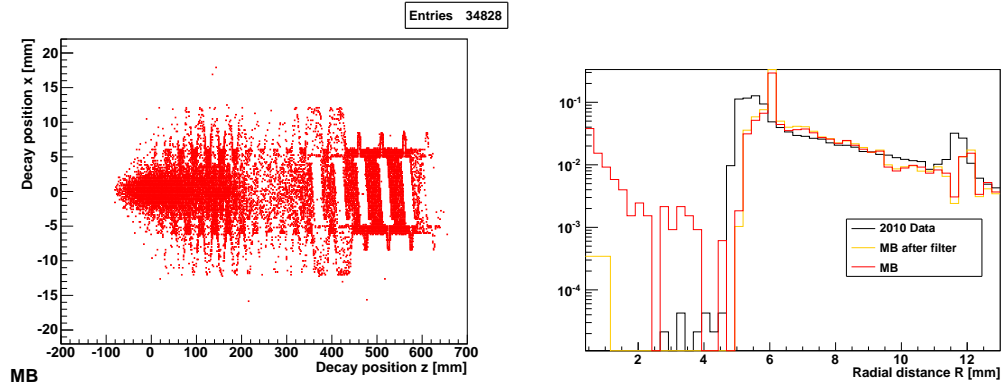


Figure 6.9: *Left*: positions of the RVs in the X-Z plane for the MB after a filter to remove the RVs from interaction with air in the vacuum tank. *Right*: radial distance of the RVs to the beam line, for $z > 300$ mm.

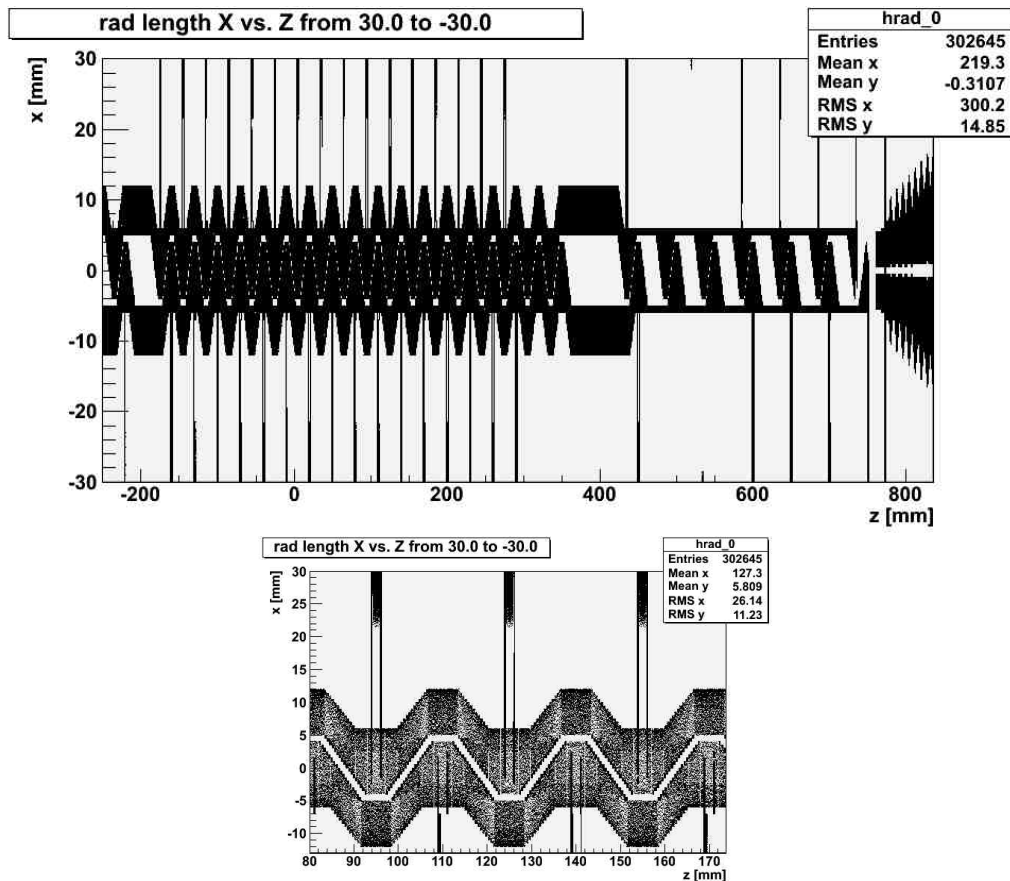


Figure 6.10: Material distribution as described in the LHCb database in the X-Z plan, integrated over $y \in [-30, 30]$ mm.

was reported that one J/ψ has been reconstructed in the 2010 data in the detector region.

From the million particles shot, 3388 vertices were reconstructed with mass greater than 9 GeV and nb of tracks > 8 . Those vertices show the same reconstructed mass distribution than the one of the $\tilde{\chi}_1^0$ from the BV48 model (see Fig. F.2, *bottom*, in the appendix). A few tens of PG events present 2 RVs, coming either from the decay of long-lived particles produced by the first interaction, or from one of the highly energetic daughters interacting later with the matter of the detector.

To sort this background from the decay of LLPs, several strategies were tested. Requesting the reconstructed vertex to point towards a PV asks for the perfect recognition of the PV, from which the interacting particle came from. This is far from trivial. What is more, the IP distributions of the LLPs are very large, causing such a cut to be quite inefficient.

Using the conservation of the baryon number also proved to be inefficient, due to the loss of many decay products outside the acceptance. Other cuts based on the structure of the jets produced, their particle (flavour) content, were left aside : at this stage, we want the selection to be as inclusive as possible.

The only satisfactory solution is resorting to a geometrical cut. A few methods were investigated and are included in the preselection and selection algorithms.

RemVtxFromDet=1 the candidate is eliminated if found to be in a material region. This method is affected by the position resolution and the precision of the description of the detector in the database.

RemVtxFromDet=2 the radiation length (X_0) $\pm DetDist$ [mm] along the reconstructed momentum is computed using the material information from the database. If X_0 is more than 10^{-10} , the vertex is considered to come from a secondary interaction of a flying particle with the detector material. For information, $X_0^{\text{vacuum}} \sim 10^{-(28-30)}$ and $X_0^{\text{matter}} \sim 10^{-(3-5)}$ for $DetDist \in [0.01, 1]$ mm.

RemVtxFromDet=3 or 4 Basically the same idea as for *RemVtxFromDet=2*. The radiation length is computed along each opposite edges of the error covariance matrix of the RV position times *DetDist*. A further factor of 5 has been added in the radial measurements to match the order of the observed discrepancy between the measured RF-Foil position and its description. If *RemVtxFromDet=4* and if the position to test in the RF-foil

area, a factor 3 is added to $DetDist$. This didn't help to improve the method, though.

So far, these methods rely on the material information given by the detector description database. This implies that the database is up-to-date and the position of all detector pieces are known with great precision. While this is true for the sensors, whose positions are known from the alignment procedure, the true position of the RF-foil - a big contributor to the radiation length - remains approximate.

RemVtxFromDet=5 defines a home-made rough description of the RF-Foil topology [119]. As the VeLo halves may be moved during a run to follow the beams, the algorithm re-align the RF-Foil with respect to the sensors, whose positions are always well-known and kept updated at run time in the database.

Figure 6.11 shows the positions of the RVs in the X-Z plane for the 2010 data (*left*) and MB (*right*) that are left after the cut. The internal part of the simulated RF-Foil is done by several cylinders of different diameters to “follow” the corrugation of the RF-Foil. This leaves a visible structure. There also seems to be some interactions with the sensors that are not removed. Finally, some vertices can escape this cut due to a large error on the reconstruction. Work is being done to improve the representation of the RF-Foil and understand all the discrepancies.

More figures of the positions of RVs from the PG samples and of the candidates from 2010 data removed from the matter veto are found in the Appendix. A full scan in longitudinal slices of the RF-Foil fiducial region can be viewed in [117].

Table 6.2 sums up the efficiency of some of the different matter veto methods on the 2010 data, MC-truth LLP candidates and, in parenthesis, for the vertices created by interaction with matter in the MC samples. The candidates are selected with $m > 5$ GeV, nb of tracks ≥ 5 and $r > 4.8$ mm, where the RF-Foil fiducial region begins. As expected, *RemVtxFromDet=5* is the most efficient method on real data. However, LLPs decaying after $r > 4.8$ mm are reduced greatly by this filter.

For the remainder of the study, method 5 will be used as the default, and just called *the* “matter” or “detector veto” when used.

6.2.3.e SM LLPs and other Cuts

The best way to remove long-lived SM particles is to cut on the number of tracks $MinNbTrks$ in the decay vertex and on the reconstructed mass $MinMass$, although the mass is estimated only from the charged decay products.

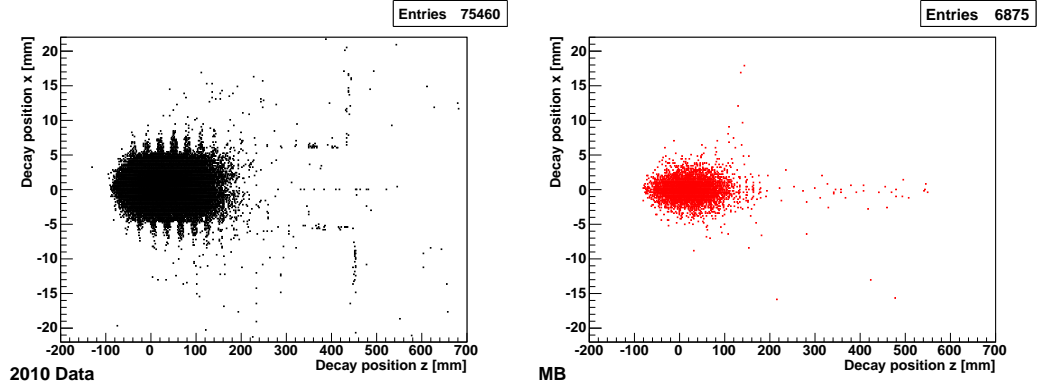


Figure 6.11: Positions of the RVs in the X-Z plane for the data (*left*) and MB (*right*) after the matter veto.

Model	2	3	5
2010	38.3	76.5	97.7
BV48	24.3 (83.8)	28.9 (97.3)	74.4 (94.6)
HV10	23.6 (84.4)	57.2 (93.8)	71.6 (96.9)

Table 6.2: Retention of candidates of the different methods to remove RV from interaction with matter. For the MC samples, the retention is given for the MC-truth LLP candidates and in parenthesis for the vertices created by interaction with matter. The candidates are selected with $m > 5$ GeV, nb of tracks ≥ 5 and $r > 4.8$ mm.

Concerning *MinNbTrks*, the philosophy is to not go beyond 4-5 tracks, the maximum a SM particle decay may generate, for the reasons already stated in Sec. 6.2.1. The focus was therefore more on the mass (*MinMass*), where most models show large mass distribution for their signal candidates.

A general feature of the decay of exotic particles is the generation of very high p_T tracks. A threshold (*MinSumpt*) on the scalar p_T sum of all the tracks in the vertex is also applied with some gain despite its strong correlation to the mass.

A cut on the total charge in the vertex has also been tried. However, due to the tracks lost, the distributions for the neutral exotic LLPs are very broad, and any cut of this kind didn't help to segregate the signal from the different kind of background.

A candidate RV may be requested to be spatially isolated from the other RVs by setting a parameter (*IsolationDistance*) to the desired isolation distance. It is unset by default.

At this stage of the selection, all cuts implying an association between the candidates and their respective PV, like the corrected mass (see Sec. 7.2), have been discarded.

A global event cut on the total transverse energy in the calorimeters E_T has been tested, but was found mildly useful only for events with $\nu \approx 1$ interaction per bunch crossing. As $\nu \approx 2.5$ in the 2010 data, this cut was not considered.

In conclusion, we have set $MinNbTrks = 4$, $MinMass = 3 \text{ GeV}$ and $MinSumpt = 3 \text{ GeV}$.

	Optimised	Standard
PVSeed3DTool		
<i>MinCloseTracks</i>	3	4
<i>TrackPairMaxDistance</i>	0.2, 0.3 mm	0.3 mm
<i>zMaxSpread</i>	1, 3 mm	3 mm
LSAdaptPVFitter		
<i>MinTracks</i>	4	5
<i>trackMaxChi2</i>	9, 16	9
<i>trackMaxChi2Remove</i>	25, 49	25
LSAdaptPV3DFitter		
<i>MinTracks</i>	4	5
<i>trackMaxChi2</i>	9	9
<i>trackMaxChi2Remove</i>	25	25
<i>maxIP2PV</i>	2 mm	2 mm

Table 6.3: Summary of the parameter values of the Standard and Optimised vertex reconstruction procedure.

6.2.4 Back to the Optimisation of the Reconstruction

Once the basic ideas of the selection have been laid out, the optimisation process was repeated, following the same protocol, and using the same criteria and samples as in Sec. 6.2.1, but applied on the selection of RVs with a reconstructed mass $M > 6 \text{ GeV}$ and a radial distance to the z axis $R > 0.3 \text{ mm}$.

The details of the optimisation process can be found in Chap. C in the Appendix. Table 6.3 sums up the values of the parameters of the standard PV procedure and the one obtained for the procedure optimised for displaced vertices.

6.2.5 Vertex Reconstruction Efficiency

This section discusses the signal reconstruction efficiency of an LLP vertex after the optimisation.

For the sake of simplicity, only the plots for the BV48 model are presented, similar conclusions can be drawn for the other models.

Figure 6.12 (*left*) shows the efficiency to reconstruct MC “reconstructible” LLPs with respect to their z decay position, for different criteria of “reconstructibility”, given here with their nickname, based on MC-truth :

- `pinacc` : LLP in acceptance, from MC-truth,
- `4trks` : at least 4 MC-truth stable charged daughters inside acceptance,
- `4rectrks` : at least 4 MC-truth daughters that are “reconstructible”, i.e. that are crossing 3 VeLo stations.
- `4asstrks` : at least 4 MC-truth daughters that have associated tracks after the reconstruction,
- `4assvelotrks` : at least 4 MC-truth daughters that have associated tracks with Velo segments.

(The 4 in front is a parameter.) By MC daughters we mean MC stable charged daughters produced at the decay vertex.

First thing to note is the capability to reconstruct vertices up to $z \sim 500$ mm. However, one also sees that the ability to reconstruct a LLP that was produced inside the LHCb acceptance cone drops sharply after $z \sim 100$ mm and only a tiny portion of them can be reconstructed.

For convenience, the efficiency is presented only with respect to the z decay position, integrated in r . A drop in efficiency for large z is often due to the candidate to be outside the VeLo in the radial direction.

The shape of the “`4rectrks`” depends on the efficiency to reconstruct the tracks and will be later explained.

By default, we have chosen the criterion of “reconstructibility” to be `4assvelotrks`. We will now refer to the efficiency as the ability to reconstruct vertices that are reconstructible according to this criterion. Figure 6.12 (*right*) shows the efficiency for the various reconstruction parameters presented in Table 6.3. The difference are in general small, about 5%.

The efficiency is somehow lower ($\sim 10\%$) in the luminous region, because vertices corresponding to too short lifetime may not be reconstructed due to the presence of the PV.

Figure 6.13 (*left*) gives an insight to the reconstruction efficiency for the various scenarios presented in Table 6.3 with respect to the distance of flight from MC-truth. One reason for having non-zero efficiencies for distances close to 0 is due to the fact that the associated RV may be produced by the decay of a long-lived daughter.

Figure 6.13 (*right*) shows for the “reconstructible” RV candidates the statistics of successfully reconstructed RV (in black). The failed reconstruction are in red. There is no indication of some “dead” region, where the reconstruction systematically fails.

We consider now all signal RV candidates which are known from MC-truth to have at least 4 daughter tracks in the acceptance.

Figure 6.14 (*left*) shows the percentage of reconstructible MC daughters having an associated track of type Velo, Upstream or Long, and Long only, with respect to the true z decay position.

We can note drops in efficiency in the z range $[50, 200]$ mm and further away at $z > 300$ mm. This is likely due to the absence of sensors in the range $z \in [289, 434]$ and $[451, 586]$ mm (left VeLo half⁵) and $z \in [291, 436]$ and $[449, 584]$ mm (right VeLo half⁶).

Figure 6.14 (*right*) shows the percentage of non-reconstructible MC-truth daughters having an associated downstream track, with respect to the true z decay position.

Figure 6.15 shows the proportion of the type of the tracks that gets associated to the daughters of the LLPs. If the Long tracks clearly dominate in the luminous region, they are then slowly overtaken by the downstream tracks, which in turn decrease till the T stations to the benefit of T tracks.

Figure 6.16 is the same as Fig. 6.15, but for the LLPs whose decay vertex has been found by the final analysis. For decay positions after $|z| \gtrsim 150$, we note that the downstream tracks make a appreciable proportion of the tracks.

6.2.6 Perspective

As already stated in Sec. 6.1.1, the reconstruction process works only for tracks that have segments in the VeLo, that is to say Long, Upstream and

⁵Left VeLo sensor z positions (-x): -176 -159 -144 -131 -116 -99 -84 -71 -56 -39 -24 -11 4 21 36 49 64 81 96 109 124 141 156 169 184 201 216 229 244 261 276 289 434 451 586 599 634 651 686 699 734 [mm].

⁶Right VeLo sensor z positions (+x): -174 -161 -146 -129 -114 -101 -86 -69 -54 -41 -26 -9 6 19 34 51 66 79 94 111 126 139 154 171 186 199 214 231 246 259 274 291 436 449 584 601 637 649 684 701 736 [mm].

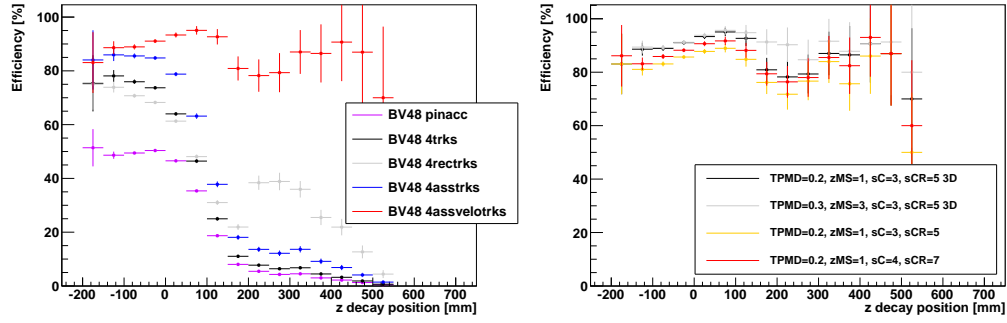


Figure 6.12: MC LLP reconstruction efficiency with respect to the true z decay position, for different criteria of “reconstructibility” (*left*). The right plot shows the efficiency when varying several vertex reconstruction parameters).

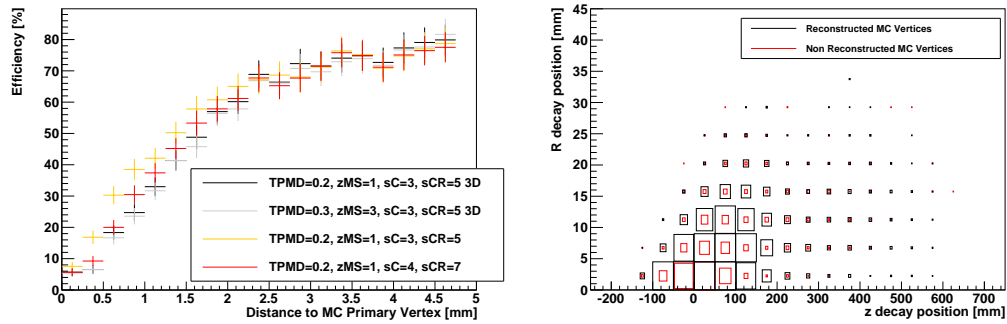


Figure 6.13: *Left* : MC LLP reconstruction efficiency w.r.t. the distance to the MC PV, for different reconstruction scenarios. *Right* : Z and radial positions of reconstructed and not reconstructed “reconstructible” candidates.

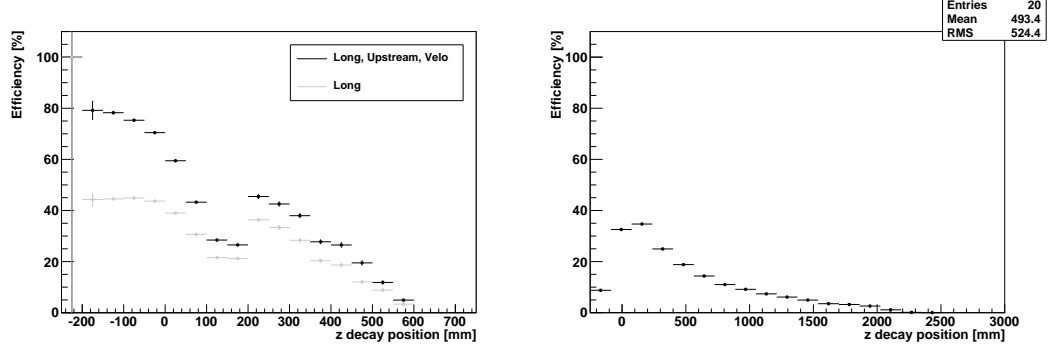


Figure 6.14: *Left* : percentage of reconstructible MC daughters having an associated track of type Velo, Upstream or Long, and Long only, with respect to the z decay position. *Right* : percentage of non-reconstructible MC daughters having an associated downstream track with respect to the z decay position.

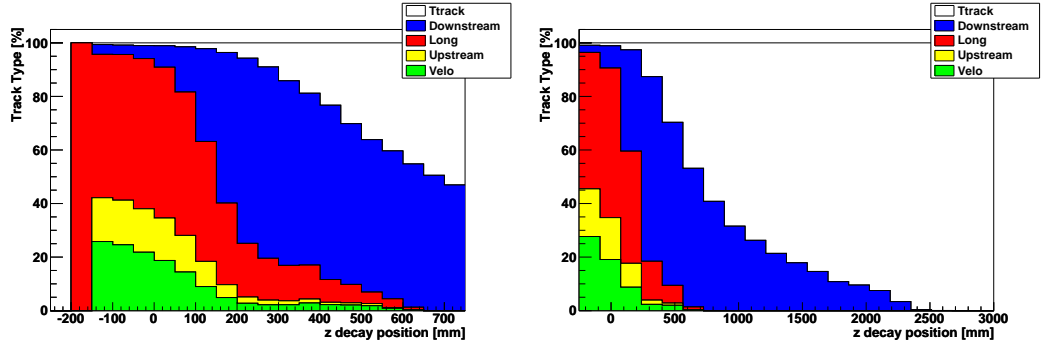


Figure 6.15: *Left* : type of the tracks associated to the daughters of reconstructible MC candidates. *Right* : idem on an extended region.

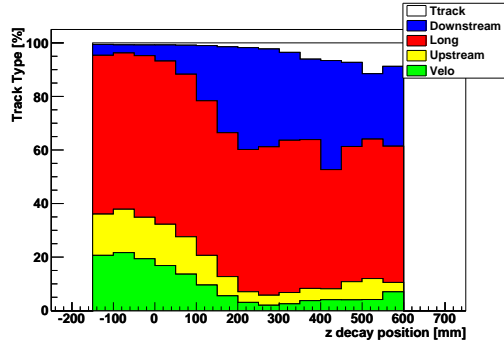


Figure 6.16: Like Fig. 6.15, but limited to tracks associated to a LLP which has been reconstructed.

Velo tracks, and thus limited to decay positions $|z| \lesssim 500$ mm. The proportion of reconstructible tracks decreases fast outside the luminous region.

Figure 6.17 shows the number of downstream tracks that are associated to daughters of LLPs (*left*), and with an associated RV (*right*). Comparison with Fig. 6.16 shows the importance of adding downstream tracks to exploit the $z \in [200, 500]$ mm region.

Table 6.4 presents two kinds of numbers. First, it shows the percentage of the MC daughter particles associated to a downstream track that have at least a certain number of associated clusters in the VeLo. In a second part, we extrapolate these downstream tracks to the various VeLo sensors and count the number of clusters that have a distance $\chi^2 < 2$ ($\sim 30 \mu\text{m}$). This is done for all LLPs and the ones with an associated RV.

In this section we have addressed the potential to reconstruct distant vertices within the VeLo sub-detector. Outside the VeLo region, a method to reconstruct the decay vertices from the downstream tracks remains to be developed. Even though, downstream tracks have a reduced resolution, the track environment is less crowded than in the VeLo.

In-between, there is a wide range in which the reconstruction efficiency could be enhanced by the use of the downstream tracks. A general method would be to reconstruct vertices with a very low track multiplicity requirement (2-3 tracks) and extrapolate the downstream tracks up to the RV. If more than a certain number of consecutive clusters are found at a very small distance, the track may be “updated” with the new states and added to the RV. Table 6.4 tells us it ought to be tried.

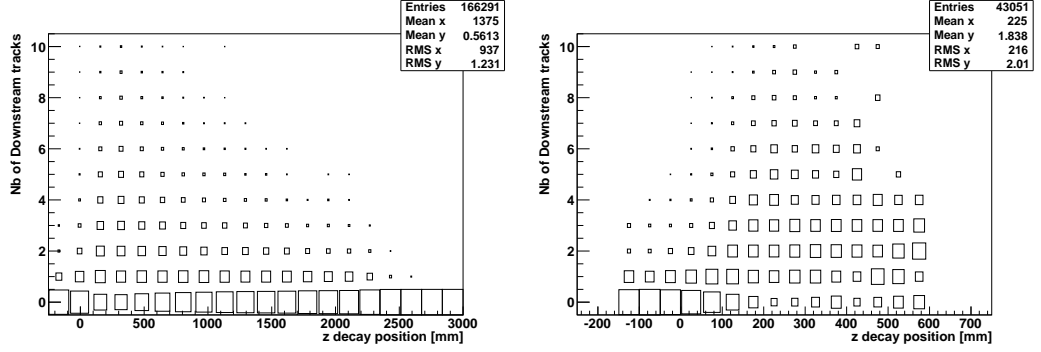


Figure 6.17: *Left* : number of downstream tracks that are associated to daughters of LLPs. *Right* : Same, but for LLPs with an associated reconstructed vertex.

	BV48	BV48_500	HV10	HV100
% MC w 2-5 VC ¹	15.2	15	4.8	19.5
% MC w ≥ 5 VC	76.4	22.8	94.4	29.7
% Trk w 2-5 VC ²	39.7	30.5	39.7	24
% Trk w ≥ 5 VC	30.4	18.5	42.6	18.3
For MC LLPs with an associated RV				
% MC w 2-5 VC	5.6	12.4	1.4	6.7
% MC w ≥ 5 VC	94.1	87.2	98.4	92.8
% Trk w 2-5 VC	47.2	46.9	41.8	39
% Trk w ≥ 5 VC	40.7	36.0	48	39.6

Table 6.4: 1: percentage of the MC daughter particles associated to a downstream track that have between 2 and 5 associated VeLo clusters (VC).

2: percentage of these downstream tracks that are associated to 2 to 5 VeLo clusters ($\chi^2 < 2$).

6.3 Properties of the Selected LLP Candidates from MC Studies

We present in this section the properties of the selected LLP candidates for all considered models.

We recall here the applied preselection :

- at least one PV candidate, as described in Sec. 6.2.2 :
 - at least 10 tracks
 - at least one forward and one backward track
 - a radial distance to the reconstructed beam position not larger than 0.3 mm
- at least one LLP candidate with :
 - 4 forward tracks, no backward tracks
 - a distance to the beam line of more than 0.3 mm
 - an invariant mass of at least 3 GeV

Figures 6.18 to 6.29 presents the topology and kinematics of some of the theoretical models.

Figure 6.22 shows the p_T distribution of the muon with highest p_T in the RV. The absence of muon is marked with a $p_T = 0$. Requesting a muon with $p_T > 5$ GeV (20 GeV) produces a drop on the acceptance of candidates of the BRpVmuq model with $m > 6$ GeV, nb of tracks > 6 , $r > 0.3$ by 27.7% (54%). Due to the insufficient number of expected MC events for the BRpVmuq model, the search for an exotic LLP containing a high p_T muon has been left aside for the moment.

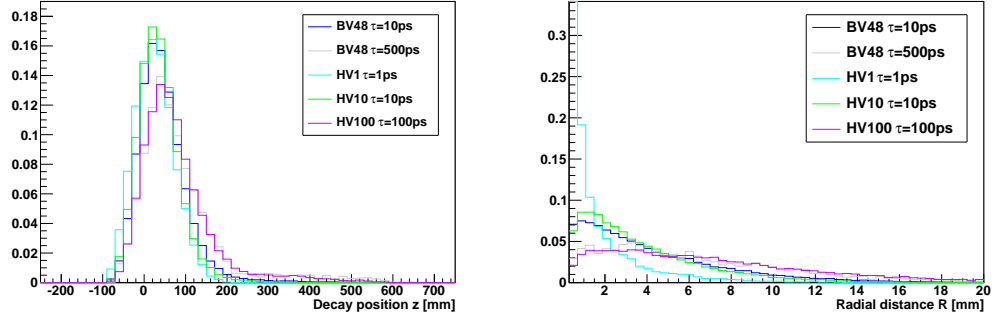


Figure 6.18: Z positions (*left*) and distance to the beam line (*right*) of the candidates of some of the selected models.

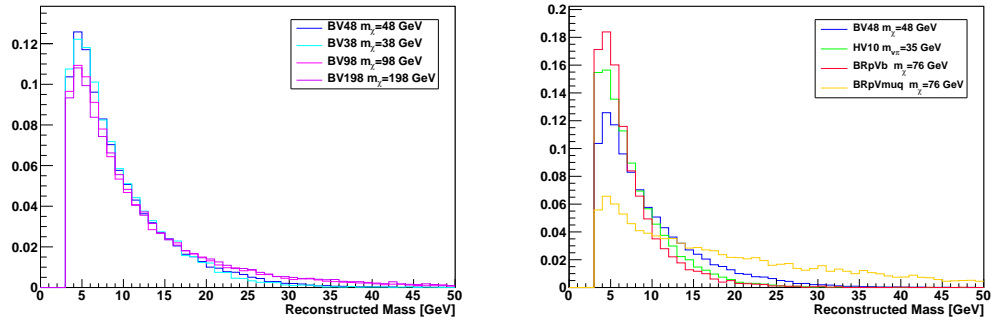


Figure 6.19: Reconstructed mass for some of the selected models.

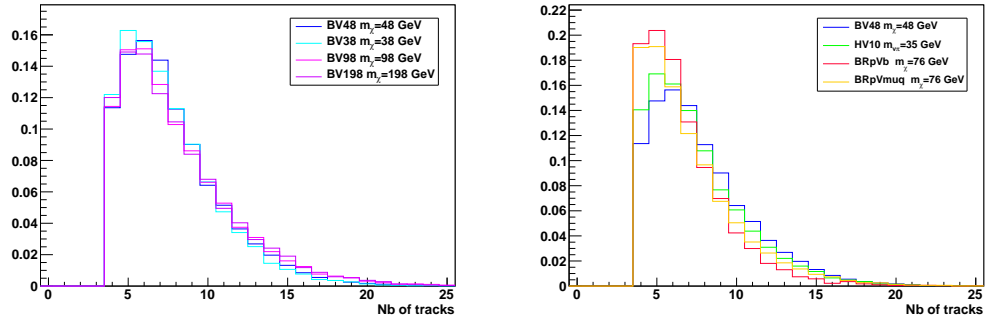


Figure 6.20: Nb of tracks in the vertex for some of the selected models.

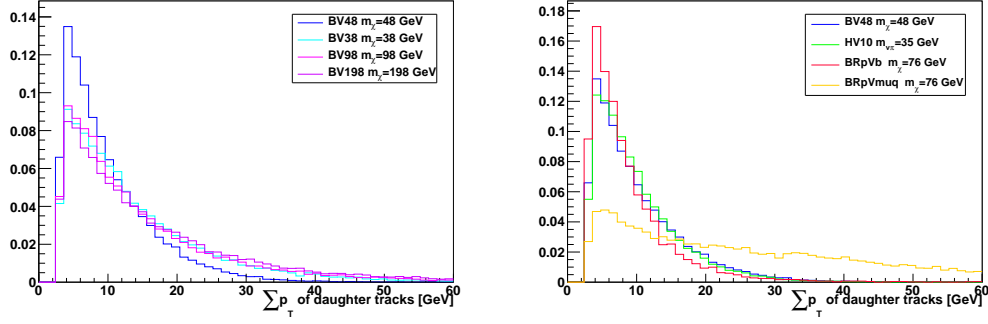


Figure 6.21: Sum of the scalar p_T of the daughter tracks for some of the selected models.

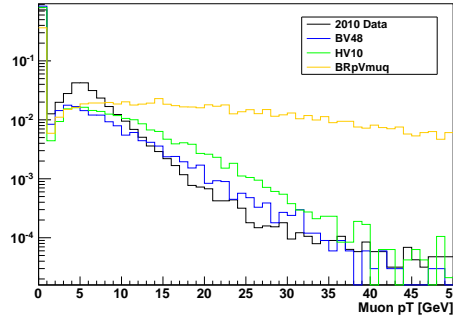


Figure 6.22: p_T distribution of the muon with highest p_T in the RV. The absence of muon is marked with a $p_T = 0$.

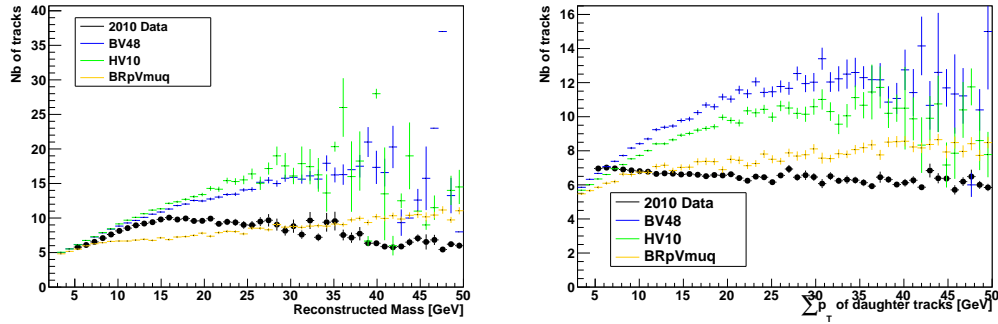


Figure 6.23: *Left* : correlation between the reconstructed mass and the number of tracks for 2010 data and some MC models.

Right : correlation between the sum of the scalar p_T of the daughter tracks and the number of tracks for 2010 data and some MC models.

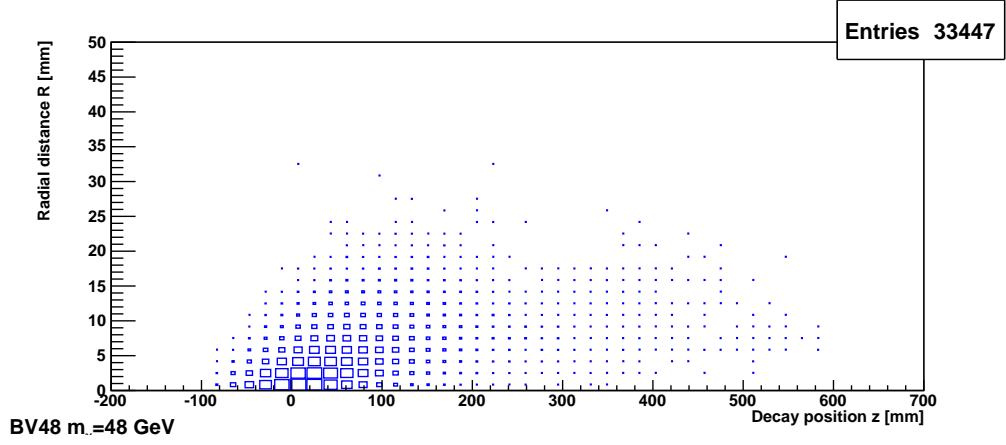


Figure 6.24: Scatter plot the radial and longitudinal positions of the reconstructed vertices for the BV48 models ($\tau_{\tilde{\chi}_1^0} = 10$ ps), to be put in contrast with Fig. 6.8.

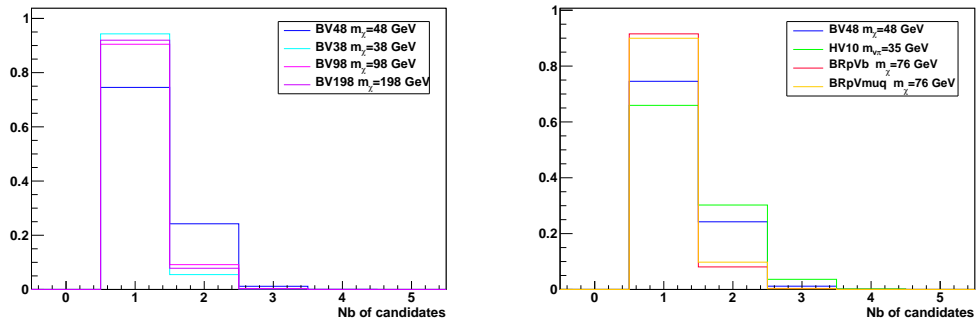


Figure 6.25: Number of candidates per event for some of the selected models. BV48 and HV10 models, featuring a h^0 decaying into 2 LLPs, have a larger distribution.

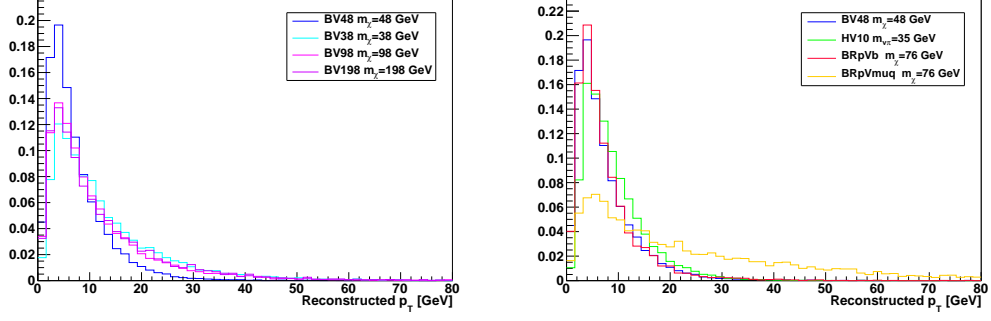
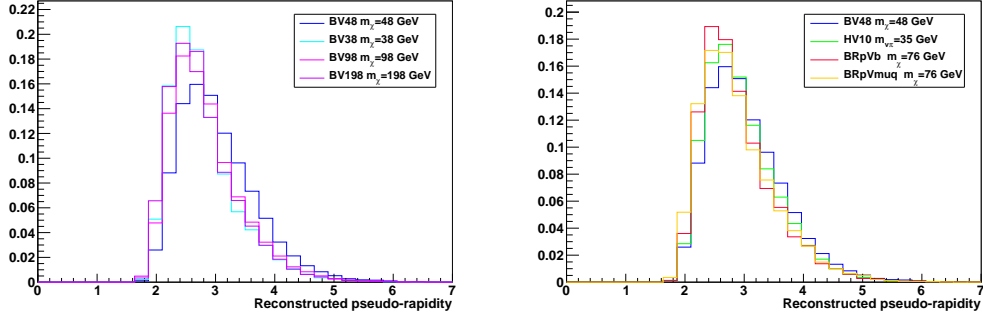
Figure 6.26: Reconstructed p_T for some of the selected models.

Figure 6.27: Reconstructed pseudo-rapidity for some of the selected models.

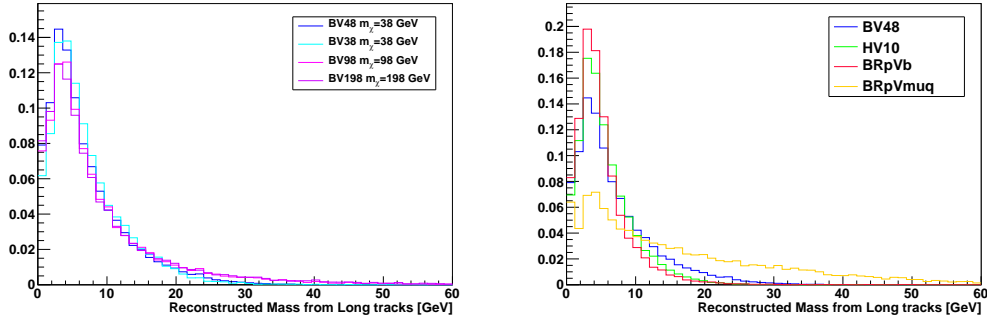


Figure 6.28: Reconstructed mass from the Long tracks only, for some of the selected models.

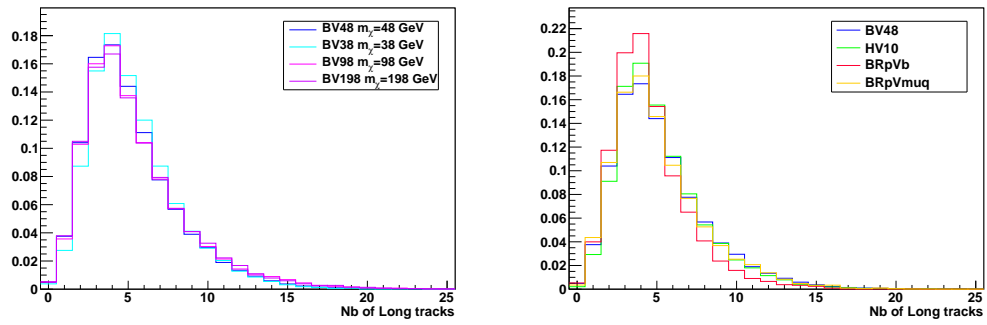


Figure 6.29: Number of Long tracks at the vertex for some of the selected models.

Name	Prescale	Cuts
Hlt2SinglePSLonglived	0.01	≥ 1 DV, $N_{min}^{track} = 4$, $M_{min}^{LLP} < 4.5$ GeV, $\sum_{min} p_T > 4.5$ GeV
Hlt2SingleLonglived	1	≥ 1 DV, $N_{min}^{track} = 5$, $M_{min}^{LLP} > 6$ GeV, $\sum_{min} p_T > 6$ GeV, $\sigma_r^{max} = 0.1$ mm and $\sigma_z^{max} = 1$ mm
Hlt2DoubleLonglived	1	≥ 2 DV, $N_{min}^{track} = 4$, $M_{min}^{LLP} > 1.5$ GeV, $\sum_{min} p_T > 3$ GeV, $\sigma_r^{max} = 0.1$ mm and $\sigma_z^{max} = 1$ mm

Table 6.5: Cuts of the HLT2 DisplVertex lines (TCK 0x002e002a and 0x002e002c). Additional cuts on the square root of the radial and z component of the position error matrix were set : $\sigma_r^{max} = 0.1$ mm and $\sigma_z^{max} = 1$ mm.

6.4 Trigger and Stripping

Results from the previous Sections have been used to design trigger⁷ and stripping selections.

Three “lines” of trigger have been written :

- two lines specialised for single LLP, from which one with weak cuts, prescaled, for efficiency studies and cross-checks.
- one line is used for double LLP configuration, Higgs decay in particular.

The parameters are given in Table 6.4. The whole details are found in Chapter D.

Four stripping selections are used with similar ideas as for the trigger. They are summarised in Table 6.4. Each line selects less than 0.05% of the real data. A complete description of these lines can be found in Chapter E in the Appendix.

The global effect of the trigger on the selection of Higgs decaying into two LLPs was found to be as low as $\sim 40\%$ (see Chapter 7). The reason has been investigated.

The effect of stripping is negligible as it is already part of the analysis.

⁷See Sec. 2.3.3 for a presentation of the trigger system.

Name	Prescale	Cuts
SingleDisplVtx	0.05	≥ 1 DV, $N_{min}^{track} = 5$, $M_{min}^{LLP} > 5$ GeV, $\sum_{min} p_T > 5$ GeV
SingleDisplVtxLowMass	1	≥ 1 DV, $N_{min}^{track} = 6$, $6.8 \text{ GeV} < M_{min}^{LLP} < 12 \text{ GeV}$, $\sum_{min} p_T > 6$ GeV, Det
SingleDisplVtxHighMass	1	≥ 1 DV, $N_{min}^{track} = 5$, $M_{min}^{LLP} > 12$ GeV, $\sum_{min} p_T > 6$ GeV
DoubleDisplVtx	1	≥ 2 DV, $N_{min}^{track} = 4$, $M_{min}^{LLP} > 3$ GeV, $\sum_{min} p_T > 3$ GeV

Table 6.6: Cuts of the stripping DisplVertex lines. Det stands for the detector cut.

Chapter 7

Search for Higgs-like Bosons Decaying into Long-lived Particles



We have analysed the data collected in 2010 to identify secondary vertices in the VeLo which can be associated long living exotic particles. In the final analysis, pairs of candidates have been combined to reconstruct a Higgs boson candidates.

IN THIS CHAPTER, we shall focus on the models featuring the decay of a Higgs-like boson into two LLPs, namely the BV48 (see Sec. 1.3.1) and HV10 (see Sec. 1.4) models.

From simulation we know (see Fig. 5.10) that the transverse momentum distribution of the Higgs mother is low enough so that the two daughters essentially decay back-to-back in the transverse plane of the collision. Requiring such a configuration offers a drastic reduction of the background while keeping reasonable efficiency on the signal.

7.1 Samples of Data and MC Events

In this section, we describe the data and MC events samples which have been used for the final analysis.

2010 data We have analysed the data recorded during the year 2010, corresponding to an integrated luminosity of 37 pb^{-1} , filtered by the stripping

selections described in Sec. 2.3.4. This provided us with four data-sets. We have used the “Single” prescaled line (with loose cuts) for the comparison of the general properties of the real data with the MC samples and various cross-checks. The “Double” line provided candidates for the final analysis. No specific trigger was required.

MC signal 54k events of BV48 have been simulated with a mean number of interaction per bunch crossing $\nu = 3$. The events are weighted to simulate $\nu = 2.5$, which is closer to the observed value in the latest runs (providing the bulk of the integrated luminosity). The sample has been filtered by the trigger, i.e. a positive “and” between the Hlt1 and Hlt2 physical decisions is required.

As discussed in Sec. D the trigger information has been obtained by a looser trigger scheme (TCK 0x002e002a). The “tighter” trigger (TCK 0x002e002c) has been “simulated” off-line by adding the ad-hoc cuts at the analysis level.

For the HV10 sample, 50k events have been simulated with $\nu = 1$. Due to persistent problems in the simulation process, it was not possible to have a sample with $\nu = 2.5$ or 3, as well as the trigger information, within the time frame of the present study.

MC background We have analysed MC MB from two samples. The larger one contains 129M events and has been simulated with $\nu = 1$, while the smaller sample contains 20M events with $\nu = 2.5$.

As it is not possible to generate enough MB events to get a large number of candidates to compare with the 2010 data, we have also considered inclusive b quark production (incl. b)¹. For incl. b a larger sample (20M events) with $\nu = 1$ and a smaller one (1M events) with $\nu = 2.5$ are available and have been used.

The production of $t\bar{t}$ decaying into hadrons, with a lepton with $p_T > 10\text{ GeV}$ has been simulated and analysed. It contains 100k events and has $\nu = 2.5$.

We will give the results for events generated with $\nu = 2.5$ but also, to some extent, with $\nu = 1$ which has much larger statistics. However, we do not believe that this set can be safely used to determine the detection efficiency with sufficient precision.

Table 7.1 summarises the properties of the MC background samples considered. It also shows the ratio of the number of MC events to the total

¹Incl. b event make 0.5% of the MB cross-section : 0.457/91.05 mbarn.

Sample	N_{evts}	N_{evts}/N_{expt}	ν	triggered
MB	129M	$3.7 \cdot 10^{-5}$	1	Yes
MB	20M	$5.7 \cdot 10^{-6}$	2.5	Yes
incl. b	20M	$4.4 \cdot 10^{-3}$	1	Yes
incl. b	1M	$2.4 \cdot 10^{-4}$	2.5	Yes
$t\bar{t}$	100k	754	2.5	Yes

Table 7.1: For the 3 kinds of background samples we give the number of analysed events, the ratio of this number to the number expected for 37 fb^{-1} , and the average number of interactions. All samples have been trigger filtered.

expected events for 37 fb^{-1} . All samples that will be used in this analysis are trigger filtered

7.2 Selection of Pairs of LLP Candidates

The LLP candidates are selected following the procedures of Chapter 6. We apply the matter veto procedure described in Sec. 6.2.3.d, and also carry out a control analysis selecting only candidates in the vacuum region $r < 4.8 \text{ mm}$. In addition, we set a lower cut $r > 0.4 \text{ mm}$ to avoid the PV region. No explicit cut on the z position is applied. We require at least two LLP candidates in the event with $N^{trk} \geq 4$ and $m > 3 \text{ GeV}$, and the presence of at least one PV upstream from the LLP candidates. In the BV48 events the probability not to find a PV when a LLP is present is about 2% (see Table 6.1).

The retention for the background samples at this stage of the analysis is given in Table 7.2. From the 17 $b\bar{b}$ events ($\nu = 2.5 \text{ set}$) we can estimate the detection efficiency, after correction for the generator cuts which accept 43.5% of the events. We obtain an efficiency of $7.4 \cdot 10^{-6}$ with a 25% statistical uncertainty. Assuming the $b\bar{b}$ inclusive cross section measured at LHCb [120] :

$$\sigma(pp \rightarrow b\bar{b}X) = (288 \pm 4 \pm 48) \mu\text{barn}$$

where the first uncertainty is statistical and the second systematic, we predict $(78 \pm 21) \cdot 10^3$ events, a result that is compatible with the 61775 observed in the data. This seems to indicate that we have mainly selected beauty events. This hypothesis is reinforced by the inspection of MC truth information of some of the selected MB events: we have only found events containing b jets.

The following plots (Fig. 7.1 to 7.4) show some of the main properties of the selected candidates in the data. We superimpose the distributions of the MC signal candidates. To further check that we are consistent with beauty

Sample	ν	Simulated	Selected	LLP candidates
$b\bar{b}$	2.5	1M	17	34
$b\bar{b}$	1	20M	348	697
MB	2.5	20M	3	6
MB	1	129M	7	14
$t\bar{t}$	2.5	0.1M	2	4

Table 7.2: Retention for the background samples at the input of the procedure for the Higgs selection.

events, two sets of figures have been made : the first one with the inclusive b events with $\nu = 2.5$ and the second one with inclusive b events with $\nu = 1$ and the requirement of only one PV in the event. To better compare the shapes, all the distributions are normalised to unity.

The plots of Fig. 7.1 show the number of tracks associated to the LLP candidate (starting from four, because of the preselection cut), reconstructed p_T , pseudo-rapidity η , and invariant mass (starting from 3 GeV). The $b\bar{b}$ inclusive sample is the one generated with $\nu = 2.5$, with only 34 LLP candidates. The same distributions, but for the larger sample of $b\bar{b}$ with $\nu = 1$, can be found in Fig. 7.2. We observe that the incl. b distributions match the shape obtained for the data.

Figure F.4 in the Appendix shows the corrected mass

$$m_{\text{corr}} = \sqrt{m^2 + |\mathbf{p}'_{T\text{missing}}|^2} + |\mathbf{p}'_{T\text{missing}}|$$

distributions, where $\mathbf{p}'_{T\text{missing}}$ is the missing momentum transverse to the direction of flight of the candidate, obtained from the PV and decay RV. A cut on the corrected mass has been discarded for two reasons. The first one is the absence of an efficient procedure to associate the candidates with their respective PVs. The second reason is that the use of a cut on m_{corr} does not bring any increase in the signal over background retention ratio for the events with an unique PV candidate.

In Fig. 7.3 we compare the position errors provided by the vertex algorithm², for data, MC signal, and inclusive b with $\nu = 2.5$. The same applies for inclusive b events with $\nu = 1$ in Fig. 7.4. Again, the shape of data and beauty events match well and no significant deviations are observed.

In general the value of the vertex error is related to the number of tracks, as can be seen in the profiles of Fig. 7.5.

²The square root of the radial and longitudinal component of the matrix of error positions.

	Gen	$N^{trk} \geq 4,$ $M^{LLP} > 3$	$N^{trk} \geq 6,$ $M^{LLP} > 6$	$N^{trk} \geq 6,$ $M^{LLP} > 6,$ $\sigma_r < 0.05,$ $\sigma_z < 0.24$
d [%]	62.2	63.1	64.8	65.5
u [%]	50.4	49.6	49.5	50.7
s [%]	62.1	62.8	63.2	63.9
c [%]	48.1	49.1	48.9	48.0
b [%]	71.5	70.4	67.7	66.8

Table 7.3: Flavour composition of MC LLP decays and reconstructed vertices after certain cuts, for the BV48 model. The cut on the mass is given in GeV, while the one on σ in mm.

In the final step of the analysis we explore cuts in the range $\sigma_r^{max} = 0.1 - 0.05$ mm and $\sigma_z^{max} = 1 - 0.20$ mm. For the BV48 model a cut $\sigma_r^{max} = 0.05$ mm and $\sigma_z^{max} = 0.24$ mm rejects about 20% of good candidates, and 22.5% for $\sigma_r^{max} = 0.04$ mm and $\sigma_z^{max} = 0.20$ mm.

From Table 7.3, we can see that the tightening of the cuts and the addition of tight $\sigma_{r,z}^{max}$ cuts do not change the quark composition significantly. The percentage of vertices with a b quark goes down from 71.5% at generator level to 66.8%. Although the tracks from tertiary vertices have a small weight, they still affect the quality of the LLP vertex and increase the error. In the case of the HV samples, a cut on these errors is less efficient, because they have larger errors closer to $b\bar{b}$ events (c.f. Fig. 7.3 and Fig. 7.4).

We also observe in Table 7.3 that the reconstruction does not favour a certain flavour. Along with the quarks, a few gluons are also produced, which will decay into quarks and are not counted.

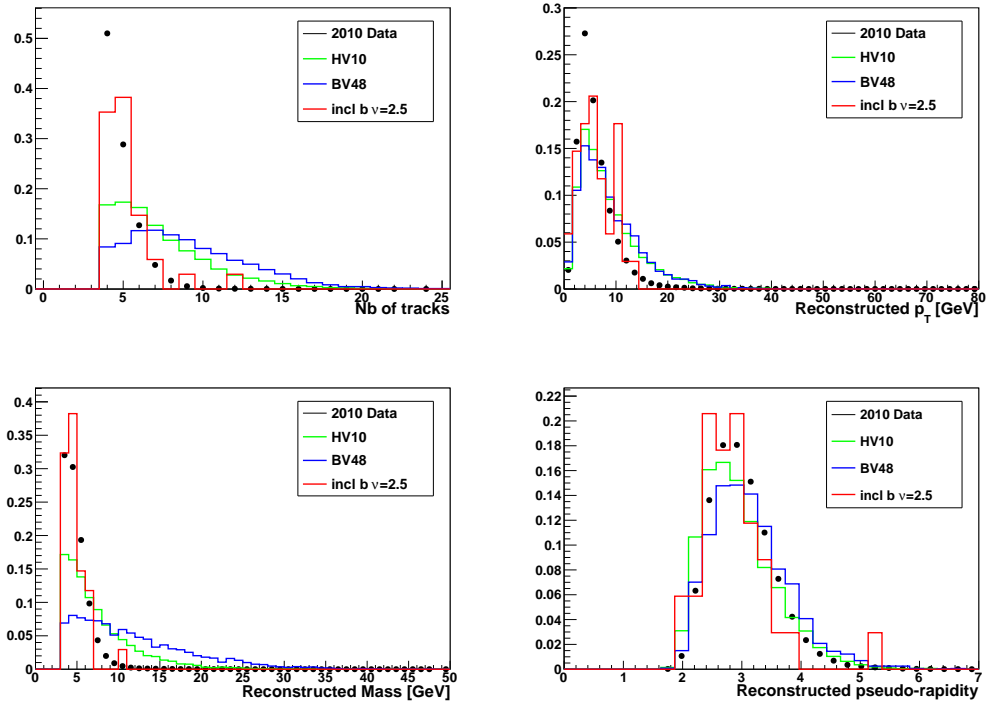


Figure 7.1: MC events compared to data results. *Top left* : number of tracks of the LLP candidate, *right* : p_T distributions. *Bottom left* : LLP invariant mass, *right* : pseudo-rapidity. Data and MC distributions are shown with unit normalisation. No restriction on the number of PVs. In these plots we have 61775 data and 17 from the initial set of 1M incl. b events generated with $\nu = 2.5$.

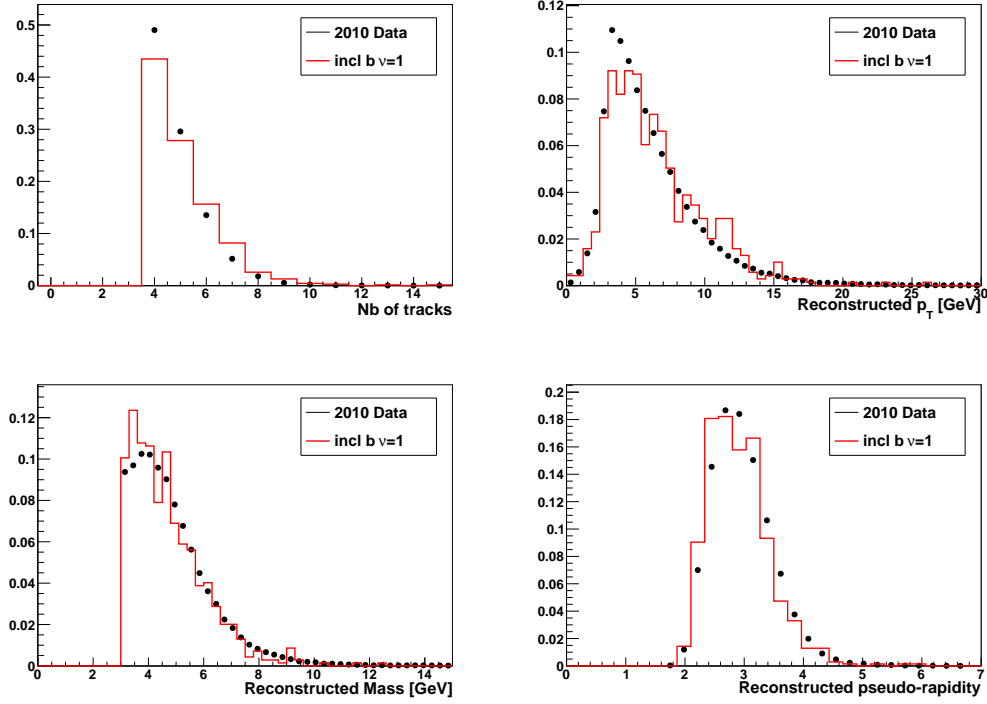


Figure 7.2: Like Fig. 7.1, but the incl. b have been generated with $\nu = 1$. We have selected 348 events from the initial set of 20M events. We request an unique PV in the event.

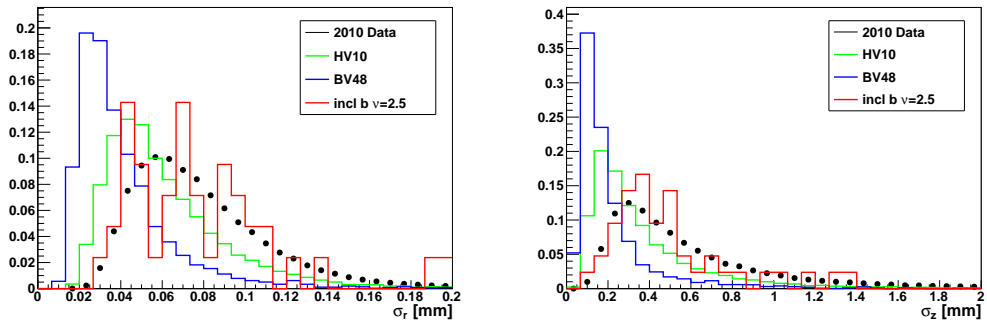


Figure 7.3: Radial and longitudinal estimated errors on the LLP vertex, provided by the vertex algorithm, for data and MC events. No restriction on the number of PVs have been applied. The MC $b\bar{b}$ sample was generated with $\nu = 2.5$.

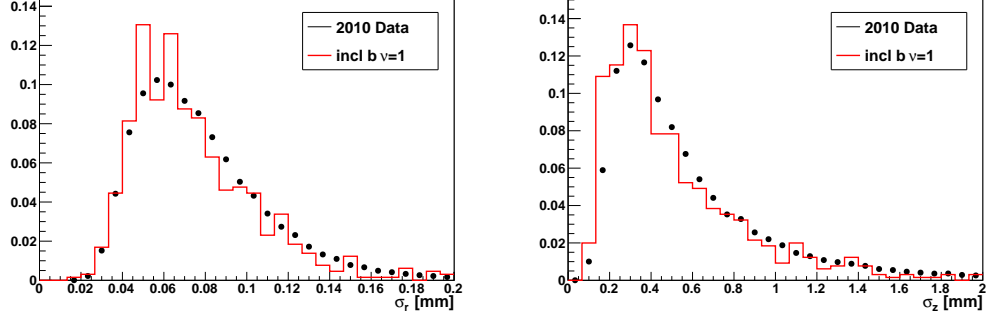


Figure 7.4: Like Fig. 7.3, but the $b\bar{b}$ sample was generated with $\nu = 1$. We request an unique PV in the event.

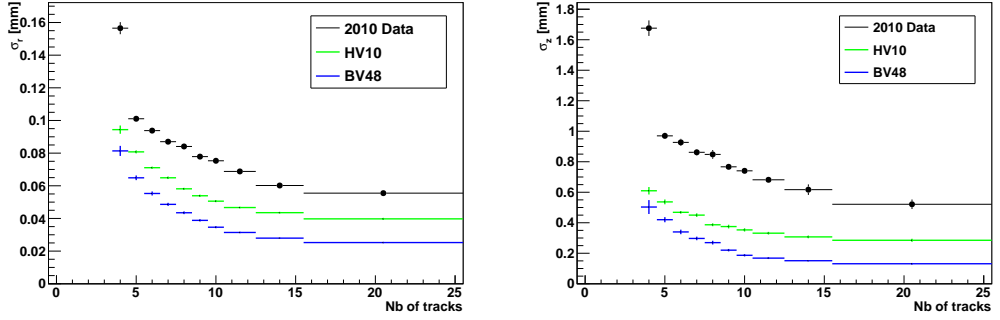


Figure 7.5: Average estimated error in r (left) and z (right) w.r.t. the number of tracks in the vertex. The difference between HV and BV seems associated with the quark composition of the decay of the LLP: HV contains only b quarks, while BV produces also light quarks.

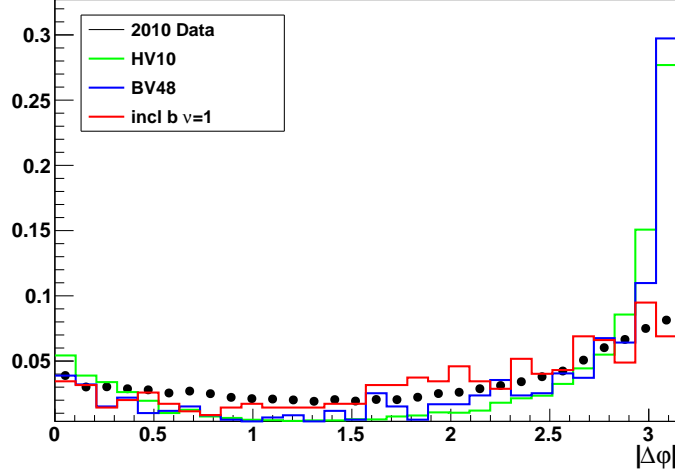


Figure 7.6: Azimuthal angle $|\Delta\varphi|$ between the two LLP candidates w.r.t. the upstream PV for data and MC events normalised to unity.

7.3 Selection of the Mother Candidates

The Higgs candidate is obtained by combining two LLPs. As we have seen in Fig. 5.10 the Higgs boson is predicted to be produced with a small transverse momentum: in the absence of radiative effects the two LLPs should fly back to back in the transverse plane. This is shown in the distributions of the azimuthal angle $|\Delta\varphi|$. Figure 7.6 shows distributions of the azimuthal angle $|\Delta\varphi|$ between the pairs of candidates. Both kinds of signals, BV and HV, are peaked at 180 degrees, while a broad distribution is found for data and inclusive $b\bar{b}$. Here the value of $|\Delta\varphi|$ is not computed from the momenta, but from the directions inferred from the the LLP reconstructed vertices, whose positions are known with excellent precision.

We can observe that 60% of pairs of MC signal candidates are found in the region with $|\Delta\varphi| > 2.8$. Pairs with $|\Delta\varphi| > 2.8$ are selected and the two LLP candidates are combined to obtain a parent (Higgs) candidate.

In case of multiple PVs, we consider each PV upstream of the two LLP candidates. The LLP pair is accepted if at least one of the PVs satisfies $|\Delta\varphi| > 2.8$.

The plots of Fig. 7.7 show the IP to the PV obtained by extrapolation of the LLP momentum from the reconstructed vertex. In case of multiple PVs, the IP used to increment the distribution is the smallest value found. Again, we observe that the $b\bar{b}$ background matches the experimental distribution.

We then obtain the set of distributions of Fig. 7.8. Remember that these results are obtained with $N_{min}^{trk} = 4$ and a cut on the LLP mass above $M_{min}^{LLP} = 3$ GeV. In the bottom plots in log scale, we can observe a long tail. When requiring two LLP candidates with $N^{trk} \geq 6$ and $M^{LLP} \geq 6$ GeV, the Higgs candidate mass distribution disappears at 40 GeV, with no tail.

Table 7.4 and 7.5 summarise the statistics at certain stages of the selection for the data and MC background events. The $t\bar{t}$ sample is not displayed, since less than 1 event is expected. Table 7.4 indicates the raw number of events selected among the original number generated, while Table 7.5 gives figures normalised to the LHCb integrated luminosity.

Considering the two $b\bar{b}$ inclusive sets, we notice a loss by about 50% in the related efficiency from $\nu = 1$ to $\nu = 2.5$ ($4058/20M = 203 \cdot 10^{-6}$ down to $101 \cdot 10^{-6}$, a factor of 0.50 with 10% statistical precision). This inefficiency is probably associated with the same pathologies observed in the trigger performance.

Secondly, we notice that the number of $b\bar{b}$ ($\nu = 2.5$) expected events³ $[5 - 30]$ k is compatible with the 14645 in the data, but the 95% CL interval is too wide to draw a conclusion. The estimated (29 ± 3) k events from the $\nu = 1$ set can be corrected for the inefficiency at $\nu = 2.5$ by applying the factor 0.5 computed above. This brings us to (15 ± 2) k events, covering the data result. This is a further indication that we are selecting mainly beauty events.

The transverse momentum and reconstructed mass of the Higgs candidates are shown in Fig. 7.9, with the predicted spectrum superimposed, assuming a pure $b\bar{b}$ background. $\nu = 1$ MC events have been used with a correction of a factor 0.5. An unique PV is also requested in the event.

As a last point we notice that the matter veto rejects half of the data (135k down to 62k), while only about 15% of the beauty events are affected. This is interpreted to be due to the large fraction of b decays taking place before the RF screen. The number of MB events is too small to verify. To clarify the question we have made an analysis requiring only one LLP candidate per event. In this case the effect on the data was a reduction by a factor 0.39 and 0.46 ± 0.06 for MB.

Note that the $b\bar{b}$ cross-section is computed at leading order by PYTHIA, resulting in a much higher value $\sigma(pp \rightarrow b\bar{b}X) = 457 \mu\text{barn}$. This leads to a higher proportion of $b\bar{b}$ events in the MC MB samples.

³Again, the $b\bar{b}$ cross-section used is the one measured at LHCb [120] : $\sigma(pp \rightarrow b\bar{b}X) = 288 \pm 4 \pm 48 \mu\text{barn}$.

Selection Simulated:	Data	MB $\nu = 2.5$ 20M	incl. b $\nu = 2.5$ 1M	MB $\nu = 1$ 129M	incl. b $\nu = 1$ 20M
Stripping “Double”, no trigger triggered	- 138111	24 6	101 22	114 9	4058 678
$r > 0.4$ mm	134588	6	21	9	645
$r > 0.4$ mm, MV	61775	3	17	9	531
$r > 1$ mm, MV	39489	2	8	6	322
$0.4 < r < 4$ mm	53358	3	15	8	468
$1 < r < 4$ mm	32672	2	7	5	270
$r > 0.4$ mm, MV, $ \Delta\varphi > 2.8$	14645	2	3	2	129

Table 7.4: Number of events at different selection stages for data and MC background with $\nu = 2.5$ and (last two columns) $\nu = 1$. For MC we also give the number of generated events. MV stands for the matter veto.

Selection	Data	MB $\nu = 2.5$	incl. b $\nu = 2.5$	MB $\nu = 1$	incl. b $\nu = 1$
Stripping “Double”, no trigger triggered	- 138111	(3.9 ± 0.8) M [0.5-1.7]M	(458 ± 46) k (100 \pm 21)k	(3 ± 0.3) M [142 – 371]k	(902 ± 14) k (151 \pm 6)k
$r > 0.4$ mm	134588	[0.5-1.7]M	(95 ± 21) k	[142 – 371]k	(143 ± 6) k
$r > 0.4$ mm, MV	61775	[0.2-1.1]M	(77 ± 19) k	[142 – 371]k	(118 ± 05) k
$0.4 < r < 4$ mm	53358	[0.2-1.1]M	(68 ± 18) k	[12 – 340]k	(104 ± 5) k
$r > 0.4$ mm, MV, $ \Delta\varphi > 2.8$	14645	[87-872]k	[5 – 30]k	[14 – 140]k	(29 ± 3) k

Table 7.5: Number of events at different selection stages for data and MC background with $\nu = 2.5$ and (last two columns) $\nu = 1$. For MC the number of expected events is given, normalised to the integrated luminosity. The figures referring to $t\bar{t}$ are not shown because the MC forcees less than 1 event. MV stands for the matter veto. Errors are statistical only. For numbers of events < 10 in the selected samples we give the 90% CL interval.

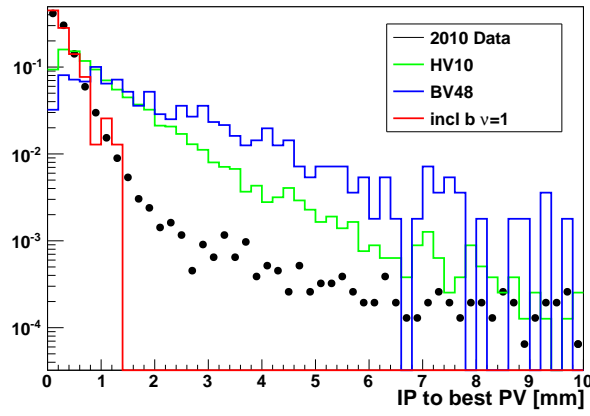


Figure 7.7: IP to the PV distribution. For this plot we have released the constraint of a single PV in the event. The IP in the distribution is the smallest value found. Data and MC distributions normalised to unity.

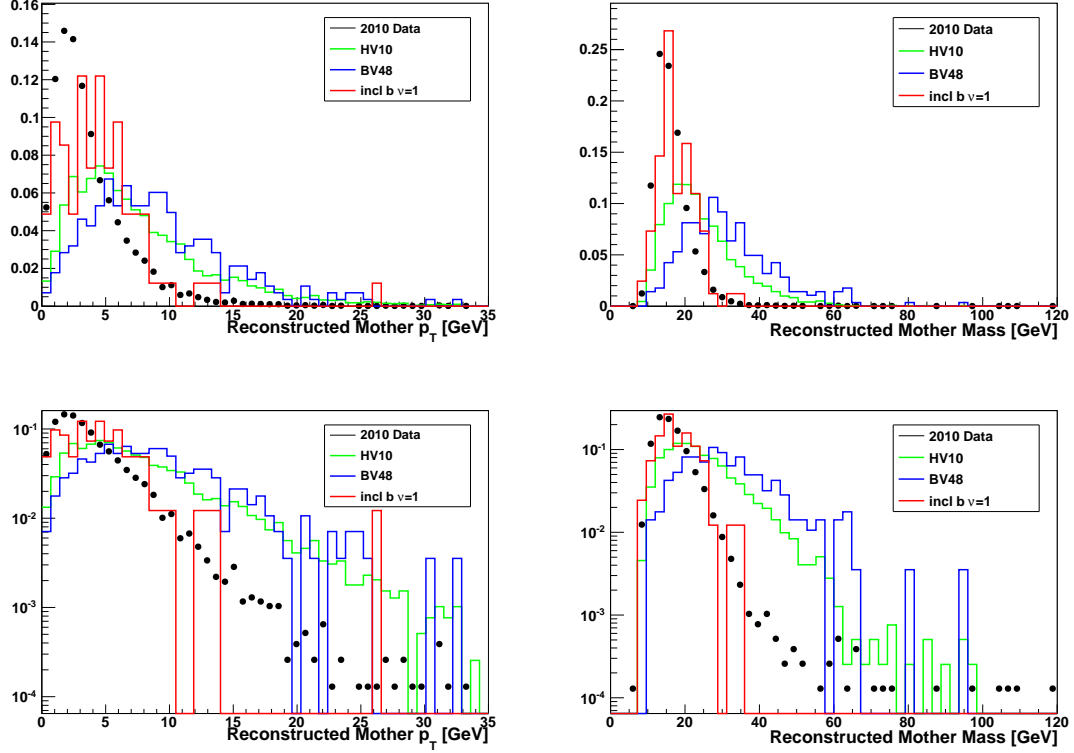


Figure 7.8: p_T distribution (*left*), and invariant mass (*right*) of the selected Higgs candidates. We show the result for MC signal and MB with unit normalisation. Plots in the bottom have log scale.

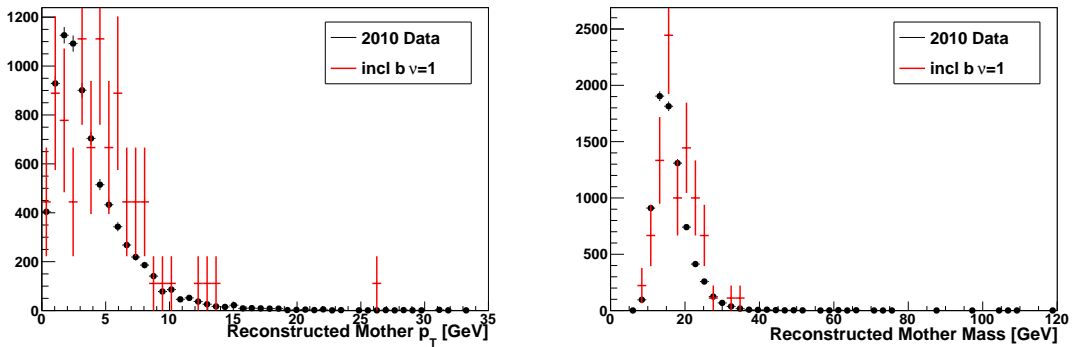


Figure 7.9: p_T distribution (*left*), and invariant mass (*right*) of the selected Higgs candidates. The figures show the true number of entries for the data and the expected nb of events for MC (see text). The errors are only statistical and we request only one PV in the event.

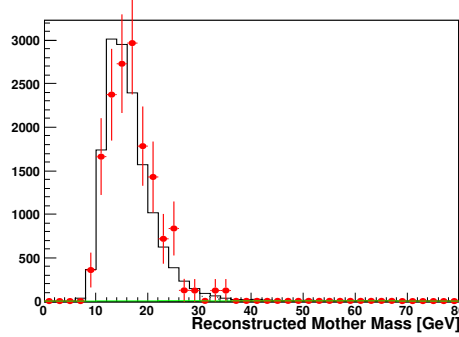


Figure 7.10: Result of the fit on the invariant mass of the Higgs candidates. The black histogram is the data, in red the fitted function. In green is the signal component which only contains 32 events.

7.4 Final Selection

From the previous sections we draw the conclusion that our requirements select mainly $b\bar{b}$ events.

The result of a fit of the invariant mass distribution for the Higgs obtained without restrictions on the number of PVs is presented in Fig. 7.10. The data has 14645 events with Higgs candidates. From the fit we obtain a number of signal events of the BV48 kind compatible with zero (32 ± 592 ; the fitted background is 15208 ± 1438). The fit assumes that the background is pure $b\bar{b}$ with the shape provided by the MC set with $\nu = 1$. The relative weight of signal and background are left to vary freely.

Because the main uncertainty comes from the $b\bar{b}$ distribution we group the bins in such a way that the $b\bar{b}$ distribution has at least 5 events in each bin. This leaves 6 DoF and the χ^2/DoF is 1.1.

The fit result does not change if we fix the normalisation (i.e. we fit $14645 \times [x \times \text{Sig} + (1 - x) \times \text{Bkg}]$, where Sig and Bkg represent the BV48 mass distribution and the $b\bar{b}$ one with unit normalisation). A crude estimate of the error associated with the calibration uncertainty is obtained by shifting the relative position of data and MC by 2 GeV. We obtain 110 ± 684 signal events instead of 32.

This method suffers from the very low statistical precision in our theoretical samples. Moreover BV48 is just one point in a huge theoretical parameter space.

For this first analysis we have used a different approach in which we have explored several cuts to try to get rid of the $b\bar{b}$ background, while keeping some efficiency on the signal. Two of the observables selected are N_{min}^{trk} and

	N_{min}^{trk}	M_{min}^{LLP}	σ_r^{max}	σ_z^{max}	MV	N_{evts}	ϵ %	N_{evts}^{MC}
1	4	3	∞	∞	No	13627	0.358	2.6
2	4	3	∞	∞	Yes	7748	0.181	1.3
3	4	3	∞	∞	$r < 4.8$	7349	0.143	1.1
4	8	7.5	0.1	1.0	Yes	0	0.074	0.55
5	6	6	0.05	0.24	Yes	0	0.080	0.59
6	6	6	0.05	0.24	$r < 4.8$	0	0.066	0.48
7	6	6	0.05	0.24	Yes	0	0.220	1.63
8	6	6	0.06	0.24	Yes	0	0.233	1.72
9	6	6	0.04	0.24	Yes	0	0.177	1.31
10	6	6	0.05	0.23	Yes	0	0.215	1.58
11	6	6	0.05	0.25	Yes	1	0.223	1.65

Table 7.6: Number of events selected for some values of N_{min}^{trk} and M_{min}^{LLP} (in GeV), and the cuts on the LLP vertex errors σ_r^{max} , σ_z^{max} (in mm). A Yes in the 6th column (MV) says that the material veto was active, while $r < 4.8$ is for the control analysis done with a restriction on the radial position . ϵ is the efficiency in percent estimated from the analysis of BV48 events. The last column gives the expected number of events for the BV48 model. The top part of the table gives figures for the restrictions to events with one unique PV found. The bottom part (lines 7–11) has no constraints of this kind.

M_{min}^{LLP} . We have also observed (see Fig. 7.4 and Fig. 7.5) that the errors on the vertex position σ_r and σ_z provided by the vertex algorithm have some selection power. It has been found that several combinations of cuts allow to suppress all the MC beauty events.

The procedure is summarised in Table 7.6 where we give the number of events observed for some values of the selection cuts.

Some parts of the analysis (line 1 to 6) require one unique PV, to compare with the $\nu = 1$ MC samples. Starting from line 7, this condition is absent. We also switched on and off the matter veto and cross checked the effect with a radial $r < 4.8$ mm restriction. In the last column we give an estimate of the measurement efficiency and also the expected number of signal events based on the model BV48.

The first three lines have larger cuts to let some events pass : in particular line 2 corresponds to the analysis conditions used to obtain the distributions displayed so far, showing that we have mainly selected $b\bar{b}$ background. Line 3 has the restriction on the radial position activated: we see that it induces

only a small change in efficiency compared to the previous line. Starting from line 4 all the background disappears and we have also zero events in the data. No events appear when we accept events with multiple PVs. The gain in efficiency is of $0.22/0.08 = 2.75$, given by the ratio between line 7 and line 5.

The last line has a weaker value of the position error and accepts one event in the data (see Sec. 7.5).

In the simplest situation where zero candidate are observed, we can estimate an upper limit for the production cross-section times branching ratio at this particular point of the BV parameter space. With the results given in line 7, we obtain $3.0/(37pb^{-1} \times 0.220 \times 10^{-2}) \sim 37$ pb. Taking into account the 22% systematics (see Sec. 7.6.2), the upper limit becomes 53 pb.

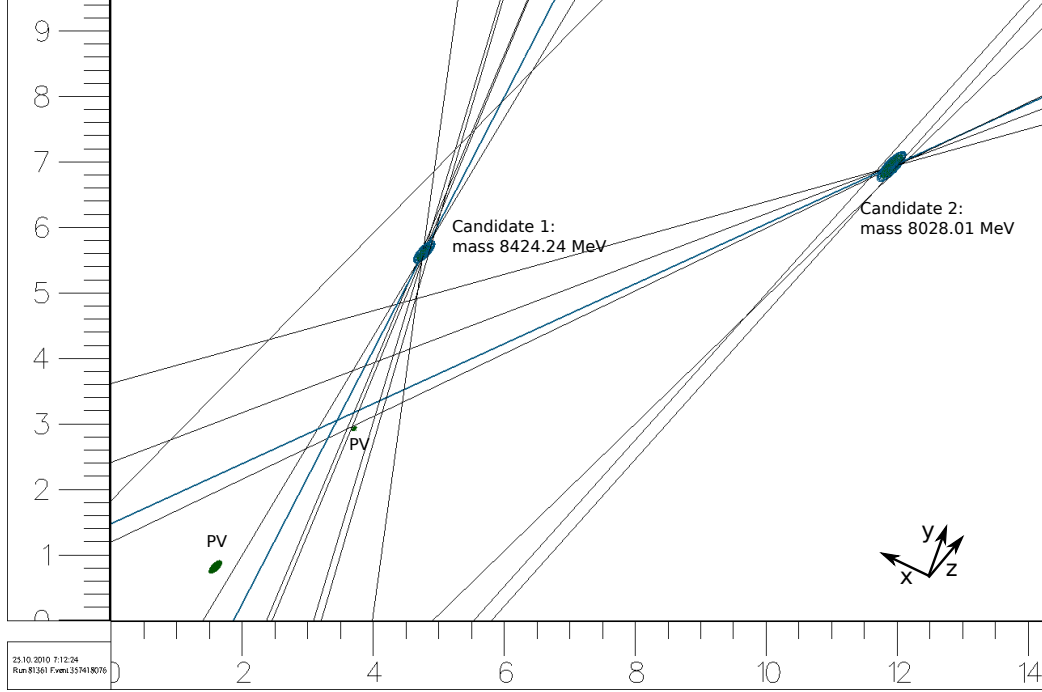


Figure 7.11: The event passing the cuts of line 8 of Table 7.6. The beam axis is at about 45 degrees, across the two PVs. The directions of the reconstructed momenta of the LLP candidates are shown by the blue lines.

7.5 The Event

We present the unique event indicated in line 11 of Table 7.6)⁴. Figure 7.11 displays a blow up view of the VeLo region for this event.

The event has two PVs and two LLP candidates with the following properties:

- beam-line reference point (0.339, -0.165, -9.949) [mm]
- first PV position (0.3692, -0.0867, 26.4747) [mm]
- second PV position (0.3533, -0.2043, 34.1136) [mm]
- first LLP candidate has $N^{trk} = 7$, $r = 1.232$ mm, Mass= 8.42 GeV, decay position (1.449, -0.700, 40.5) [mm], momentum = (0.203, -1.903, 95.06, 97.34) GeV, $p_T = 1.914$ GeV, IP to best PV 0.36 mm

⁴This event has Event-number=357418076, and Run-number=81361.

- second LLP candidate has $N^{track} = 6$, $r = 2.945$ mm, Mass = 8.03 GeV, decay position (-2.563, 0.337, 57.503) [mm], momentum (-5.749, 1.635, 43.48, 44.61) GeV, $p_T = 5.977$ GeV, IP to best PV 0.38 mm
- $|\Delta\varphi| = 2.90$ rad
- distance of closest approach of the two LLPs is 0.33 mm
- mass of the parent = 20.8 GeV

The IP LLP₁ to PV₁ is of 0.64 mm and 0.36 mm to PV₂. For LLP₂ the IP to PV₁ is 1.37 mm and 0.38 mm to PV₂. It is most likely that both LLP candidates come from the second PV.

Assuming a mass calibration factor 3–4 (from generator studies, Fig. 5.6) we have a “likely” mass value of the parent around 60–80 GeV.

In the b inclusive MC samples events have been studied with only one LLP passing the selection cuts applied on the individual candidate, i.e. matter veto, $r > 0.4 < mm$, $m > 6$ GeV, $\sigma_r > 0.06$ mm and $\sigma_z > 0.25$ mm. They show the same properties as the collected data.

From the probability for one selected LLP candidate to pass those tight cuts and the probability to have one Higgs candidate, we can estimate that the expected number of such events is in the order of 1.

Taking a closer look at the vertices of these heavy inclusive b candidates, we can observe that some of the daughter tracks also have a very small IP to the PV. The heavier vertex mass might just come from the “steal” of one track from the PV. This case must be studied in more details for the forthcoming 2011 data.

7.6 Systematic Effects

The detection efficiency ϵ is determined by the analysis of MC events. As already stated, an event re-weighting has been applied to correct from the generated bunch crossing multiplicity $\nu = 3$ down to the experimental value $\nu = 2.5$.

We need to understand how well the MC can be trusted considering that the key point is the vertex reconstruction efficiency, in a region which is beyond the typical b-hadron decay.

At the level of the LLP selection we have already seen some comparison of data distributions with MB MC events (Fig. 7.1 to 7.4). In the next section we suggest to take advantage of the presence of matter to further assess the reliability of the simulation concerning the vertex finding procedure.

7.6.1 Cross Check with Vertices from Matter Interactions

We consider vertices produced by the impact of particles on the material in the RF-shield region, which are normally discarded by the matter veto.

The plots of Fig. 7.12 and Fig. 7.13 show several variables observed in the data and MB MC events, when the matter **anti**-veto is applied. We have selected candidates in the luminous region $-50 < z < 200$ mm and in a radial window $4.8 < r < 12$ mm.

Figure 7.12 shows the plots made for the MB with $\nu = 1$, with the requirement of an unique PV in the event.

The same variables are shown in Fig. 7.13 for the MB with $\nu = 2.5$ and no requirement on the number of PVs. Note that unlike the figures presented in the previous sections, the output stream of the “Single” stripping line has been used for its larger statistics on MC samples. In this line, candidates have $N^{trk} \geq 5$ and $m > 5$ GeV.

We can observe that the general shapes of the distributions of the MB match well the data for both samples.

We have also compared data and MC in a larger z region $300 < z < 600$, in a region which is beyond the typical b-hadron decay. Due to the low statistics ($\mathcal{O}(1)$), the plots are not shown. The few MC candidates reconstructed are consistent with the data.

Despite the poor statistics, we conclude that no major discrepancies are present in this MC–data comparison.

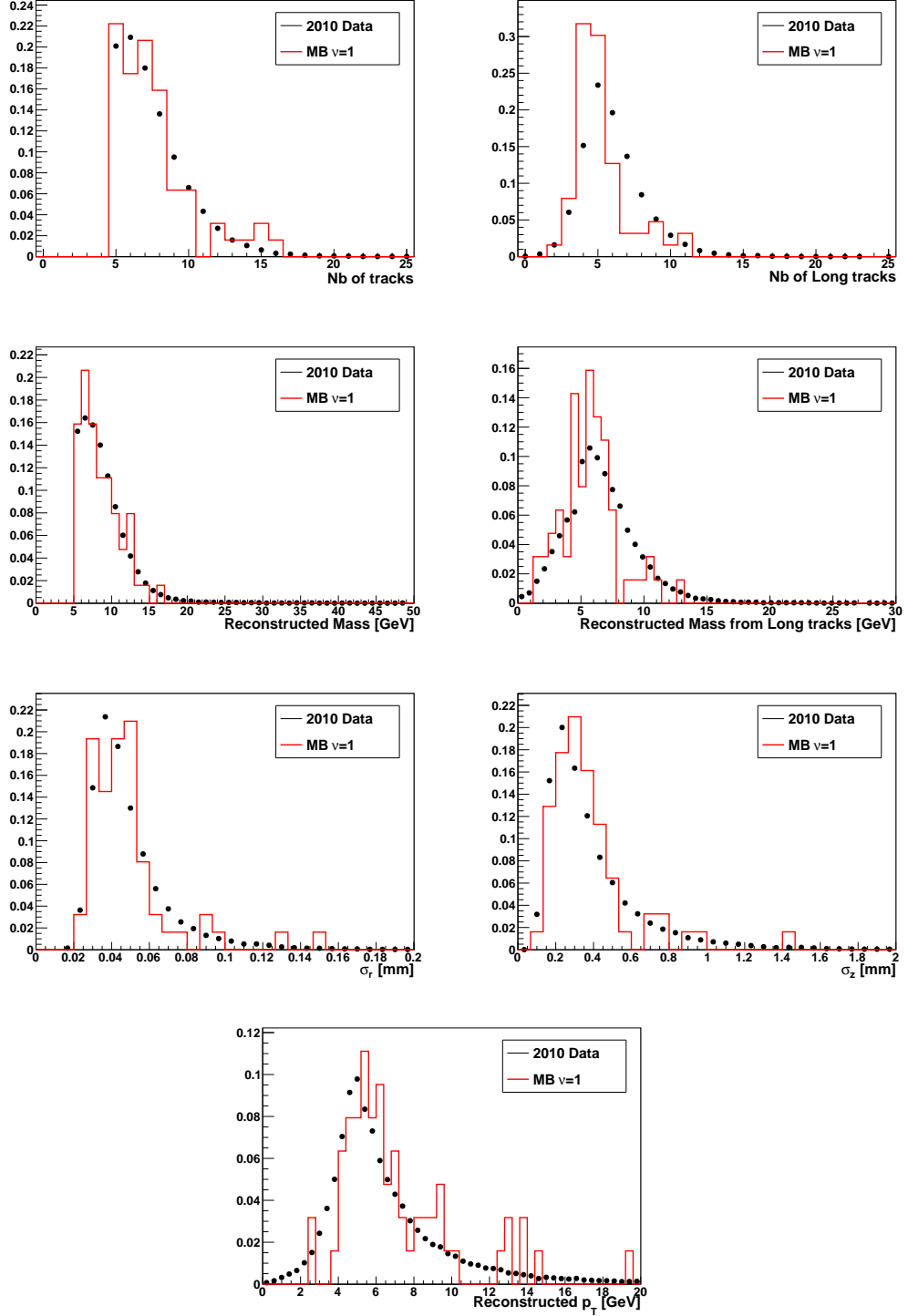


Figure 7.12: From left to right and from top to bottom: distributions of the number of tracks, Long tracks, of the mass of all tracks and long tracks only, of the radial and longitudinal errors, provided by the vertex finding algorithm, and finally the reconstructed p_T . Matter anti-veto, $4.8 < r < 12$ mm and $-50 < z < 200$ mm are applied. Data and MB MC ($\nu = 1$) events are compared. One PV only is required.

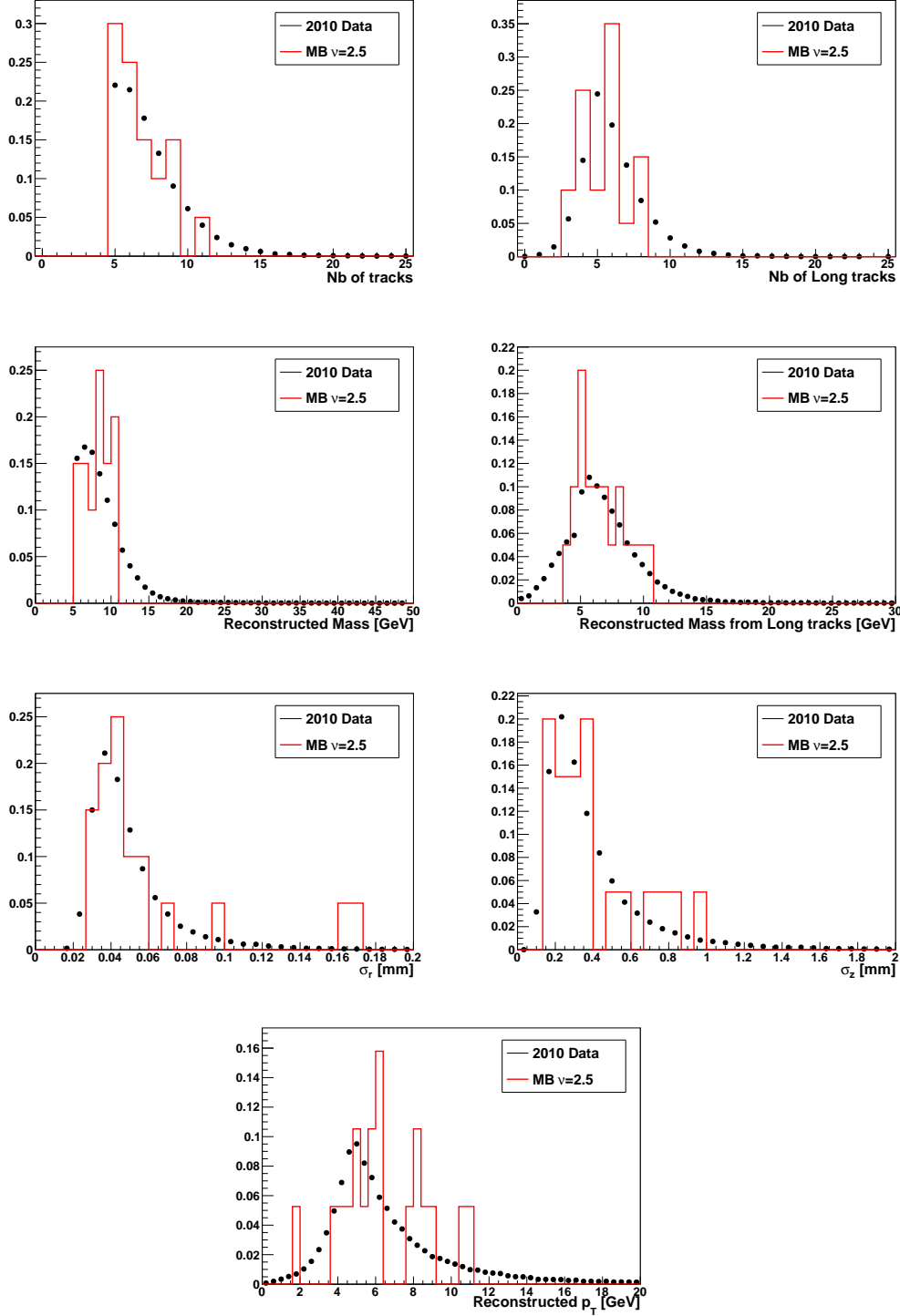


Figure 7.13: From left to right and from top to bottom: distributions of the number of tracks, Long tracks, of the mass of all tracks and long tracks only, of the radial and longitudinal errors, provided by the vertex finding algorithm, and finally the reconstructed p_T . Matter anti-veto, $4.8 < r < 12$ mm and $-50 < z < 200$ mm are applied. Data and MB MC ($\nu = 2.5$) events are compared.

	source	ϵ [%]
1	one LLP in acceptance (generator cut)	28.5
2	LLP preselection	48.3
3	Trigger	28.9
4	LLP selection (line 8 Table 7.6)	(66.9)
5	Prob to find the PV, LLP in acceptance	(97.6)
6	LLP vertex errors cuts	(87.3)
7	two LLP found (line 8 Table 7.6)	8.4
8	$ \Delta\varphi $ cut	65.7
	total	0.220
	total w/o trigger	0.374

Table 7.7: Contributions to ϵ at different stages of the event selection, based on MC BV48 events. The total is given by the product of the five contributions, lines 1, 2, 3, 7 and 8. Lines 4, 5 and 6 are given for information.

7.6.2 Contributions to the Efficiency and Systematics Estimate

A summary of the contributions to the detection efficiency ϵ is given in Table 7.7. They are valid for BV48. We should notice that the trigger selection discards 41% of the reconstructible events. The origin of this large contribution has been tracked down to the HLT1 (Hlt1Track lines), see Sec. D.

Our present estimates of systematic effects to ϵ are summarised in Table 7.8. In the table we also indicate a 10% error on the integrated luminosity.

We have considered the following contributions :

- The precision on the implementation of the **trigger** in the simulation has been set at 10%. This is a back-of-the-envelope estimate. A way to study this error would be to assess the efficiency of the trigger lines on events triggered by the micro-bias lines.
- The **tracking efficiency** contribution is estimated at the fast simulation level (in preparation), assuming an efficiency of $95\% \pm 2.5\%$ per track in the event. The variation of 2.5% on the track direction probability results in the variation of 5% of ϵ . (A similar approach on full simulation is under study.)
- For the **vertex resolution**, we take half of the difference between lines 8 and 9 of Table 7.6, which gives us 13%.

- For the **VeLo tracks** we consider the effect due to the inclusion in the analysis of tracks found only in the VeLo with no momentum information. In the analysis we assign a p_T of 400 MeV for these tracks (a most probable value). Given the satisfactory match shown in Fig. 7.12 and 7.13, we consider the contribution of this effect to be smaller than $\sim 5\%$.
- For the **Pt and mass calibration** we consider a calibration error in p_T and invariant mass of 10%. By moving the cuts by this amount, we obtain a contribution of 6%.
- For the **matter-veto** we have compared the behaviour of data and MC $b\bar{b}$ when we switch from matter veto to the control analysis performed in the region $0.4 < r < 4$ mm. The difference is less than 2%. Considering that the $b\bar{b}$ cannot be very representative of decays with lifetime much larger than the ps, we have restricted the region to $1 < r < 4$ mm, again obtaining 2%. We increase it to 4%.
- Finally, a bias may also come from the radial cut with respect to the beam line. We remember here that a moving average over 30 events is used to compute the beam position. Imprecision might stem from the fact that events on tape are not consecutive. This is because the HLT is run asynchronously on 16k different CPU cores. The subsequent processing introduces additional mixing. Figure 7.14 shows the standard and maximum deviation of GPS times in bunches of 30 consecutively saved events⁵. We observe deviations up to 10 seconds. To evaluate the possible error we have performed the analysis taking as the reference the upstream PV as described in Sec. 6.2.3.a. The effect of using such a radial cut results in variations smaller than 1%. The efficiency of our beam line method is due to the excellent stability of the beams achieved in 2010 (see Fig. F.6).

⁵Done on run 78287.

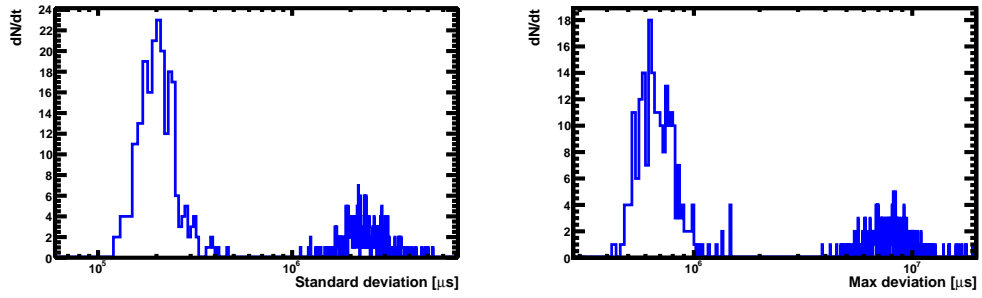


Figure 7.14: Standard and max deviation of GPS time in bunches of 30 consecutive saved events (run 78287).

	source	%
1	Integrated Luminosity	10.0
2	Trigger	10.0
3	tracking efficiency	5.0
4	Vertex resolution	13
5	VeLo tracks	5
6	Pt and Mass calibration	6
7	Matter-veto	4
8	Beam line	1
	total	22

Table 7.8: Contributions to the error on the efficiency, assuming the underlying simulation model. The error on the integrated luminosity is 10 %

7.7 Discussion and Outlook

7.7.1 Background

Here is a list of contributions to the background we have considered :

- For the present analysis the most important source of background is due to interaction with matter. Most of this contribution was removed by a veto on the region known to contain matter. We have also carried out an analysis with a cut which limits the radial distance of the LLP decaying vertex from the beam line in a region known to be matter-free (except for residual gas), obtaining consistent results.
- The effect of the interactions with the residual gas in the beam pipe have been estimated from MC events in Sec. 6.2.3.c. As stated previously the VeLo vacuum tank has been simulated with air inside. By taking the number of LLP candidates which are known to have originated from an interaction with air molecules, and scaling down to 10^{-10} Torr, we obtain a number of LLPs which is completely negligible. For the same reasons, beam-halo interactions with the residual gas should also be negligible.
- LLPs faked by split PVs are not likely to contribute significantly, given our quite generous radial cut of $r > 0.4$ mm. Indeed, no events were found with two LLP candidates at the same time close to each other, close to the beam line, and distant from any PV.
- Another source which might need to be considered in the future are wrong reconstructions in general.
- About physical sources of background from SM processes : we have examined a set of $t\bar{t}$ events, corresponding to about 1000 times the present statistics on tape. No events passed our cuts.

We have also analysed the $b\bar{b}$ events. Again no events passed the selection, but in this case we have only 10^{-4} of the present expected yield. For $b\bar{b}$ events we have to define a strategy, based on fast simulation sideband technique, etc.

We have observed some cases where the RV of a decayed B mesons has “stolen” a track from the PV, increasing artificially its mass. We have to compute this probability and investigate ways of minimising this thread. A possible improvement would be to remove the tracks from the RV that have a low IP to any of the PVs candidates.

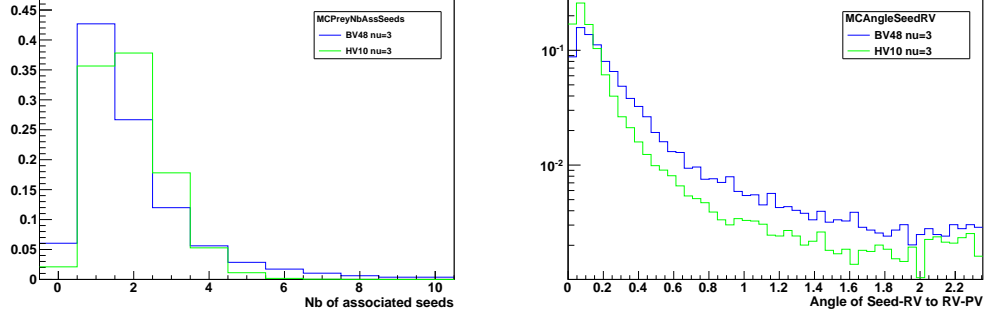


Figure 7.15: *Left* : numbers of seeds found after the LLP decay position and which are daughters of the LLP. *Right* : angle in radian formed by the Seed-RV line with the RV-PV line.

- Other non-SM phenomena can possibly contribute.

After the LLP decay, subsequent decays of beauty and charmed particles have not been taken into account. We think that this complex topology can be exploited to improve the background rejection, and mass resolution.

Figure 7.15 (*left*) shows the number of seeds, checked from MC-truth that are found after the LLP decay position (tertiary vertices) and which are daughters of the LLP. For that purpose, the seeding presented in Sec. 6.1.1 has been run with *MinCloseTracks*= 2. 97.9% and 94% of HV10 and BV48 candidates, respectively, have ≥ 1 associated seeds. As expected HV10 has more seeds than BV48, due to the presence of a larger number of b quarks. Figure 7.15 (*right*) shows the angle formed by the Seed-RV line with the RV-PV line. Asking for tracks with large p_T and IP to the RV in a certain window might prove useful.

We didn't apply any topological selection which involves the PV, except for the determination of the $|\Delta\varphi|$ angle between the two LLP candidates.

With the present quite strong cuts we can make all the background disappear, preserving some efficiency for the signal topology of the LLPs considered in this study.

Here is a list of items which should be considered to improve the analysis :

- Adding neutrals could improve the mass resolution. As said before, the identification of subsequent decays of heavy quarks could in principle improve the resolution.

A jet analysis should also be considered and this will be the preferred choice to get a mass estimate, in case a signal is detected.

- In case of the presence of LLP candidates, a lifetime measurement requires the choice of the “most likely” PV, in the case of multiple PVs in the event. In the present analysis the PV was not explicitly used except for the $|\Delta\varphi|$ calculation. For instance we didn’t impose any explicit cut on the LLP direction, to be coherent with the (most likely) PV.

7.7.2 How to present these Results ?

We are interested to provide results which can be considered as much “model independent” as possible. The central question is how to present them. A solution would be an efficiency map, as a function of the physical variables. In our scenario we have three physical variables : the lifetime and mass of the LLP and the mass of the Higgs. The map should have a sufficient coverage and precision, considering that it is in principle a 3-D matrix. Given the exotic nature of the phenomenon considered, the only possibility to build the map is to use MC events.

Unfortunately we have to observe that a PYTHIA based simulation contains unavoidable theoretical assumptions, on which the efficiency values will depend. For instance the number of tracks in the BV class of models is related to the MSSM branching ratios defined by PYTHIA and by the hadronisation process [26]. Therefore it does not seem possible to be totally model independent. To keep this problem under control, it is important to specify in an exhaustive manner the MC generation context.

In principle, the detector simulation by GEANT needs some further cross-check but it should not contribute more than 10–20% to the systematic error. On the other hand, given the low measurement efficiency a detailed efficiency map cannot be prepared from fully simulated events, but only from a fast simulation capable to reproduce the relevant features of the full simulation. A cross-check and a re-normalisation of the map can be obtained from the comparison with fully simulated events, generated at some chosen points of the parameter space.

As suggested by a recent discussion with some theoreticians, it could be envisaged that this kind of parametrised “fast simulation” could be made public, after validation. The program could be used by non-LHCb members to normalise their models (see the usage of pretty good simulations (PGS) in [118]).

Work is on-going to prepare a preliminary efficiency table and define a fast simulation procedure.

7.7.3 Results from more Points in the BV Parameter Space

To help assessing an efficiency table as discussed in the previous Section, more points in the BV parameter space have been fully simulated. Two more points have been added with slightly lower (5 ps) and larger (15 ps) $\tilde{\chi}_1^0$ lifetimes, two others with lighter $\tilde{\chi}_1^0$ masses (20 GeV and 35 GeV) and finally one with a lower h^0 mass (100 GeV). The parameters of these new points are shown in Table 7.9, along with the h^0 and $\tilde{\chi}_1^0$ properties. The description files steering the various option files for the production of the new samples and their EventType number are listed in Table 7.10.

The new samples have been generated with conditions as close as possible to the most recent data taken in 2010⁶, among others with $\nu = 2.5$. For this occasion and to stay coherent, a new BV48 sample has been re-generated with the same conditions.

Table 7.11 shows the reconstruction efficiency (ϵ) in percent for the considered BV models and for some values of the selection cuts, while Table 7.12 shows the expected number of events for the BV models for an integrated luminosity of 37 pb^{-1} . These tables complete Table 7.6 presented in Sec. 7.4. The BV48_500 is not shown as its efficiency is very small ($\mathcal{O}(10^{-3})$).

Some 50% difference can be observed between the BV48 $\nu = 3$ and new $\nu = 2.5$ samples, between line 7 of Table 7.6 and line 3 of Table 7.11 for example. The BV48 $\nu = 3$ was generated before the start of the 2010 measures, therefore before knowing the 2010 running conditions (beam parameters, ν ...). Since then much development has been achieved in various fields, particularly in the event reconstruction algorithms and in the description of the detector.

It is impossible to interpolate between the points as the measure of the efficiency depends on many factors - such as the kinematics, the reconstruction efficiency w.r.t. the position, the effect of the cuts, etc.

No set of cuts allows the BV20 model to have a number of expected events for 37 pb^{-1} close to 1. When the mass of the $\tilde{\chi}_1^0$ is too small, i.e. 20 GeV, the track multiplicity and reconstructed mass are too small to let a significant number of events pass the cuts.

The probability to find two back-to-back $\tilde{\chi}_1^0$ from the cascade decay of more massive particles is not negligible in some part of the parameter space, as shown in Table 7.13. For 20 GeV $\tilde{\chi}_1^0$, the direct production of neutralinos from quark fusion counts up to 10% of the total cross-section ($\mathcal{O}(10^{-9})$ mbarn). This kind of “background” must be considered in searches

⁶The very same conditions as the $\nu = 2.5$ samples presented in Sec. 7.1.

Model	M_1 [GeV]	M_2 [GeV]	$\tan \beta$	m_{h^0} [GeV]	$m_{\tilde{\chi}_1^0}$ [GeV]	τ [ps]
BV48	63	250	5	114	48	10
BV48_500	63	250	5	114	48	500
BV48_5	63	250	5	114	48	5
BV48_15	63	250	5	114	48	15
BV20	28	250	5	114	20	10
BV35	46	250	5	114	35	10
BV48_mh100	71	250	2.4	100	48	10

Table 7.9: Theoretical mass of the h^0 , the $\tilde{\chi}_1^0$, its lifetime, and the parameters of the models. $\mu = 140$ GeV.

Name	Event type
KaplanNeutralino,mN=48GeV,tN=5ps.dec	45000012
KaplanNeutralino,mN=48GeV,tN=15ps.dec	45000013
KaplanNeutralino,mN=20GeV,tN=10ps.dec	45000060
KaplanNeutralino,mN=35GeV,tN=10ps.dec	45000050
KaplanNeutralino,mN=48GeV,tN=10ps,mH=100GeV.dec	45000070

Table 7.10: The dec files steering the various option files for the production of the new samples, and their EventType number. This table completes Table 4.1. For the significance of the EventType, see Sec. 4.5.

for $h^0 \rightarrow \tilde{\chi}_1^0 \tilde{\chi}_1^0$ with light $\tilde{\chi}_1^0$ masses.

This work needs to be continued for different models, like for instance the Hidden Valley class of models.

	N_{min}^{trk}	M_{min}^{LLP}	σ_r^{max}	σ_z^{max}	N_{evts}^{2010}	$\epsilon^{BV48.5}$ %	ϵ^{BV48} %	$\epsilon^{BV48.15}$ %	ϵ^{BV20} %	ϵ^{BV35} %	$\epsilon^{BV48.mh100}$ %
1	4	3	∞	∞	14645	0.526	0.915	1.02195	0.478292	0.977	0.455
2	8	7.5	0.1	1.0	0	0.134	0.23	0.256	0.029	0.180	0.123
3	6	6	0.05	0.24	0	0.178	0.333	0.379	0.020	0.175	0.169

Table 7.11: Number of 2010 events selected for some values of N_{min}^{trk} and M_{min}^{LLP} (in GeV), and the cuts on the LLP vertex errors σ_r^{max} , σ_z^{max} (in mm). The last columns show the efficiency (ϵ) in percent for the BV models.

	N_{min}^{trk}	M_{min}^{LLP}	σ_r^{max}	σ_z^{max}	N_{evts}^{2010}	$N_{evts}^{BV48.5}$	N_{evts}^{BV48}	$N_{evts}^{BV48.15}$	N_{evts}^{BV20}	N_{evts}^{BV35}	$N_{evts}^{BV48.mh100}$
1	4	3	∞	∞	14645	3.9	6.8	7.6	5.9	10.3	3
2	8	7.5	0.1	1.0	0	0.99	1.7	1.89	0.36	1.9	0.83
3	6	6	0.05	0.24	0	1.31	2.5	2.8	0.25	1.85	1.15

Table 7.12: Number of 2010 events selected for some values of N_{min}^{trk} and M_{min}^{LLP} (in GeV), and the cuts on the LLP vertex errors σ_r^{max} , σ_z^{max} (in mm). The last columns show the expected number of events for the BV models ($L = 37 \text{ pb}^{-1}$).

	N_{min}^{trk}	M_{min}^{LLP}	σ_r^{max}	σ_z^{max}	$N_{evts}^{BV48.5}$	N_{evts}^{BV48}	$N_{evts}^{BV48.15}$	N_{evts}^{BV20}	N_{evts}^{BV35}	$N_{evts}^{BV48.mh100}$
1	4	3	∞	∞	0.86	0.91	0.93	0.35	0.61	0.72
2	8	7.5	0.1	1.0	0.86	0.93	0.94	0.32	0.52	0.79
3	6	6	0.05	0.24	0.88	0.93	0.94	0.38	0.62	0.80

Table 7.13: Fraction of events with the LLPs decaying from a Higgs mother for some values of N_{min}^{trk} and M_{min}^{LLP} (in GeV), and the cuts on the LLP vertex errors σ_r^{max} , σ_z^{max} (in mm).

Conclusion and Outlook

“The state of particle physics is not unlike the one in a symphony hall before the start of a concert. On the podium one will see some but not all of the musicians. They are tuning up. Short brilliant passages are heard on some of the instruments; improvisations elsewhere; some wrong notes too. There is a sense of anticipation for the moment when the concert starts.”

Abraham Pais

The LHC experiments have just started to deliver the first results based on data collected during the year 2010 at $\sqrt{s} = 7\text{ TeV}$, a centre-of-mass energy unprecedented in the history of particle physics. We are at the dawn of a new exciting era of discoveries. Will a Higgs boson show up and complete the Standard Model ? How will it look like ? Will we be able to *see* it ? And what lies beyond the Standard Model, beyond the present frontier of 100 GeV ?

This thesis work started in 2007, during the last phase of commissioning of the LHCb spectrometer. At that time, the structures to hold the Inner Track detector boxes were being set up and the production of the silicon sensor modules was being finalised. During one year and a half, hundreds of modules had to be tested. Their quality had to be assessed to ensure their operation for at least 4 years. From the first mounted detector box, the serial production had to be organised. A great thoroughness and infinite patience was necessary. Indeed the smallest error in the assembly of the very fragile components would have caused irreparable damages. The assembly process was described in details in Chapter 3. Inner Tracker detectors boxes were installed in the LHCb cavern in Summer 2008. After software alignment, the overall precision of the Inner Tracker modules position is on average $19\text{ }\mu\text{m}$ along the relevant direction. The careful box assembly and the quality tests accompanying it allowed to keep the fraction of dead strips below 1%.

The Standard Model of Particle Physics was presented in Chapter 1, along its theoretical and experimental limitations. Then several theoretical

models were discussed extending it in a coherent fashion into a more general framework, emphasising models that predicts long-lived particles that are potentially detectable in LHCb.

Originally conceived for SM events, the simulation software chain was thoroughly reviewed and adapted in order to simulate a subset of the presented models (Chapter 4). This allowed to produce a set of samples with the relevant topologies. The main features of the LLP candidates, such as a long lifetime, therefore a large radial distance to the beam interaction line, a large daughter multiplicity and a high reconstructed mass, were examined at generator level in Chapter 5.

New algorithms and methods had to be developed to reconstruct and select vertices that are consistent with the decay of exotic long-lived particles. These methods were presented in detail in Chapter 6. Key features of the candidates for the selected models were shown, followed by the design of trigger and offline event selections. The concern of building an event selection as inclusive as possible led to an approach based on tracks only. The more delicate jet reconstruction has been left aside for the moment.

The arrival of the first data in 2009 and then the fast increasing luminosity demanded constant monitoring and development of the algorithms. Considerable adaptations were needed to meet the tightening data retention targets, without losing the inclusivity of the selections.

The difficulty of this task has absorbed a large amount of resources. This has forced us to reduce the original goal of this work : evidence or exclusion of the existence of single exotic long-lived particles with a decay in the VeLo region. Instead we have focused on Higgs decay, requiring two LLPs in coincidence.

From simulation, the transverse momentum distribution of the Higgs boson is known to be low enough, so that the two daughters essentially decay back-to-back in the transverse plane of the initial pp collision. Requiring such a configuration offered a drastic reduction of the background while keeping reasonable efficiency on the signal.

In Chapter 7, the whole data-set collected in 2010, representing 37 pb^{-1} , has been analysed to identify secondary vertices which can be associated to the decay of LLPs. The candidates have been combined to reconstruct a parent Higgs boson candidate. The analysis has selected zero candidates, with an efficiency to the signal at the level of 0.2-0.3% for some chosen points in the parameter space of a chosen theoretical model. This allowed to set limits on their production cross-section. The analysis of background MC events is consistent with an expectation of zero event for our integrated luminosity.

Several possible improvements of the analysis have been listed, to improve

the resolution on the mass.

With more data the background will certainly enter the game, in particular $b\bar{b}$ events. To anticipate, we have performed an analysis with weaker cuts and one event has been accepted. This Higgs candidate is likely from two decayed B hadrons which have *stolen* tracks from the PV, increasing artificially their mass. An improvement of the selection method would be to remove tracks from the reconstructed vertex that have a low IP to any of the primary vertices candidates.

This first analysis of exotic displaced vertices is a pioneer work : it has showed the potential of the LHCb detector in an unexplored territory, and has raised numerous questions. Among them is the central question of how to provide results which can be considered as “model independent” as possible, and as a consequence which can be used by theoreticians to put bounds on their models. A solution that has been put forward would be to build an efficiency map, in function of the physical variables. However, given the low measurement efficiency, it is not feasible to prepare a detailed efficiency map from a full detector Monte-Carlo simulation. Another possibility is to provide a fast (parametrised) simulation, validated by the collaboration.

The LHC has seen its first period of data-taking, but the facility is already preparing for the next phase which will run the experiment till 2012. The amount of data collected will amount hopefully 50 times the present data. The LHC adventure has just started.

Appendix A

Properties of the Selected PVs

We present in this section some general properties of PVs reconstructed by the standard (STD) procedure and the one described in this work (OPT). In both cases, at least 5 backward and forward tracks are required in the vertex.

We will refer as the (estimated) “error” (σ) for the component of the covariant matrix of estimated position errors.

The data and MC distributions of the position on the x axis have a larger tail for the OPT reconstruction than STD, as can be seen on Fig. A.1 (*left*). These large x positions come from errors in the reconstruction process or “split” PVs. Those vertices have very large distance to their MC-truth (Fig. A.10). Let us remind you that these vertices are removed in STD by the usage of separation cuts (Sec. 6.1.1).

By looking at the distributions of Fig. A.2, one can see that our MC samples suggest that both schemes provide the same resolution. The distributions in the MC MB are larger than the signal MC for the reason that in the latter only the associated PV producing the LLPs is taken, while in the MC MB, all selected PVs are shown, in particular the “split” PVs and errors.

Figure A.1 (*right*) shows the track multiplicity distributions. Note the discrepancy between the PVs in MC MB and in real data samples, particularly visible in Fig. A.1 (*left*). This discrepancy is studied in Sec. 6.2.3.b. It is more visible at low track multiplicities.

Figure A.3 shows the radial and longitudinal distance to MC-truth with respect to the errors on the position of the selected PVs for both procedures. A correlation is to be seen, highlighted in Fig. A.4. However, cutting on the radial error for instance would also remove candidates with small r^{rec-MC} , while letting too many candidates with large r^{rec-MC} . It does not seem to get improved by the usage of the LSAdaptPVFitter algorithm (STD) instead of LSAdaptPV3DFitter (OPT).

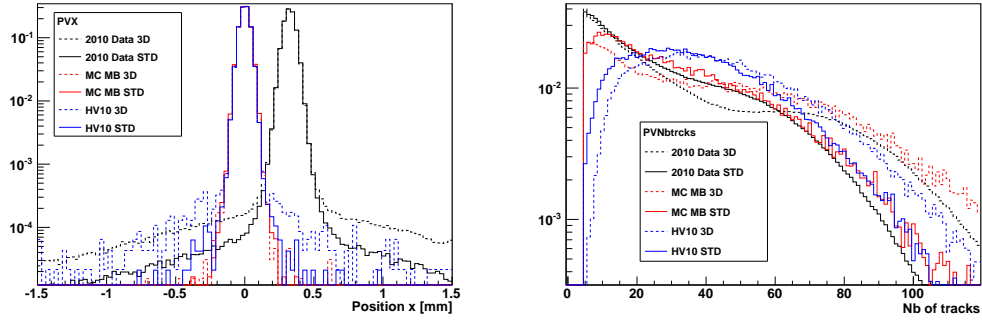


Figure A.1: X position (*left*) and track multiplicity (*right*) of the selected PVs for the standard procedure (STD) and the one defined in this work (OPT).

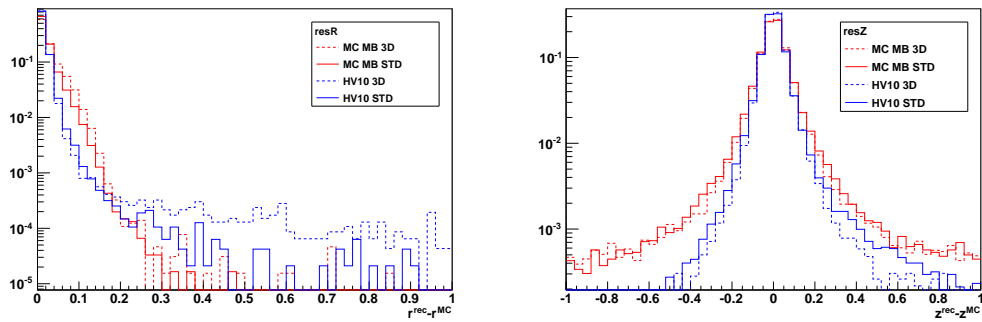


Figure A.2: Radial (*left*) and longitudinal (*right*) difference between the reconstructed and MC-truth positions of the selected PVs for the standard (STD) and the one defined in this work (OPT).

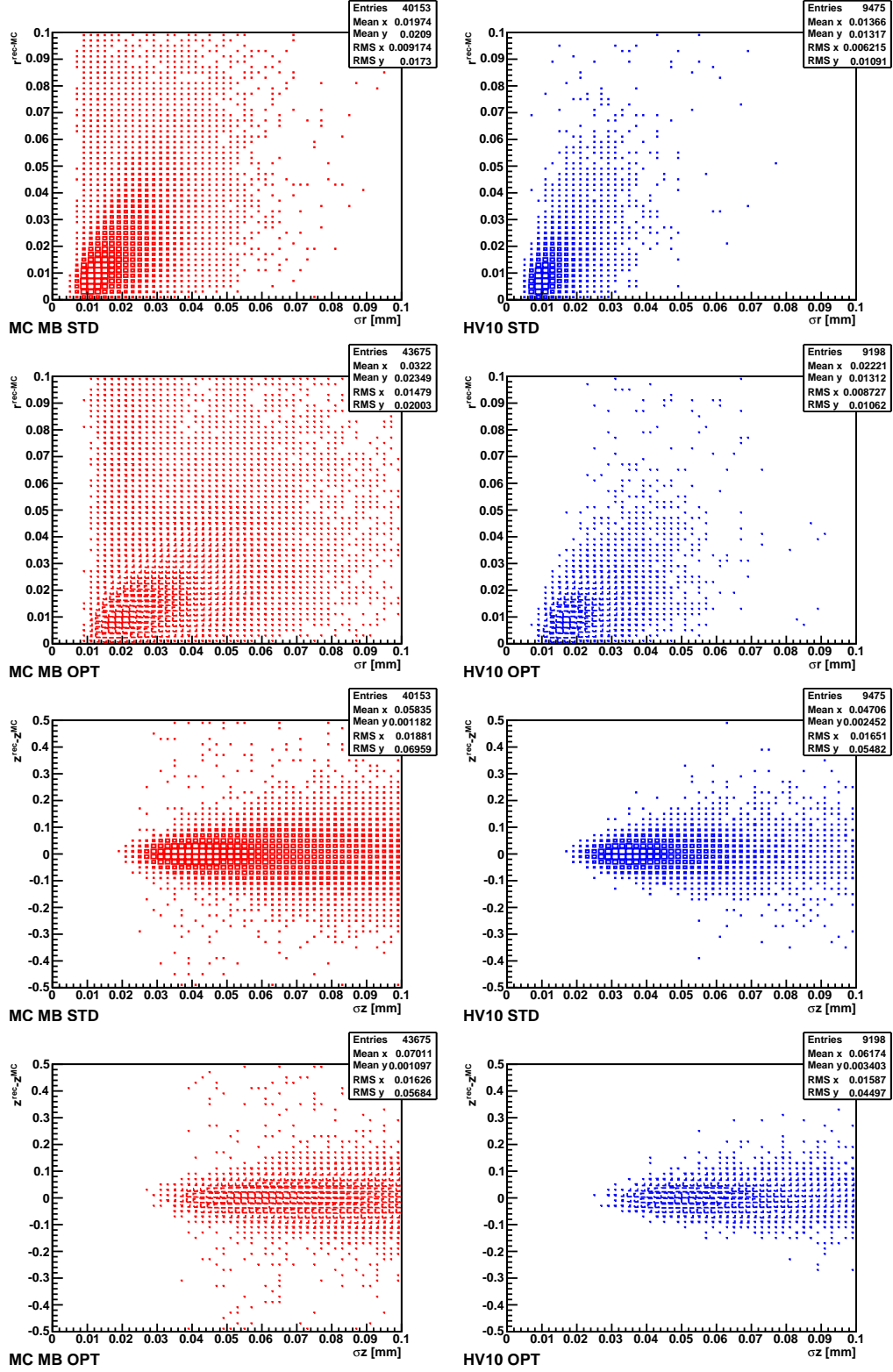


Figure A.3: Radial (*top*) and longitudinal (*bottom*) distance to MC-truth w.r.t. the errors on the position of the selected PVs for the standard (STD) and own (OPT) vertex reconstruction.

The following plots will be presented for STD reconstruction only. However conclusions remains the same for both methods.

Figure A.5 shows the correlation between the track multiplicity and the estimated errors on the position, on the z axis and x-y plan (radial), respectively. Figure A.8 and Fig. A.9 shows the track multiplicity with respect to the z and radial distance to MC-truth, respectively. The distance to MC-truth and errors get lower with the increase of number of tracks in the vertex.

Figure A.6 shows the radial position with respect to the radial error. Cutting on σ_r has proved to be less effective to remove vertices with large reconstructed radial distance.

Figure A.7 shows the longitudinal with respect to the radial errors. A correlation can be seen.

Finally, Fig. A.10 shows the radial position with respect to the radial distance to the MC-truth. A correlation can be seen. It tells us that at larger r this distance is of the same order.

As a conclusion, it must be said that by choosing either method for selecting PVs - the one from the standard or the one from the LLP reconstruction - it is important to keep in mind the process which they were reconstructed from. For each one its own errors. It is important to check the properties of the candidates.

Because of the isolation cuts, it might be safer to use STD. But when the LLP candidates have very short flying distance - $L \sim \mathcal{O}(1)$ mm - the PV may be biased by the presence of the heavy LLP. In that case, using the adequate optimised reconstruction may be more appropriate. And apply further requirements to avoid selecting uninteresting PVs.

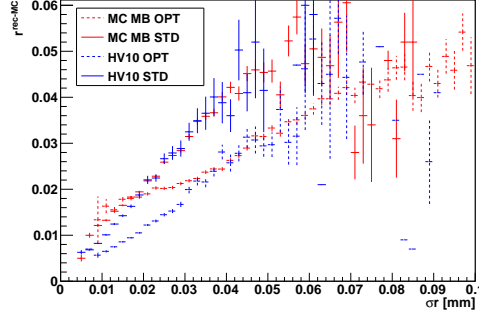


Figure A.4: Correlation between the radial error and distance to MC-truth, for the standard (STD) and own (OPT) vertex reconstruction.

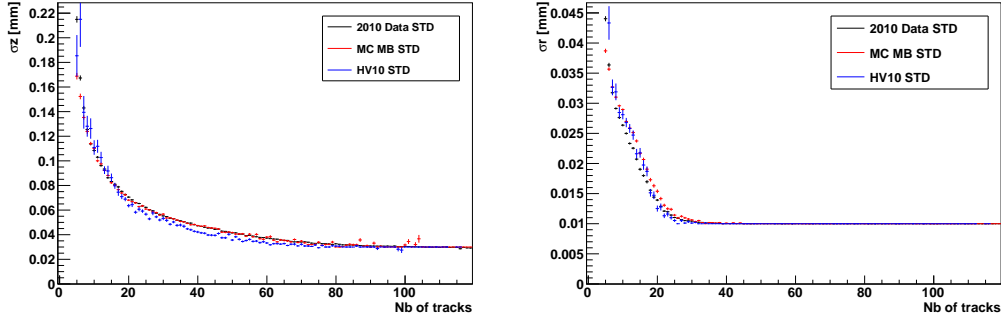


Figure A.5: Correlation between the track multiplicity and the estimated longitudinal and radial error on the position.

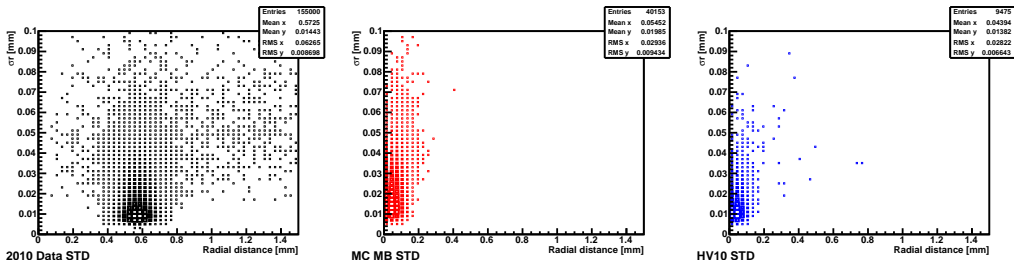


Figure A.6: Radial position w.r.t. the error.

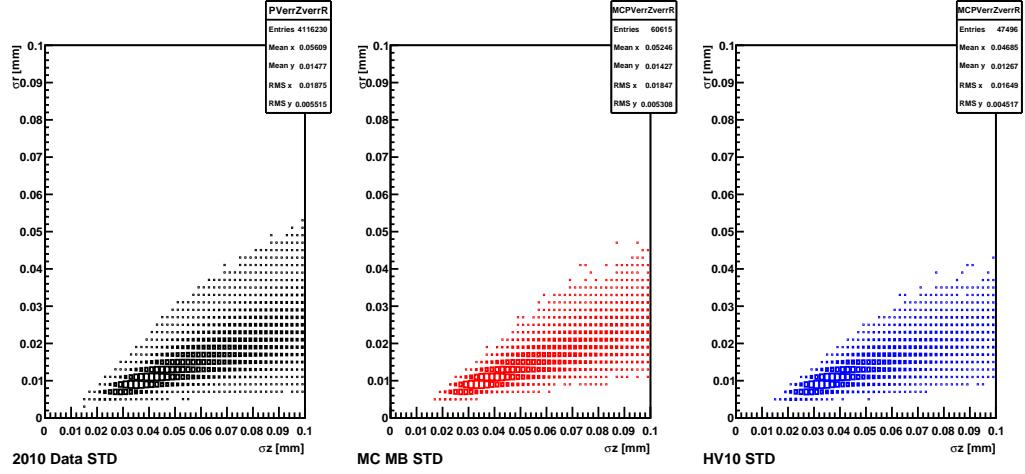


Figure A.7: Longitudinal error w.r.t. the radial error.

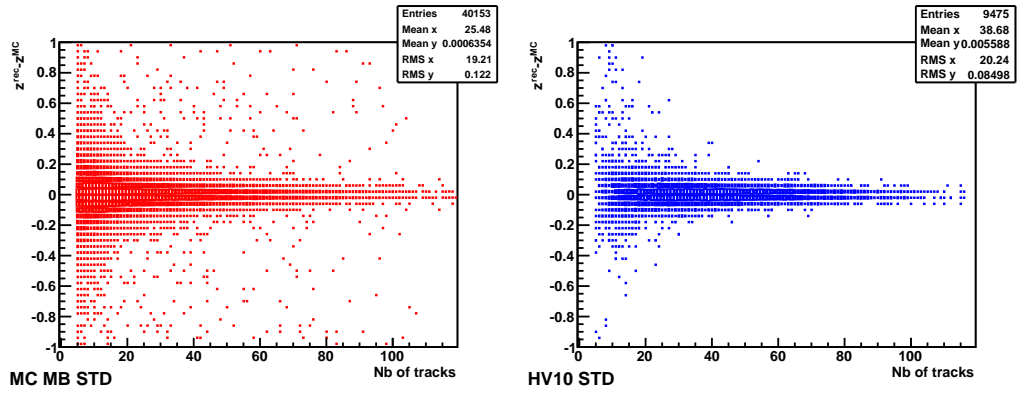


Figure A.8: Track multiplicity w.r.t. the longitudinal distance to MC-truth.

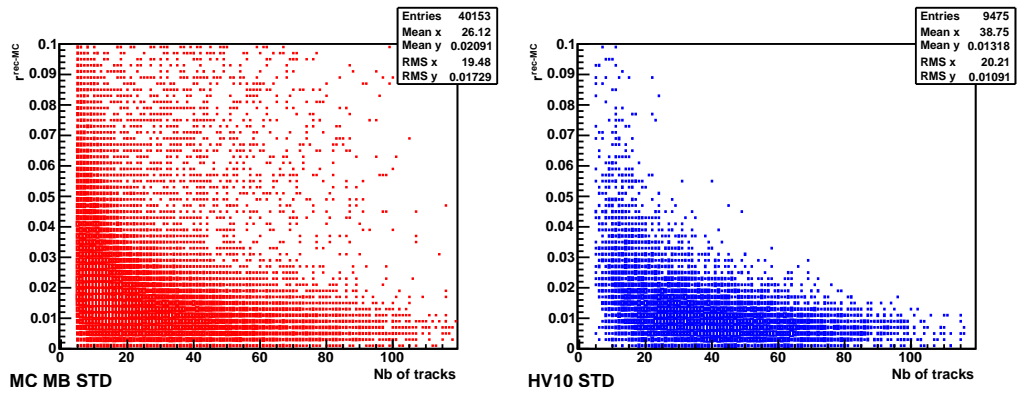


Figure A.9: Track multiplicity w.r.t. the radial distance to MC-truth.

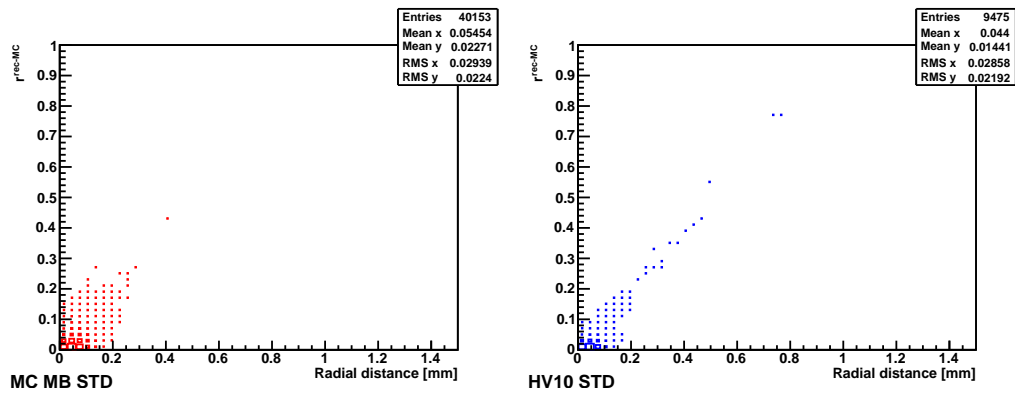


Figure A.10: Radial position w.r.t. the radial distance to MC-truth. A correlation can be clearly drawn.

Appendix B

Optimisation of the Vertex Reconstruction

This Chapter follows Chapter 6.2.1 and gives more details on the optimisation process.

Figure B.2 shows the percentage of MC PVs from MB events that have one associated RV with at least one backward and at least one forward tracks (PV), and at least one other RV with no backward tracks that could become a possible (background) candidate.

In a first phase, the seeding parameters *TrackPairMaxDistance* and *zMaxSpread* have been tried first on the range $[0.1, 1]$ mm and $[0.5, 5]$ mm, respectively. During this process, the other parameters are kept to their default value, with the exception of *PVsChi2Separation* and *PVsChi2SeparationLowMult* which have been set to infinity (no spatial cuts). LSAdaptPV3DFitter has been used.

Considering Fig. 6.3, B.1 and B.2, we can see that *TrackPairMaxDistance* and *zMaxSpread* in the ranges $[0.2, 0.3]$ mm and $[1, 4]$ mm, respectively, provide the highest reconstruction efficiency for the MC signal while keeping the probability to split the PVs and RVs at their lowest values. The reconstruction efficiency with respect to the distance to the MC PV shows only negligible variations on the considered interval. The radial resolution remains unchanged, while slight variations can be observed for the z coordinate ($\delta\text{RMS} \sim \pm 0.02$ mm).

For the remainder of the optimisation process, two points with opposite directions of the (*TrackPairMaxDistance*, *zMaxSpread*) parameter space have been retained : (0.2,1) and (0.3,3), fulfilling the criteria. For the sake of simplicity, only the plots made with (0.2,1) are shown, the conclusions remaining the same for both points.

In a second phase $\sqrt{trackMaxChi2}$ ($\sqrt{\chi_{IP,max}^2}$) and $\sqrt{trackMaxChi2Remove}$ ($\sqrt{\chi_{IPR,max}^2}$) have been varied over $[1, 7]$ for both LSAdaptPVFitter and LSAdaptPV3DFitter. We immediately note that these parameters have a much larger impact on the result of the reconstruction.

All values starting from $\sqrt{\chi_{IP,max}^2} \geq 3$ (and $\sqrt{\chi_{IP,max}^2} \geq 2$) for LSAdaptPVFitter (LSAdaptPV3DFitter) show reconstruction efficiencies of $\sim 80\%$ for both the HV10 and BV48 samples. The probability to split the RVs gets lower as one moves away from the diagonal (see Fig. B.2).

The reconstruction efficiency with respect to the MC PV decreases with the increase of $\sqrt{\chi_{IPR,max}^2}$. To get a picture, the reconstruction efficiency at 2 mm is about 80%, 70% and 60% of the one 4 mm away for the points (3,3), (3,5) and (3,7), respectively, in the $(\sqrt{\chi_{IP,max}^2}, \sqrt{\chi_{IPR,max}^2})$ parameter space.

The resolution follows the same tendency as the splitting probability of the PVs. The more splitting, the larger the resolution. It is essentially the same both LSAdaptPVFitter and LSAdaptPV3DFitter. The same trend can be observed in sample BV48.

From all the above considerations, the (3,5) default point has been kept for both LSAdaptPVFitter and LSAdaptPV3DFitter.

Finally, the impact of $maxIP2PV$ has been tested on the range $[0.25, 5]$ mm for the LSAdaptPV3DFitter tool. Setting $maxIP2PV = 2$ mm ensures a very efficient preselection of the tracks for the track fit and allows an average gain in CPU time of 0.1 ms compared to $maxIP2PV = \infty$

The other parameters entering the reconstruction process play secondary roles. Values defined by default in the tools are kept. Optimisation of $PVsChi2Separation$ and $PVsChi2SeparationLowMult$ is kept for the optimisation of trigger and stripping selections.

The purity of the reconstructed candidates remains higher than 99% for the whole of all the tested parameter ranges.

The average CPU time consumed per event is very stable over the considered ranges of parameters. It never varies more than 10 – 30%. The usage of LSAdaptPV3DFitter instead of LSAdaptPVFitter reduces the CPU time consumption by $\mathcal{O}(20\%)$, as the latter, adapted for off-line use (see Sec. 6.1.1), makes use of track extrapolators and other CPU intensive tools.

For simplicity, the development of the tools for the selection of the RVs has been performed using LSAdaptPV3DFitter with default values for both HLT and off-line contexts. Conservative values of PVSeed3DTool have been set : $TrackPairMaxDistance = 0.2$ mm and $zMaxSpread = 1$ mm.

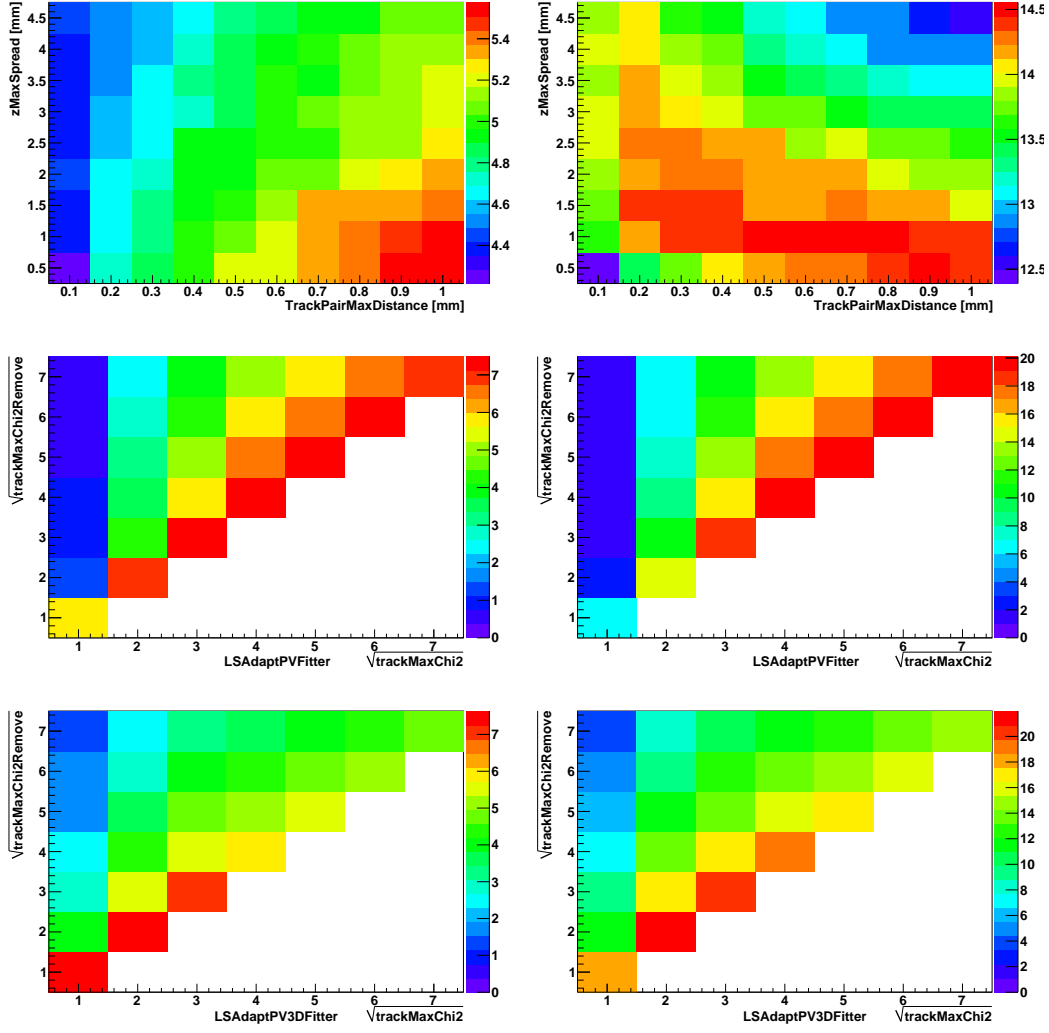


Figure B.1: Percentage of MC LLP decay vertices that have been split in two or more RVs, for BV48 (*left*) and HV10 (*right*), as a function of some the reconstruction parameters.

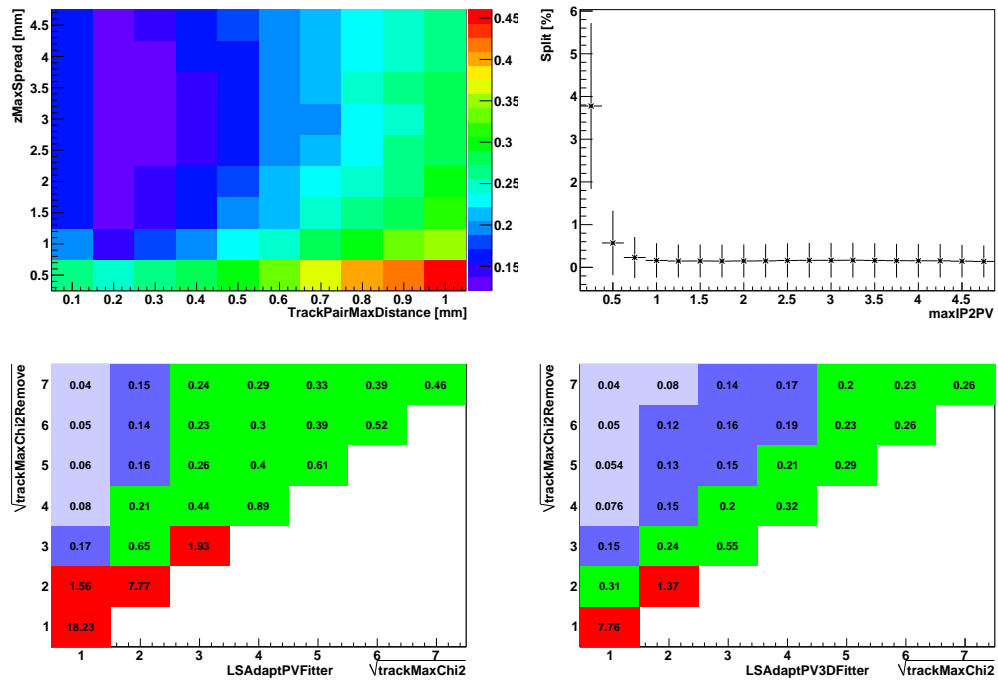


Figure B.2: Percentage of MC PV that have at least 2 associated reconstructed vertices, in MB events, as a function of some the reconstruction parameters.

Appendix C

Re-Optimisation of the Vertex Reconstruction

This Chapter shows the details of the re-optimisation process of the vertex reconstruction done after the basic ideas of the selection of LLP candidates have been lay out. The same protocol has been followed and the same criteria used as in Sec. 6.2.1 and Sec. B, but on the selection of RVs with a reconstructed mass $M > 6$ GeV and a radial distance to the z axis $R > 0.3$ mm.

Figure C.1 shows the LLP MC candidate reconstruction efficiency for BV48 (*left*) and HV10 (*right*). Two main facts are to be noted. The first one is the secondary roles played by $zMaxSpread$ and $TrackPairMaxDistance$ once $\sqrt{\chi_{IP,max}^2}$ and $\sqrt{\chi_{IPR,max}^2}$ are set. Their effect become almost negligible. Second point is the lower reconstruction efficiency for LSAdaptPVFitter : $\sim 10\%$. In the “3D” version, the computed track errors are generally larger, which allows more tracks to get assigned to a vertex. This fact becomes more obvious with the tighter mass requirement.

Figure C.2 gives a view of the percentage of MC LLP decay vertices that have more than one associated RV.

At that point, one may wonder what is the percentage of split MC PV furnishing a vertex with no backward tracks and a radial distance greater than 0.3 mm.

Figure C.3 points towards keeping values of $TrackPairMaxDistance$ and $zMaxSpread$ as low as possible. It also suggests trying $\sqrt{\chi_{IP,max}^2} = 3 - 4$ and $\sqrt{\chi_{IPR,max}^2} = 7$ for LSAdaptPVFitter to help reduce the rate of vertex pollution from split PVs.

Figure C.3 (*top right*) shows the distribution of the radial distance R of those “split” PVs for some parameter values discussed above. In general,

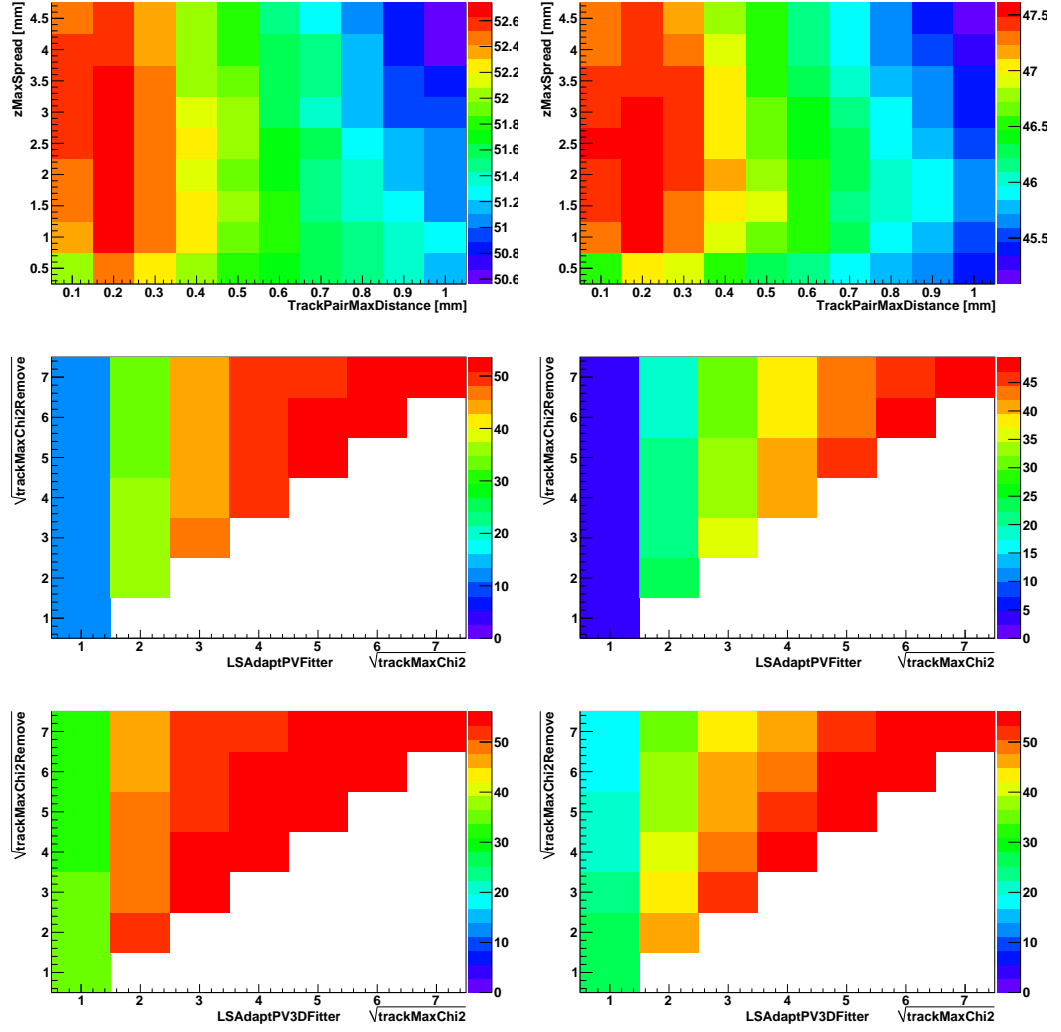


Figure C.1: LLP MC candidate reconstruction efficiency for BV48 (*left*) and HV10 (*right*). Same as Fig. 6.3, with $M_{RV} > 6$ GeV and $R > 0.3$ mm.

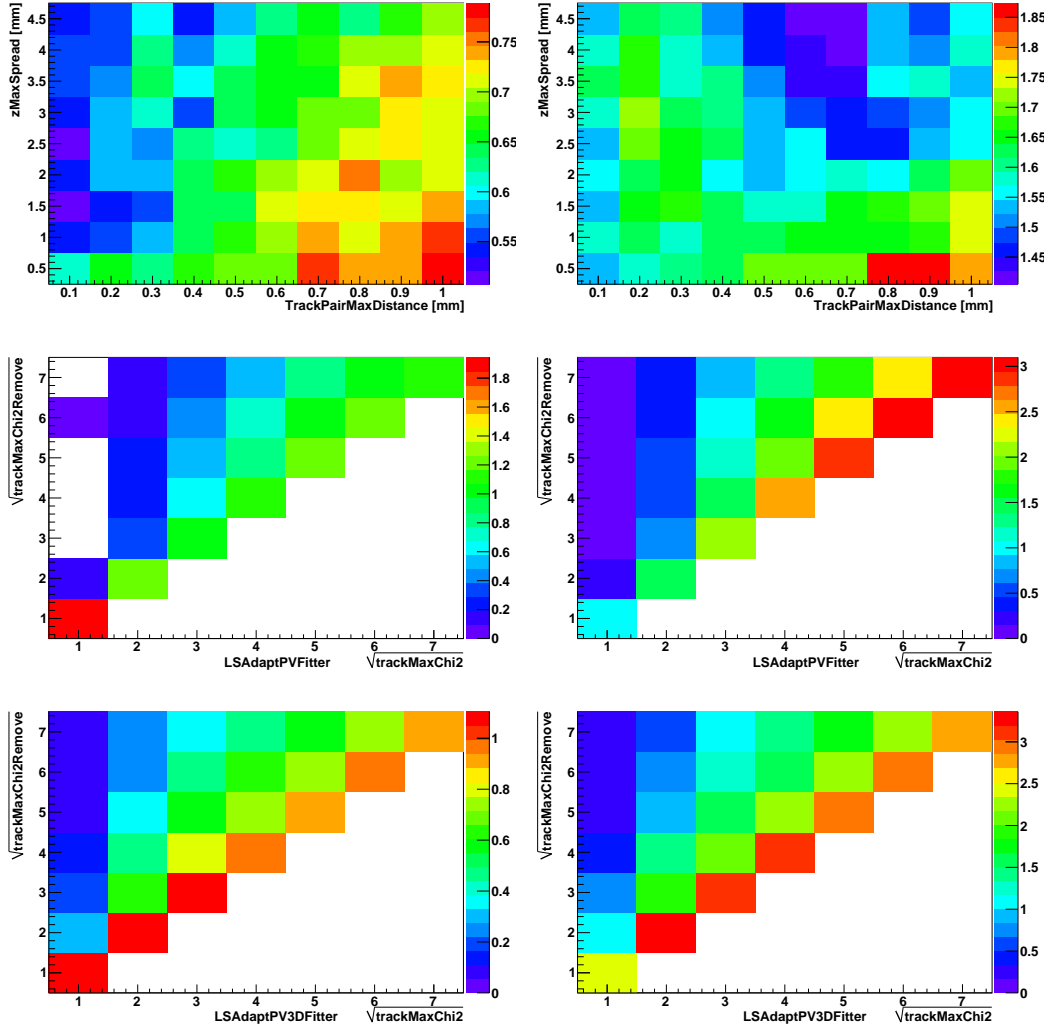


Figure C.2: Percentage of MC LLP decay vertices that have more than one associated RV, for BV48 (*left*) and HV10 (*right*). Same as Fig. B.1, with $M_{\text{RV}} > 6 \text{ GeV}$ and $R > 0.3 \text{ mm}$.

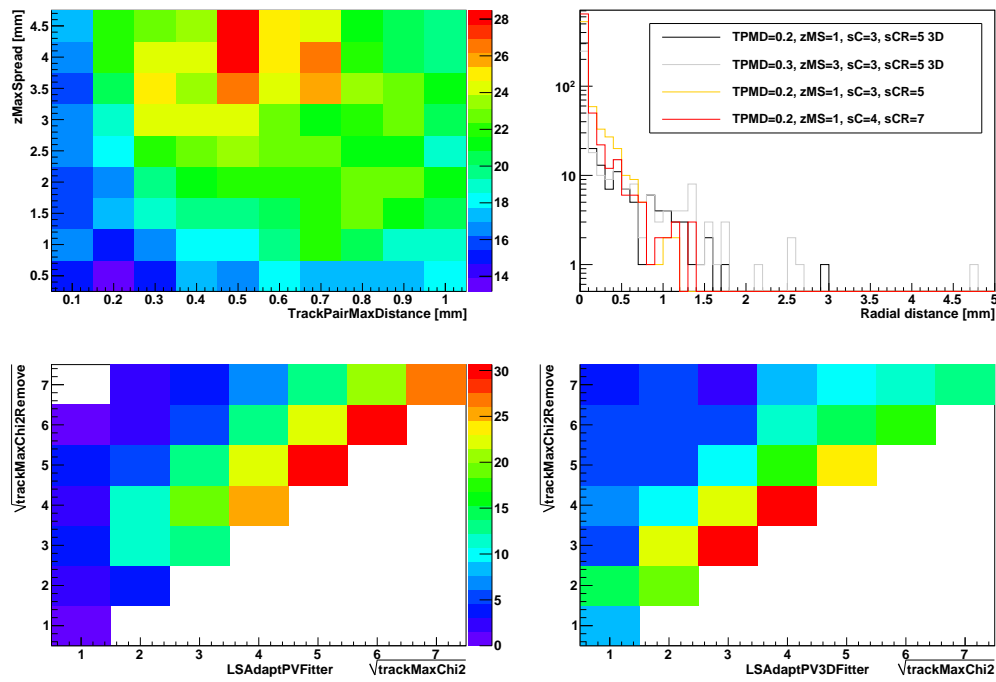


Figure C.3: Percentage of the “split” MC PV providing a vertex with no backward tracks and a radial distance to the z axis greater than 0.3 mm. *Top right* : distribution of the radial distance of the split vertex for certain parameters.

all values provide very similar distributions, but due to the limited MC MB available, it is difficult to draw any trend. Using LSAdaptPVFitter instead of LSAdaptPV3DFitter does not seem to reduce the maximal radial distance. Split vertices with large R ($\mathcal{O}(1)$ mm) have in general also large z distance ($\mathcal{O}(10)$ mm).

To close this chapter, we should stress that the optimisation always depends on what final objects are wished. If, for instance, we are interested only in vertices that are very radially distant from the beam interaction region ($R > \mathcal{O}(5)$ mm or $|z| > 300$ mm), we can choose a set of parameters based only on the reconstruction efficiency (high $\sqrt{\chi_{IP,max}^2}$ and $\sqrt{\chi_{IPR,max}^2}$ values), irrespectively on their incidence on the PVs.

Finally, Table 6.3 sums up the values of the parameters of the standard PV procedure and the one retained for the procedure optimised for LLP selection.

Appendix D

The Three Trigger Selections

Three trigger “lines” (selections) have been designed to filter events with displaced vertices¹. Chosen parameter values of the tools used for the reconstruction are shown in Table E.1. The parameters used for the development of the algorithms (see Sec. 6.2.1) were also kept for the development of the trigger lines, as they provided satisfactory results.

We have kept the default isolation cuts $PVsChi2Separation= 25$ and $PVsChi2SeparationLowMult= 91$, which were found to have a small impact on the signal MC, while achieving a large reduction of the background. For example, they reduce the retention of BV48 candidates ($m > 6 \text{ GeV}$, nb of track > 10 , $r > 0.3$) by 0.6%. They affect mostly low mass ($< 10 \text{ GeV}$) and low track multiplicity (< 10) candidates

The HLT is configured via a unique key, named TCK, that defines the sequence of algorithms, and their cuts. The quasi totality of the 2010 data have been taken with two sets of trigger settings, coded as TCK 0x002e002a and 0x002e002c. They differ only by the reduction of the cut on the SPD multiplicity from 900 to 450 maximum, applied in the hadron and electron (photon) triggers. As the latter cut has only a limited impact of $\sim 1\%$ on our signal, we will consider only TCK 0x002e002c in the following of this study.

Table 6.4 shows the values of the different cuts used in the selections. To meet the requirements of staying close to the allowed 1 Hz, additional cuts on the square root of the radial and z component of the position error matrix were set at $\sigma_r^{max} = 0.1 \text{ mm}$ and $\sigma_z^{max} = 1 \text{ mm}$. They will be justified in Chap. 7.

As both $RCutMethod = \text{”FromBeamLine”}$ and $RCutMethod = \text{”FromUpstreamPV”}$ (see Sec. 6.2.3.a) gave similar results on the test raw data-set, “FromUpstreamPV” was kept at this stage for simplicity.

¹See Sec. 2.3.3 for a presentation of the trigger system.

It was found that the best strategy was to have one line requesting at least one candidate with tighter cuts (Hlt2SingleLonglived) and a second line requesting at least two candidates with very loose cuts (Hlt2DoubleLonglived). This allows to maximise the efficiency for the signal featuring a mother decaying into two LLPs. The third line (Hlt2SinglePSLonglived), heavily prescaled, is there only for providing some amount of candidates with low reconstructed mass, and also to control the effect of the σ cuts.

The trigger retention rates for some selected models (for TCK 0x002e002c) are summed up in Table D. Only the lines firing more than 1% are shown. L0Global stands for the level-0 decision, Hlt1Physics (Hlt2Physics) for the “and” between all the Hlt1 (Hlt2) physical lines. Hlt2DisplVertices (Hlt2Topo) refers to the “and” between the DisplVertices (topological) lines. Keep in mind that the samples have been simulated with a higher mean number of interaction per bunch crossing $\nu = 3$, instead of $\nu = 2.5$, which is closer to the reality.

Without surprise, the L0 hadron line is the most firing. While the L0 is very efficient ($\sim 100\%$) for events with a heavy candidate ($m > 5 \text{ GeV}$), the HLT1 efficiency is very low.

For BV48 events with at least one candidate with more than 6 tracks, $r > 0.3 \text{ mm}$ and $m > 6 \text{ GeV}$, the HLT1 efficiency is 41.4%. The Hlt2DisplVertices retention is 28.2%, while it would increase to 68% if the decision would be taken irrespectively of any HLT1 decision.

The problem has been tracked down to the Hlt1Track lines [116]. The event reconstruction begins with the VeLo pattern recognition and PV finding. In essence, VeLo tracks are selected according to their IP and track quality and are extrapolated to the tracking stations in order to measure their momentum. A final event selection is performed based on the track momentum, p_T , χ^2 , and χ^2_{IP} .

Part of the loss of efficiency comes from the fact that the LLP candidate is found among the PVs and the algorithms triggers on the tertiary products, with respect to the LLP or the PV. The values of the cuts are optimised for the retention of B signals, which we may not have. The IP and p_T cuts have also been identified as serious signal killers. Indeed, the p_T distributions of the products of the B meson decay are narrower when the B has been produced by an exotic LLP. Another source of worries is the cut on the number of hits assigned to the VeLo track. This strategy is clearly not adapted for very long lifetimes. A proposal has been made to recover part of the loss, in time for the 2011 data runs.

The HLT2 topological lines in their latest form [115] are found to have good retention on most exotic signal. They are designed to trigger efficiently on all n-body B decays ($n=2,3,4$, for the 3 lines) and their optimisation

and cuts are adapted for B mesons only. They follow a different inclusive strategy, based on a good PV recognition and the topology of SM B mesons production.

It is not known precisely on what kind of objects they really trigger on. It was just observed a very unequal retention with respect to the track multiplicity and reconstructed mass. What is more, we do not want to trigger only on candidates decaying into b quarks, but eventually also in the other flavours. For those reasons, it would be dangerous to rely only on the topological lines.

Finally, Table D shows the retention for BV48 simulated with $\nu = 1$. With the increase of the mean interaction multiplicity from 1 to 3, we observe a loss of 21.2% of the triggered data. This gives us an idea of the effect of the GEC (see Sec. 2.3.3.d) on our samples.

Line	BV48	BV48 $\nu = 1$	BV48_500	BV38	BV98	BV198	BRpVb	BRpVmuq
L0Global	0.527	0.589	0.525	0.775	0.733	0.71	0.724	0.921
L0DiMuon	0.044	0.018	0.038	0.055	0.048	0.046	0.096	0.278
L0Electron	0.192	0.25	0.205	0.457	0.408	0.405	0.384	0.349
L0Hadron	0.393	0.499	0.4	0.689	0.643	0.63	0.597	0.573
L0Muon	0.147	0.1	0.129	0.178	0.17	0.147	0.268	0.839
L0MuonHigh	0.098	0.069	0.087	0.127	0.117	0.105	0.213	0.813
L0Photon	0.104	0.153	0.106	0.228	0.206	0.199	0.18	0.176
Hlt1Physics	0.22	0.268	0.08	0.286	0.305	0.286	0.259	0.471
Hlt1TrackAllL0	0.175		0.035	0.186	0.211	0.191	0.165	0.236
Hlt1TrackMuon	0.017		0.003	0.013	0.014	0.011	0.036	0.138
Hlt1TrackPhoton	0.056		0.024	0.092	0.1	0.089	0.072	0.075
Hlt2Physics	0.156	0.198	0.03	0.17	0.184	0.17	0.133	0.344
Hlt2DisplVertices	0.108	0.144	0.009	0.084	0.117	0.109	0.03	0.124
Hlt2DisplVerticesDouble	0.047		0.001	0.009	0.018	0.014	0.006	0.015
Hlt2DisplVerticesSingle	0.1		0.009	0.081	0.114	0.107	0.027	0.123
Hlt2Topo	0.097	0.124	0.011	0.116	0.096	0.075	0.077	0.07
Hlt2TopoOSTF2Body	0.079		0.007	0.094	0.076	0.06	0.056	0.055
Hlt2TopoOSTF3Body	0.065		0.007	0.085	0.06	0.045	0.05	0.042
Hlt2TopoOSTF4Body	0.04		0.005	0.057	0.033	0.022	0.03	0.022

Table D.1: Trigger retention rates for some selected models. TCK 0x002e002c has been used. Only the lines firing more than 1% are shown. L0Global stands for the level-0 decision, Hlt1Physics (Hlt2Physics) for the “or” between all the Hlt1 (Hlt2) physical lines. Hlt2DisplVertices (Hlt2Topo) refers to the “or” between the DisplVertices (topological) lines. Unless specified, $\nu = 3$.

Appendix E

The Four Stripping Selections

During the first half of the 2010 runs, the parameters of the reconstruction were the same as those used in the trigger. They were later reviewed and we decided to switch to the one presented in Table E.1. Larger, these parameters allow a greater acceptance of MC signal, especially with B mesons among the decay products of the exotic LLP. The subsequent increase of data retention was found manageable with light increase of the mass cut. It was then not possible to adapt this decision to the HLT2 lines for the second half of the 2010 runs.

For the 2011 runs, it is planned to use the off-line intended LSAdapt-PVFitter, to work with the full error parametrisation of the tracks. This tool is now perfectly adapted to the reconstruction of distant vertices and all discrepancies observed with LSAdaptPV3DFitter are understood.

To complete our physical goals and meet the requirement of a maximum retention per line smaller than 0.05% on the data kept by the trigger, our selection was divided into 4 individual lines. The strategy remains the same as for the trigger, with the difference that the “Single” line has been split in 2. SingleLowMass is dedicated to low mass candidate. To keep the retention to an acceptable level, the matter veto (see Sec. 6.2.3.d) has been activated. SingleHighMass aims at selecting very massive candidates. No detector veto are applied. The Single line, heavily prescaled, is there only for providing some amount of candidates with low reconstructed mass.

A line dedicated to decays containing a high p_T muon has been used in some older stripping. The present lines cover efficiently this kind of decay without the need to apply a cut on a possible muon.

For the big reprocessing of the 2010 data, Table 6.4 sums up the cuts applied and the retention achieved on the triggered data. Note that the σ cuts were not repeated in the stripping framework, as the isolation cuts. On the small datasets used for the optimisation of the lines, both methods

	HLT2	Stripping	Standard
PVSeed3DTool			
<i>MinCloseTracks</i>	3	3	4
<i>TrackPairMaxDistance</i>	0.2 mm	0.3 mm	0.3 mm
<i>zMaxSpread</i>	1 mm	3 mm	3 mm
LSAdaptPV3DFitter			
<i>MinTracks</i>	4	4	5
<i>trackMaxChi2</i>	9	9	9
<i>trackMaxChi2Remove</i>	25	25	25
<i>maxIP2PV</i>	2 mm	2 mm	2 mm

Table E.1: Summary of the standard and chosen parameter values of the tools used for the reconstruction.

to remove vertices in the beam interaction region (see Sec. 6.2.3.a) showed similar results. Our choice fell on the rejection method based on the radial distance to the measured beam line¹ for the following reasons : high precision rejection on very large data-set in a high ν environment is crucial for final analysis, as much as a robust PV selection. Both require to know precisely the position of the beam line. What is more, these information may be very useful in the final analysis. If they are not reconstructed on-line or during the stripping process, the available statistics in each runs in the output stream of each line is not sufficient to rebuild safely this information.

Table E, in turn, shows the efficiency of the lines on the selected MC samples, with in parenthesis the efficiency with the trigger applied. The events have been re-weighted to simulate a mean number of interactions closer to the one observed in the 2010 data $\mu = 2.5$.

¹ *RCutMethod* = "FromBeamLine".

Model	Single	SingleLowMass	SingleHighMass	Double	OR
BV48	0.697 (0.254)	0.220 (0.075)	0.293 (0.146)	0.254 (0.122)	0.555 (0.226)
BV48_500	0.580 (0.180)	0.135 (0.038)	0.187 (0.090)	0.033 (0.014)	0.335 (0.131)
BV38	0.697 (0.322)	0.167 (0.067)	0.254 (0.150)	0.057 (0.037)	0.441 (0.228)
BV98	0.731 (0.328)	0.178 (0.070)	0.341 (0.201)	0.095 (0.060)	0.538 (0.276)
BV198	0.735 (0.322)	0.188 (0.069)	0.359 (0.204)	0.080 (0.047)	0.564 (0.277)
HV10	0.685	0.263	0.187	0.341	0.587
BRpVmuq	0.753 (0.576)	0.078 (0.050)	0.551 (0.467)	0.100 (0.085)	0.638 (0.521)
BRpVb	0.510 (0.234)	0.151 (0.071)	0.113 (0.069)	0.085 (0.051)	0.311 (0.163)

Table E.2: Retention efficiencies of the stripping DisplVtx lines for some selected MC models. The efficiencies with the trigger applied are given in parenthesis when available. “Or” refers to the logical OR between the SingleLowMass, SingleHighMass and Double lines.

Appendix F

More Figures

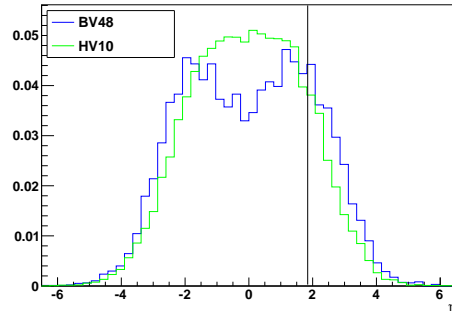


Figure F.1: Pseudorapidity distributions of the LLP determined at generator level for some selected models. Distributions are normalised to unity. The vertical bar at 1.8 indicates the chosen generator cut.

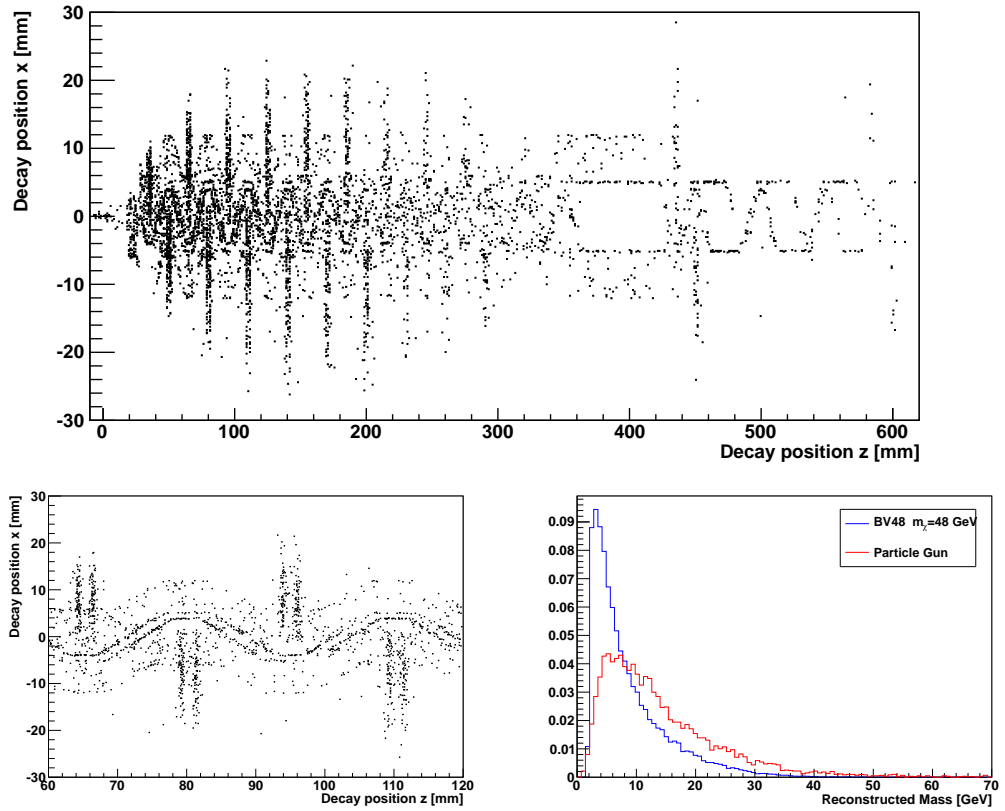


Figure F.2: Position in the X-Z plan and reconstructed mass of vertices from interaction of flying particles with the matter of the detector from the PG sample (see Sec. 6.2.3.d). Their reco. mass is very similar to the one of $\tilde{\chi}_1^0$ from BV48, and the sensors and RF-Foil are clearly identifiable.

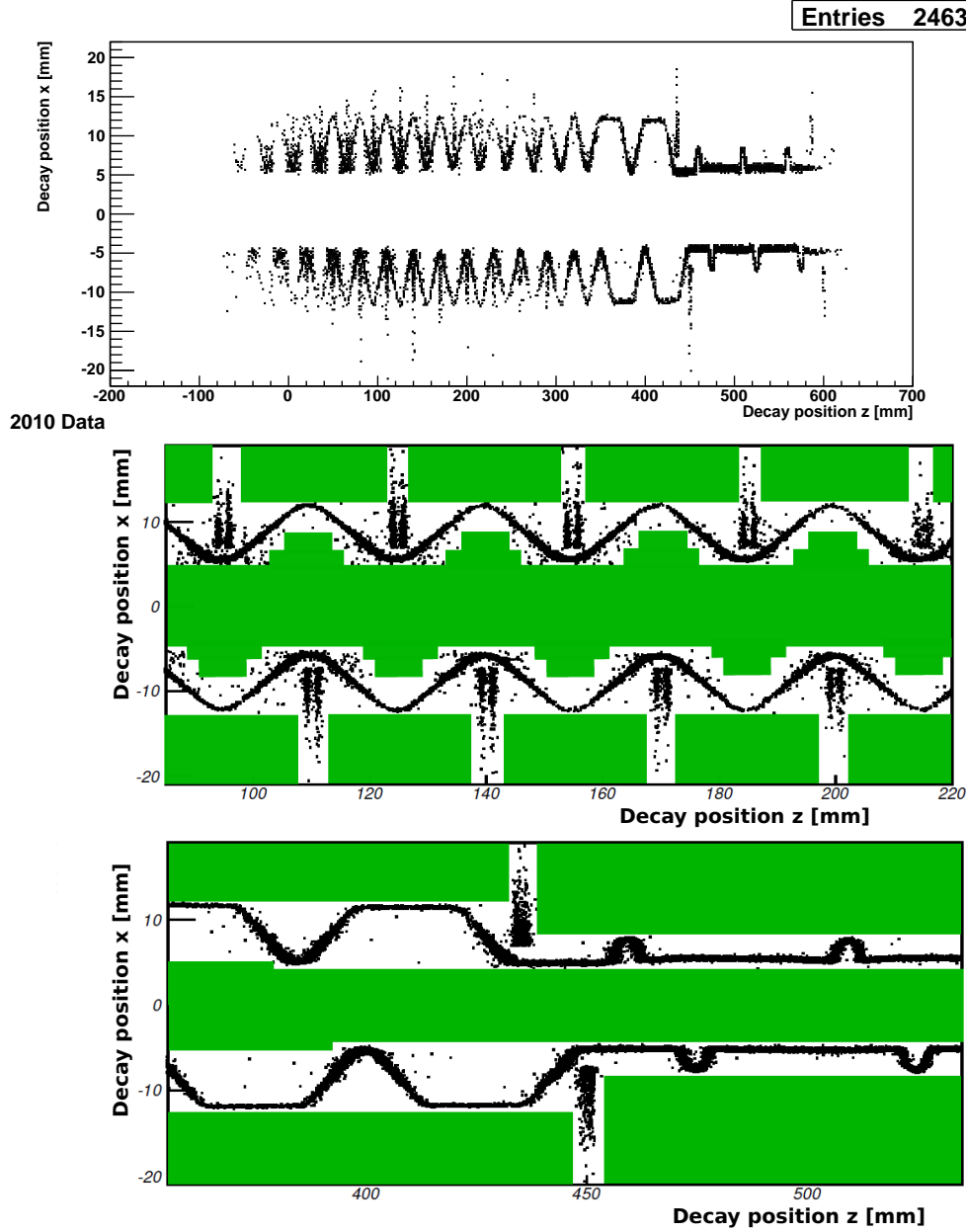


Figure F.3: Position for a 2 mm slice in y of the RVs from 2010 data removed by the “matter veto” (see Sec. 6.2.3.d). The two bottom figures are zooms on small z and high z regions in the VeLo. The green boxes show the signal acceptance region. A full scan in longitudinal slices can be viewed in [117].

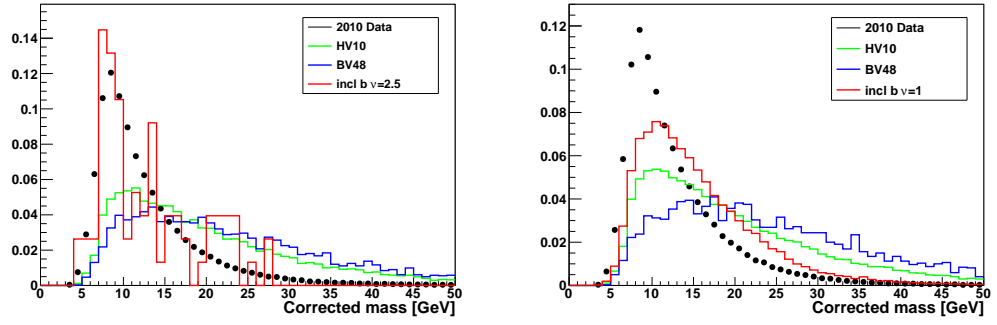


Figure F.4: Corrected mass $m_{\text{corr}} = \sqrt{m^2 + |\mathbf{p}'_{\text{Tmissing}}|^2} + |\mathbf{p}'_{\text{Tmissing}}|$ for MC events and data events. $\mathbf{p}'_{\text{Tmissing}}$ is the missing momentum transverse to the direction of flight of the candidate, obtained from the PV and decay RV. In the absence of a procedure to associate the candidates with their respective PVs, an unique PV is requested in the event and used as the PV.

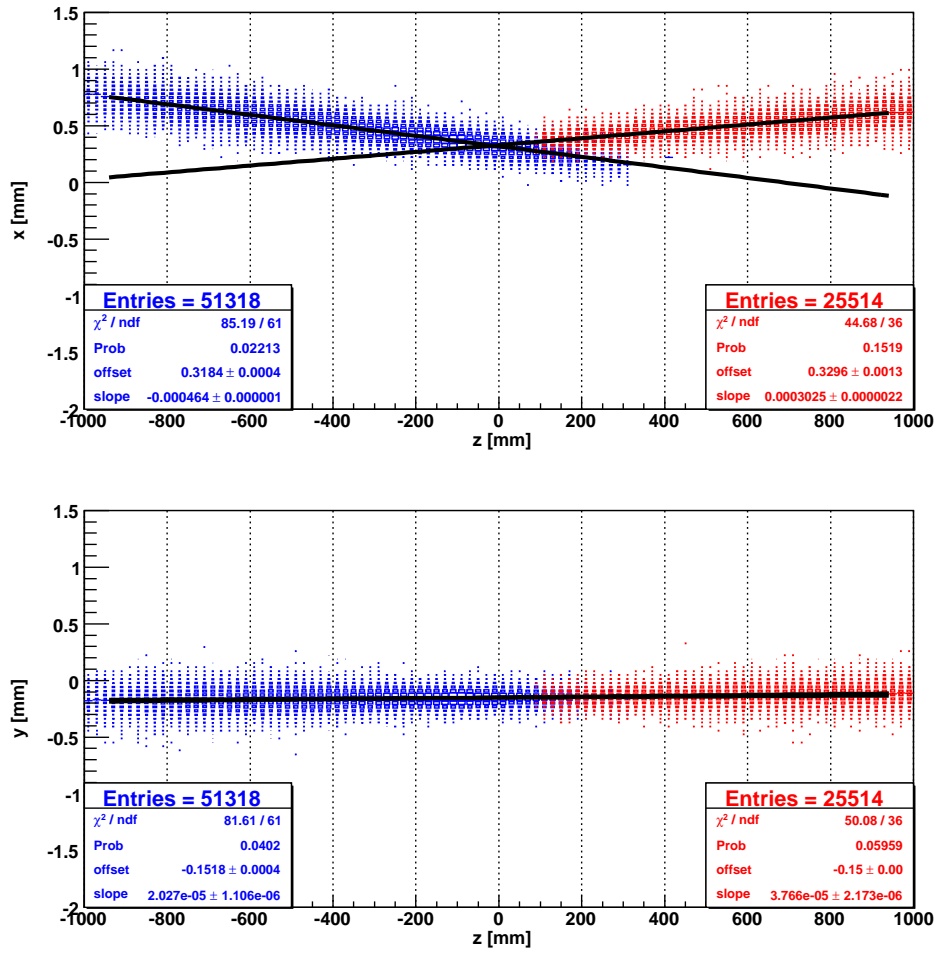


Figure F.5: Positions of the two beams, done by fitting the positions of RVs from beam-gas interactions (fill 1443) [112]. At least ten tracks are required in the vertex and all tracks in the same direction.

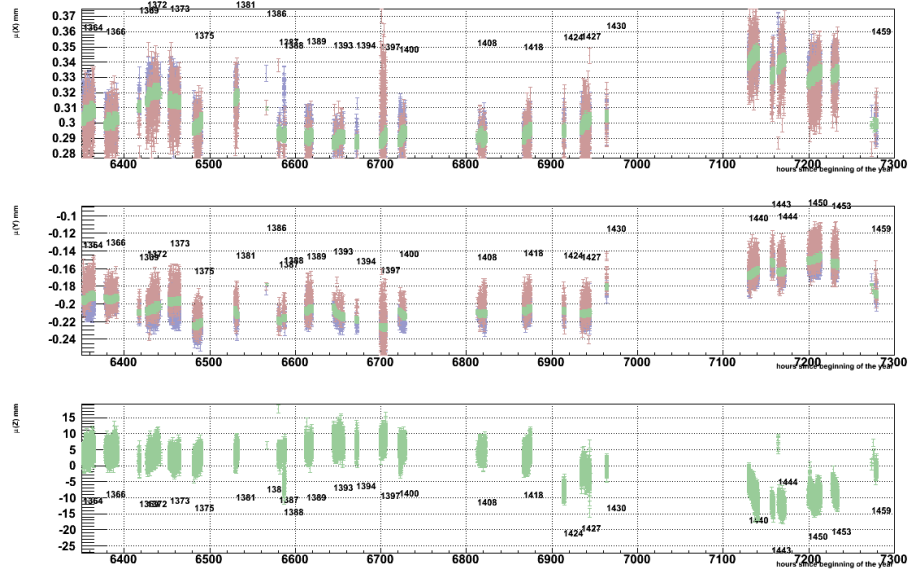


Figure F.6: Variation of the average position in mm of the beam line over time (from top to bottom: x, y, z) [124]. Within a fill (consecutive entries marked with a number, i.e. 1369), the variation is less than $10 \mu\text{m}$, while between the fills it can be as high as $50 \mu\text{m}$.

Acronyms

Please find below a list of the numerous acronyms used in this thesis and their meaning.

AMSB	anomaly mediated supersymmetry breaking.....	19
ATLAS	a toroidal LHC apparatus	
BEAMS	beam pipe approach monitoring system	
BSM	beyond the Standard Model	10
$B\bar{P}_R$	bilinear R-parity violation	27
CERN	european organisation for nuclear research	
CM	center-of-mass	39
CMB	cosmic microwave background	8
CMS	compact muon solenoid	
DSS	detector safety system	73
DST	data summary tape	63
DoCA	distance of closest approach	116
DV	displaced vertex	115
ECAL	electromagnetic calorimeter	46
ED	extra dimensions	36
FCNC	flavour changing neutral currents	19
GEC	global event cuts	61
GMSB	gauge-mediated supersymmetry breaking	19
GUT	grand unified theory	11
HCAL	hadronic calorimeter	46
HLT	high-level trigger	50
HSCP	heavy stable charged particle	30

HV	hidden valley	
HV	high voltage	69
IP	impact parameter	49
IT	inner tracker	45
LEP	large electron–positron collider	6
LHC	large hadron collider	6
LHCb	LHC beauty	
L0	level-0 trigger	57
L0DU	L0 decision unit	59
MC	Monte-Carlo	56
LLP	long-lived particle	98
LSP	lightest superpartner	18
MB	minimum bias	
MSSM	Minimal Supersymmetric Standard Model	14
mSUGRA	minimal supergravity	
NLSP	next-to-lightest superpartner	29
NMSSM	next-to-minimal supersymmetric standard model	34
QCD	quantum chromodynamics	5
QED	quantum electrodynamics	4
OT	outer tracker	48
PCB	printed circuit board	74
PDG	particle data group	104
PG	particle gun	132
PGS	pretty good simulations	179
PID	particle identification	60
PS	preshower	46
PV	primary vertex	42
RICH	ring imaging cherenkov	
RMS	radiation monitoring system	77
\cancel{P}_R	R-parity violation	23
RV	reconstructed vertex	117

SLHA	supersymmetry Les Houches accord.....	97
SM	Standard Model.....	5
SPD	scintillator pad detector.....	46
SPS	super proton synchrotron.....	92
SSB	spontaneous symmetry breaking	
SUSY	supersymmetry	
TCK	trigger configuration key	
TPMD	<i>TrackPairMaxDistance</i>	
TT	tracker turicencis.....	46
UED	universal extra dimensions	
upPV	upstream primary vertex.....	129
VeLo	vertex locator.....	26
VEV	vacuum expectation value.....	12
zMS	<i>zMaxSpread</i>	
$\sqrt{\chi_{IP,max}^2}$	$\sqrt{trackMaxChi2}$	
$\sqrt{\chi_{IPR,max}^2}$	$\sqrt{trackMaxChi2Remove}$	

List of Figures

1.1	Extrapolation at high energies of the 3 SM gauge couplings. . .	12
1.2	Extrapolation at high energies of the three (inverse) SM and MSSM gauge couplings.	16
1.3	Illustration of a typical SUSY <i>cascade</i>	22
1.4	Neutralino decaying into three quarks via an off-shell squark. .	24
1.5	Gluino lifetime as a function of \tilde{m}	32
1.6	Illustration of a Hidden Valley.	35
1.7	Direct v-hadrons and H^0 production.	35
2.1	Some of the LHC detectors.	43
2.2	View of the LHCb detector [75].	44
2.3	Probability to observe $N = 0,1,2,3$ interactions per bunch crossing w.r.t. \mathcal{L}	45
2.4	The Tracking System of the LHCb detector [75].	47
2.5	View of the inner VeLo from an incoming proton.	48
2.6	The VELO layout	50
2.7	The VELO Sensors layout	50
2.8	ATLAS Pixel detector	52
2.9	CMS Pixel detector	52
2.10	Inside zoom of RF-foil and sensors	52
2.11	Exploded view of the inner VeLo.	52
2.12	Characterisation of the tracks	54
2.13	Tracks reconstruction display	54
2.14	Radiation length of material in the VeLo.	55
2.15	Flow-diagram of the different trigger sequences [75].	57
3.1	Illustration of IT detector.	67
3.2	Support used for the metrology measurements.	70
3.3	Nominal, measured and aligned sensor positions.	72
3.4	Pictures of the foam protections.	74
3.5	Pictures of a glued thermoswitch and an empty box container. .	75

3.6	A cover mounted on its support.	75
3.7	Details of the assembly of a column, a fork, and two colonnettes.	76
3.8	A BEAMS device and the ground wire of the box external shield.	78
3.9	Intervals between cooling rod crenels.	79
3.10	A cooling rod under pressure test.	79
3.11	A cooling rod mounted on its support.	80
3.12	A cover laid on its set-up.	81
3.13	Application of the thermal grease.	84
3.14	Fixing of the modules on the cooling rod.	84
3.15	Closing of the cooling circuit.	87
3.16	Measurement of the distance between the cover and the tip of the sensor modules.	89
3.17	Test of the height of the sensor modules.	91
3.18	A glass frame used to adapt the depth of the container. The sliding set-up and a box being closed.	91
4.1	Justification of the generator cuts.	101
5.1	Flight distance of the LLP.	105
5.2	Flight distance and radial distance of the LLP decay vertex to the z axis.	105
5.3	Radial distance to the z axis of the LLP.	106
5.4	Decay position in z of the LLPs.	106
5.5	Track multiplicity and reconstructed mass w.r.t. <i>IPMax</i>	109
5.6	Track multiplicity and reconstructed mass.	109
5.7	Reconstructed mass from all stable daughters, stable charged and neutral daughters in the acceptance, stable charged in the acceptance only and from all daughters in a cone of radius R=1.	110
5.8	Distance in the $\eta - \varphi$ plane of the LLP daughters.	110
5.9	p_T distribution of the daughter tracks.	113
5.10	Rec. p_T and mass of Mother.	113
6.1	Radial position in the global frame of the reconstructed pri- mary vertices for the 2010 data.	118
6.2	Percentage of VeLo tracks that have a related “long” track and p_T distribution of MC pions.	120
6.3	LLP MC candidate reconstruction efficiency as a function of some the reconstruction parameters.	124
6.4	Position of the upstream PV.	126
6.5	Longitudinal position of the PVs candidates and their radial position w.r.t. the calculated beam axis	126

6.6	Radial distance between the reconstructed and MC-true position and X position of PVs w.r.t. the track multiplicity.	128
6.7	Radial distance of RVs to the beam line and to the upstream PV.	129
6.8	Positions of the RVs in the X-Z plane for the 2010 data and MB.	131
6.9	Positions of the RVs in the X-Z plane for the MB after a filter to remove the RVs from interaction with air in the vacuum tank.	133
6.10	Material distribution as described in the LHCb database in the X-Z plan, integrated over $y \in [-30, 30]$ mm.	133
6.11	Positions of the RVs in the X-Z plane for the 2010 data and MB.	136
6.12	MC LLP reconstruction efficiency w.r.t. the true z decay position, for different criteria of reconstructibility.	141
6.13	<i>Left</i> : MC LLP reconstruction efficiency w.r.t. the distance to the MC PV, for different reconstruction scenarios. <i>Right</i> : Z and radial positions of reconstructed and not reconstructed “reconstructible” candidates.	141
6.14	Percentage of reconstructible MC daughters having an associated track and percentage of non-reconstructible MC daughters having an associated downstream track w.r.t. the z decay position.	142
6.15	Type of the tracks associated to the daughters of reconstructible MC candidates.	142
6.16	Like Fig. 6.15, but limited to tracks associated to a LLP which has been reconstructed.	142
6.17	Nb of downstream tracks that are associated to daughters of LLPs.	144
6.18	Z positions (<i>left</i>) and distance to the beam line (<i>right</i>) of the candidates of some of the selected models.	146
6.19	Reconstructed mass for some of the selected models.	146
6.20	Nb of tracks in the vertex for some of the selected models.	146
6.21	Sum of the scalar p_T of the daughter tracks for some of the selected models.	147
6.22	p_T distribution of the muon with highest p_T in the RV. The absence of muon is marked with a $p_T = 0$	147
6.23	<i>Left</i> : correlation between the reconstructed mass and the number of tracks for 2010 data and some MC models. <i>Right</i> : correlation between the sum of the scalar p_T of the daughter tracks and the number of tracks for 2010 data and some MC models.	147

6.24	Scatter plot the radial and longitudinal positions of the reconstructed vertices for the BV48 models ($\tau_{\tilde{\chi}_1^0} = 10$ ps), to be put in contrast with Fig. 6.8.	148
6.25	Number of candidates per event for some of the selected models. BV48 and HV10 models, featuring a h^0 decaying into 2 LLPs, have a larger distribution.	148
6.26	Reconstructed p_T for some of the selected models.	149
6.27	Reconstructed pseudo-rapidity for some of the selected models.	149
6.28	Reconstructed mass from the Long tracks only, for some of the selected models.	149
6.29	Number of Long tracks at the vertex for some of the selected models.	150
7.1	MC events ($\nu = 2.5$) compared to data results.	158
7.2	MC events ($\nu = 1$) compared to data results.	159
7.3	σ_r and σ_z for data and MC events ($\nu = 2.5$).	159
7.4	σ_r and σ_z for data and MC events ($\nu = 1$).	160
7.5	σ_r and σ_z w.r.t. the number of tracks.	160
7.6	$ \Delta\varphi $ between the two LLP candidates w.r.t. the upstream PV.	161
7.7	IP to the PV distribution.	164
7.8	p_T and mass of the selected Higgs candidates.	165
7.9	p_T and mass of the selected Higgs candidates.	165
7.10	Result of the fit on the invariant mass of the Higgs candidates.	166
7.11	Illustration of a selected event.	169
7.12	Properties of matter interaction from data and MB MC ($\nu = 1$).	172
7.13	Properties of matter interaction from data and MB MC ($\nu = 2.5$).	173
7.14	Standard and max deviation of GPS time in bunches of 30 consecutive saved events.	176
7.15	Properties of seeds found after the LLP decay position.	178
A.1	X position and track multiplicity of the selected PVs.	190
A.2	Radial and longitudinal difference between the reconstructed and MC-truth positions of the selected PVs.	190
A.3	Radial and longitudinal distance to MC-truth w.r.t. the σ of the selected PVs.	191
A.4	Correlation between the radial error and distance to MC-truth.	193
A.5	Correlation between the track multiplicity and σ	193
A.6	Radial position w.r.t. the error.	193
A.7	Longitudinal error w.r.t. the radial error.	194

A.8	Track multiplicity w.r.t. the longitudinal distance to MC-truth.	194
A.9	Track multiplicity w.r.t. the radial distance to MC-truth. . . .	194
A.10	Radial position w.r.t. the radial distance to MC-truth.	195
B.1	Percentage of MC LLP decay vertices that have been split w.r.t. the reconstruction parameters.	199
B.2	Percentage of MC PV that have at least 2 associated RVs w.r.t. reconstruction parameters.	200
C.1	LLP MC candidate reco. efficiency.	202
C.2	Percentage of MC LLP decay vertices that have more than one ass. RV.	203
C.3	Percentage of the “split” MC PV providing a vertex with no backward tracks and a radial distance to the z axis greater than 0.3 mm. <i>Top right</i> : distribution of the radial distance of the split vertex for certain parameters.	204
F.1	LLPs η distributions at generator level.	215
F.2	X-Z positions and reco. mass of vertices from interactions with matter (PG).	216
F.3	Position for a 2 mm slice in y of the RVs from data removed by the matter veto.	217
F.4	Corrected mass distribution of the LLP candidates.	218
F.5	Positions of the two beams obtained from beam-gas interactions.	219
F.6	Variation of the beam line mean position over time.	220

List of Tables

1.1	New fundamental particles of the MSSM.	15
1.2	Parameters of the BV models.	26
1.3	Parameters of the BRpV models.	30
2.1	Some main characteristics of the ATLAS, CMS and LHCb experiments.	51
4.1	The dec files steering the various option files for the production of exotic long-lived particles, and their EventType number. . .	100
5.1	Percentage of events passing the generator cuts, $\sigma \times \text{BR}$ and expected number of events.	114
5.2	Estimation of σ and nb of events for h^0 production.	114
6.1	Percentage of MC signal events with at least one displaced candidate with $M > 3 \text{ GeV}$ that have the reconstructed (true) PV fulfilling the requirements.	127
6.2	Retention of candidates of the different methods to remove RV from interaction with matter.	136
6.3	Summary of the parameter values of the Standard and Optimised vertex reconstruction procedure.	138
6.4	1: percentage of the MC daughter particles associated to a downstream track that have between 2 and 5 associated VeLo clusters (VC). 2: percentage of these downstream tracks that are associated to 2 to 5 VeLo clusters ($\chi^2 < 2$).	144
6.5	Cuts of the HLT2 DisplVertex lines.	151
6.6	Cuts of the stripping DisplVertex lines.	152
7.1	Characteristics of background samples.	155
7.2	Retention for the background samples at the input of the procedure for the Higgs selection.	156

7.3	Flavour composition of MC LLP decays for the BV48 model. .	157
7.4	Number of events at different selection stages for data and MC background.	163
7.5	Number of estimated events at different selection stages for data and MC background.	163
7.6	Number of events selected after the analysis cuts.	167
7.7	Contributions to the detector efficiency at different stages of the event selection.	174
7.8	Contributions to the error on the detector efficiency.	176
7.9	Parameters of the new BV models.	181
7.10	The dec files steering the various option files for the production of the new samples.	181
7.11	Number of 2010 events and detector efficiency for the new BV models.	183
7.12	Number of 2010 events and expected number of events for the new BV models.	183
7.13	Proportion of true Higgs Mothers.	183
D.1	Trigger retention rates.	210
E.1	Summary of the reconstruction parameters.	212
E.2	Retention efficiencies of the stripping DisplVtx lines.	213

Bibliography

- [1] L. Ryder, *Quantum field theory*, Cambridge University Press, 1985.
- [2] The Large Electron–Positron Collider, http://en.wikipedia.org/wiki/Large_Electron-Positron_Collider.
- [3] LEP Collaborations/LEP Electroweak Working Group/SLD Heavy Flavour and Electroweak Groups, *A Combination of Preliminary Electroweak Measurements and Constraints on the Standard Model*, arXiv:hep-ex/0612034v2, <http://lepewwg.web.cern.ch/LEPEWWG/Welcome.html>.
- [4] LEP Electroweak Working Group (Status 2006), <http://lepewwg.web.cern.ch/LEPEWWG/Welcome.html>.
- [5] R. Oerter, *The Theory of Almost Everything: The Standard Model, the Unsung Triumph of Modern Physics*, Plume (2006).
- [6] B. Schumm, *Deep Down Things: The Breathtaking Beauty of Particle Physics*, John Hopkins Univ. Press (2004).
- [7] G. Coughlan, J. Dodd, B. Gripaios *The Ideas of Particle Physics: An Introduction for Scientists*, 3rd ed. Cambridge Univ. Press (2006).
- [8] Y. Fukuda and al. (Super-Kamiokande Collaboration), Phys. Rev. Lett. 81,1562(1998).
- [9] Q. R. Ahmad et al. [SNO collaboration], Phys. Rev. Lett. 89 (2002) 011301.
- [10] For a simple explanation of the seesaw mechanism :
<http://www.quantumfieldtheory.info/TheSeesawMechanism.htm>,
<http://www.fynu.ucl.ac.be/librairie/theses/gustaaf.brooijmans/node14.html>,
http://en.wikipedia.org/wiki/Seesaw_mechanism.

- [11] Pictures borrowed from the Particle Data Group : <http://pdg.lbl.gov/>
- [12] <http://pdg.lbl.gov/>
- [13] E. Witten, Phys. Lett. B 105 267(1981).
- [14] P. Ramond, *Journeys beyond the Standard Model*, Perseus Books, Cambridge, 1999.
- [15] P. West, *Introduction to Supersymmetry and Supergravity*. World Scientific, 1990.
- [16] M. Sohnius, *Introducing Supersymmetry*, Phys. Rep 128(1985)39.
- [17] J. Wess and J. Bagger, *Supersymmetry and Supergravity*, Princeton University Press, 1992.
- [18] M. Rocek, W. Siegel, S. J. Jr. Gates and M. Grisaru, *Superspace, or One Thousand and One Lessons in Supersymmetry*, Benjamin/Cummings, 1983.
- [19] P. Freund, *Introduction to Supersymmetry*, Cambridge University Press, 1986.
- [20] H. Nilles, *Supersymmetry, Supergravity and Particle Physics*, Phys. Rep. 110 (1984),1.
- [21] H. Haber, G. Kane, *The Search for Supersymmetry: Probing Physics beyond the Standard Model*. Phys. Rep. 117 75, 1985.
- [22] J. Ellis, *Limits of the Standard Model*, Cern-TH/2002-320, hep-ph/0211168.
- [23] E. Nikolidakis, C. Smith, *Minimal Flavor Violation, Seesaw, and R-parity*, Phys. Rev. D77:015021 (2008), [arXiv:0710.3129v2]
- [24] S. P. Martin, *A Supersymmetry Primer*, arXiv:hep-ph/9709356 v4, 2006.
- [25] L. M. Carpenter, D. E. Kaplan and E.-J. Rhee, *Reduced Fine-Tuning in Supersymmetry with R-parity Violation*, Phys. Rev. Lett. 99, 211801 (2007)
- [26] T. Sjöstrand, P. Z. Skands, *Baryon number violation and string topologies*, Nucl. Phys. B 659, 243 (2003).

- [27] Jonathan M. Butterworth, John R. Ellis, Are R. Raklev, and Gavin P. Salam, *Discovering Baryon-Number Violating Neutralino Decays at the LHC*, Phys. Rev. Lett. 103, 241803 (2009), arXiv:0906.0728.
- [28] Y. Okada, M. Yamaguchi, T. Yanagida, Prog. Theor. Phys. 85 (1991) 1.
- [29] E. Cremmer and al, Nucl. Phys. B212 (1983) 413.
- [30] H. Goldberg, Phys. Rev. Lett. 50 (1983) 1419.
- [31] M. S. Roberts, A. H. Rots, *Comparison of Rotation Curves of Different Galaxy Types*, Astronomy and Astrophysics 26, 483 (1973).
- [32] A. G. Riess et al. [Supernova Search Team], *Observational Evidence from Supernovae for an Accelerating Universe and a Cosmological Constant*, Astron. J. 116, 1009 (1998) [astro-ph/9805201].
S. Perlmutter et al. [Supernova Cosmology Project], *Measurements of Ω and Λ from 42 High-Redshift Supernovae*, Astrophys. J. 517, 565 (1999) [astro-ph/9812133].
- [33] D. N. Spergel et al. [WMAP collaboration], *Wilkinson Microwave Anisotropy Probe (WMAP) Three Year Results: Implications for Cosmology*, Astrophys. J. Suppl. 170, 377 (2007) [astro-ph/0603449].
- [34] L. E. Ibáñez and G. G. Ross, Nucl. Phys. B 368(1992)3.
- [35] R. Barbier et al., Phys. Rept. 420,, 1 (2005), [hep-ph/0406039]; M. Chemtob, Prog. Part. Nucl. Phys. 54, 71 (2005) [hep-ph/0406029]; B. Allanach, A. Dedes and H.K. Dreiner, Phys. Rev. D 69, 115002 (2004) [hep-ph/0309196]; B. Allanach et al., [hep-ph/9906224]; R. Barbier et al., [hep-ph/9810232]; G. Bhattacharyya, Nucl. Phys. Proc. Suppl. 52A, 83 (1997) [hep-ph/9608415]; H.K. Dreiner, ed. G.L. Kane, World Scientific, 1998, [hep-ph/9707435].
- [36] C. D. Carone, *Low-Scale Quantum Gravity and Double Nucleon Decay*, hep-ph/0103180.
- [37] Searches for Higgs Bosons, extracted from: The Review of Particle Physics (2006) in <http://pdg.lbl.gov>.
- [38] A. Djouadi, *The anatomy of electro-weak symmetry breaking*. Tome I: The Higgs Boson in the Standard Model, hep-ph/0503172, Tome II: The Higgs Bosons in the Minimal Supersymmetric Model, hep-ph/0503173.

- [39] H. Pagels, J.R. Primack, *Phys. Rev. Lett.* 48, 1982 (223), E. Cremer et al., *Phys. Lett. B* 79, 1978 (231).
- [40] J. Schwarz, M. Green, E. Witten, *Superstring Theory*. Cambridge University Press, 1987.
- [41] G. Jungman, M. Kamionkowski, K. Griest, *Supersymmetric dark matter* Physics Reports, v. 267, p. 195-373, 1996.
- [42] P. Achard et al. (L3 Collaboration), *Phys. Lett. B* 524, 65 (2002).
A. Heister et al. (ALEPH Collaboration), *Eur. Phys. J. C* 31, 1 (2003).
J. Abdallah et al. (DELPHI Collaboration), *Eur. Phys. J. C* 36, 1 (2004), *Eur. Phys. J. C* 37, 129 (2004).
- [43] D0 Collaboration, D0 Note 5312 (2007).
- [44] L3 collaboration, *Phys. Lett. B* 524 (2002) 65 [hep-ex/0110057];
ALEPH collaboration, *Eur. Phys. J. C* 31 (2003) 1 [hep-ex/0210014];
DELPHI collaboration, *Eur. Phys. J. C* 36 (2004) 1 [hep-ex/0406009].
- [45] P. Janot, *Phys. Lett. B* 594 (2004) 23 [hep-ph/0403157].
- [46] J. M. Butterworth, J. R. Ellis, A. R. Raklev and G. P. Salam, *Discovering Baryon-number Violating Neutralino Decays at the LHC*, arXiv:0906.0728v1
- [47] Y. Kawamura, *Prog. Theor. Phys.* 105 999 (2001).
- [48] H. K. Dreiner, M. Kramer, B. O'Leary, *Bounds on R-parity violating supersymmetric couplings from leptonic and semi-leptonic meson decays*, *Phys. Rev. D* 75:114016 (2007), [hep-ph/0612278]
- [49] F. de Campos, O. J. P. Eboli, M. B. Magro, D. Restrepo, *Searching Supersymmetry at the LHCb with Displaced Vertices*, *Phys. Rev. D* 79, 055008 (2009)
- [50] Following a discussion with O. J. P. Eboli.
- [51] J. Mira et al. *Bilinear R-parity Violation and Small Neutrino Masses: a Self-consistent Framework*, *Phys. Lett. B* 492:81-90, 2000, [hep-ph/0007266]
- [52] The webpage of M. Strassler about Hidden Valleys : <http://www.physics.rutgers.edu/~strassler/hv/hv.htm>.

- [53] M. J. Strasser and K. M. Zurek, *Echoes of a Hidden Valley at Hadron Colliders*, Phys. Lett. B 651, 374 (2007) [hep-ph/0604261].
- [54] M. J. Strasser and K. M. Zurek, *Discovering the Higgs Through Highly-Displaced Vertices*, Phys. Lett. B 661, 263 (2008) [hep-ph/0605193].
- [55] M. J. Strassler, *Possible Effects of a Hidden Valley on Supersymmetric Phenomenology*, [hep-ph/0607160].
- [56] See for example : D. Hooper and K. Zurek, Phys. Rev. D 77, 087302 (2008). N. Arkani-Hamed and N. Weiner JHEP12(2008)104.
- [57] J. Hubisz, D. Bunk, *Revealing Randall-Sundrum Hidden Valleys*, [arXiv:1002.3160v1], J. Hubisz and al., *Odd Decays from Even Anomalies: Gauge Mediation Signatures Without SUSY*, Phys.Rev.D79:105016, 2009 [arXiv:0901.2933v3].
- [58] N. Arkani-Hamed, S. Dimopoulos,[hep-ph/0405159], G.F. Giudice, A. Romanino, [hep-ph/0406088], W. Kilian, T. Plehn, P. Richardson, E. Schmidt, *Split supersymmetry at colliders*, Eur. Phys. J. C 39, 229–243 (2005) [hep-ph/0507137].
- [59] See for example : http://en.wikipedia.org/wiki/Anthropic_principle.
- [60] G. Farrar, P. Fayet, *Phenomenology of the production, decay, and detection of new hadronic states associated with Supersymmetry*, Phys. Lett. B 76 (1978) p.575.
- [61] A. Belyaev, C.-R. Chen, K. Tobe, C.-P. Yuan, *Phenomenology of Littlest Higgs Model with T-parity: including effects of T-odd fermions*, Phys. Rev. D 74, 115020 (2006), [hep-ph/0609179v2]
- [62] Following a discussion with Alexander Belyaev.
- [63] L. Basso, A. Belyaev, S. Moretti, C. H. Shepherd-Themistocleous, *Phenomenology of the minimal B-L extension of the Standard model: Z' and neutrinos*, [hep-ph/0812.4313v1]
- [64] ATLAS collaboration, *Expected Performance of the ATLAS Detector in GMSB Models with τ final States*, ATL-PHYS-PUB-2009-089, 2009.
- [65] CMS collaboration, *Search for Heavy Stable Charged Particles with 100 pb^{-1} and 1 fb^{-1} in the CMS experiment*, CMS-PAS-EXO-08-003, 2009.

- [66] T. Applequist, H.-C. Cheng and B. Dobrescu, *Bounds on Universal Extra Dimensions*, Phys. Rev. D 64, 035002, 2001.
- [67] Presentation from V. Gligorov, 37th LHCb Software week, 17/6/2009.
- [68] M. Bajko et al., *Report of the Tasf Force on the Incident of 19th September 2008 at the LHC*, CERN Report LHC-PROJECT-Report-1168, 2009.
- [69] Presentation from P. Spradlin, HLT2-physics meeting, 16/7/2009.
- [70] G. Aad et al. [ATLAS collaboration], *The ATLAS Experiment at the LHC*, JINST 3, S08003 (2008), <http://atlas.ch/>.
- [71] R. Adolphi et al. [CMS collaboration], *The CMS Experiment at the LHC*, JINST 3, S08004 (2008), <http://cms.cern.ch>.
- [72] G. Anelli et al. [TOTEM collaboration], *The TOTEM Experiment at the LHC*, JINST 3, S08007 (2008), <http://totem-experiment.web.cern.ch/totem-experiment/>.
- [73] O. Adriani et al. [LHCf collaboration], *The LHCf Detector at the LHC*, JINST 3, S08006 (2008), <http://hep.fi.infn.it/LHCf/>.
- [74] K. Aamodt et al. [ALICE collaboration], *The ALICE Experiment at the LHC*, JINST 3, S08002 (2008), <http://alice.cern.ch>.
- [75] A. Alves et al. [LHCb collaboration], *The LHCb Detector at the LHC*, JINST 3, S08005 (2008), <http://lhcb.cern.ch>.
- [76] MoEDAL collaboration, *Technical Design Report*, CERN-LHC-2009-006.
- [77] P. R. Barbosa-Marinho et al. [LHCb collaboration], *LHCb VELO (VErtex LOcator): Tech-nical Design Report*, CERN Report LHCC-2001-11, 2001.
- [78] R. Antunes-Nobrega et al. [LHCb collaboration], *LHCb Reoptimized Detector Design and Performance: Technical Design Report*, CERN Report LHCC-2003-030, 2003.
- [79] S. Amato et al. [LHCb collaboration], *LHCb Magnet: Technical Design Report*, CERN Report LHCC-2000-007, 2000.

- [80] P. R. Barbosa-Marinho et al. [LHCb collaboration], *LHCb Inner Tracker: Technical Design Report*, CERN Report LHCC-2002-29, 2002.
- [81] P. R. Barbosa-Marinho et al. [LHCb collaboration], *LHCb Outer Tracker: Technical Design Report*, CERN Report LHCC-2001-024, 2001.
- [82] M. Whiteheada, T. Lathama and T. Gershon, *Vertex Locator Simulated Material Description*, LHCb internal note, LHCb-INT-2010-054.
- [83] G. Barrand et al., *Gaudi - A Software Architecture and Framework for Building HEP Data Processing Applications*, Comput. Phys. Commun. 140, 45 (2001), <http://proj-gaudi.web.cern.ch/proj-gaudi/>.
- [84] I. Belyaev et al., *Simulation Application for the LHCb Experiment*, [physics/0306035] (2003), <http://lhcb-release-area.web.cern.ch/LHCb-release-area/DOC/gauss/>.
- [85] I. Belyaev, N. Gauvin et al., *Handling of the generation of primary events in Gauss, the LHCb simulation framework*, LHCb-PROC-2010-056 ; CERN-LHCb-PROC-2010-056.
- [86] T. Sjostrand et al., *The PYTHIA event generator webpage*, <http://home.thep.lu.se/~torbjorn/Pythia.html>.
- [87] D. J. Lange, *The EvtGen Particle Decay Simulation Package*, Nucl. Instrum. Meth. A462, 152 (2001), <http://www.slac.stanford.edu/~lange/EvtGen/>.
- [88] S. Agostinelli et al. [Geant4 collaboration], *Geant4: A simulation toolkit*, Nucl. Instrum. Meth. A506, 250 (2003), <http://geant4.web.cern.ch/geant4/>.
- [89] LHCb collaboration, *The Boole project*, <http://lhcb-release-area.web.cern.ch/LHCb-release-area/DOC/boole/>.
- [90] LHCb collaboration, *The Brunel project*, <http://lhcb-release-area.web.cern.ch/LHCb-release-area/DOC/brunel/>.
- [91] LHCb collaboration, *The DaVinci project*, <http://lhcb-release-area.web.cern.ch/LHCb-release-area/DOC/davinci/>.

-
- [92] LHCb collaboration *The Panoramix project*, <http://lhcb-release-area.web.cern.ch/LHCb-release-area/DOC/panoramix/>.
- [93] GaudiPython twiki, <https://twiki.cern.ch/twiki/bin/view/LHCb/GaudiPython>.
- [94] The ROOT project's website, <http://root.cern.ch>.
- [95] N. Gauvin and M.-O. Bettler, *Qualification of Thermic C05 06 and Honeywell 2455R Thermostats for Use in Magnetic Fields*, CERN EDMS ID 982702.
- [96] M.-O. Bettler, N. Gauvin et al., *Assembly of the Inner Tracker Detector Boxes*, CERN Report LHCb-2008-074, 2007.
- [97] R. Antunes-Nobrega et al. [LHCb collaboration], *LHCb Reoptimized Detector Design and Performance: Technical Design Report*, CERN Report LHCC-2003-030, 2003.
- [98] M. Agari et al., *Test Beam Results of Multi-Geometry Prototype Sensors for the LHCb Inner Tracker*, CERN Report LHCb-2002-058, 2002.
- [99] C. Bauer et al., *Test Beam Results on Inner Tracker Silicon Prototype Sensors*, CERN Report LHCb-2001-135, 2001.
- [100] R. P. Bernhard et al., *The LHCb Silicon Tracker*, NIM A596 (2008) 17, CERN Report LHCb-2007-126, 2007.
- [101] H. Voss et al., *The LHCb Inner Tracker Module Production Steps and Quality Assurance*, CERN Report LHCb-2004-107, 2010.
- [102] S.Koestner, H. Voss, *Long term performance studies of the silicon strip detectors of the LHCb SiliconTracker*, Nucl. Instrum. Meth. A553:259-262,2006.
- [103] L. Roy, *Detector Safety System of the Inner Tracker Detector*, EDMS ID 830675.
- [104] M. Agari et al., *Radiation Monitoring System for the LHCb Inner Tracker*, CERN-LHCb-2007-062.
- [105] M. Capeans, R. Chritin and F. Perez, *Tightness specifications and Test Procedure for the final connections of the cooling and active gas circuits of the ATLAS TRT detector*, EDMS ID 681672.

- [106] G. Conti et al., *Inner Tracker Survey Strategy*, CERN-LHCb-2008-068.
- [107] G. Corti et al., *Monte Carlo Event Type Definition Rules*, LHCb-2005-034, CERN-LHCb-2005-034.
- [108] A. Gallas, N. Gauvin et al., *First Operational Experience from the LHCb Silicon Tracker*, LHCb-PROC-2009-051.
- [109] J. van Tilburg, N. Gauvin et al., *Commissioning and Performance of the LHCb Silicon Tracker*, LHCb-PROC-2010-004, LHCb-CONF-2010-004.
- [110] M. Needham, J. Luisier, *Measurement of the Inner Tracker Efficiency*, CERN-LHCb-INT-2010-031, 2010.
- [111] H. Frampton, P. Q. Hung, M. Sher, Phys. Rept. 330, 263 (2000).
- [112] Courtesy of P. Hopchev.
- [113] A. Djouadi and J. Baglio, *Higgs production at the LHC*, CERN-PH-TH/2010-289, arXiv:1012.0530v2 [hep-ph].
- [114] J. Albrecht et al., *Commissioning and performance of the LHCb hlt1 muon trigger*, Technical Report LHCb-INT-2010-042. CERN-LHCb-INT-2010-042, CERN, Geneva, Aug 2010.
- [115] M. Williams, V. Gligorov et al., *The HLT2 Topological Lines*, LHCb-PUB-2011-002, 2010.
- [116] V. Gligorov, *A single track HLT1 trigger*, LHCb-PUB-2011-003, 2011.
- [117] V. Coco et al., Full scan of the RF-Foil fiducial region using 2010 data, <https://twiki.cern.ch/twiki/pub/LHCb/DisplacedVertexTwiki/movieRFFoil.avi>.
- [118] D. S. M. Alves, E. Izaguirre, and J. G. Wacker, *It's On: Early Interpretations of ATLAS Results in Jets and Missing Energy Searches* ArXiv:1008.0407.
- [119] Work done by V. Coco.
- [120] LHCb collaboration, *Measurement of J/Ψ production in pp collisions at $\sqrt{s} = 7\text{ TeV}$* , Submitted to Eur. Phys. J. C, arXiv:hep-ex/1103.0423v1.

- [121] ATLAS collaboration, *Charged-particle multiplicities in pp interactions measured with the ATLAS detector at the LHC*, arXiv:hep-ex/1012.5104.
- [122] CMS collaboration, *Charged particle multiplicities in pp interactions at $\sqrt{s} = 0.9, 2.36$, and 7 TeV*, JHEP 1101:079,2011.
- [123] Alice collaboration, *Charged-particle multiplicity with ALICE at the LHC*, arXiv:hep-ex/1102.2369.
- [124] Courtesy of Malcolm John.

Curriculum Vitæ

Neal Gauvin

E-mail: neal.gauvin@a3.epfl.ch
Date of Birth: january 12th 1982
Nationality : Swiss

Education, Degrees obtained

May 2011	Ph.D. degree, EPFL
2007 – 2011	Ph.D. Thesis in High-Energy Physics on <i>Search for Higgs Bosons Decaying into Long-Lived Exotic Particles in the LHCb Experiment</i> , LPHE, EPFL Developpment of softwares for the simulation and selection of rare events Contribution to the construction of a subdetector Thesis supervisor: Prof. Aurelio Bay
March 2007	Master in Physics, EPFL <i>Searching for a supersymmetric Higgs Boson in LHCb</i>
2006	Minor in Sustainable Development <i>Environnental Impacts of a Hydrogen-based Economy</i>
2005	Bachelor in Physics, EPFL
2001	1 year exchange, Blaine High School, WA State, USA
2000	Maturité Fédérale, type modern languages, distinction Lycée Denis de Rougemont, Neuchâtel
1997	Ecole secondaire du Val-de-Travers, scientific class, distinction

Other Work Experience and Skills

2007 – 2011	System Administrator (Linux Server)
Programming languages	Mathematica, C/C++, FORTRAN, Python, L ^A T _E X, script like bash, tcsh